AN ABSTRACT OF THE DISSERTATION OF

Ruander Cardenas for the degree of Doctor of Philosophy in Mechanical Engineering presented on September 28, 2011.

Title: Submerged Jet Impingement Boiling Thermal Management.

Abstract approved:

Vinod Narayanan

Technologies such as avionics and power electronics are driving the demand for thermal management schemes towards high heat fluxes and low surface temperatures. Typically, these applications require the dissipation of heat fluxes in the rage of 100-1000 W/cm^2 while maintaining surface temperatures lower than about 85 ^{o}C. Phase-change heat transfer schemes such as pool boiling, flow boiling in mini/micro-channel heat sinks, and sprays and jet impingement boiling are frequently used to meet this demand. This dissertation documents global heat transfer characteristics of submerged jet impingement boiling for high heat flux, low surface temperature applications. The effect of geometrical and flow parameters on heat transfer performance are examined for a single circular jet using water and FC-72 as working fluids. Exclusive to this

study is the comparison of distinct jet fluids at a fixed saturation temperature, which is achieved by comparing sub-atmospheric jet impingement boiling data of water with atmospheric FC-72 experiments. Under sub-atmospheric conditions, the liquid-to-vapor density ratio of water is within a range that has not been studied in previous jet impingement boiling experiments. Varied geometrical parameters include the surface-to-nozzle diameter ratio, surface roughness, and jet configuration. Varied fluidic parameters include pressure, jet exit Reynolds number, fluid subcooling, and fluid properties. Global experimental data collected during this study are used to document the relationship between surface temperature and surface heat flux through boiling curves. The global data are augmented by qualitative high-speed visualization.

Experimental data demonstrate enhanced heat transfer capabilities beyond those of pool boiling by using a submerged impinging jet. For a fixed saturation temperature, significantly higher heat transfer rates are attainable using water in comparison to FC-72. A CHF map for submerged jet impingement boiling is developed based on experimental evidence. A general submerged jet impingement CHF correlation is developed based on a well known CHF model in literature. A novel, passive means of preventing temperature overshoot of highly-wetting fluids during submerged jet impingement boiling is introduced.

Submerged Jet Impingement Boiling Thermal Management

by

Ruander Cardenas

A DISSERTATION

submitted to

Oregon State University

in partial fulfillment of
the requirements for the
degree of

Doctor of Philosophy

Presented September 28, 2011

Commencement June 2012

Doctor of Philosophy dissertation of Ruander Cardenas presented on September 28, 2011.

APPROVED:

Major Professor, representing Mechanical Engineering

Head of the School of Mechanical, Industrial and Manufacturing Engineering

---

Dean of the Graduate School

I understand that my dissertation will become part of the permanent collection of Oregon State University libraries. My signature below authorizes release of my dissertation to any reader upon request.

Ruander Cardenas, Author

ACKNOWLEDGEMENTS

A special thank you goes to my parents, Alice Salazar and Jose Cardenas, and to my brothers, Jose and Andres Cardenas, for all their support and encouragement throughout these years. Without the help and support of Louis and Leona Michalek and the whole Michalek family, none of this would have been possible. I thank my advisor, Vinod Narayanan, for providing me with many opportunities that have allowed me to grow personally and professionally. I am also grateful with many faculty members, especially Sourabh Apte, Jim Liburdy, and Deborah Pence all whom I have learned much from and who have provided guidance to my research work at OSU. I would like to acknowledge the work of the students that have interned in our lab; Connor Dokken: assisted setting-up the experimental facility and collected data, Joseph Kleinhenz: developed the image processing algorithm for contact angle measurements, and Nakul Sridhar: collected the contact angle data. I am indebted to Preeti Mani for all her collaboration with my work and to the rest of my past and present lab mates and friends: Benn Eilers, Mohammad Ghazvini, Whitney Green, David Haley, Douglas Heymann, Florian Kapsenberg, Vishal Patil, Maria Quiroz, Chris Stull, Hadi Tabatabaee, and James Yih for their friendship, help, and support. I also thank my GCR, Henri Jansen, for overseeing the development of my PhD curriculum. The financial support for this project, provided by National Science Foundation under award number 0748249, is also greatly appreciated.

TABLE OF CONTENTS

Page

TABLE OF CONTENTS (Continued)

Page

TABLE OF CONTENTS (Continued)

Page

LIST OF FIGURES

Figure Page

LIST OF FIGURES (Continued)

Figure Page

LIST OF FIGURES (Continued)

Figure Page

LIST OF FIGURES (Continued)

Figure Page

LIST OF FIGURES (Continued)

Figure Page

LIST OF FIGURES (Continued)

LIST OF TABLES

LIST OF APPENDICES

LIST OF APPENDIX FIGURES

LIST OF APPENDIX FIGURES (Continued)

Figure A Page

LIST OF APPENDIX TABLES

NOMENCLATURE

Roman

A area [m^2]

Bo Boiling number $\left(Bo = \frac{q''_{CHF,sat}}{Gh_{lv}} \right)$

Bond Bond number $\left(\frac{g\left[\rho_l - \rho_v\right] d_j^2}{\sigma} \right)$

d diameter [m]

Cp specific heat at constant P [J/kg-K]

G liquid mass flux $\left(G = \rho_l V_j \right)$ [kg/m^2-s]

Gr Grashof number $\left(Gr = \frac{g\beta\Delta T d_{surf}{}^3}{\nu^2} \right)$

g acceleration due to gravity [m/s^2]

H nozzle to surface distance [m]

h heat transfer coefficient [W/m^2-K]

h_{lv} specific latent heat [J/kg]

Ja Jakob number, $\left(Ja = \frac{\rho_l}{\rho_v} \frac{Cp\Delta T_{sub}}{h_{lv}} \right)$

k thermal conductivity [W/m-K]; CHF model factor

$\dot{m}$ mass flow rate [kg/s]

Nu Nusselt number $\left(Nu = \frac{hd}{k_l} \right)$

P pressure [bar]

Pr Prandtl number $\left(\mathrm{Pr} = \frac{Cp\mu}{k} \right)$

q" heat flux [W/cm^2]

r radius [m]

Re Reynolds number $\left(\mathrm{Re} = \frac{\rho_l V_j d_j}{\mu_l} \right)$

Ra roughness average parameter [nm]

$Ra_{d_{surf}}$ Rayleigh number $\left(Ra_{d_{surf}} = Gr\,\mathrm{Pr} \right)$

T temperature [^{o}C]

V velocity [m/s]

x distance [m]

Subscripts

avg average

c critical

CHF critical heat flux

D most dangerous

fd fully developed

H Helmholtz

i incipience

j jet

l liquid

pool pool

sat saturation

sin single-phase

sub subcooled

surf surface

TC thermocouple

v vapor

Greek

α thermal diffusivity [m^2/s]

β expansion coefficient [1/K]

β_n CHF correlation exponent

Δ difference

ε jet impingement boiling effectiveness, correction for subcooling

Θ contact angle [^{o}]

κ CHF model constant [m^{-n}] where n depends on Eq. 14

λ wavelength [m]

μ dynamic viscosity [$N\text{-}s/m^2$]

ν kinematic viscosity [m^2/s]

ν_{lv} specific volume difference [m^3/kg]

ρ density [kg/m^3]

σ surface tension [N/m]

ϕ CHF enhancement [W/cm^2]

SUBMERGED JET IMPINGEMENT BOILING THERMAL MANAGEMENT

1 INTRODUCTION

Advances in many current and new technologies depend strongly on the ability to dissipate large quantities of heat from progressively smaller packages. Figure 1, adapted from Kandlikar and Bapat [1], depicts the relationship between surface heat flux and surface temperature for current and projected thermal management applications in comparison to other conventional heat transfer systems. As seen from this figure, the trend for current chip technology and future military and space applications is leading towards increasing heat fluxes and low surface temperatures. The trend shown in the figure for current chip technology is expected to continue to even higher heat flux values with the ongoing development of three-dimensional chip architecture [2]. The adequate dissipation of heat in high heat flux applications presents a significant thermal management challenge, especially when low surface temperatures are prescribed.

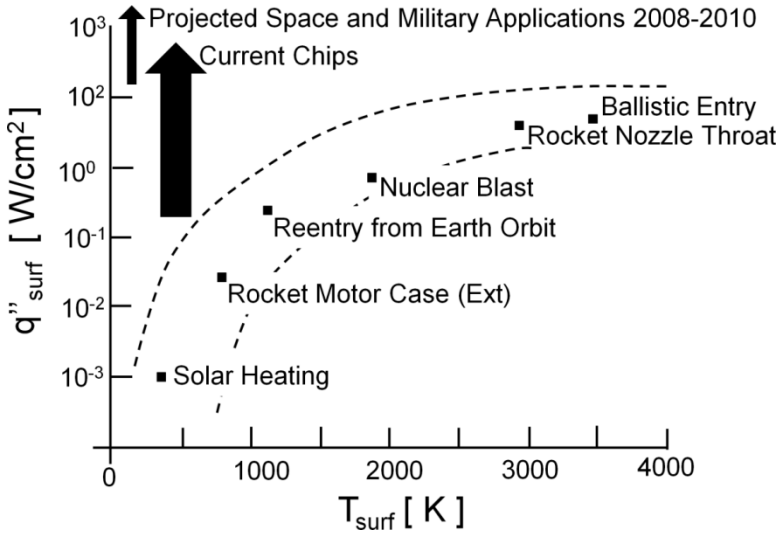

Figure 1: Current and projected demand for thermal management with comparison to other heat transfer applications, modified from Kandlikar and Bapat [1]

Several cooling schemes have been widely employed for the dissipation of thermal energy including natural convection, single-phase forced convection, and boiling heat transfer. Figure 2 illustrates the range of possible heat transfer coefficients attainable with different cooling schemes and heat transfer fluids. Single-phase jet impingement cooling provides one way of achieving high heat transfer coefficients for single-phase convection, and thus, it is currently used in demanding heat transfer applications such as cooling of gas turbine blades, drying of textiles and food, and metals processing. However, for high flux and low temperature applications, boiling heat transfer is essential. Boiling heat transfer achieves the highest heat transfer coefficients (Fig. 2), accommodating large heat flux values with relatively small increments in surface temperature in comparison to single-phase cooling. The combination of jet

impingement with boiling heat transfer offers an attractive opportunity to dissipate extreme levels of heat flux within permissible surface temperature limits.

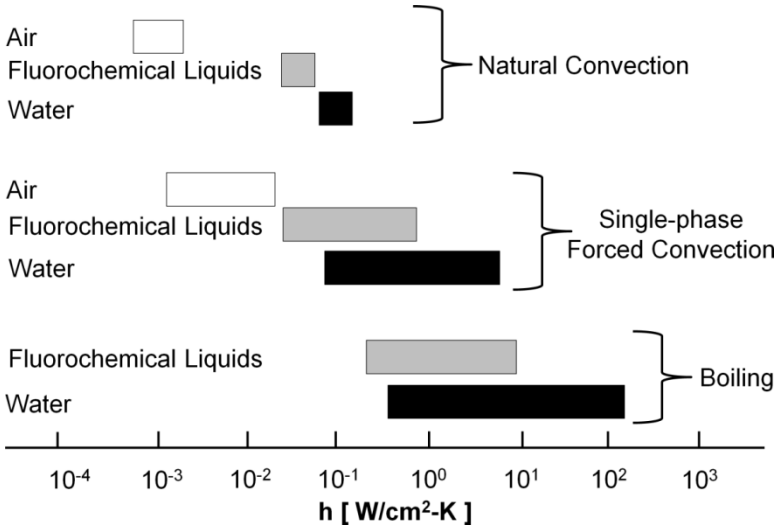

Figure 2: Attainable heat transfer coefficients with natural convection, single-phase liquid forced convection and boiling heat transfer, modified from Mudawar [3]

Jet impingement boiling refers to a condition where a single-phase liquid jet impinges on a heated surface and undergoes phase change at that surface. Numerous studies on jet impingement boiling on a heated surface exist in the context of metals processing, and more recently, electronics cooling. Wolf et al. [4] provide an exhaustive summary of work performed until 1993 in this field. Literature on four different types of liquid jet impingement boiling (Fig. 3) was summarized in their review paper, namely, (i) free surface liquid jets, (ii) submerged jets, (iii) plunging jets, and (iv) confined jets. The majority of jet impingement boiling research has been performed on free surface

liquid jets, wherein the liquid jet issues from the nozzle and is surrounded by a gaseous environment. In contrast, submerged jets refer to a condition where the jet issues into a fluid with the same environment as the jet. Plunging jets issue as a free surface jet, but enter a pool of liquid prior to impinging on the surface. Confined jets are a particular case of submerged jet wherein the liquid surrounding the nozzle is constrained by an upper wall.

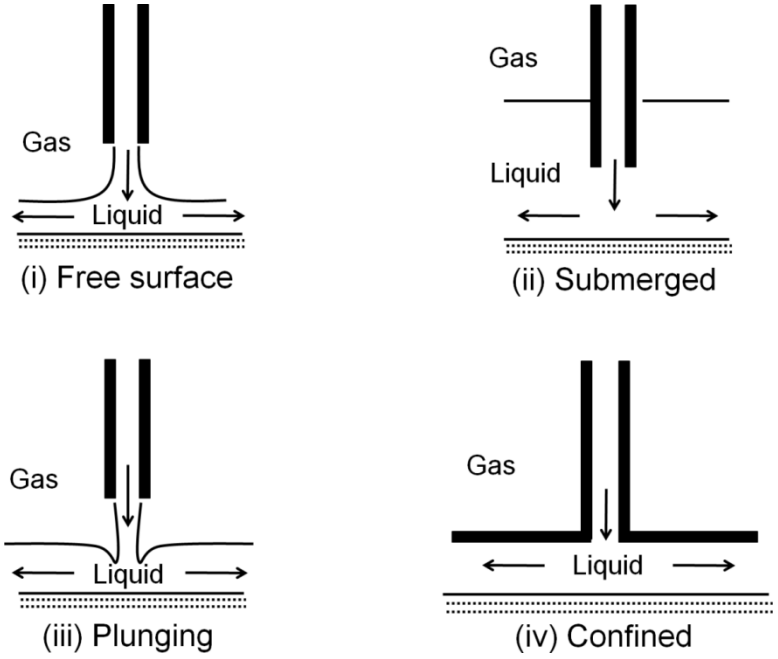

Figure 3: Various jet configurations

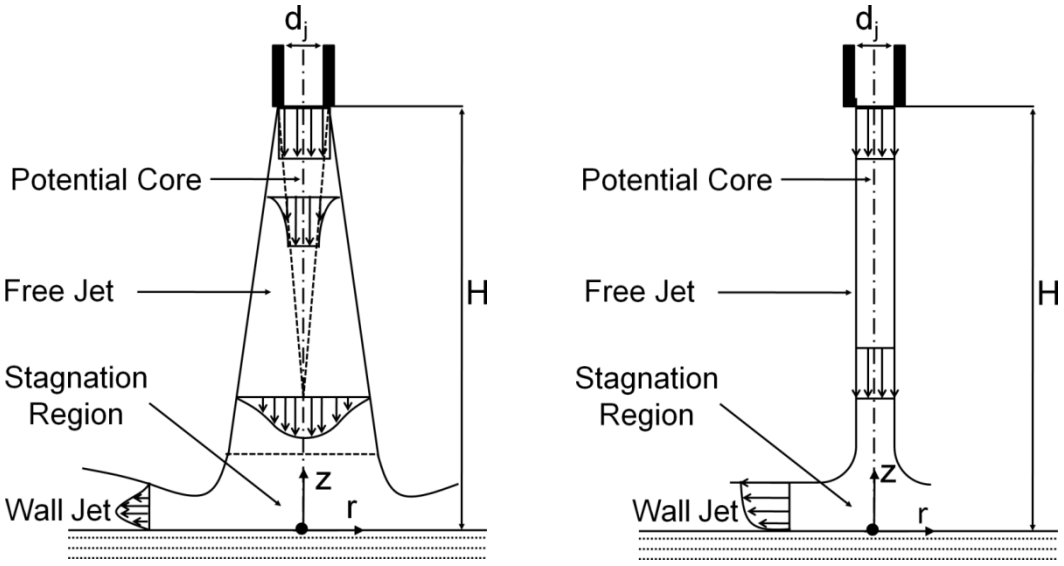

(a) (b)

Figure 4: Flow structure: (a) submerged jet and (b) free surface jet configuration

Jet impingement boiling combines the benefits of the latent heat of the working fluid through the phase-change process and the forced convection enhancement imposed by the jet flow field. Figure 4(a) depicts the flow structure of an axisymmetric impinging submerged jet discharged into a quiescent environment from a circular nozzle of inner diameter d_j. The flow conditions at the nozzle exit determine the initial velocity distribution. If the jet flow in the nozzle is turbulent, the exit velocity profile is close to uniform as shown in Fig. 4. As the distance from the nozzle exit increases, significant momentum exchange between the jet and the ambient fluid causes the free jet boundary to broaden and the potential core, the region within which the initial velocity profile is maintained, to contract. Once the potential core of the jet

disappears, the maximum centerline velocity decreases with increasing distance from the exit. The flow region that is unaffected by the impingement surface is known as the free jet region. At the stagnation region, the region which is affected by the presence of the surface, the flow must decelerate in the normal direction (z) because of the presence of the solid wall and it accelerates in the transverse direction (r) causing a maximum local pressure at the stagnation point. The transverse flow continues to exchange momentum with the surrounding fluid creating a wall jet that broadens as the transverse distance from the stagnation point is increased. For the case shown, the wall jet velocity profile is characterized by the no-slip condition at the free and impingement surface. As seen in Fig. 4(b), the flow structure for an impinging free surface jet is different from that of a submerged jet. In the case of a free surface jet, significantly less momentum exchange occurs with the surrounding fluid, thereby leaving the potential jet core and jet boundary largely unaffected in the free jet region and creating a relatively uniform thickness wall jet. In addition, the wall jet produced by a free surface jet obeys the no-slip boundary condition at the impingement wall and a no-shear boundary condition at the free surface.

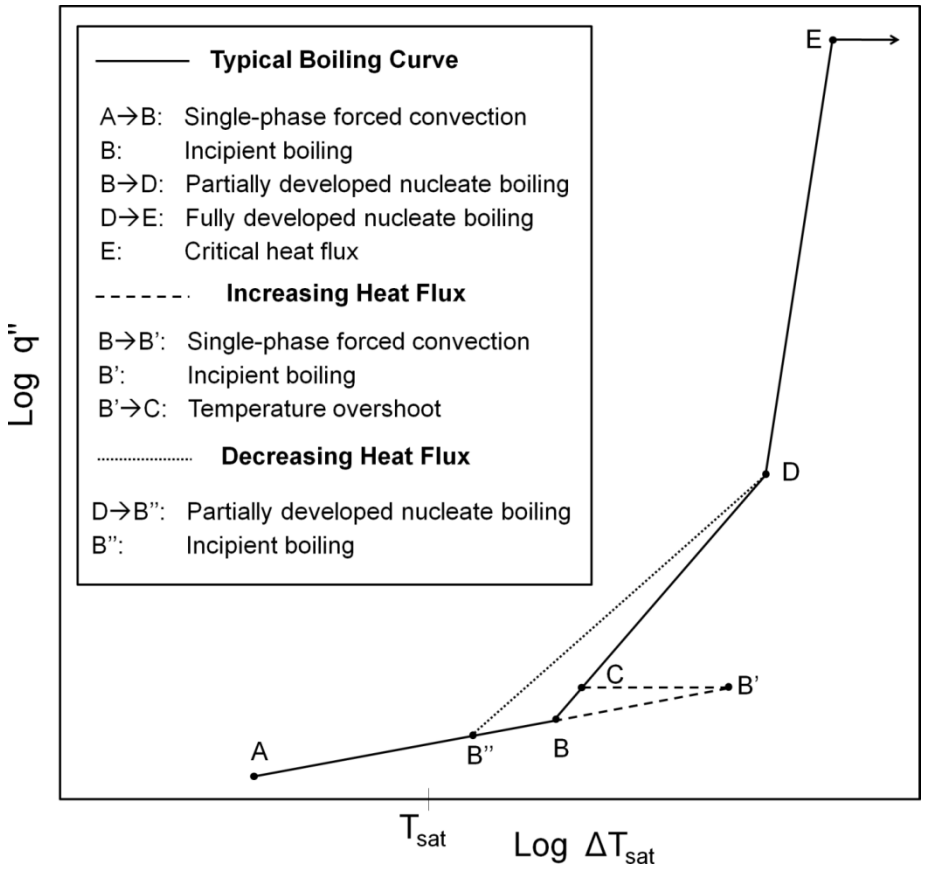

Figure 5: Jet impingement boiling curve including boiling hysteresis for a heat flux controlled surface

Boiling heat transfer characteristics are commonly represented on a log-log plot of wall heat flux as a function of wall superheat. This type of plot is known as a boiling curve [5]. Figure 5 shows an idealized typical boiling curve including boiling hysteresis for jet impingement boiling on a heat flux control surface. The major difference between a boiling curve for jet impingement boiling and a boiling curve for pool boiling is the distinctive regions of partially developed and fully developed nucleate boiling found in the former. Unlike pool boiling, where nucleation is initiated equally over heated surface, in jet impingement boiling nucleation is initiated at the

periphery of the heated surface that is farthest away from the jet influence. Nucleation then proceeds inwards with increasing heat flux until it covers the entire surface. During the boiling phase at low heat fluxes, both single-phase force convection and boiling heat transfer cool the heated surface simultaneously in a process referred to in jet impingement boiling literature as partially developed nucleate boiling. At high heat fluxes, boiling occurs over most of the surface or its entirety, a condition that is known as fully developed nucleate boiling. Similarly to pool boiling, there exists a critical heat flux (CHF) limit that dictates the maximum heat flux value that can be removed from the heated surface.

This study investigates the global boiling heat transfer characteristics of submerged jet impingement boiling focused on high heat flux low temperature applications. The effect of fluidic and geometrical parameters on heat transfer performance is investigated using two distinct working fluids. Experimental results are presented and compared using boiling curve plots. A critical heat flux model is used to develop a jet impingement CHF correlation which can be used to properly predict maximum heat flux limits as a function of important system parameters.

2 LITERATURE REVIEW

This chapter presents a review of relevant jet impingement boiling studies found in literature. The review divides the literature findings into particular regions of interest that are found along a boiling curve for jet impingement boiling up to critical heat flux. The reader is referred to Fig. 5 for a schematic representation of a general jet impingement boiling curve for a heat flux controlled surface. Table 1 at the end of this chapter summarizes the experimental conditions of the most relevant jet impingement boiling studies discussed in this section.

2.1 SINGLE-PHASE FORCED CONVECTION

Single-phase forced convection is the first mode of heat transfer that is encountered under the effect of an impinging liquid jet. This region describes the heat transfer characteristics that are established in complete absence of phase-change [4]. From nucleation theory [6], it is known that the surface temperature must exceed the saturation temperature of the fluid for vapor bubbles to sustain stable nucleation. Therefore, single-phase heat transfer exists below surface temperatures somewhat higher than the fluid saturation temperature (typically 5 ^{o}C higher for water [5]). The review papers by Martin [7] and Viskanta [8] provide hydrodynamics and heat transport basics for single-phase jet impingement and also serve as excellent compendia of work performed in the field.

For single-phase jet impingement, the heat transfer coefficient is only a function of fluid properties, jet flow conditions, and geometry, and does not directly depend on the heat flux or the temperature difference (except through temperature dependency of fluid properties [9]). However, the local heat transfer coefficient varies as a function of location on the surface due to hydrodynamic variations along the wall jet [4]. For average surface conditions, the correlation recommended by Martin (see [5]) for a singular round nozzle indicate that the average heat transfer coefficient over the entire heated surface increases with increasing jet Reynolds number (Re). A study by Ma and Bergles [10] on a submerged R-113 jet showed that during single-phase forced convection, the wall heat flux was noticeably increased with increasing jet velocity for a fixed wall superheat. This trend is indicative of an increased single-phase averaged heat transfer coefficient over the entire surface with increasing jet Re.

2.2 INCIPIENT BOILING

The onset of nucleate boiling for jet impingement occurs at the perimeter of the heated surface where the convective heat transport is lowest [9]. Bergles and Rohsenow [11] defined incipient boiling as the first significant increase of the heat transfer rate from the predicted single-phase forced convection value. This definition was also adopted by Ma and Bergles [10] and Zhuo et al. [12]. This increase in heat transfer coefficient is caused by the initiation of significant phase-change on the heated surface. At boiling

incipience, discrete vapor bubbles are formed and begin to detach from the surface enhancing local fluid motion and heat transfer, which until this point was solely governed by single-phase forced convection [9]. The heat flux at which the incipient boiling occurs has been shown to strongly depend on the size of nucleation sites present on the heated surface and fluid properties [6].

Ma and Bergles [10] and Zhuo et al. [12] experimentally observed that incipient boiling occurred at higher wall superheats for increasing heat flux compared to the case of decreasing heat flux. As stated by [12] ,the term superheat excursion was defined by You et al. [13] at boiling inception as "the maximum temperature difference (along a line of constant heat flux) between the surface temperature for increasing heat flux and that for decreasing heat flux." The incipient boiling point observed for decreasing heat flux is of interest for characterizing the surface since it captures a stable and established boiling behavior [10]. For surfaces where the largest nucleation cavities were restricted by a maximum radius r_c, the range of cavity sizes present on the heated surface has been successfully estimated by [10] and [12] using the decreasing heat flux incipient boiling,

$$q''_i = \frac{k_l \left(\Delta T_{sat}\right)_i}{r_c} - 2\frac{\sigma k_l T_{avg} v_{1v}}{h_{lv} r_c^2} \tag{1}$$

Incipient boiling can also be influenced by the interactions between the liquid and the heated surface. Liu and Qiu [14] and Qiu and Liu [15] studied boiling heat transfer from a free surface water jet on a copper surface coated with TiO_2. For the untreated

coated surface, the measured contact angle of a sessile drop was between 20^{o} and 40^{o}. When the coated surface was gradually treated with ultra-violet light, it became superhydrophilic and the sessile drop contact angle decreased to less than 5^{o} [14]. Their studies found that incipient boiling on the superhydrophilic surface was greatly delayed compared to the untreated surface case consistent with theory [6].

Liu and Zhu [16] studied the boiling heat transfer characteristics of an impinging free surface jet for a surface-to-nozzle diameter ratio of unity and found that higher jet velocities delayed incipient boiling. Van Carey [6] suggest that the reduction in the thermal boundary layer thickness associated with higher jet velocities may suppress the onset of nucleation to higher wall superheats. For a surface-to-nozzle diameter ratio of approximately seven, Zhou et al. [12] found incipient boiling to be independent of jet parameters. This discrepancy in experimental findings could be caused by the distinctive surface-to-nozzle diameter ratios which determine the distance between the stagnation zone and the periphery of the heated surface.

Liu et al. [17] found that for jet impingement boiling, a higher fluid subcooling delayed incipient boiling to higher wall superheats. This result agrees with Hsu's model for heterogeneous nucleation [6]. In the contrary, Zhou et al. [12] found lower boiling incipience superheats with increasing fluid subcooling. The authors argued that higher fluid subcoolings causes an increase in surface tension and increases the capability of the bulk fluid to trap residual vapor resulting in a lower incipient boiling

superheat. In the review paper, Wolf et al. [4] documented a similar discrepancy on the dependency of incipient boiling with fluid subcooling.

Incipient boiling can also be affected by other factors which are specific to the particular test methodology. Zhou et al. [12] identified surface aging as an important factor on boiling heat transfer particularly near boiling incipient using fully degassed L12378 and R-113 as working fluids. The authors found that immersing the surface for 10 hours prior to an experiment compared to only one hour prior to an experiment shifted the boiling curve to the left resulting in a lower incipient boiling. Consistent experimental results were obtained for surfaces that were immersed for 10 hours prior to an experiment. In the same study it was found that heat transfer characteristics without degassing have poor repeatability near boiling incipience. It was reported that dissolved gasses enhanced heat transfer and resulted in a lower incipient boiling.

2.3 TEMPERATURE OVERSHOOT

Heated surfaces that are not strictly temperature controlled often reach the incipient boiling through a surface temperature overshoot. Dukle and Hollingsworth [18] defined the temperature overshoot, as “the amount by which the wall superheat attained just prior to the initiation of boiling exceeds the wall superheat attained immediately after.” Note that there is a difference between the terms superheat excursion and temperature overshoot. A boiling curve with no temperature overshoot

can still have a superheat excursion due to the differences in incipient boiling with increasing and decreasing heat flux.

Zhou et al. [12] suggested that temperature overshoot is a macro-manifestation of the deactivation of vapor embryos on the heated surface. If the heated surface is completely wetted by the liquid, the cavities on the surface during increasing heat flux conditions do not have entrapped vapor and require large wall temperatures to become active, resulting in a temperature overshoot at boiling incipience. For decreasing heat flux conditions, the cavities are already active and are able to sustain stable nucleation down to lower surface temperatures in comparison to increasing heat flux conditions. For this reason, temperature overshoot occurs mainly on highly polished smooth heated surfaces and it is augmented by the small surface tension of highly wetting fluids. The combination of these two aspects eventually leads to a temperature overshoot [12]. During temperature overshoot, the surface can be 10 ^{o}C to 30 ^{o}C higher than the fluid saturation temperature [18].Therefore, temperature overshoot becomes extremely important in temperature sensitive cooling applications on which failure to initiate boiling can cause severe damage.

Nakayama et al. [19] reported a slightly increasing temperature overshoots with increasing jet velocity using a confined jet. The authors attributed this behavior partly to the increase on the local pressure near the surface with increasing jet velocities. Ma and Bergles [10] found that the temperature overshoot was more significant for a saturated fluid compared to a subcooled fluid.

2.4 PARTIALLY DEVELOPED NUCLEATE BOILING

Increases in heat flux beyond incipient boiling leads into the partially developed nucleate boiling mode. In this region, both jet impingement and boiling heat transfer simultaneously cool the heated surface. Boiling is limited to small numbers of vapor bubbles and the jet flow continues to strongly influence the heat transfer from the surface [9]. Dukle and Hollingsworth studied the effect of a monotonic [18] and a nonmonotonic [20] distribution of the single-phase heat transfer coefficient during partially developed jet impingement boiling using liquid crystal imaging. For a surface-to-nozzle spacing of 8.2 jet diameters [18], the single-phase forced convection heat transfer coefficient monotonically decreased from a maximum value at the stagnation point. This distribution of heat transfer coefficient caused the surface temperature to rise smoothly along the streamwise direction and boiling to initiate on the surface region furthest away from the stagnation point. As the heat flux was increased, the region cooled by single-phase force convection adjacent to the boiling front reached the necessary conditions to initiate nucleation and the boiling front lurched inwards in a process that the authors defined as annexing. For a surface-to-nozzle spacing of 2.3 jet diameters [20], the single-phase forced convection heat transfer coefficient showed a secondary local maximum at about 3.5 nozzle radii from the stagnation point. This secondary peak was attributed to a laminar to turbulent transition of the boundary layer of the wall jet [20] and caused a local minimum and maximum in surface temperature near the stagnation zone. A similar inwards movement of the boiling front was observed under these circumstances compared to

the monotonic case. However, as the heat flux was increased, the location on the surface with a secondary maximum temperature approached the onset of boiling. This eventually resulted in a sudden boiling front collapse inwards over a significant region on the heated surface.

Wolf et al. [9] showed that increasing jet velocities significantly enhanced heat transfer during partially developed nucleate boiling. Similar results have been reported by Qiu and Liu [21] and Zhou and Ma [22] confirming the importance of forced jet flow convection during partially developed nucleate boiling. In addition to the jet flow, bubble-enhanced mixing and the latent heat of vaporization significantly improves cooling, yielding higher heat transfer rates than those found for the single-phase forced convection alone. Fluid subcooling was found to enhance heat transfer rates during partially developed nucleate boiling [10, 12, 17, 22].

On the boiling curve, the partially developed nucleate boiling region outlines a gradual transition between single-phase forced convection and fully developed nucleate boiling. This region is often known as the "knee" of the boiling curve. Ma and Bergles [10] successfully employed an interpolation method proposed by Bergles and Rohsenow [11] of the form

$$q'' = \left[q''_{\sin}{}^{n} + \left(q''_{fd} - q''_{i} \right)^{n} \right]^{\frac{1}{n}} \tag{2}$$

with n=2 to trace the outline of the boiling curve from single-phase forced convection to fully developed nucleate boiling including the partially developed region. This method reduces the heat flux to the single-phase forced convection at low values of heat flux and gradually leads to the fully developed heat flux at high heat flux values. More recently, Zhou and Ma [22] found that Eq. 2 with n=3 better fit their data. For system exhibiting a temperature overshoot, Eq. 2 can only be used to trace the decreasing heat flux boiling curve.

2.5 FULLY DEVELOPED NUCLEATE BOILING

The transition between partially developed and the fully developed nucleate boiling is seen as a second increase in the slope of the boiling curve [9]. This enhancement in heat transfer is caused by a significant increase in bubble population density on the surface. Under these conditions, heat transfer becomes dominated by bubble formation and departure from the heated surface [9]. Wolf et al. [9] found that the streamwise distance from the stagnation point had no significant effect on the heat transfer during fully developed nucleate boiling and that the surface temperature became nearly uniform everywhere that boiling took place.

Katto and Kunihiro [23] found no differences in the fully-developed nucleate boiling region of the boiling curve between pool boiling and jet impingement boiling for both free surface and submerged jet configurations using saturated water as the working

fluid. The authors reported that, in jet impingement, the fully developed nucleate boiling region took the form of a monotonous extension of the fully developed pool boiling curve. Monde and Katto [24] found that for a free surface jet configuration, boiling curves for fully developed nucleate boiling were independent of jet velocity, nozzle diameter, heated surface diameter, and heated surface orientation. A common conclusion among jet impingement boiling studies [9, 16, 17, 22, 24] has been that fluid motion on the heated surface for fully developed nucleate boiling is so active that it is hardly affected by the jet forced convection. It is believed by these studies that most of the heat removed from the surface is through the latent heat of vaporization of the fluid and the intense mixing induced by vapor bubbles leaving the surface regardless of jet parameters and configuration.

Zhou and Ma [22] reported that the fully developed nucleate boiling curve shifted toward the left with increasing fluid subcooling for a submerged jet configuration. In contrast, Liu et al. [17] found that the fully developed nucleate boiling curve was insensitive to fluid subcooling for a free surface jet. While it is not clear if the jet configuration plays a significant role, Wolf et al.'s [4] literature review reported similar contradictions regardless of jet configuration. For the simpler case of pool boiling, it has been suggested that fluid subcooling shifts the boiling curve to the left improving heat transfer performance [6].

Surface conditions can also affect the fully developed nucleate boiling curve. Ma and Bergles [10] reported day-to-day shifts in the fully developed nucleate boiling curve

using R-113, despite the rigorous procedure taken to ensure uniform surface conditions. The general trend was toward improved heat transfer characteristics over time. The authors suggested that surface "rejuvenation" through dissolution of contaminants that appreciably reduced the number and size of cavities could have caused this trend.

2.6 CRITICAL HEAT FLUX

Buoyancy is fundamental for the efficiency of boiling heat transfer from a horizontal surface facing up. This force removes the vapor bubbles that are generated and allows the fluid to continuously re-wet the surface [25]. At elevated values of heat flux, the rate of surface re-wetting becomes insufficient to balance the rate of evaporation and a catastrophic increase in surface temperature occurs which can lead to surface burnout. This maximum heat flux that leads to a catastrophic increase in surface temperature corresponds to the critical heat flux (CHF).

It has been suggested that CHF in pool boiling is associated to the consumption of fluid within a thin liquid layer maintained on the heated surface during nucleate boiling [26]. Therefore, CHF occurs by an imbalance in the supply and consumption of fluid in this liquid layer. Katto and Kunihiro [23] were among the first to suggest the use of an impinging liquid jet to increase the fluid supply to the surface and thus increase CHF. Their study showed that CHF increased with increasing jet velocity

reaching higher magnitudes than pool boiling CHF and highlighted the benefits of using an impinging jet to control CHF.

Gambill and Lienhard [27] showed that, for many flow boiling configurations, the majority of CHF studies in literature have only reached about 10 percent of the maximum possible heat flux predicted by kinetic theory. A recent study by Mitsutake and Monde [28] on a highly subcooled (ΔT_{sub}=115 ^{o}C) high velocity (V_j=35 m/s) water jet reported a CHF value of 21.19 kW/cm^2 corresponding to 48 percent of the theoretical maximum. This result reveals the benefit of using jet impingement boiling to effectively increase the upper limit of cooling.

Katto and Shimizu [29] suggested the existence of at least three different CHF regimes for free surface jet impingement boiling. The first regime (D-regime or L-regime [30]) occurs due to the deficiency of the liquid supply compared to the heat load. In this regime, CHF is reached prematurely due to insufficient jet latent heat capacity rate. The second and more common CHF regime (V-regime) is that of variation of CHF with jet velocity, which occurs when the heat transfer rate from the surface is only a small fraction of the jet latent heat capacity rate. In the third regime (I-regime), CHF is independent of jet velocity. This last regime was experimentally observed at relatively high system pressures (P=15-25 bar [29]) . While the existence of these three CHF regimes has been reiterated in free surface jet configurations [4], little information exist on the applicability of these conditions in the submerged jet configuration.

CHF dictates the upper limit of cooling beyond which a catastrophic surface temperature overrun occurs. For this reason, significant attention in literature has been given to study and quantify changes in CHF with jet flow in the V-regime. CHF enhancement for free surface jet impingement boiling has been studied extensively [16, 24, 29-34] and several correlations have been proposed for this jet configuration. In general, these correlations for free surface jet predict a CHF dependency on jet exit velocity of the form $q''_{CHF} \propto V_j^n$ where the value of n lies in the range $0.16 < n < 0.44$ [35] with n=1/3 being the most cited value. Mudawar and Wadsworth [35] found $n = 0.7$ for a confined jet configuration. In general, the liquid-to-vapor density ratio has been an important parameter that appears in most jet impingement CHF correlations developed so far. However, no consistent dependency of CHF on the liquid-to-vapor density ratio has been established.

CHF studies for submerged jet impingement boiling have been more limited and CHF correlations for this jet configuration are sparse. For this reason, CHF in submerged jet configurations is often compared against CHF correlations developed for free surface jets. For example, Zhou and Ma [22] compared CHF data from a submerged R-113 jet against a CHF correlation for free surface jet configuration developed by Monde and Katto [24] and found that the correlation only captured 85% of the data within a ±40% error. The free surface jet CHF correlation under predicted the CHF data by Zhou and Ma for 87% of the cases considered. While no clear explanation was provided to

account for the discrepancy, the jet configuration itself could have contributed to this difference.

In free surface jets, droplet breakup and ejection could occur at high heat fluxes or under insufficient liquid supply. Such a condition would not exist for submerged jet configurations due to the presence of the liquid pool. In addition, for submerged jets, entrainment results in spread of the jet prior to impingement. Entrainment of vapor bubbles departing from the surface back into the flow of a submerged jet could create additional nucleation sites on the surface. Based on these arguments, it would be reasonable to anticipate differences in the heat transfer characteristics of submerged and free surface configurations, especially at elevated values of heat flux. Few studies have directly compared the heat transfer characteristics of free surface and submerged jet configurations. Katto and Kunihiro [23] compared CHF values between these two jet configurations and found that CHF for submerged jets consistently exceeded that of the free surface jet configuration for jet exit velocities of less than 3 m/s. This trend agrees with the higher CHF values found by Zhou and Ma [22] in the submerged jet configuration when compared to free surface jet data from Monde and Katto [24]. These results suggest that CHF correlations developed for free surface jets cannot be reliably used to predict CHF in the submerged jet configuration.

Jet impingement CHF has been shown to increase significantly with an increase in liquid subcooling regardless of jet configuration [17, 19, 24, 28]. A similar trend has been documented for the simpler case of pool boiling CHF [36]. Surface tension and

contact angle also play an important role in jet impingement CHF. Liu and Qiu [14] found that the CHF on a superhydrophilic surface was about 50 percent greater than that of a plain surface. Nakayama et al. [19] and Mitsutake and Monde [28] found that the size (amount of thermal mass) and dimensions of the heater are also important factors in jet impingement CHF.

Table 1 summarizes the experimental conditions considered in the most relevant jet impingement boiling studies mentioned above. Experiments have been performed for free surface, submerged, plunging, and confined jet configurations using a number of different fluids. Different jet heights and nozzles sizes have been studied using either circular or slot jet geometries. Saturated and subcooled fluid temperatures have been considered for a large range of jet exit velocities. In general, these studies have found that jet impingement boiling enhances heat transfer in the single-phase and the partially developed nucleate boiling regions of the boiling curve. In the fully developed nucleate boiling region, heat transfer characteristics have been reported to be rather independent of jet parameters. Critical heat flux has been found to significantly increase with jet exit velocity and fluid subcooling.

Despite the vast amount of research performed on the field of jet impingement boiling, distinctions between the heat transfer characteristics from different jet configurations are not entirely clear. In comparison to the free surface jet configuration, studies using the submerged jet configuration have been more limited. Submerged jet impingement boiling is an attractive mechanism to augment the heat transfer capabilities of two-

phase liquid immersion cooling which is already being used on demanding electronic cooling applications. This study characterizes the benefits gained by using submerged jet impingement boiling beyond the capabilities of conventional pool boiling heat transfer. The experimental conditions considered in this study are of importance to high heat flux and low surface temperature cooling applications.

Table 1: Summary of experimental conditions for relevant jet impingement studies

Ref	Jet Config.	Fluid	Jet Height [mm]	Nozzle Size [mm]	Surface Size [mm]	ΔT_{sub} [^{o}C]	V_j [m/s]
[9]	Free^{V}	Water	H=102	10.2x102	35.7x260	50	2-5
[10]	Submerged^{H}	R-113	H=2.14, 3.62 (H/d_j=2)	d_j=1.07, 1.81	5x5 3x3	0, 12.5, 20.5	0-10.5
[12]	Submerged^{H}	R-113 L12378	unknown	d_j =0.96, 1.01	5x5	4.7-28.4	0-11.35
[14]	Free^{V}	Water	H=5	d_j =4, 8	d_{surf}= 4, 8	0-80	0.5-8 Re= $2.5x10^4$-$4x10^5$
[15]	Free^{V}	Water	H=5	d_j =4	d_{surf}= 20	0-74	0.5-6.5 Re= $2.5x10^4$-$4x10^5$
[16]	Free^{V}	Water	H=10	d_j =10, 6, 2	10x10, 6x6, 2x4	0	0.5-6
[17]	Free^{V}	Water	H=5	d_j =3, 6, 8, 12	d_{surf}= 12, 8, 6, 3	15-80	0.5-6
[18]	Submerged^{V}	R-11	H=61.5	d_j =7.5	114x114	5	Re= 37080, 27810, 18540
[20]	Submerged^{V}	R-11	H=17.25	d_j =7.5	114x114	5	Re= 37080, 27810, 18540
[19]	Confined^{H}	FX3250	H=2	1x35	35x24	20, 10, 2	0.35-5
[21]	Free^{V}	Water Ethanol R-113 R-11	H=5	d_j =3-12	d_{surf}=3-12	0	0.5-10
[22]	Submerged^{H}	R-113	unknown	d_j =0.96, 1.01	5x5	18.5-27.6	0-11.36
[23]	Free^{V} Plunging^{V} Submerged^{V}	Water	H=1-30	d_j =0.71, 1.165, 1.6	d_{surf}=10	0	0-3
[24]	Free^{V}	Water R-113	unknown	d_j=2- 2.5	d_{surf}= 11-21	0-30	2.04-26
[28]	Free^{V}	Water	H=5	d_j=2	5x4 10x4	80-170	5-60
[29]	Free^{V}	Water R-12 R-113	unknown	d_j=2	d_{surf}=10	0	0.5-18

V: vertical jet orientation, H: horizontal jet orientation

3 OBJECTIVES

The overall objective of this study was to experimentally investigate the effect of geometric and fluidic parameters on global heat transfer characteristics of submerged jet impingement boiling. In particular, this study was focused on low surface temperature, high heat flux thermal management. This work was inspired by the practical application of cooling high power electronics that normally requires surface temperatures to be maintained below 85 ^{o}C while sustaining heat fluxes of more than 100 W/cm^2 [2]. Typically, dielectric fluids like FC-72 are used to cool such electronic devices. However, pure deionized water has superior thermal properties, including an enthalpy of vaporization that is two orders of magnitude higher than most dielectric and heat transfer fluids (Table A 1 in appendix1), and is hence the fluid of choice for high flux cooling applications. However, to apply jet impingement boiling using water to high flux electronics cooling, experiments must be performed at sub-atmospheric pressures, thereby reducing the fluid saturation temperature to meet prescribed maximum surface temperature requirements.

Geometrical parameters of interest included surface roughness, jet nozzle diameter, and jet configuration. Fluidic parameters of interest included pressure, jet exit momentum, fluid subcooling, and fluid properties. To assess the effect of system parameters on the heat transfer performance of submerged jet impingement boiling, several non-dimensional groups and equations that are of importance to this cooling scheme were considered. The effect of jet exit momentum and fluid viscosity on heat

transfer performance was captured with variations in jet exit Re. The effect of fluid subcooling was incorporated with changes in Jakob number (Ja). Pressure and fluid property effects were considered with changes in liquid-to-vapor density ratio (ρ_l/ρ_v). Surface tension forces were considered with changes in Bond number (Bond). CHF limits were captured with Kutateladze CHF correlation for pool boiling and with Boiling number (Bo) and enhancement ratios (CHF/CHF_{pool}) for jet impingement boiling. Variations in jet diameter were evaluated with varying surface-to-nozzle diameter ratios (d_{surf}/d_j). Surface roughness was incorporated by using an average surface roughness measurement (Ra). The configuration effects were evaluated by performing preliminary free surface jet impingement boiling experiments and comparing them with the submerged jet impingement boiling data. Figure 6 summarizes the geometrical and fluidic parameters considered during submerged jet impingement boiling and the two-phase regions of the boiling curve which were studied.

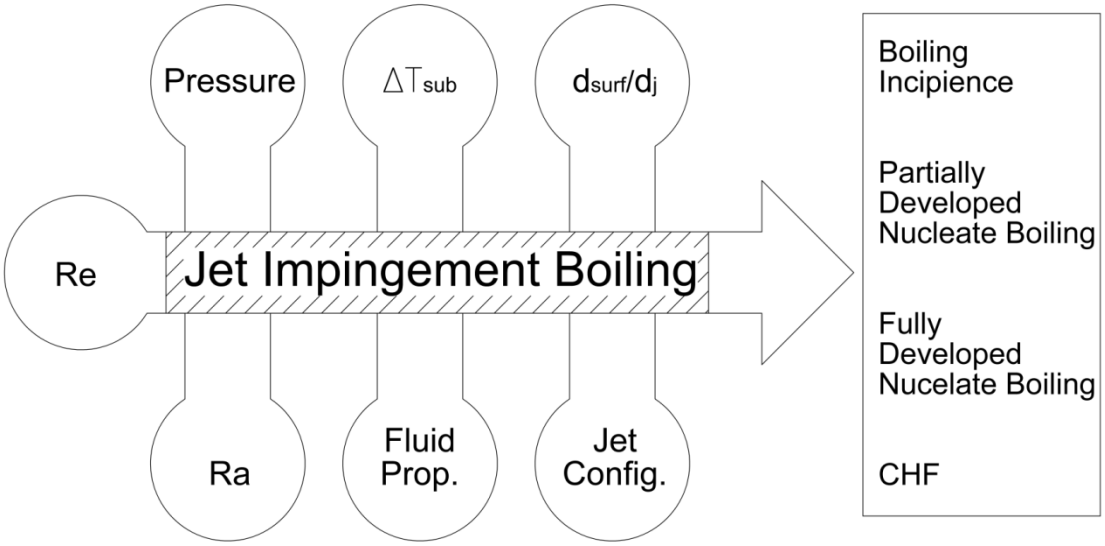

Figure 6: Geometrical and fluidic parameters considered and two-phase boiling curve regions studied

Experiments were performed at a fixed non-dimensional nozzle-to-surface distance, H/d_j , of six which corresponds to an approximately optimum spacing for heat transfer performance in single-phase jet impingement [5]. Water jet impingement boiling experiments were performed at three sub-atmospheric pressures of 0.176 bar, 0.276 bar, and 0.477 bar with corresponding fluid saturation temperatures of 57.3 ^{o}C, 67.2 ^{o}C, and 80.1 ^{o}C. The corresponding density ratios, ρ_l/ρ_v, at these sub-atmospheric conditions were between 5.3 and 2.1 times larger than at atmospheric pressure, conditions that have not been previously reported in literature for jet impingement boiling despite the importance of this parameter on jet impingement CHF. At each pressure, the jet exit Re was varied from 0 (pool boiling) to 14500. Two distinct surface finishes with values of Ra of 123 nm and 33 nm were tested. Experiments were performed at saturated and subcooled fluid temperatures. Jet and pool

temperatures were maintained at the same value, so that thermal entrainment can be neglected.

To quantify the effect of fluid properties, two fluids with distinctive thermal-physical properties, namely water and FC-72, were contrasted. At the lowest pressure of 0.176 bar, the saturation temperature of water (T_{sat}=57.3 ^{o}C) was comparable to that of FC-72 at atmospheric pressure (T_{sat}=56.6 ^{o}C). Therefore, the boiling heat transfer characteristics obtained for water were directly compared against those obtained using a dielectric fluid (FC-72) for an almost equivalent fluid saturation temperature. For FC-72, three surface-to-nozzle diameter ratios, d_{surf}/d_j, of 23.8, 12.1, and 7.0 were compared by variation of the jet nozzle diameter. A comparison between submerged jet impingement boiling and free surface jet impingement boiling using water as the working fluid was performed to capture the effect of jet configuration. High-speed photography was also conducted to qualitatively capture changes in two-phase flow behavior with changes in system parameters.

4 EXPERIMENTAL FACILITY AND METHODS

This chapter describes the experimental test facility and introduces the design of the test chamber and test section utilized to collect data. A detailed list of equipment and instrumentation is provided and other important components in the system are included. The considered experimental conditions are presented and the methods for gathering data are explained. Finally, the corresponding steps implemented for data reduction are given and uncertainty estimates are provided.

4.1 TEST FACILITY

Figure 7 provides a simplified schematic of the experimental facility developed for jet impingement boiling experiments. The facility comprised a test chamber and seven auxiliary sub-systems: (a) pool pressure control sub-system, (b) degassing chamber, (c) jet flow loop, (d) test section, (e) pool temperature control loop, (f) vapor condensation loop, and (g) data acquisition sub-system. The test chamber, separately illustrated in Fig. 8, consisted of a 10 x 7.5 x 10 in^3 (0.0123 m^3) stainless steel 316 box that contained the pool of fluid during the experiments. The ½ in thick walls of the test chamber were welded together to provide a vacuum tight seal. Three ½ in thick clear polycarbonate windows permitted flow visualization during boiling studies. Removable sections of the test chamber, which included the windows, the chamber top plate, and the test section, were sealed using standard o-rings and backup rings

where necessary. Table A 2 in appendix 2 contains a detailed list of the location of the o-rings, o-ring type, and materials used which were compatible with both working fluids. Standard screw fasteners were utilized to affix these removable sections to the test chamber while applying uniform pressure on the o-ring seal. Table A 3 in appendix 2 shows a list of the type of screws used and their required length. The test chamber windows were pressed against the o-ring seal through the use of ¼ in think stainless steel flanges. Detailed part drawings of the test chamber can be found in appendix 3.

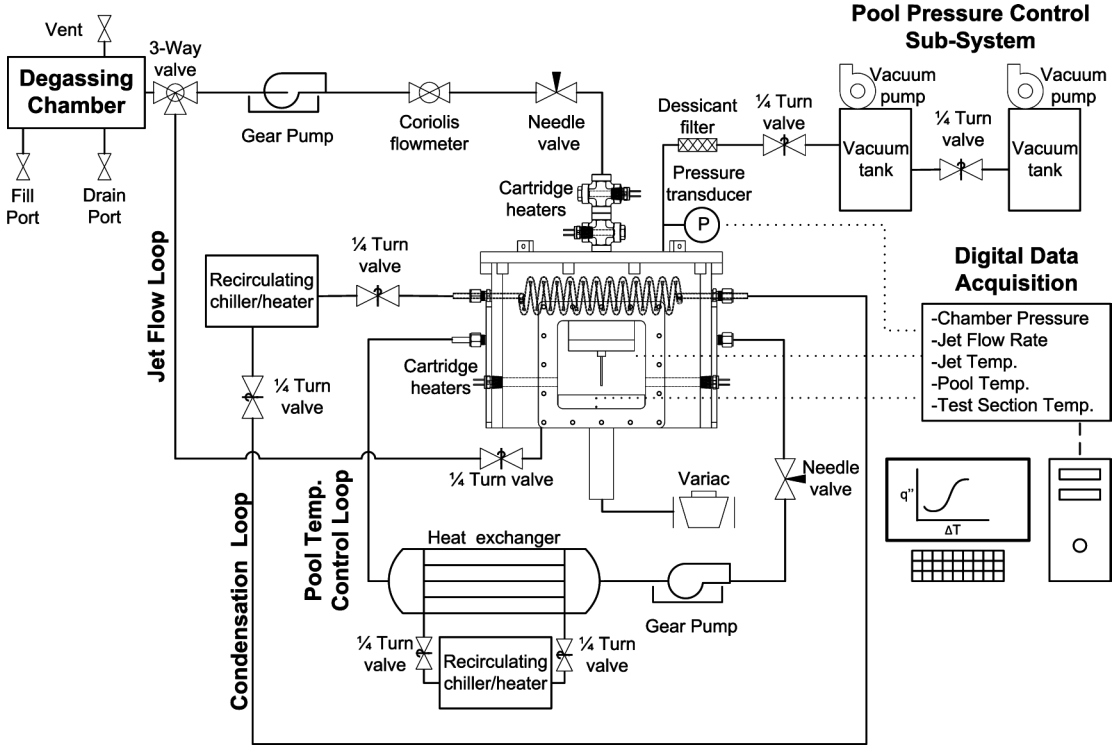

Figure 7: Simplified schematic of the experimental test facility

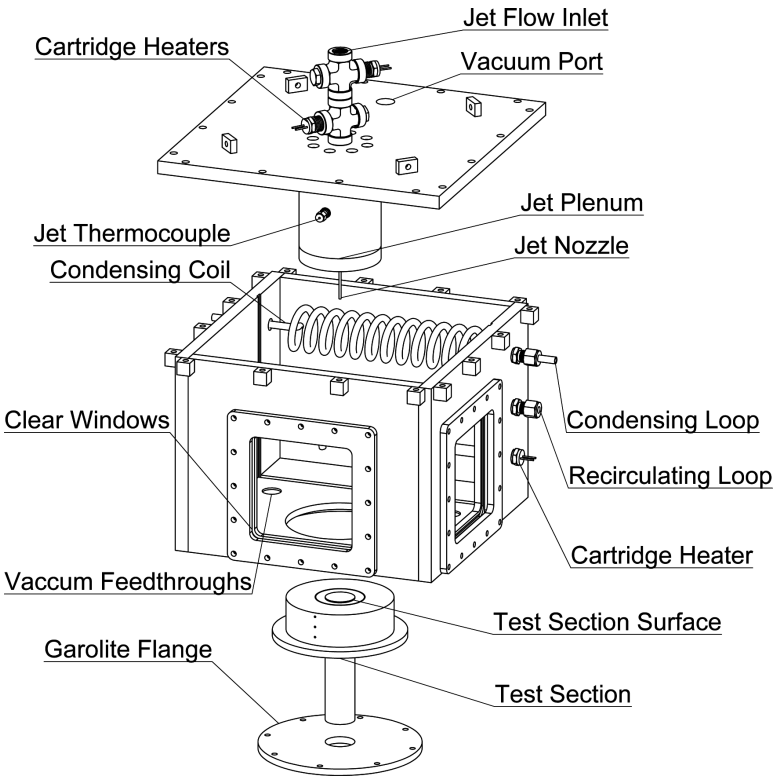

Figure 8: Test chamber

Stable and controllable pool pressures during sub-atmospheric testing were maintained using a vacuum sub-system. This sub-system consisted of two vacuum pumps (Alcatel, 2008AC and Welch Scientific, Duo Seal) and two vacuum tanks (SpeedAire and Brunner Manufacturing) connected in line for a total vacuum reservoir volume of over 50 times the volume of the test chamber. Disposable desiccant filters (Parker, DD10-02) connected at the inlet of each tank and prior to each vacuum pump were used to protect the vacuum sub-system from the water vapor generated during the experiment, and were changed regularly as needed. The vacuum pressure of the tanks was measured using an analog pressure gauge (Omega, PGT-45L-30V) as well as an

NIST absolute pressure calibrator module (Omega, PCL-MB) connected to a hand held calibrator device (Omega, PCL-1B). The vacuum sub-system was directly connected to the test chamber allowing for a stable vacuum pressure during the duration of each experiment. A calibrated digital pressure transducer (Omega, PX302-030AV) recorded the pool pressure inside the chamber to assure that the chamber pressure corresponded to that of the tanks.

A six gallon commercial household water heater (Rudd, PEP6-1) was modified to serve as a degassing chamber. The modifications consisted of replacing the pressure relief valve with a permanent vent to atmosphere and of replacing the original temperature control unit with a custom PID controller. A T-type thermocouple (Omega, TTSS-18U-12) was inserted near the bottom of the water heater to read the inside fluid temperature. The temperature signal was read by a PID controller (Omega, CNi3253-DC) which then controlled the temperature of the fluid to a user specified value through a high power solid state relay (Omega, SSR330DC50) mounted on a finned heat sink (Omega, FHS-7). All the plumbing connected to the water heater was made out of stainless steel 316 to avoid rusting of the system. The degassing chamber was connected to the jet flow loop through a 3-way valve allowing easy transport of the fluid from the degassing chamber to the test chamber. The dissolved oxygen content of the degassed fluid was measured using a dissolved oxygen meter (Extech Instruments, 407510) with a resolution of 0.1 mg/L and an accuracy of ±0.4 mg/L.

The jet flow loop consisted of a variable-speed gear pump (Micropump, GB-P25JDS-A) that supplied deionized, degassed water to the jet plenum in the test chamber. A Coriolis flow meter (Micromotion Elite II, CMF010 and 2700 transmitter) monitored the jet mass flow rate, which was adjusted by using the variable speed controller of the pump and a needle valve located upstream of the flow meter. As shown in Fig. 8, two 250-watt cartridge heaters (Watlow, E2A72-BG12H) located just prior to the inlet of the chamber were used to control the jet temperature. The power to cartridge heaters was controlled manually using a variac (Superior Electric, 3PN1010) and the jet temperature was measured inside the jet plenum using a k-type thermocouple (Omega, KMTXL). The fluidic lines in the system were made of 6.35 mm outer diameter stainless steel 316 tubing with 0.889 mm wall thickness and were connected utilizing Swagelok type compression fittings. Flexible 6.35 mm outer diameter tubing sections required at the inlet and outlet of the test chamber were made out of crack-resistant Teflon® PFA with 1.189 mm wall thickness. Variable diameter and length nozzles could be affixed at the end of the jet plenum using either a 1/4-28 Upchurch flangeless ferrule and nut fitting (for a jet nozzle outer diameter of 1 mm, 2 mm, and 3 mm) or a standard 1/8 NPT bore-through fitting (for a jet nozzle outer diameter of 6.35 mm). The flow exited the nozzle either as a submerged or free-surface circular jet, depending on the height of the liquid pool, and impinged normally on a flat circular heated test section. For submerged jet impingement boiling experiments, the height of the liquid pool above the heated surface was approximately 90 mm.

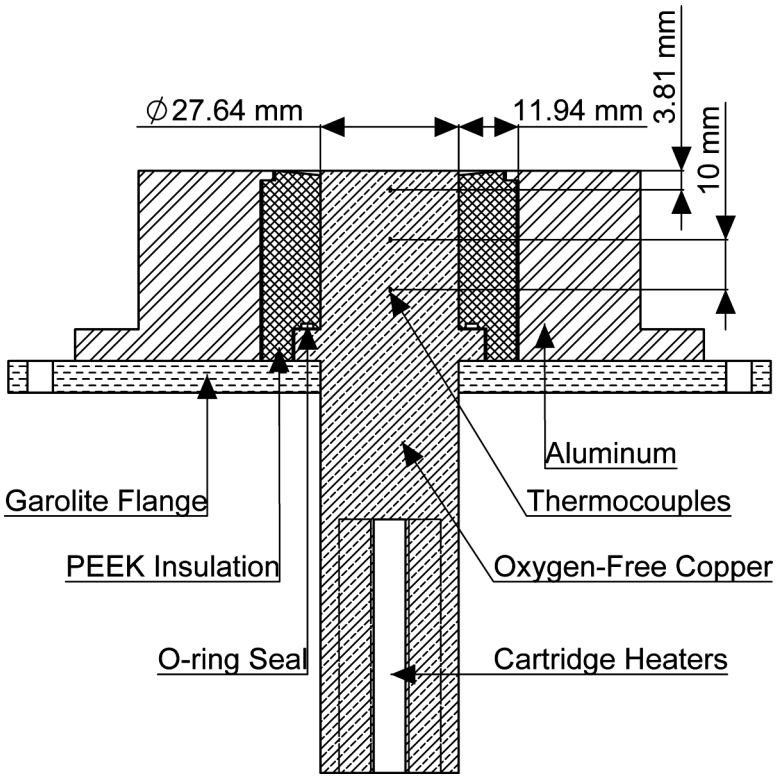

Figure 9: Test section schematic

The test section, shown schematically in Fig. 9, consisted of a 120.65 mm long and 27.64 mm diameter oxygen-free copper cylinder whose top surface was exposed to the working fluid. Five 250-watt cartridge heaters (Watlow, E2A72-L12) inserted at the bottom of the copper cylinder were used to provide the power to the heated surface. A variable transformer (Philmore, 48-1310) supplied the necessary electrical power to the cartridge heaters. To minimize heat losses and thereby ensure heat conduction along the copper rod axis, the sides of the copper test section were thoroughly insulated. On the upper part, which was inserted in the pool of fluid, the sides of the copper test section were insulated with an 11.94 mm thick PEEK sleeve inserted

inside an aluminum housing. This thickness of the PEEK sleeve was deemed sufficient to prevent significant heat conduction losses based on a one-dimensional radial heat conduction thermal resistance network. On the lower part of the copper test section protruding out of the test chamber, high-temperature Pyrogel XT® insulation was used. The PEEK sleeve was affixed to the aluminum housing using Permatex high-temperature red RTV silicone. High-temperature RTV was also used to seal the gap between the PEEK sleeve and the copper cylinder. Three k-type thermocouples (Omega, KMTXL) of 0.794 mm diameter were located along the axis on the upper part of the copper test section and were used to determine the heat flux based on a one-dimensional steady state heat conduction model. The small dimension of the axial thermocouples was chosen to reduce the intrusion of the measurement and the heat conduction along the axis of the thermocouple body. The one-dimensionality of heat flux profile and placement of thermocouples was based on a three-dimensional finite element analysis simulation performed in ANSYS® and later confirmed experimentally. Due to their small size, the thermocouple holes were made by electric discharge machining (EDM). The top thermocouple was located 3.8 mm below the heated surface and was used to determine the surface temperature by extrapolation of the temperature gradient. The copper test section had a lip that pressed against a high-temperature o-ring located on the PEEK sleeve providing a seal between these two parts. A ½ in thick Garolite flange backed by a ¼ in thick stainless steel flange was used to hold the test section in place at the bottom of the test chamber. An o-ring, located on the bottom face of the test chamber, provided a seal between the aluminum

housing of the copper test section and the test chamber. The total surface area for heat transfer during jet impingement boiling was six square centimeters corresponding to a heated surface diameter of approximately 2.764 cm. Appendix 3 provides detailed part drawings of the components of the test section.

Pool subcooling was maintained using a loop that consisted of a vane pump (Teel, 4RM64) and a custom made shell and tube heat exchanger. A recirculating heater/chiller (ThermoHaake, C30P) provided the necessary heating/cooling to the heat exchanger. In addition to this loop, two 550-watts cartridge heaters (Watlow, G4A-15283) were immersed in the fluid and were used to heat the pool to a user specified value using a PID controller code written in LabVIEW. The PID controller utilized a 5 V analog output from the data acquisition board (National Instruments, PCI-6221) to control a high power solid state relay (Omega, SSR330DC50) mounted on a finned heat sink (Omega, FHS-7) which in turn controlled the power to the pool cartridge heaters. Pool temperature was monitored at the front, the middle, and the back of the chamber using k-type thermocouples (Omega, KMTXL) to verify the uniformity of the temperature inside the pool.

The vapor condensation loop consisted of a custom made condensing coil located at the upper back side of the test section. The coil was made with 6.35 mm outer diameter and 0.508 mm wall thickness stainless steel tubing. A thinner wall thickness tube was selected to reduce the heat conduction resistance through the walls of the coil. The outer surface of the coil was sandblasted to increase its surface roughness

and thereby enhance condensation. Compression bore-through fittings at the inlet and outlet of the condensing loop were used to provide a vacuum tight seal between the tube and the walls of the test chamber. A recirculating chiller (Thermo Scientific, Neslab ThermoFlex5000) provided chilled water through the condensation coils to maintain appropriate condensation rates on the coil surface. For atmospheric testing using FC-72, an additional glass Graham condenser was added in parallel to the condensing coils to avoid potential lost of fluid to the atmosphere.

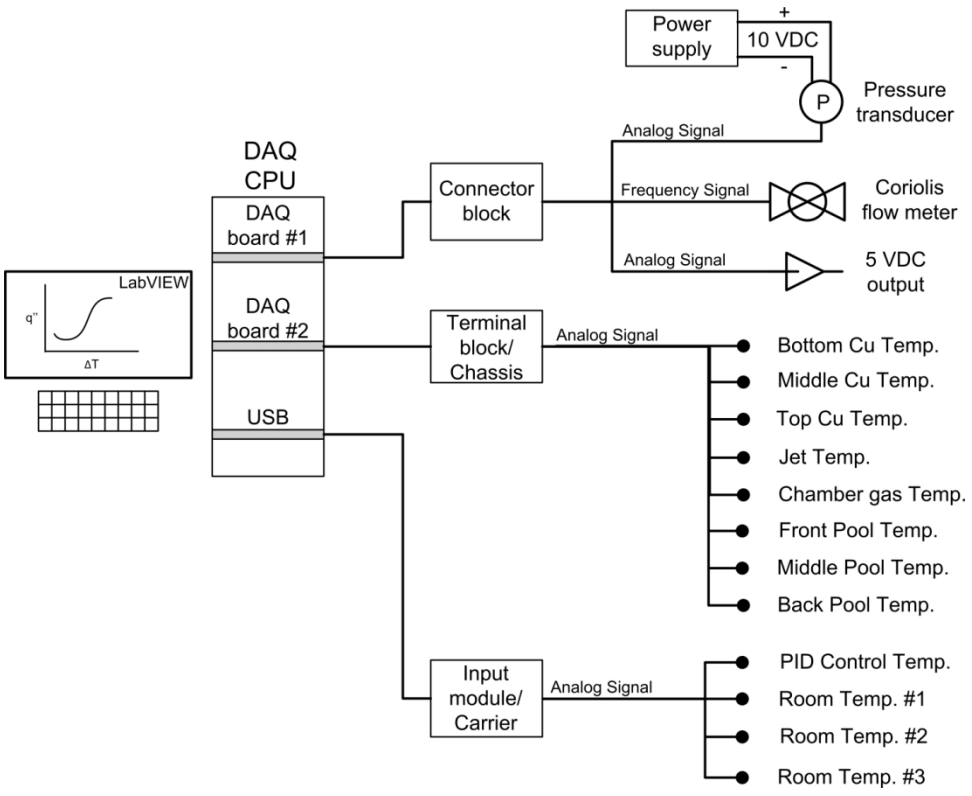

Figure 10: Simplified data acquisition diagram

Figure 10 shows a simplified diagram of the data acquisition set-up. Instruments used for measuring temperature and pressure were calibrated using a NIST-traceable standard. Corresponding calibration curves can be found in appendix 4. Data were recorded using signal conditioning and data acquisition boards through LabVIEW. The absolute pressure transducer was powered by a precision power supply (Tektronics, PS 5004) with 10 VDC. The voltage output reading from the transducer (0-100 mV) was directly connected to a connector block (National Instruments, CB-68LPR) that transferred the signal to the DAQ board (National Instruments, PCI-6221) located within the data acquisition computer (Dell, Optiplex 960). The frequency signal of the jet mass flow rate transmitted by the Coriolis flow meter was measured by the digital counter in the DAQ board. All the temperature readings from the k-type thermocouples located inside the chamber were recorded by an isothermal terminal block (National Instruments, SCXI-1328) mounted on a 4-slot chassis (National Instruments, SCXI-1000) that was connected to a separate DAQ board in the computer (National Instruments, PCI 6036E). Additional T-type thermocouples were used for the PID controller and room temperature measurements. These measurements were recorded by a USB thermocouple input module (National Instruments 9211) together with a USB module carrier (National Instruments, USB-9162) that was directly connected to a USB port on the data acquisition computer. A detailed list of the equipment and instrumentation used, their measurement range, and uncertainties are tabulated in Table 2 and Table 3 respectively.

Table 2: List of equipment

Description	Quantity	Make/Model	Range	Resolution
Variable Speed Gear Pump	1	Micropump/ GA-V21 .J8FTA	21-336 ml/min ΔP_{max}: 517 kPa	-
Variable Speed Gear Pump	1	Micropump/ GB-P25JDS-A	290-5220 ml/min ΔP_{max}: 551 kPa	-
Vane Pump	1	TEEL/4RM64	unknown	-
Recirculation Chiller	1	Thermo Scientific/ NeslabThermoFlex5000	5-40 ^{o}C	±0.01^{o}C
Recirculation Chiller	1	ThermoHaake/C30P	-30^{o}C – 200 ^{o}C	±0.01^{o}C
Power Supply	1	Tektronics/PS 5004	0-10 V 300 mA	±0.001V
Computer	1 1	Dell/Optiplex 960 HP/ Z400 Workstation	Inter Core 2 Vpro Intel Xeon	-
External Hard Drive	1	MicroNet/RaidBank5	Up to 10TB	-
Camera Lens	1 1	Nikon/Micro-Nikkor Nikon/ Micro-Nikkor	60mm f/2.8D 105mm f/28.D	-
PID Controller	1	Omega/CNi3253-DC	TC types : J, K, T, E, R, S, B, C, N, L	±0.1
Solid State Relay	2	Omega/SSR330DC50	24-330 V 0.1-50 A	-
Heat Sink	2	Omega/FHS-7	-	-
Cartridge Heaters	5 2	Watlow/E2A72-L12 Watlow/ E2A72-BG12H	250-Watts	-
Cartridge Heaters	2	Watlow/G4A-15283	550-Watts	-
Vacuum Pump	1	Alcatel/2008AC	28-0 inHg vac	-
Vacuum Pump	1	Welch Scientific/ Duo Seal Vacuum Pump	28-0 inHg vac	-
Vacuum Tank	1 1	SpeedAire Brunner Manufacturing	0-215 psia	-
Water Heater	1	Ruud/PEP6-1	6 gallons	-
NIST Calibrator	1	Omega/PCL-1B	-	-
NIST Pressure Module	1	Omega/PCL-MB	0-6.895 bar	±0.001 bar
NIST Temp. Module	1	Omega/PCL-MR-1	400 Ohms	-
Variac	1	Staco Energy Products/ 3PN1010	0-120 V 0-10 A	1 %
Variac	1	Superior Electric/ 3PN116B	0-140V 0-10 A	1%
Variac	1	Philmore/ 48-1310	0-130V 0-10 A	1%
Shop Crane	1	Central Hydraulics/35915	0-2 Tons	-
Desiccant Filter	4	Parker/DD10-02	0-125 psi	-
Oil Bath	1	Cole-Parmer/12107-70	40-200 ^{o}C	±0.1 ^{o}C

Table 3: List of instrumentation

Instrumentation	Quantity	Make/ Model	Range	Average Uncertainty
Pressure Transducer	1	Omega/ PX302-030AV	0 to 2.1 bar	±0.0037 bar
Analog Pressure Gauge	1	Omega/ PGT-45L-30V	0-30 inHg vac	0.25% FS
K-type Thermocouple	8	Omega/ KMTXL	-200°C - 1250°C	±0.4 °C
T-type Thermocouple	4	Omega/ TMQSS	-250 – 350 °C	±0.3 °C
T-type Thermocouple	1	Omega/ TTSS-18U-12	-250 – 350 °C	±0.3 °C
NIST RTD Probe	1	Omega/ PR-11-2-100-1/8-9-E-TA4F	-30-1350 °C	0.3 °C
Coriolis Flow Meter	1	Micromotion/ CMF010 sensor & 2700 transmitter	0-108 kg/h	±0.2 g/min
Data Acquisition Board	1	NI/PCI-6221	16-Bit 250 ks/s 16 AI ±10 V	-
Data Acquisition Board	1	NI/PCI-6036E	16-Bit 200 ks/s 16 AI ±10 V	-
Thermocouple Input Module	1	NI/9211	4-Channels 24-Bit 14 S/s ±80 mV	-
Isothermal Terminal Block	1	NI/SCXI-1328	18 screw terminals	-
I/O Connector Block	1	NI/CB-68LPR	68 terminals	-
AC-powered Chasis	1	NI/SCXI-1000	4-slots	-
USB Module Carrier	1	NI/USB-9162	1-slot	-
Dissolved Oxygen Meter	1	Extech Instruments/ 407510	0-19.9 mg/L	±0.4 mg/L
High-Speed Camera	1	Phantom/V310	26.5x11.9 mm CMOS sensor	-
Camera	1	Casio Exilim/ EX-FH25	10.1 Mega Pixels	-

Qualitative flow visualization was performed through one of the test chamber windows using a high-speed camera (Phanton, V310) mounted on a tripod head which in turn was mounted on an x-y stage. A workstation computer (HP, Z400) was dedicated to operate the camera and record the high-speed images. Two halogen light sources were used to illuminate the test surface. A 60 mm lens (Nikon, Micro-Nikkor) or a 105 mm lens (Nikon, Micro-Nikkor) were used to collect the images. The camera was connected to the computer through a 1GB Ethernet port. The images were saved either in the 1TB workstation computer hard drive (HP, Z400) or in an external 10 TB hard drive (MicroNet, RaidBank5). An additional photographic camera (Casio, EX-FH25) was used to collect single shot images at varying power levels through a different window on the test chamber. These single shot images had a larger field of view compared to the high-speed images and permitted qualitative flow structure comparison on a larger scale.

4.2 SURFACE PREPARATION AND CONDITION

Preliminary data was taken at first with the unaltered original machined surface finish of the copper test section. However, surface staining was observed during the high temperatures and long duration of the tests. These stains on the surface became more evident immediately after reaching CHF and worsened with periodic testing. A similar surface staining phenomena was reported by Monde [37] for water jet

impingement boiling on a heated copper surface. Surface cleaning procedures similar to those used by Katto and Kunihiro [23], Monde and Katto [24], and Han and Griffith [38] were adopted to mitigate this problem. Before a day of testing, the surface was sanded by hand, using powder-free nitrile gloves. The sanding was accomplished through a circular clock-wise movement of the thumb while apply uniform pressure onto the surface. Silicon carbide emery paper of 600, 800, 1200, and 1500-grit were used progressively going down in roughness (up in grit size) to attain a variety of sanding levels. Between each sanding level, the surface was cleaned by blowing it with compressed air and the gloves were changed to avoid contamination from the prior sanding dust. After sanding, the surface was cleaned using acetone and a cotton pad followed by rinsing with deionized water. The surface was then blown dry using compressed air.

It became evident after more preliminary testing that the sanding level can significantly impact the heat transfer characteristics of the surface, especially at critical heat flux. Heat transfer characteristics from two surface sanding levels, 600-grit and 1500-grit, were compared. To quantitatively characterize the surface roughness conditions obtained from these two sanding levels, a ZE metrics high-resolution Optical Profiler (ZeScope) was used. Since the actual test surface was too large to accommodate in this measuring device, smaller sample pieces of equivalent material (oxygen-free cooper) were used. Two samples for each grit sanding were prepared to quantify repeatability of the surface finish for each sanding level. Surface

preparation procedures for the sample pieces were identical to the procedures used for sanding the actual test surface.

Surface roughness measurements were taken with a 5X objective over a relatively large region of the surface. Several images were taken with the optical profiler and were stitched together with a 20 percent overlap using the Zemaps Software to obtain a single file of surface height measurements over the two-dimensional region in space where the measurements were taken. The data were exported into MATLAB where surface roughness parameters were computed based on the ASME Standard B46.1-1995 [39]. A large-scale surface curvature with an apparent wavelength of approximately 9.5 mm and one mm amplitude was observed on the collected data, potentially due to the uneven flatness of the test surfaces, making proper estimations of one-dimensional surface roughness parameters difficult. To overcome this problem, surface roughness statistics were computed by sub-sampling the entire data set in sub-sets of 50x50 data points which contained sufficient data points (2,500) to provide proper surface statistics. The large-scale surface curvature at the small scale of the data sub-sets appeared as inclinations on the plane of the data. This inclination was removed by subtracting a best fit plane to the data. Prior to computing the surface roughness statistics, one pass of a three-sigma filter was applied since a few regions on the surface contained high levels of measurement noise. Table 4 shows the surface roughness statistics obtained for each sample. Measurement repeatability for all computed roughness statistics for the 600-grit surface finish was less than four percent while for the 1500-grit surface finish was less than 12 percent. The roughness average

measured, Ra, for the 600-grit surface was on average 123 nm and for the 1500-grit surface was on average 33 nm, corresponding to a 3.7 times smaller roughness average for the 1500-grit compared to the 600-grit surface. Jones et al. [40] studied the influence of surface roughness on pool boiling of water and FC-77 on an aluminum surface that was either polished using sandpaper or EDM machined to introduce surface roughness. In their study, surface roughness average for the polished aluminum surface, which was achieved by using successively finer grits of sandpaper, ranged between 27 nm and 38 nm. This range of average roughness is comparable to what was obtained in the present study for the 1500-grit surface finish.

Table 4: Surface roughness statistics

	600 (#1)	**600 (#2)**	**1500 (#1)**	**1500 (#2)**
Total Number of Images	48	80	48	80
Approx. Size of Region Measured [mm^2]	4.8x4.8	6.3x5.9	4.8x4.8	6.3x5.9
Total Number of Data Points	3243x3268	4030x4308	3253x3271	4047x4330
Roughness Average (Ra) [nm]	124.4	122.0	30.7	34.5
RMS Roughness (Rq) [nm]	158.1	155.9	41.2	44.7
Maximum Height of Profile (Rt) [nm]	975.6	959.4	284.4	285.1
Maximum Profile Valley Depth (Rv) [nm]	493.7	495.8	171.9	164.1
Maximum Profile Peak Height (Rp) [nm]	481.9	463.6	112.5	120.9

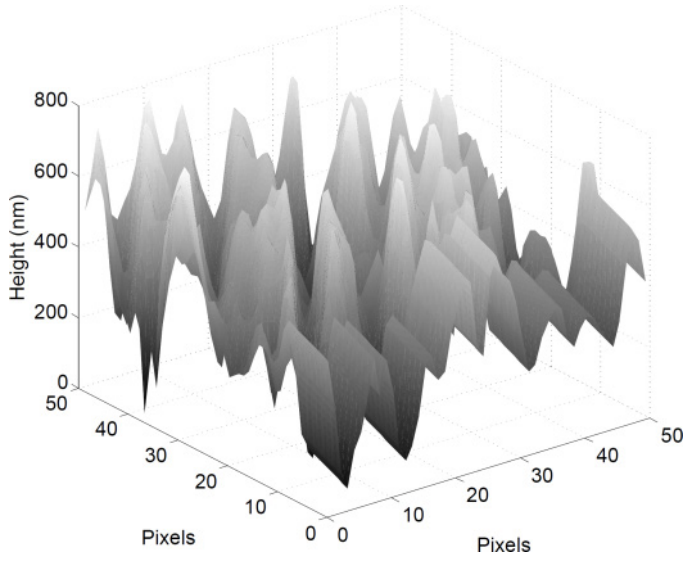

(a) Ra=123 nm

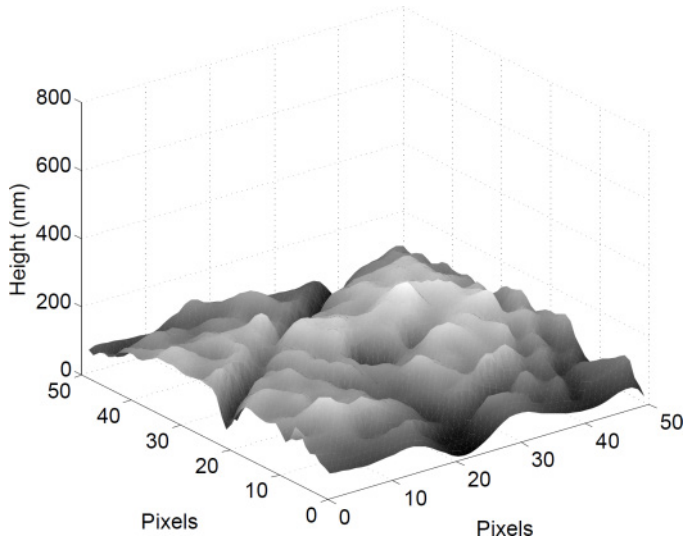

(b) Ra=33 nm

Figure 11: Surface roughness profile sample over a 73x73 μm^2 area (50x50 pixels) for (a) a 123 nm Ra surface and (b) a 33 nm Ra surface

Figure 11(a) and (b) show sample surface roughness profiles over a 73x73 μm^2 area (50x50 pixels) for a 600-grit surface finish and a 1500-grit surface finish respectively. Both profiles were plotted on the same scale to facilitate a visual comparison. It is evident from these figures that the 1500-grit surface finish resulted in a significantly smoother surface profile than the 600-grit surface finish. To the naked eye, a 1500-grit surface sanding provided an almost mirror-like finish while the 600-grit surface exhibits fine scratches.

4.3 SURFACE WETTING CHARACTERISTICS

In most practical applications, boiling heat transfer occurs directly on heated surfaces through heterogeneous nucleation. For this reason, the liquid-vapor-surface interactions are important in the resultant heat transfer characteristics. When a liquid is brought in contact with a solid surface which is submerged on a second immiscible fluid (liquid vapor for example), the resultant liquid-solid contact area depends on the affinity of the liquids for the solid and it is commonly referred as fluid wettability [6]. In a liquid-vapor-solid system, fluid wettability can be characterized by the equilibrium contact angle (Θ) defined as the angle, measured through the liquid phase, that the liquid-vapor interface makes with the solid surface at the contact line. Low contact angles are characteristic of wetting fluids ($0^o < \Theta < 90^o$) while high contact angles ($90^o < \Theta < 180^o$) are characteristic of non-wetting fluids. Important two-phase heat transfer relationships along the different boiling regimes such as vapor trapping

mechanisms [6], the pool boiling Moissis-Bereson transition from the isolated bubble regime to the slugs and column regime [6], and Kandlikar's theoretical pool boiling CHF model [41] are directly dependent on the contact angle. These relationships demonstrate the importance of contact angle on boiling heat transfer characteristics at the different stages of boiling.

Surface roughness can alter the wetting characteristics of the surface in a fixed liquid-vapor-solid system. For wetting fluids, the result is a decrease in equilibrium contact angle for a rough surface in comparison to a smooth surface [6]. A sessile drop experiment was performed to measure the equilibrium contact angle of a water droplet on a copper surface having an average surface roughness of 123 nm and 33 nm. These surfaces were the same as those utilized to collect surface roughness measurements. Recall that these surfaces were prepared utilizing the identical procedures as those used to prepare the heat transfer surface for jet impingement boiling experiments. The water droplet was generated by dispensing fluid from a fixed syringe utilizing a micrometer adjustment. The syringe had a one inch long 16 gauge hypodermic needle with a nominal inner diameter of 1.194 mm (PrecisionGlide®). Approximately equal droplet sizes with an average mass of 20 mg were generated by slowly pressing on the syringe with the micrometer adjustment until the droplet fell under the effect of gravity. The tip of the hypodermic needle was placed directly above the copper surface at a height of approximately 13 mm. Once the droplet impacted the surface, images were taken to determine the equilibrium contact angle. Although the equilibrium contact angle measurements were consistent for repetitive experiments,

the contact angle decreased with time as the droplet evaporated. For this reason, images were also taken as a function of time until the droplet evaporated completely from the surface.

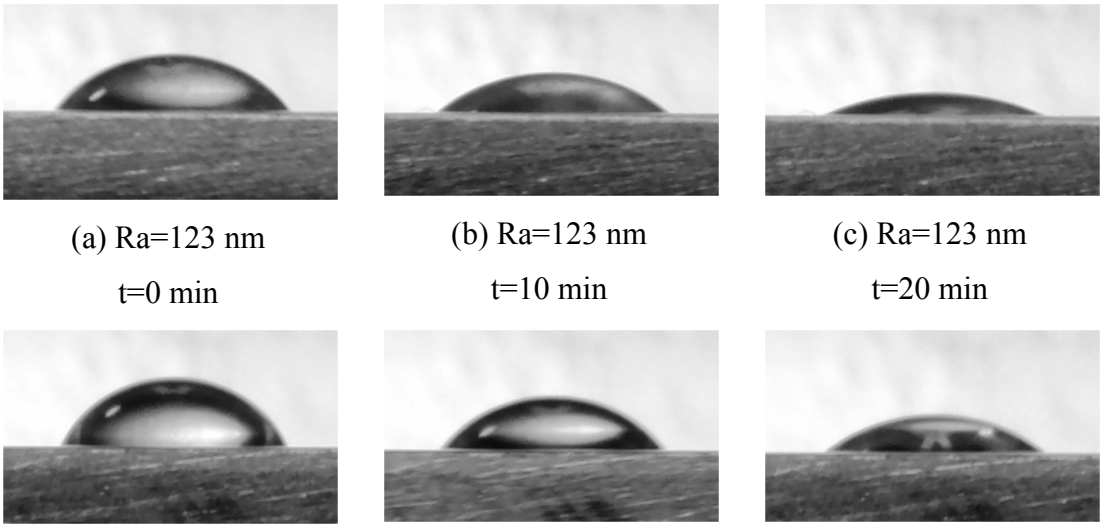

(a) Ra=123 nm t=0 min | (b) Ra=123 nm t=10 min | (c) Ra=123 nm t=20 min

(d) Ra=33 nm t=0 min | (e) Ra=33 nm t=10 min | (f) Ra=33 nm t=20 min

Figure 12: Profile shape of a water droplet on a 123 nm and 33 nm Ra copper surface as a function of time

Figure 12 show the profile shape for a water droplet on a 123 nm Ra surface (a-c) and on a 33 nm Ra surface (d-f) as a function of time. In these figures, t=0 minutes correspond to images taken within a few seconds after the droplet impacted the surface. It is evident from this picture that for any of the two surfaces, the apparent contact angle decreased as a function of time. It appears as if the contact line of the droplet remained pinned at a fixed location on the surface. Therefore, the apparent

contact angle decreased as the droplet evaporated. Nevertheless, at any given time, it is qualitatively evident from these images that the 123 nm Ra surface exhibited a lower contact angle compared to that of the 33 nm Ra surface indicating enhanced wetting on the rougher surface.

Quantitative contact angle measurements were made from the droplet profile images by using image processing tools in MATLAB. Each profile image was binarized and filled to detect the edged of the droplet profile. Ten pixels were used to find the tangent line of the droplet profile on both the left and right side of the images at the contact point. Two contact angle measurements were obtained from these tangent lines which usually were within 2 ^{o} of each other and that were visually confirmed to be proper measurements. These two angles were averaged to report a single contact angle value for each surface at any given time. Figure 13 shows a plot of the contact angle measured as a function of time for both the 123 nm Ra surface and the 33 nm Ra surface. Note that consistently, the smoother 33 nm Ra surface exhibited a contact angle that was on average 11.4 ^{o} higher than the rougher 123 nm.

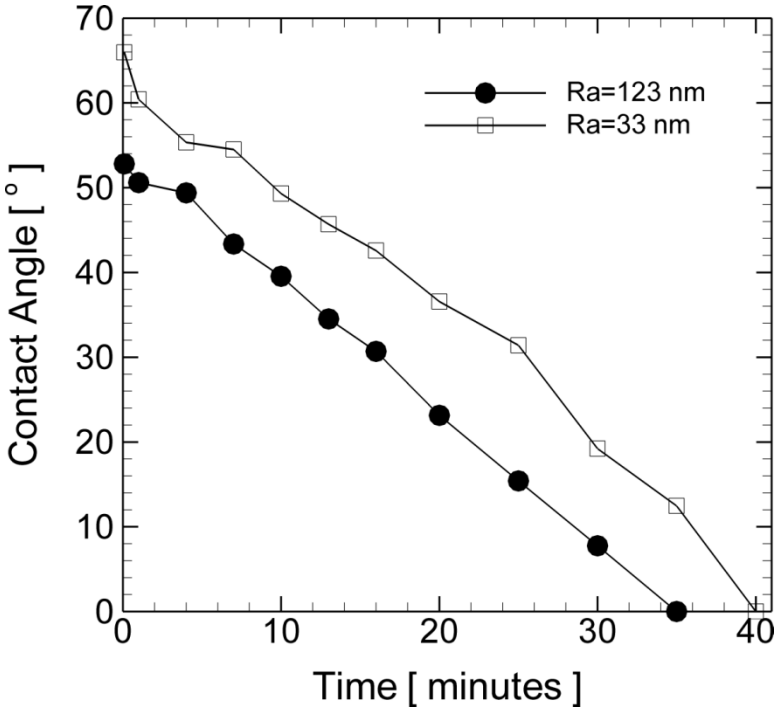

Figure 13: Contact angle measurements on the 123 nm and 33 nm Ra copper surfaces

4.4 EXPERIMENTAL PROCEDURES

This section explains the standard operating procedures followed to operate the experimental facility and to collect data. It is important to note that the operating procedures varied slightly depending on test pressure, working fluid, and jet configuration. A thoroughly detailed explanation of the operating procedures is given for the case of submerged sub-atmospheric jet impingement boiling of water. For free surface jet impingement and FC-72 testing, only important differences are discussed.

4.4.1 WATER: SUBMERGED SUB-ATMOSPHERIC JET IMPINGEMENT BOILING EXPERIMENTS

Prior to each experimental day, the heated surface was refinished following the procedures given in Section 4.2. Approximately 3.5 gallons of deionized water were transferred to the degassing chamber from a storage container. This amount of fluid guaranteed that the heating element of the water heater was completely submerged and also allowed enough empty space inside the water heater for the fluid to boil freely without splashing out of the vent. The fluid was boiled for several hours the night prior to the experiment and then again for about an hour on the day of the experiment. The measured oxygen content was lower than the accuracy of the meter used (< 0.4 mg/L). In addition to this, degassed water from the degassing chamber flowed into the previously evacuated, low pressure test chamber. Thereby, it was believed that the dissolved oxygen content of the testing fluid was kept at a minimum.

The two vacuum pumps were used simultaneously to lower the pressure inside the vacuum tanks to approximately the required set point of the experiment. The test chamber was then evacuated by allowing it to reach pressure equilibrium with the tanks. Saturated fluid from the degassing chamber was permitted to flow into the test chamber driven by the pressure differential between the test chamber and ambient. The test section was filled to a level just above the window height (approximately 90 mm above the heated surface) while leaving the condensing coils above the fluid. At this pool height, the test chamber contains approximately 1.5 gallons of fluid. Once

again both vacuum pumps were utilized to bring down the pressure in the entire system to the actual pressure set-point of the experiments.

The temperature control loop was initiated by selecting the required pool temperature on the recirculation chiller and allowing its flow through the custom made shell and tube heat exchanger. The vane pump was turned on to continuously recirculate the pool fluid through the heat exchanger. The immersed pool cartridge heaters were turned on by selecting the appropriate temperature set-point on the PID controller. Sufficient time (approximately two to three hours) was allowed for the fluid to reach the required temperature for the experiment and for the system to reach steady state conditions. To speed up the heating process and to degas the heated surface, the power to the copper test section cartridge heaters was activated to a relatively low boiling heat flux that allowed the surface to boil for approximately 30 minutes prior to starting the experiment.

The jet flow loop was started by activating the gear micropump. With the needle valve fully opened, the jet flow rate was adjusted using the variable speed controller of the pump to approximately 40 g/min - 80 g/min higher than the actual set-point. Using the needle valve, the jet mass flow rate was then lowered to the required value. This method of adjusting the flow provided stable flow rates over the extended period of time necessary to run the experiment. Small temperature adjustments to the jet flow rate were accomplished by manually controlling the variac that powered the jet

cartridge heaters located at the inlet of the test chamber. This process of adjusting the jet mass flow rate and jet temperature required a few iterations.

The initial steady state condition at each experimental run was determined by looking at the variations in temperature of the copper test section, jet flow, and liquid pool. Once this condition was reached, the data acquisition program was set to record data continuously through the entire duration of the experiment at a rate of one sample per second. The electrical power to the cartridge heaters was manually controlled using the variac. The voltage was increased from zero in small increments of two percent all the way up to critical heat flux conditions. At each power level, sufficient time was allowed for the experiment to reach equilibrium conditions (usually six to seven minutes) and one additional minute was permitted for the data acquisition program to collect steady state data. Prior to increasing the electrical power to the next level, a Boolean switch was manually triggered in the data acquisition program which flagged the ending period of a power level and the beginning of the next in the saved data record.

Upon nearing critical heat flux, the electrical power increments were reduced as necessary in order to approach CHF in a steady fashion and to reduce the severity of CHF caused by sudden transients in electrical power. CHF conditions were determined by a sudden large increment in surface temperature accompanied by wall heat flux degradation. At this point, the power to the copper cartridge heaters was cut immediately and the vacuum pressure of the chamber was released. Releasing the

vacuum pressure was the quickest way to get rid of the vapor blanket on the surface and to return to the nucleate boiling region. In addition to releasing the pressure, the jet flow rate was increase to its maximum value to help cool the surface. At this point, the save data command on the data acquisition program was disabled and once again the experimental set up was adjusted for the next experimental run.

Flow imaging was accomplished throughout the experiment through the clear windows of the test chamber. Halogen light sources were used to illuminate the surface from the opposite window from which the high-speed camera was placed. This back-lighting allowed for small exposure times (30 μs) and high frame rate (~9200 fps) with a relatively large image size (656 x 456 pixels). Videos were taken just prior to increase the power to the heaters. In the interest of hard drive space, only a section of the entire video containing approximately 3000 to 6000 images was saved corresponding to approximately 1.7 to 3.4 GB respectively. A plastic bag cover was placed over the camera and lens while carefully avoiding blockage to the cooling air inlet and outlet. This plastic cover protected the camera from potential unexpected leaks during the experiment.

After a complete day of testing, the fluid in the test chamber was emptied and disposed. The test chamber top plate was opened by removing the screws and lifting it with a shop crane. The top was removed while the walls of the chamber were still warm to help evaporate the remaining fluid in the chamber. Keeping the test chamber dry when not in use helped maintain the chamber free of rust and biological

contaminants. The shop crane was able to lift and maintain the chamber top plate suspended for extended periods of time and permitted easy access to the inside of the chamber and the jet nozzle.

4.4.2 WATER: FREE SURFACE SUB-ATMOSPHERIC JET IMPINGEMENT BOILING EXPERIMENTS

For the most part, the experimental procedures for free surface sub-atmospheric jet impingement boiling experiments were identical to those implemented for the submerged case. However, in the free surface jet case, the height of the fluid in the chamber was maintained to just below the heated surface. This lower height of fluid in the chamber did not allow for the use of the pool control loop and the pool cartridge heaters. Instead, the temperature of the fluid was solely controlled through the jet inlet cartridge heaters. Reaching steady state under these circumstances took much longer than the submerged jet case and it was not practical. In order to increase the amount of heat that can be added to the system, a pre-heating section prior to the jet cartridge heaters was added using a rope heater, and a silicon rubber blanket heater was placed on the back wall of the chamber. Both of these heaters were controlled manually using a variac and a DC power supply respectively. The addition of these two heaters together with the jet cartridge heaters allowed the test section to achieve steady state in four to five hours. Despite the increase in the capabilities of the system, saturated flow

conditions were not attainable at the jet exit for Re less than approximately 6000 at P=0.276 bar due to heat losses in the system.

In addition to the difficulties in keeping a saturated jet temperature, other difficulties arise at low flow rate conditions. A blob of fluid formed on the surface potentially due to the high surface tension of water. This blob of water simulated conditions that were similar to pool boiling on the heated surface regions below it. Low jet flow rates also had difficulties wetting the surface completely and dry surface patches appeared with increasing heat flux that were either permanent or sporadic. Flow imaging of the free surface jet was also more challenging compared to the submerged case and often not possible due to fogging of the windows during flow boiling conditions. To help mitigate this problem, an additional halogen light was placed near the imaging window to provide heat and reduce fogging. Nevertheless, completely clear images were not attainable most of the time.

4.4.3 FC-72: Submerged Atmospheric Jet Impingement Boiling Experiments

Experimental procedures for submerged jet impingement boiling of FC-72 were similar to those implemented for water apart from the different system pressures. However, to reduce the amount of fluid required due to the limited available quantity of FC-72, the degassing chamber and the pool temperature control loop were deactivated. The test chamber was filled with FC-72 by pumping the fluid from the

storage container to the test chamber using the jet flow loop. Degassing of FC-72 prior to testing was accomplished by boiling the fluid inside the test chamber for at least three hours using the pool cartridge heaters directly. Degassing inside the test chamber permitted dissolved gasses to escape to the atmosphere through a vent in the Graham condenser while the FC-72 vapor was condensed and returned to the test chamber. The use of the Graham condenser reduced the amount of FC-72 lost in the degassing process. The oxygen content measured after the degassing procedure was on average 2 mg/L ($0.13x10^{-4}$ moles/mole). For comparison, the study by You et al. [42] for pool boiling of FC-72 reported a nominal dissolved gas content after degassing of $0.2x10^{-3}$ moles/mole. Owing the significantly lower CHF of pool boiling for FC-72 compared to water, the pool cartridge heaters were connected to a variac that only provided 55 V to the pool cartridge heaters instead of the nominal 120 V. Limiting the voltage to the pool cartridge heaters avoided CHF to occur on the cartridge heater surface. For this same reason, three out of the five cartridge heaters in the copper test section were deactivated. Having only two cartridge heaters for FC-72 testing, instead of the five used for water, allowed for a much finer control of the surface heat flux using the variac over the lower range of heat fluxes attainable with this low enthalpy of vaporization fluid. It is noted that the necessary amount of time required for FC-72 testing to achieve equilibrium conditions at each power level was slightly larger than for water and was approximately eight to 11 minutes.

Pool recirculation, necessary to maintain uniform pool temperature, was accomplished through the jet flow loop. For jet impingement experiments, the inherent recirculation

of the jet flow was sufficient to maintain uniform pool temperatures. For pool boiling experiments, fluid recirculation was achieved using the jet flow loop connected to the fluid inlet at the back of the chamber that was previously used for the pool recirculation loop. At the end of the day of each experiment, the fluid in the chamber was allowed to cool to at least 32 ^{o}C. To speed up the cooling process, all heaters in the system were turned off and the pool recirculation was continued while cooling the test chamber with an electric fan. The fluid was then drained back into a storage container which was sealed to avoid losing fluid through evaporation.

Two differences in system behavior were found between submerged jet impingement boiling testing of FC-72 and water that eased testing with the former. The first difference is the very small and slowly rising temperature increases (~2 ^{o}C) encountered at CHF conditions for FC-72 compared to the very large and sudden temperature rise (~80 ^{o}C) encountered for water. The reason for this difference in behavior was perhaps mainly attributed to the significantly lower CHF values of FC-72 compared to water. The much lower surface tension of FC-72 compared to water could have also aided this process. A lower surface tension fluid would have more difficulty maintaining a vapor blanket over the entire surface than a high surface tension fluid. On occasion, jet impingement boiling experiments for water were observed to go from CHF conditions immediately into the film boiling regime generating a vapor blanket that covered the entire surface. Such conditions were never witnessed for FC-72. As a result of this milder reaction of the system to CHF conditions using FC-72, it was only necessary to cut the electrical power to the test

section cartridge heaters and the system quickly returned to the nucleate boiling regime without causing burnout damage. The second difference that eased FC-72 testing compared to water was that no appreciable surface discoloration appeared on the surface after periodic testing with the former fluid. For this reasons, it was not necessary to refinish the surface daily.

4.5 DATA ANALYSIS

The surface heat flux, q", was calculated from three temperature measurements collected axially along the copper test section using a one-dimensional steady state heat conduction model,

$$q'' = -k\frac{\Delta T}{\Delta x} \tag{3}$$

where k is the copper thermal conductivity, ΔT is the temperature difference between two axial thermocouples inserted inside the copper rod, and Δx is the corresponding spacing between the thermocouples (Fig. 9). The copper thermal conductivity used in the model was evaluated at the average temperature between the two thermocouple measurements. Three different values of heat flux were calculated from the three temperature measurements and their corresponding spacings. The different values of heat flux were within 0.1 percent of each other in the nucleate boiling regime. The

heat flux values used in the filtering algorithm correspond to the average of the three heat flux values calculated from this method.

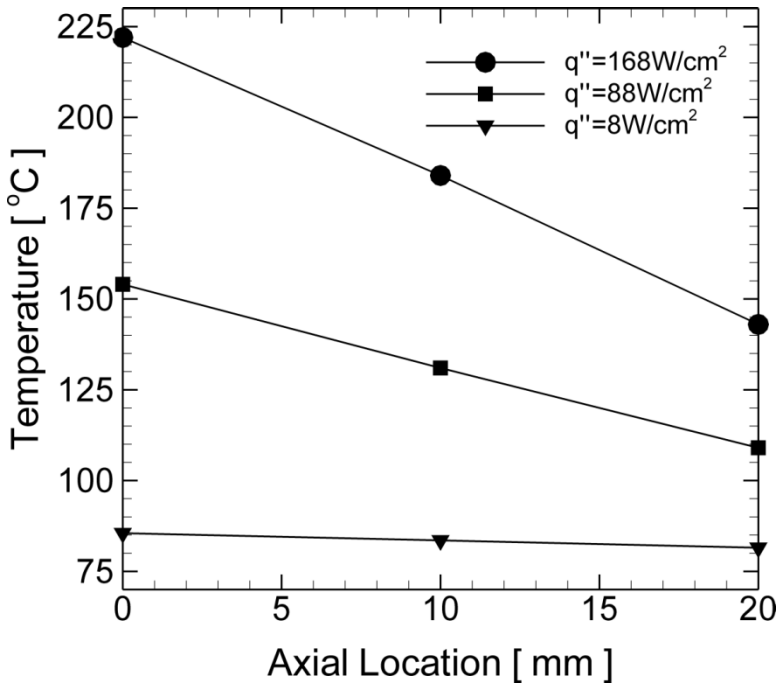

Figure 14: Temperature distribution of thermocouples in heated copper rod

Figure 14 shows the steady state time average temperature distribution of the three axial thermocouples at three distinct heat flux values, covering the range of most experimental conditions. As expected from a steady state head conduction model, the temperature distribution follows a linear profile. A linear regression analysis showed that the R-square value for the three cases considered was equal or greater than

0.9997. These results validate the assumption made to compute surface heat flux from the measured axial temperatures. A similar check was performed by [21] to validate their experimental test section which also consisted of a copper rod with axial thermocouples for heat flux measurements.

The thermocouple closest to the heated surface was located 3.81 mm below the surface. The calculated heat flux value was used together with a one-dimensional conduction model to extrapolate the temperature of the surface,

$$T_{surf} = T_{TC} - q'' \frac{\Delta x_{surf}}{k} \tag{4}$$

At high heat flux values, the surface temperature was significantly lower (up to 17 ^{o}C lower at 180 W/cm^2) than the temperature measured 3.81 mm beneath the surface despite the high thermal conductivity of copper. The saturation temperature needed to compute the wall superheat was found from the averaged pressure measured throughout the entire experiment, which did not varied appreciably.

The jet exit Re was computed based on the jet exit velocity and the local liquid fluid properties,

$$\mathrm{Re} = \frac{\rho_l V_j d_j}{\mu_l} \tag{5}$$

where ρ_l is the liquid density of the working fluid, V_j is the jet exit velocity, d_j is the jet nozzle inner diameter, and μ_l is the liquid viscosity of the working fluid. The jet

exit velocity was calculated from the measured mass flow rate and the jet nozzle inner diameter,

$$V_j = \frac{\dot{m}_j}{\rho_l A_j} \tag{6}$$

where $\dot{m}_j$ is the mass flow rate of the jet and A_j is the cross-sectional area of the jet nozzle. All fluid properties for water were evaluated at the measured temperature and pressure utilizing fluid property routines in Engineering Equation Solver© (EES) [43]. For FC-72, atmospheric fluid properties were obtained from temperature dependent relationships provided by 3M [44] and tabulated values given in [3]. These relationships are provided in appendix 5.

Thermocouples were calibrated using a NIST-traceable RTD (Omega, PR-11-2-100-1/8-9-E-TA4F) inside a constant temperature oil bath (Cole-Parmer, 12107-70). Sub-atmospheric pressures were calibrated using a precision analog gauge (Omega, PGT-45L-30V) and a NIST absolute pressure calibrator module (Omega, PCL-MB) which was used as the standard. The Coriolis flow meter (Micromotion Elite II, CMF010 and 2700 transmitter) that measured the mass flow rate of the jet was factory calibrated. An uncertainty analysis was performed on the measured and determined global variables and is reported in Table 5. The Kline and McKlintock method [45] was used to propagate errors from measured to calculated variables in EES. Uncertainty in reported temperatures, pressure, and flow rate included thermocouple bias and precision errors, pressure bias and precision errors, and flow rate bias and

precision errors. Uncertainty in reported heat flux included temperature difference calibration curve fit error, average precision error of the thermocouples during the experiments, spacing uncertainty, and an estimated 0.25 percent uncertainty in thermal conductivity. Data reproducibility was studied by performing repetitions and replications of experiments and it was found that CHF varied between four and six percent. Reported values of heat flux and wall superheat correspond to data that was filtered and which best represent the steady state average measurements. Detailed information regarding data filtering can be found next in Section 4.6.

Table 5: Representative measurement uncertainty estimate

Variable	Average Uncertainty
Pressure	± 0.004 bar
Pool Temperature	± 0.5 ^{o}C
Jet Temperature	± 0.4 ^{o}C
Surface Temperature	± 0.8 ^{o}C
Excess Temperature	± 0.9 ^{o}C
Jet Flow Rate	± 0.9 g/min
Re	± 1 %
V_j	± 0.8 %
CHF (water)	± 0.5 W/cm^2
CHF (FC-72)	± 0.2 W/cm^2
Heat Flux	
1 W/cm^2 - 5 W/cm^2	19.6 % - 3.9%
6 W/cm^2 - 10 W/cm^2	3.3% - 2%
11 W/cm^2 - 15 W/cm^2	1.8% - 1.4%
16 W/cm^2 - 20 W/cm^2	1.2% - 1%
21 W/cm^2 - 25 W/cm^2	1% - 0.85%
26 W/cm^2 - 30 W/cm^2	0.83% - 0.74%
31 W/cm^2 - 190 W/cm^2	0.72% - 0.36%

4.6 DATA FILTERING

Upon reaching an initial steady sate, experimental data were collected continuously throughout the duration of each experiment at a rate of one sample per second using a LabVIEW based data acquisition VI. As mentioned earlier, the voltage to the test section was increased in two percent increments and sufficient time (six to 11 minutes depending on flow conditions) was allowed to reach steady state at each incremental level. Following this procedure, the typical duration of each experiment varied between two and three hours depending on the magnitude of CHF. Therefore, each data record consisted of approximately 7,000 and up to 11,000 data points. It should be mentioned that because the power to the test section was increased in small increments, all the collected data points followed the general shape of a steady state boiling curve. This can be confirmed by looking at Fig. 15(a), which shows the original raw data set and the averaged data at each heat flux increment for subcooled jet impingement boiling of water at Re=4141. At each power increment, the average was calculated from the last 60 seconds of data collected at steady state prior to increasing the electrical power to the next power level. Based on the agreement between the raw and averaged data, it was considered worthwhile to seek a continuous representation of all raw data by applying a Locally Weighted Scatterplot Smoothing (LOWESS) filter ([46, 47]) on the raw data. The LOWESS filter performs a weighted least-squares regression of the raw data within a user-prescribed span about the excess temperature. A single filtered value of heat flux at each excess temperature is obtained

as an output of the filtering algorithm. The excess temperature span (T_{surf}-T_{sat}) was selected differently for each boiling curve such that the root of the sum of the squares (RSS) of the difference between the averaged and filtered data was a minimum. An example plot of the RSS error as a function of excess temperature span is seen in Fig. 15(b). For this particular example, a span of (T_{surf}-T_{sat}) of 0.44 ^{o}C minimized the RSS error between the raw averaged data and the LOWESS filtered values. Figure 15(c) shows a comparison between the averaged data and the filtered data on to the same excess temperature grid. Note that the filtered data agrees very well with the averaged data. An additional advantage of using the LOWESS filtering technique is that the filtered heat flux can be computed at any specified excess temperature within the range of the experimental data. For example, Fig. 15(d) shows the filtered data plotted every 0.5 ^{o}C excess temperature along with the averaged data for the same data record. Comparing the raw data in Fig. 15(a) and the discrete filtered data in Fig.15(d) demonstrates that the filtering procedure is very successful in predicting the boiling curve trend between two steady state measurements by more effectively utilizing the entire set of raw data collected.

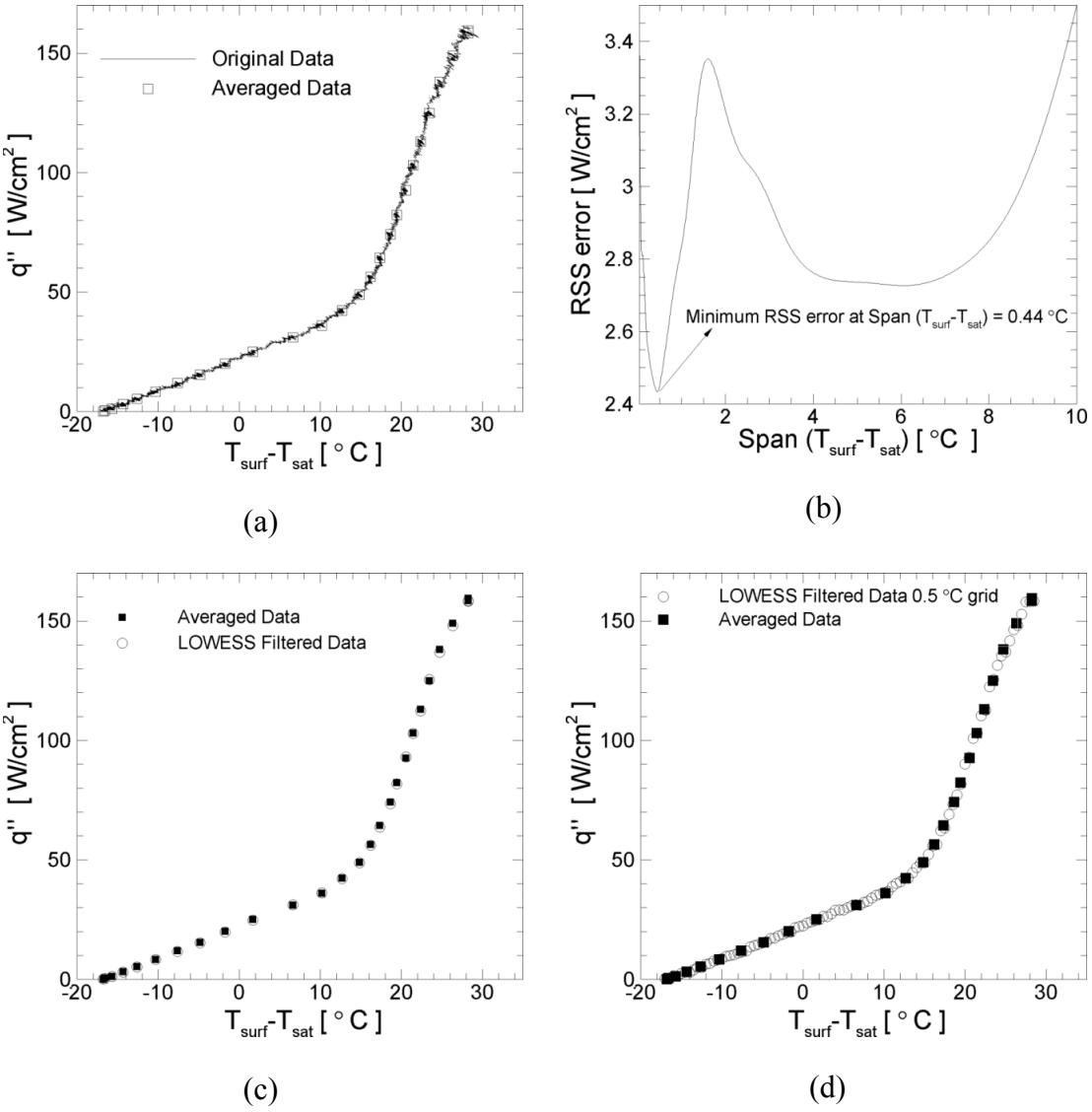

Figure 15: Procedure for data filtering: (a) Comparison of raw and steady-state averaged data, (b) Error in heat flux as a function of chosen span of excess temperature for filtering, (c) Comparison between the average and filtered data, and (d) Representation of the boiling curve using filtered data at intermediate values of excess temperature.

4.7 EXPERIMENTAL TEST CONDITIONS

The experimental test conditions were based upon variations in jet exit Re number ranging from 0 to approximately 14500. The upper limit of Re was dictated by the pump at q" < 190 W/cm^2 and by the heater power at q" > 190 W/cm^2. The jet and pool temperatures were maintained equal so that thermal entrainment from the surrounding fluid into the jet stream was negligible. The heated surface diameter remained fixed at 27.64 mm. Two fluids with clearly distinct thermo-physical properties, namely water and FC-72, were considered. Table 6 shows the comparison of the saturated fluid properties for these two fluids at the considered test pressures. For water, two heated surface finishes having an average roughness of Ra=123 nm and Ra= 33 nm were studied. Fluid subcooling during pool boiling was varied from 0 ^{o}C up to 40 ^{o}C. For jet submerged impingement, two fluid subcoolings of 0 ^{o}C and 17 ^{o}C were considered. Three sub-atmospheric pressures of 0.176 bar, 0.276 bar, and 0.477 bar were studied. In addition to the submerged jet configuration, the free surface jet configuration was also investigated. For submerged jet impingement of FC-72, three jet nozzles of inner diameter of 1.16 mm, 2.29 mm, and 3.96 mm were used with corresponding surface-to-nozzle diameter ratios of 23.8, 12.1, and 7.

Table 6: Comparison of saturated fluid properties

	Water (P=0.176 bar)	Water (P=0.276 bar)	Water (P=0.477 bar)	FC-72 (P=1.01 bar)
T_{sat} [^{o}C]	57.31	67.18	80.14	56.6
ρ_l [kg/m^3]	984.5	979.3	971.7	1594
ρ_v [kg/m^3]	0.1158	0.1766	0.2949	13.43
μ_l [kg/m-s]	0.0004862	0.0004202	0.0003538	0.0004377
σ [N/m]	0.0667	0.06498	0.06264	0.008024
h_{lv} [J/kg]	$2.36x10^6$	$2.34x10^6$	$2.31x10^6$	$8.8x10^4$
Cp_l [J/kg-K]	4182	4185	4194	1101
k_l [W/m-K]	0.6383	0.6472	0.6563	0.05384
Pr	3.19	2.72	2.26	8.95

For convenience, the experimental test conditions have been divided into three experimental test matrixes. Table 7 shows the experimental test matrix for submerged sub-atmospheric jet impingement boiling of water. Table 8 shows the experimental test matrix for submerged atmospheric jet impingement boiling of FC-72. Table 9 shows the experimental test matrix for free surface sub-atmospheric jet impingement boiling of water.

Table 7: Test matrix for submerged sub-atmospheric water testing

d_j [mm] (d_{surf}/d_j) - H/d_j -	Ra [nm]	ΔT_{sub} [^oC]	P [bar] (T_{sat} [^oC])	Re	V_j [m/s]	CHF [W/cm^2]
1.16 (23.8) - 6 -	123	0	0.084 (42.4)	0*	0	43.2
			0.176 (57.3)	0*	0	65.0
				1830	0.81	70.6
				3573	1.58	81.8
				5510	2.43	94.1
				8844	3.86	117.7
			0.276 (67.2)	0*	0	77.3
				1968	0.75	88.7
				5731	2.20	115.6
				9168	3.48	143.3
			0.478 (80.2)	0*	0	94.5
				1853	0.61	105.2
				5472	1.83	134.4
				9105	3.04	161.6
				12634	4.18	190.6**
	33	0	0.176 (57.3)	0*	0	54.6
				1862	0.84	60.9
				3655	1.64	65.3
				5478	2.44	76.6
				6757	3.03	88.5
		17		0*	0	126.4
				1486	0.84	135.7
				2881	1.63	149.4
				4141	2.34	158.2
				5966	3.37	183.0**
		32		0*	0	Not reached
		42		0*	0	Not reached
		0	0.276 (67.2)	0*	0	66.3
				1967	0.74	72.7
				3837	1.44	78.0
				5757	2.18	91.9
				9156	3.48	117.0
				10876	4.13	125.7
			0.476 (80.1)	0*	0	87.3
				1940	0.62	94.3
				3960	1.27	101.3
				5751	1.83	110.0
				9413	3.02	139.4
				12708	4.08	155.5
				14337	4.61	166.9

* pool boiling, **imminent CHF

Table 8: Test matrix for submerged atmospheric pressure FC-72 testing

d_j [mm] (d_{surf}/d_j) - H/d_j -	Ra [nm]	ΔT_{sub} [^oC]	P [bar] (T_{sat} [^oC])	Re	V_j [m/s]	CHF [W/cm^2]
1.16 (23.8) - 6 -	33	0	1.01 (56.6)	0*	0	15.2
				2133	0.51	15.2
				3795	0.90	15.7
				5570	1.32	17.5
				7162	1.71	18.3
				9316	2.21	18.8
				12484	2.97	21
				14216	3.38	21.9
2.29 (12.1) - 6 -				0*	0	14.4
				1893	0.23	14.9
				3631	0.44	15.4
				5553	0.67	15.6
				7111	0.85	15.9
				9089	1.1	16.7
				12503	1.5	18
				14111	1.7	18.5
3.96 (7.0) - 6 -				0*	0	14.9
				1935	0.13	15.1
				3622	0.25	14.5
				5539	0.39	14.8
				6971	0.49	14.7
				8331	0.58	15.3

* pool boiling

Table 9: Test matrix for free surface sub-atmospheric water testing

d_j [mm] (d_{surf}/d_j) - H/d_j -	Ra [nm]	ΔT_{sub} [^oC]	P [bar] (T_{sat} [^oC])	Re	V_j [m/s]	CHF [W/cm^2]
1.16 (23.8) - 6 -	33	0	0.176 (57.3)	1641	0.79	34
				3709	1.60	32.2
				5641	2.41	60.5
				7777	3.31	84.5
				10196	4.36	130.2
			0.276 (67.2)	6078	2.26	98.4
				7926	2.94	103.2
				9584	3.55	128.6
				11178	4.14	142.3
				13123	4.86	159.6
				15859	5.88	185.4

5 RESULTS AND DISCUSSION

This chapter presents the salient results of the study. Validation results are presented first followed by jet impingement boiling data. Even though it is customary in literature to plot boiling curves on a log-log scale, a linear-linear scale has been adopted all throughout this chapter for ease of comparison between boiling curves at different experimental conditions. The experimental data are validated against standard single-phase and pool boiling heat transfer correlations. Data repeatability is demonstrated with acceptable levels of variability. Boiling curves for water and FC-72 at different experimental conditions are provided and compared. For FC-72, the probability of boiling incipience and a passive means to eliminate temperature overshoot are presented. Variations in critical heat flux are captured in a non-dimensional CHF map and a general CHF correlation for submerged jet impingement boiling is developed. The effect of fluid subcooling on the resultant boiling curves and CHF limits is presented. Heat transfer characteristics between water and FC-72 are compared for an approximately equivalent fluid saturation temperature. Preliminary free surface jet impingement data is compared against submerged jet impingement data to investigate the effect of jet configuration. High-speed images are provided to qualitatively compare the effect of system parameters on jet impingement boiling.

The saturation temperature used in the jet impingement boiling curves presented in this chapter is based on the system pressure. Note that an increase in heated surface

stagnation pressure occurs as a result of the impinging jet flow. Zhou and Ma [22] considered it necessary to incorporate a correction for the increase in stagnation pressure (and hence saturation temperature) in terms of a subcooling effect for jet exit velocities in excess of 10 m/s for a R-113 jet. This correction shifts the boiling curve for high velocity jets to the left. For an impinging velocity of 5 m/s, which is approximately the highest jet exit velocity considered in this study, the increase in stagnation pressure is approximately 0.12 bar for water and 0.20 bar for FC-72. Since some of the present water experiments were performed at sub-atmospheric conditions, a small increase in stagnation pressure could significantly raise the saturation temperature of the fluid, which is more sensitive to pressure at low absolute values. For the worst case scenario of Re=8844 at the lowest pressure of 0.176 bar, the rise in stagnation pressure of 0.073 bar corresponds to a 41 percent increase in pressure and a 13.2 percent increase in fluid saturation temperature. However, taking into consideration that this increase is experienced over a very small region of the surface (owing to the large d_{surf}/d_j ratio for the high jet exit velocity cases) as well as the reduction in momentum prior to impingement due to mass entrainment in the submerged jet configuration, a correction was not deemed necessary

5.1 TEST SET-UP VALIDATION

Validation tests were performed to corroborate that the test set-up performed as intended. Natural convection and pool boiling data under ordinary conditions were compared against standard heat transfer correlations. Data repeatability was examined under experimental repetition and replication for various experimental conditions.

5.1.1 DATA VALIDATION

Data from a preliminary validation experiment were used to benchmark single-phase natural convection and pool boiling heat transfer against standard correlations in literature. The experiment was performed using water at atmospheric pressure with a nominal pool temperature of 29.5 ^{o}C corresponding to a 70.5 ^{o}C pool subcooling. For this experiment, the heated surface had a recently machined surface finish. Figure 16 shows a plot of wall heat flux as a function of wall superheat over the single-phase heat transfer region. These data are compared against a standard natural convective correlation for an upward facing horizontal heated surface [5]

$$\overline{Nu_{d_{surf}}} = 0.54 Ra_{d_{surf}}^{1/4} \tag{7}$$

This correlation is valid for a range of Rayleigh numbers ($Ra_{d_{surf}}$) from 10^4 to10^7 which comprises the range of the experimental data. Considerably good agreement

(within 6.5 percent on average) is observed between the correlation and the experimental data.

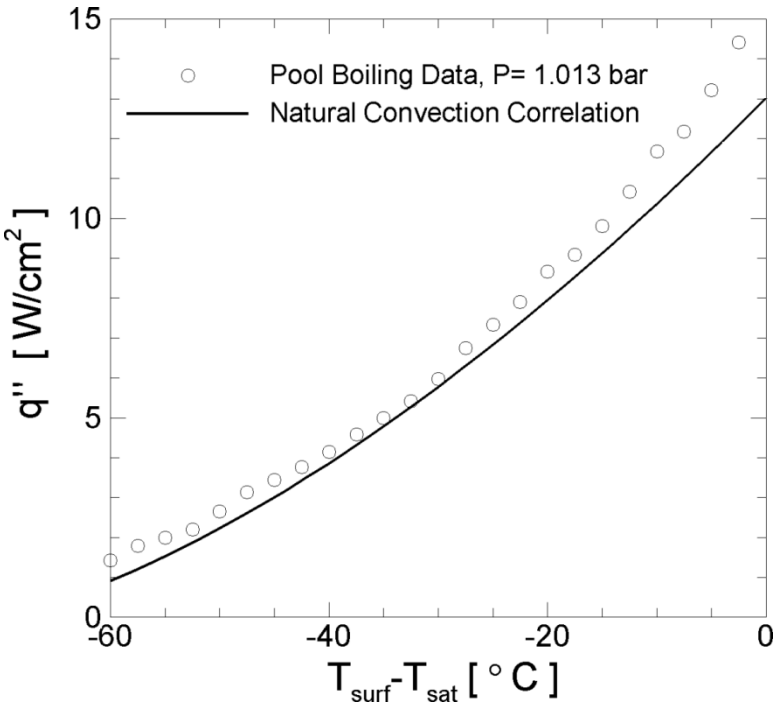

Figure 16: Comparison of single-phase data with natural convection correlation

The nucleate boiling data from the same experimental run were compared against Rohsenow's correlation for fully developed nucleate boiling [5],

$$q''_{surf} = \mu_l h_{lv} \left[\frac{g(\rho_l - \rho_v)}{\sigma} \right]^{1/2} \left(\frac{C_{p,l}[T_{surf} - T_{sat}]}{C_{surf,l} h_{lv} \mathrm{Pr}_l^n} \right)^3 \quad (8)$$

A $C_{surf,l}$ value of 0.0128 for water on a polished copper surface and a Prandtl number exponent of unity, as recommended for water, were used in the correlation. The fully developed nucleate boiling data shown in Fig. 17 was found to be in good overall agreement with the predictions from Rohsenow's correlation. In general, the correlation predicts a slightly lower (2 ^{o}C - 3 ^{o}C) wall superheat for a given wall heat flux, but the data are within the experimental uncertainty of the correlation which according to [5] can be as large as 100 percent when used to estimate wall heat flux for a given wall superheat. However, to estimate a wall superheat for a given wall heat flux, the errors are reduced by a factor of three.

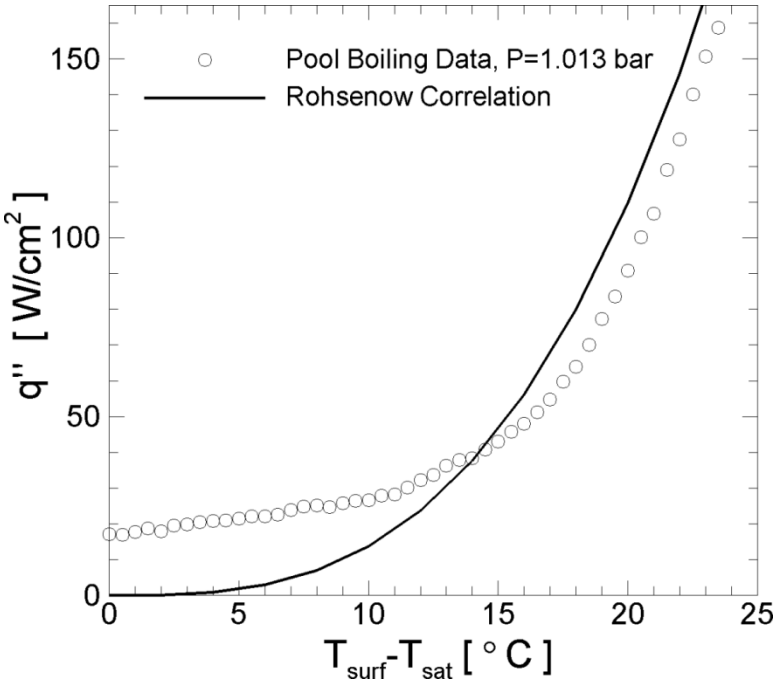

Figure 17: Comparison of nucleate boiling data with Rohsenow's correlation

5.1.2 WATER DATA REPEATABILITY

Water data repeatability was tested at the lowest pressure of P = 0.176 bar for saturated conditions by performing experimental repetitions and replications. Due to surface discoloration that occurred after periodic testing, the surface had to be periodically re-sanded. Therefore, data repeatability was tested for surface sanding as well as flow conditions. Figure 18(a-c) shows the corresponding data repeatability during saturated pool boiling for 600-grit, 1200-grit, and 1500-grit sanding surface finish respectively. Test #1 and test #2 corresponded to repetition experiments wherein the second test was performed following the first one. Test #3 was performed on a different day. For this test, the test chamber was opened and put back together, the water in the facility was changed, and the surface was re-sanded. This third test therefore characterizes the replication error in the measurement. Figure 18(d) shows a data replication experiment on a 1500-grit surface finish during saturated jet impingement boiling with average Re of 1862. The discrepancy observed in the partially developed nucleate boiling region in Fig. 18(d) is attributed to variations in experimental conditions during data replication. For fixed experimental conditions, good agreement is observed between the experimental repetitions and replications. In all plots in Fig. 18, the CHF varied within 6 percent for all cases considered, indicating acceptable level of data repeatability using the adopted test procedures.

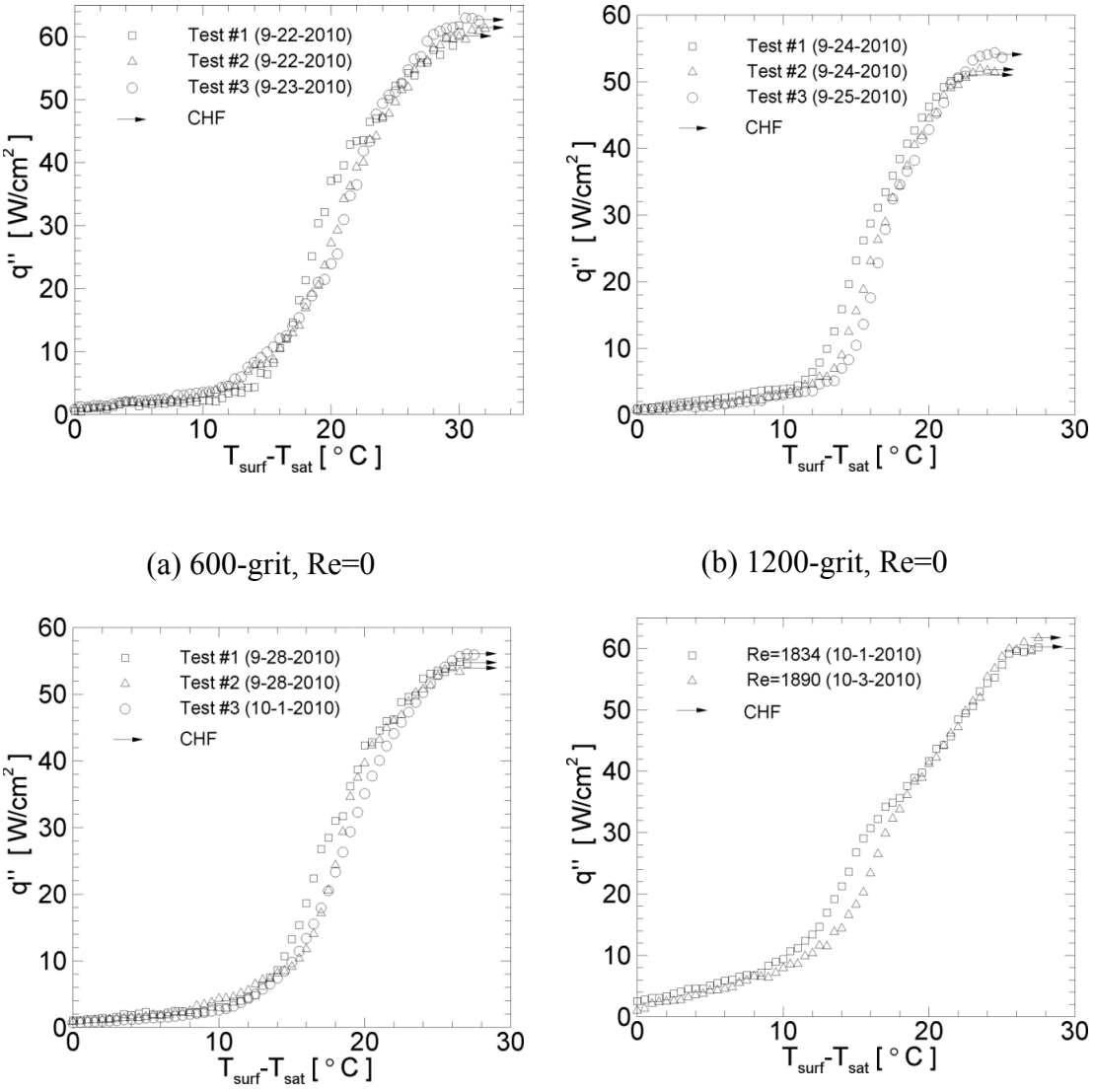

(a) 600-grit, Re=0

(b) 1200-grit, Re=0

(c) 1500-grit, Re=0

(d) 1500-grit, Re=1862

Figure 18: Data repeatability at P = 0.176 bar for saturated conditions

Not surprisingly, it was found that the sanding level played a key role in achieving repeatable results. Figure 19 shows saturated pool boiling curves for three different surface finishes obtained using 600-grit, 1200-grit and 1500-grit sandpapers. It should

be noted that the higher grit sanding was performed subsequent to the coarse grit sanding. Each of the pool boiling curves shown in Fig. 19 is an average of three repeat experiments. Figure 19 demonstrates the usefulness of the LOWESS filter in providing a convenient method of representing average boiling curves since data for each curve could be recorded at different heat fluxes and superheat levels. This filter also facilitates easier comparison between different boiling curves since filtered data can be reconstructed at exactly identical superheat levels across these different curves. Recall from Sections 4.2 and 4.3 that the 600-grit sanding resulted in an average surface roughness (Ra=123 nm) that was about 3.7 times larger than the 1500-grit sanding (Ra=33 nm) and also consistently exhibited a lower contact angle. The CHF for the 600-grit surface finish is observed to be 15.5 percent higher than that for the finer grit surface finishes, while the CHF for the higher grit surface finishes are within 6.9 percent of each other. The difference in the CHF of the 1200 and 1500-grit surface finishes are close to the replication error limits of six percent and hence the difference between 1200-grit and 1500-grit CHF data might not be significant.

The present data indicate that for the same level of superheat, a higher q" is observed for the finer grit surface finishes of 1200 and 1500-grit compared with the 600-grit finish. This trend is in contradiction with that predicted by Rohsenow's correlation, which indicates that scored surfaces have a higher q" for the same superheat as compared with a polished surface. The reason for this discrepancy is unclear. However, it is to be noted that all surface finishes reported here, including the 600-grit, are considered fine by most commercial standards. The most important aspect

highlighted by the data in Fig. 19 is the need for consistent and meticulous surface preparation procedures to obtain repeatable data. Based on these results, it was decided to perform experiments with the two most distinct sanding levels of 600-grit and 1500-grit, corresponding to average surface roughness of 123 nm and 33 nm respectively.

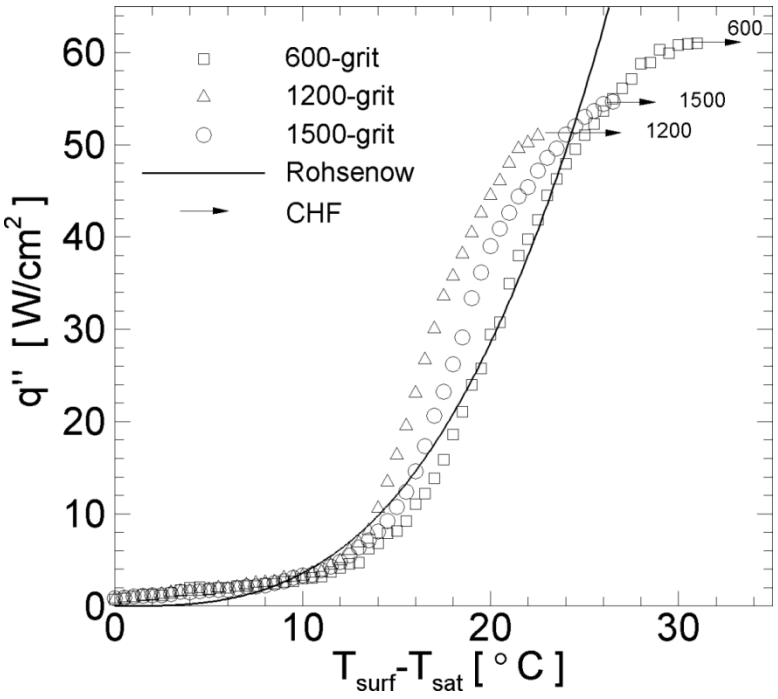

Figure 19: Effect of surface roughness on saturated pool boiling data, Ra=123 nm for 600-grit and Ra=33 nm for 1500-grit

5.1.3 FC-72 DATA REPEATABILITY

Data repeatability for saturated FC-72 was evaluated at a fixed sanding level of 1500-grit corresponding to a 33 nm average surface roughness. Figure 20(a) shows three boiling curves corresponding to three FC-72 pool boiling replication experiments. Note that each of these experiments was performed several days apart from each other. For each experimental replication the heat transfer surface was re-sanded and the working fluid was drained and poured back into the test chamber for degassing. Figure 20(b) shows three jet impingement boiling curves for submerged jet impingement boiling of FC-72 for an average Re of 12583 using a 1.16 mm inner diameter jet nozzle. On this figure, the two tests performed on the same day correspond to an experimental repetition while the tests performed on different dates correspond to a replication experiment. For fixed experimental conditions, good agreement is observed between the experimental repetitions and replications for both pool boiling and jet impingement boiling curves. Similar to the water case, the magnitude of the CHF for FC-72 varied within six percent for all cases considered, indicating acceptable level of data repeatability using the adopted test procedures. However, the boiling incipience superheat and thus the magnitude of the temperature overshoot, which occurred as a result of the low surface tension of the working fluid, was not repeatable. Boiling incipience for pool boiling of FC-72 have been reported to vary widely for identical test conditions and predictions of incipience superheat has been deemed very difficult and have been tackled using a probabilistic approach [42].

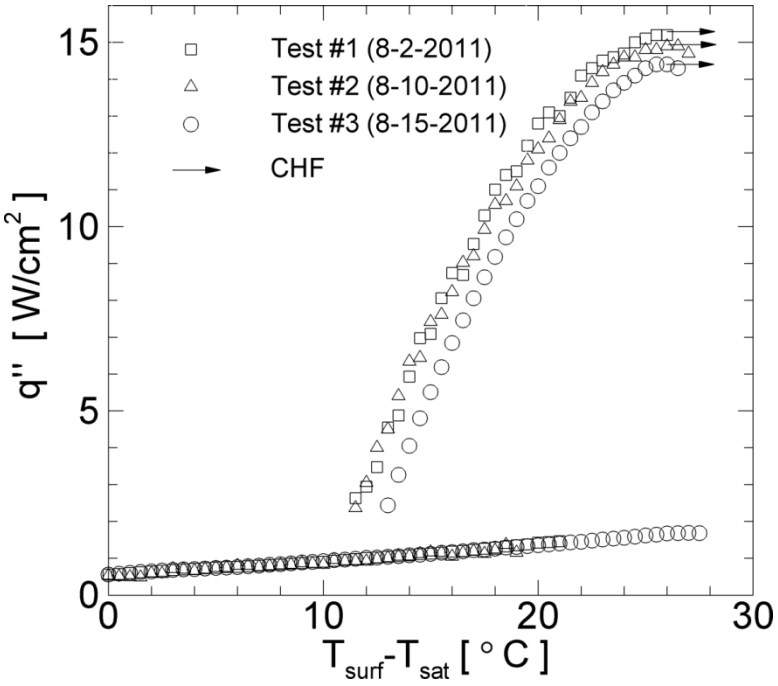

(a) Re=0

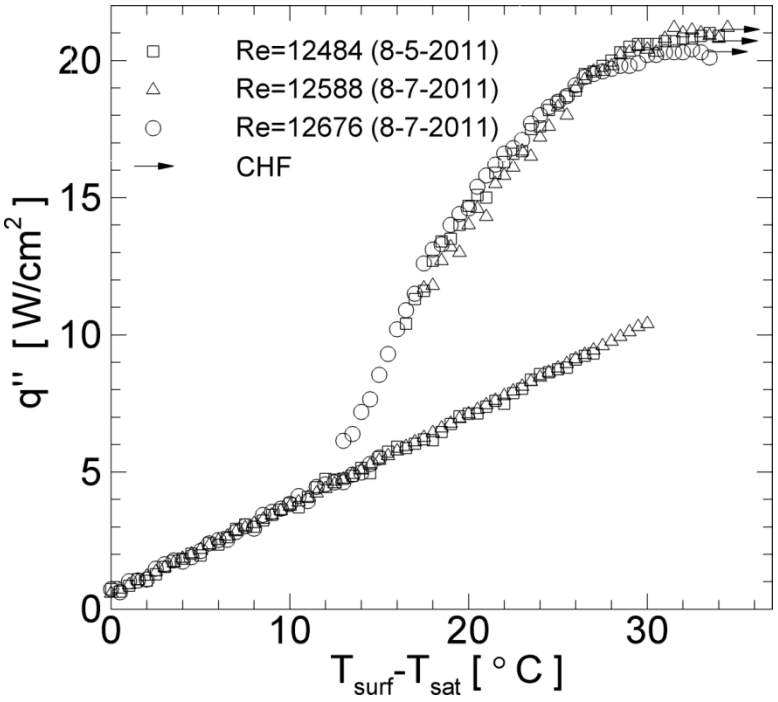

(b) Re=12583, d_j=1.16 mm

Figure 20: Data repeatability for saturated FC-72 on a Ra= 33 nm surface

5.2 WATER: SUBMERGED SUB-ATMOSPHERIC BOILING

This section summarizes all the experimental results obtained for water under submerged and sub-atmospheric conditions. For a detailed list of the experimental conditions considered, refer back to the experimental test matrix in Table 7 Chap. 4 . Preliminary testing indicated no evidence of hysteresis on the resultant boiling curves for this fluid. Therefore, all boiling curves shown for this fluid were recorded under increasing heat flux conditions alone.

5.2.1 SATURATED POOL BOILING

As a check of the current data with literature, and in order to provide a baseline condition for comparison with jet impingement data, saturated pool boiling experiments were performed at four different sub-atmospheric pressures. Figure 21 presents pool boiling curves at pressures of 0.084 bar, 0.176 bar, 0.276 bar, and 0.478 bar for a 123 nm average roughness surface. Rohsenow's correlation (Eq. 8) for saturated fully developed nucleate pool boiling [5] for a pressure of 0.276 bar is also plotted for comparison. A $C_{surf,l}$ value of 0.0128 for water on polished copper surface and a Prandtl number exponent of unity, as recommended for water, were used in the correlation. Although only the 0.276 bar comparison is shown, note that all boiling curves plotted agree reasonably well with Rohsenow's correlation in the fully developed nucleate boiling region, prior to CHF.

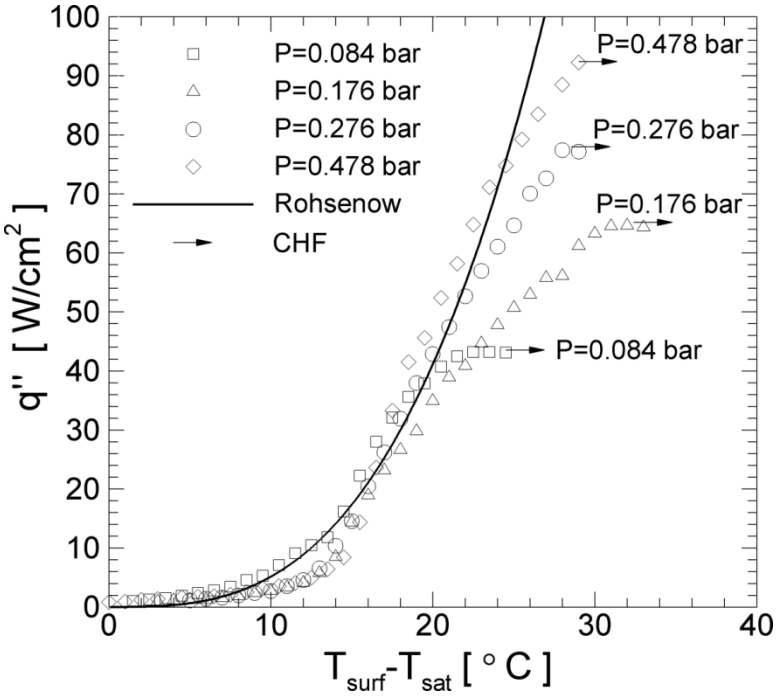

Figure 21: Saturated Water Pool Boiling Curves for a 123 nm Ra Surface

An increase in critical heat flux is observed with increasing pressure. This trend is captured by the standard and widely used CHF pool boiling correlation of the form [5],

$$q''_{CHF,sat,pool} = Ch_{lv}\rho_v\left[\frac{\sigma g\left(\rho_l-\rho_v\right)}{\rho_v^2}\right]^{1/4} \tag{9}$$

This correlation was originally developed by Kutateladze using dimensional analysis [48] and later derived by Zuber through a hydrodynamic instability pool boiling CHF model [49]. Using C=0.149, as proposed by Lienhard and Dhir [6] for a large

horizontal heated surface, Eq. 9 captures the CHF values from the experimental data within four percent average error and 7.4 percent maximum error. Although pressure is not directly included in the correlation, its effect is implicitly captured by the change in vapor density since Eq. 9 implies that critical heat flux for a saturated pool is proportional to the vapor density to the one half power.

The trend of increasing pool boiling CHF with increasing pressure seen in Fig. 21, which is captured in Eq. 9 through the variations in vapor density, can be explained by the size of the vapor bubbles observed at varying pressures. Figure 22(a-d) shows photographs of saturated pool boiling at a heat flux of approximately 10 W/cm^2 on a 33 nm average roughness surface for pressures of 0.084 bar, 0.176 bar, 0.276 bar and 0.478 bar, respectively. Note that although the nozzle is seen in these pictures, there is no jet flow. These photographs qualitatively indicate that the bubble size decreased with increasing pressure from 0.084 bar to 0.478 bar. For a fixed evaporating fluid mass, this decrease in bubble size can be explained partly by an increase in the vapor density by five times from 0.084 bar to 0.478 bar. In addition, surface tension is 10.5 percent higher at the lowest pressure in comparison to that at the higher pressure due to the lower saturation temperature of the fluid, which also results in larger bubble departure diameters. Larger bubbles tend to coalesce at the surface more readily leading to the lower CHF value seen at lower pressures.

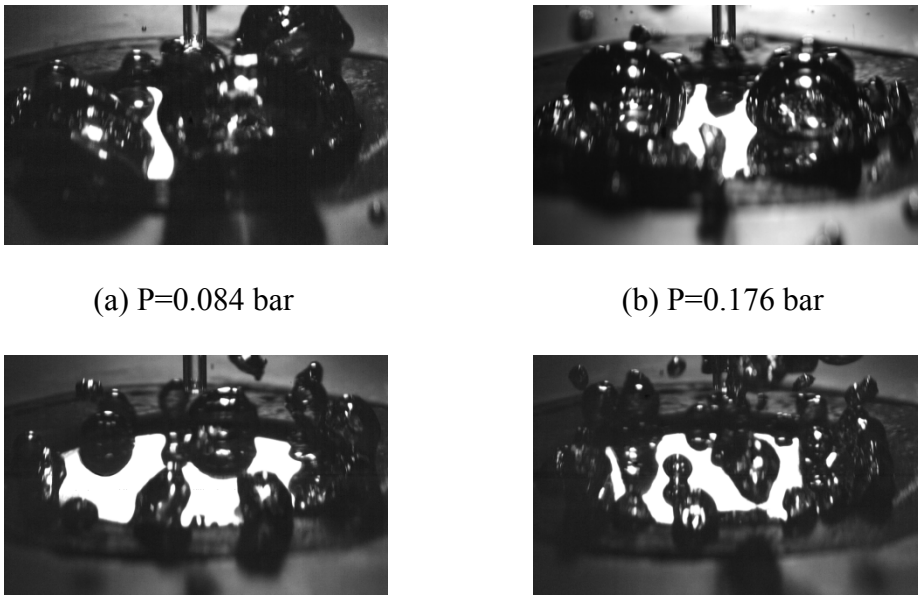

(a) P=0.084 bar (b) P=0.176 bar

(c) P=0.276 bar (d) P=0.478 bar

Figure 22: Bubble size comparison at saturated pool boiling conditions for a surface heat flux of q"=10 W/cm^2 on a 33 nm Ra surface

5.2.2 SUBCOOLED POOL BOILING

When the bulk fluid temperature in a pool boiling system is maintained at a temperature lower than the fluid saturation temperature, the system is said to be subcooled. To establish the effect of fluid subcooling in the pool boiling configuration, prior to study its effect during jet impingement boiling, subcooled pool boiling experiments were performed at a pressure of P=0.176 bar. Fluid subcooling is well known for increasing CHF in pool boiling systems [5, 6, 36]. However, the effect of fluid subcooling on the nucleate boiling region of the boiling curve is not entirely clear. Some consider the effect of fluid subcooling to be negligible during nucleate

boiling [5], while others mention observing a small shift of the boiling curve to the left as a result of a subcooled pool [6]. It is for this reason that, in most cases, it is often suggested that saturated pool boiling correlations can be used to approximate the heat transfer characteristics from a subcooled pool boiling system with fair amount of accuracy.

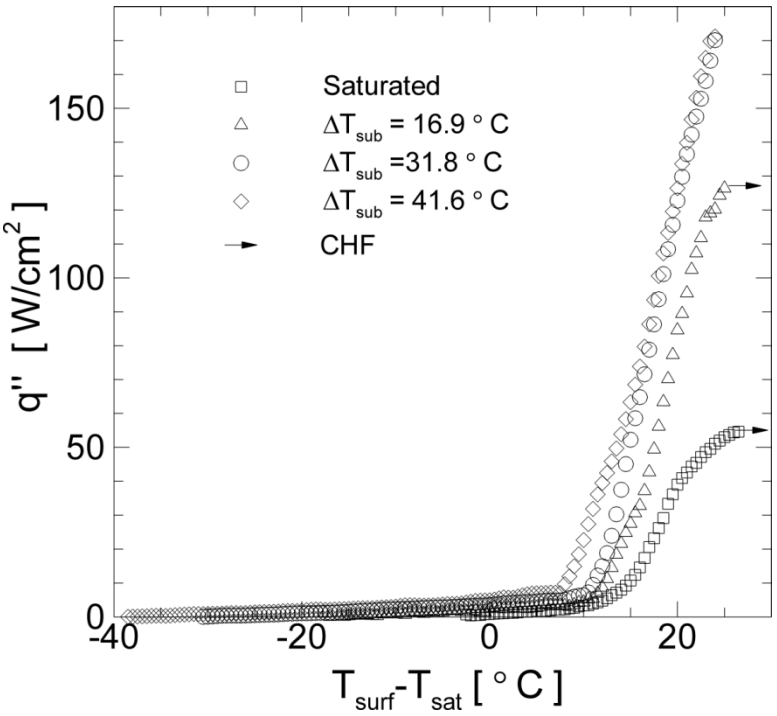

Figure 23: Effect of fluid subcooling on pool boiling of water at P=0.176 bar on a 33 nm Ra surface

Figure 23 shows the effect of fluid subcooling on pool boiling of water at a pressure of 0.176 bar on a 33 nm Ra surface. The general trend is for the boiling curve to shift to

the left with increasing fluid subcooling indicating enhanced heat transfer performance at lower fluid temperatures. Note that leftward shift of the boiling curve is more evident at low fluid subcoolings. At the two highest fluid subcoolings of 31.8 ^{o}C and 41.6 ^{o}C, there is evidence of the boiling curves merging at high heat flux values. This trend could indicate that the boiling curves tend to become insensitive to fluid temperature at high subcoolings. The critical heat flux was also found to increase with increasing fluid subcooling. Note that CHF could not be attained due to the heater power limitations at subcooling levels of 31.8 ^{o}C and 41.6 ^{o}C.

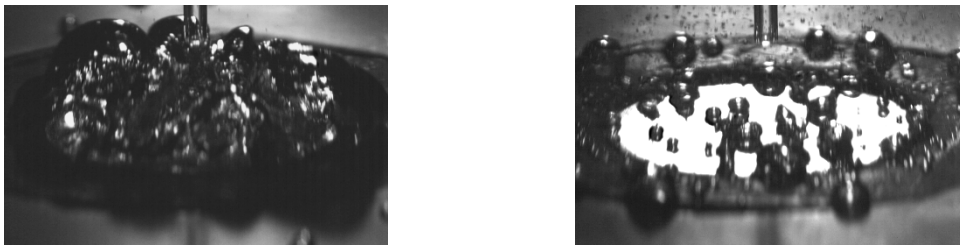

(a) ΔT_{sub}= 0 ^{o}C (b) ΔT_{sub}= 17 ^{o}C

Figure 24: Saturated and subcooled pool boiling visualization at P=0.176 bar on a 33 nm Ra surface for a heat flux of q"=50 W/cm^2

Visual observations of the pool boiling process under saturated and subcooled conditions showed significant differences. Figure 24(a) and (b) shows photographs of saturated and subcooled pool boiling respectively at a heat flux of approximately 50 W/cm^2 on a 33 nm average roughness surface for a pressure of 0.176 bar. Note that

although the nozzle is seen in these pictures, there is no jet flow. For saturated pool boiling at elevated heat fluxes, bubbles are formed, grow, and coalesce to form vapor slugs near the heated surface making this condition more prone to reach CHF and more difficult to visualize. These vapor slugs grow larger in size and periodically leave the surface as large vapor mushrooms. For subcooled boiling, bubbles which are formed grow to a smaller size in comparison to the saturated case as they condense near the heated surface. Therefore, these bubbles are less likely to coalesce near the surface retarding CHF to higher magnitudes in comparison to the saturated case. Once the CHF condition is reached for subcooled pool boiling, its consequences are more dramatic because of a larger and much more sudden temperature excursion as compared with saturated pool boiling. For saturated conditions, the boiling process was more likely to enter the transition boiling regime at CHF, while for subcooled conditions, the boiling process immediately jumped into the film boiling region upon reaching CHF.

5.2.3 Jet Impingement Flow Visualization

In pool boiling, the boiling activity is initiated everywhere on the heated surface at the same time due to a nearly uniform surface heat transfer coefficient. In contrast, during jet impingement boiling, the significant radial variations in heat transfer coefficient cause the boiling activity to begin on the periphery of the heated surface where the

heat transfer coefficient is the lowest. The boundary between the regions on the surface cooled by single-phase forced convection and boiling heat transfer is known as the boiling front. Figure 25(a-c) shows the progression of the boiling front for saturated jet impingement boiling and (d-f) for subcooled jet impingement boiling at a pressure of 0.176 bar and on a 33 nm average roughness surface. The Re was 5478 for the saturated condition and 4141 for the subcooled condition. For the subcooled visualization, the fluid temperature was maintained at 17 ^{o}C below the fluid saturation temperature.

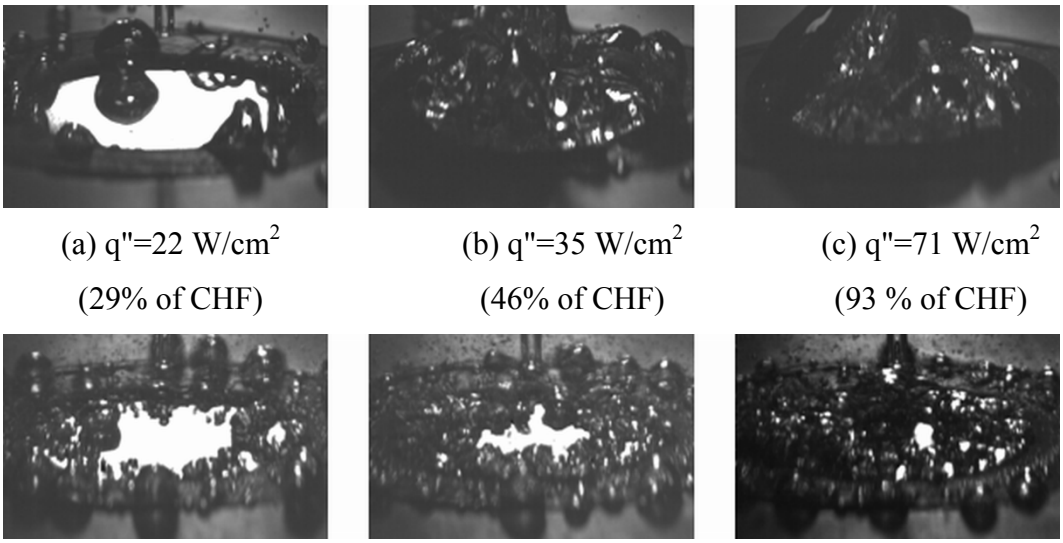

(a) q"=22 W/cm^2 (29% of CHF) (b) q"=35 W/cm^2 (46% of CHF) (c) q"=71 W/cm^2 (93 % of CHF)

(d) q"=108 W/cm^2 (68% of CHF) (e) q"=137 W/cm^2 (87% of CHF) (f) q"=157 W/cm^2 (99% of CHF)

Figure 25: Jet impingement boiling visualization at P=0.176 bar on a 33 nm Ra surface for (a-c) saturated Fluid and (d-f) 17 ^{o}C subcooled fluid

Figure 25(a) shows how boiling was initiated on the periphery of the heated surface during saturated conditions. The boiling front then progressed inwards towards the center with increasing heat flux in a heat transfer process known as partially developed nucleate boiling. Figure 25(b) shows that upon application of a sufficiently high heat flux, boiling occurred over the entire heated surface reaching a fully developed nucleate boiling stage. Figure 25(c) indicates that at higher heat fluxes, vapor bubbles merged to form even larger vapor slugs that periodically departed from the surface. These vapor slugs obscured most of the surface and eventually led to critical heat flux conditions. Note that at elevated heat flux values near CHF, the jet impingement boiling process was visually analogous to pool boiling.

Similar observations as those made from saturated jet impingement boiling were made about the subcooled case. However, under subcooled conditions, bubbles collapsed quickly and the surface remained more optically accessible making it easier to visualize. Images are provided starting at a heat flux of approximately 108 W/cm^2, which corresponds to 68 percent of the CHF value. All heat fluxes lower than about 55 W/cm^2 (35 percent of CHF value) were dominated by single-phase forced convection at this fluid subcooling. Figure 25(d) and (e) show how the boiling process was initiated on the periphery of the heated surface and progressed inwards with increasing heat flux. However, it is noted that the impingement zone resisted the initiation of boiling up to heat flux values near CHF. Therefore, for the subcooled case, the boiling heat transfer entered the fully developed nucleate boiling region of the boiling curve when a portion of the surface was not actively boiling. In accordance with the

observations made by Dukle and Hollingsworth [18, 20], at a fixed heat flux, while there were instantaneous variations in the shape of the boiling front, on a time-averaged sense, the jet flow stabilized the location of the boiling front. This observation was made more evident at subcooled conditions.

5.2.4 SATURATED JET IMPINGEMENT BOILING

Saturated jet impingement boiling experiments on a 123 nm Ra surface were performed at pressures of 0.176 bar, 0.276 bar, and 0.478 bar corresponding to fluid saturation temperatures of 57.3 ^{o}C, 67.2 ^{o}C, and 80.2 ^{o}C respectively. Jet impingement data at the lowest pressure of 0.084 bar could not be collected due to the limitation of the pump at this lower pressure. The upper limit of Re was dictated by the pump at low pressures and by the heater power at higher pressures. Critical heat flux for P=0.478 bar and Re=12634 was not attained owing to heater power limitations. However, visual observations indicated that the CHF condition was imminent, and hence this data point is included in the experimental test matrix in Table 7.

Figures 26, 27, and 28, present saturated jet impingement boiling curves at P = 0.176 bar, 0.276 bar, and 0.478 bar, respectively for the 123 nm roughness average surface. Rohsenow's correlation for saturated fully developed nucleate pool boiling, Eq. 8, evaluated at the corresponding pressure, is also given in these plots as a reference. Irrespective of the pressure, for a fixed wall superheat, the jet flow consistently

enhanced the heat flux from the surface in the partially developed nucleate boiling region, which existed for wall superheats past inception to less than approximately 20 ^{o}C. Also note that in this region of the boiling curve, increases in Re increased the slope of the curve indicating enhanced heat transfer coefficients. These trends indicate that both single-phase forced convection and two-phase heat transfer are important heat transfer mechanisms over this region of the boiling curve, as it was indicated visually in Fig. 25(a).

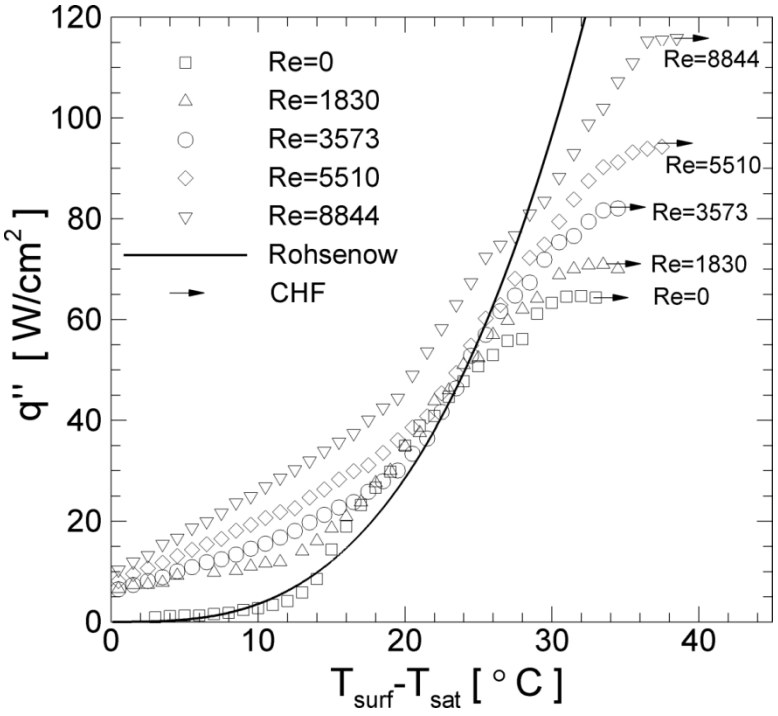

Figure 26: Saturated jet impingement boiling at P=0.176 bar on a 123 nm Ra surface

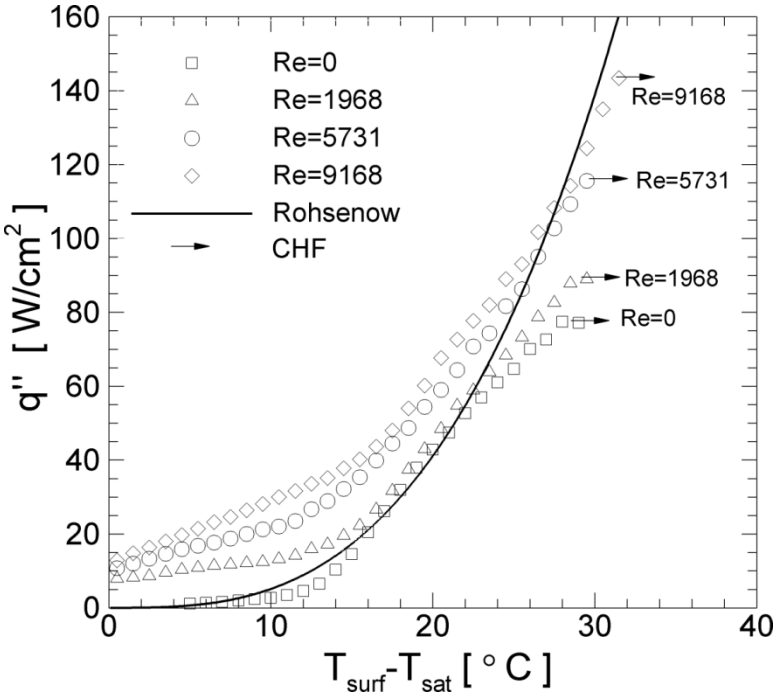

Figure 27: Saturated jet impingement boiling at P=0.276 bar on a 123 nm Ra surface

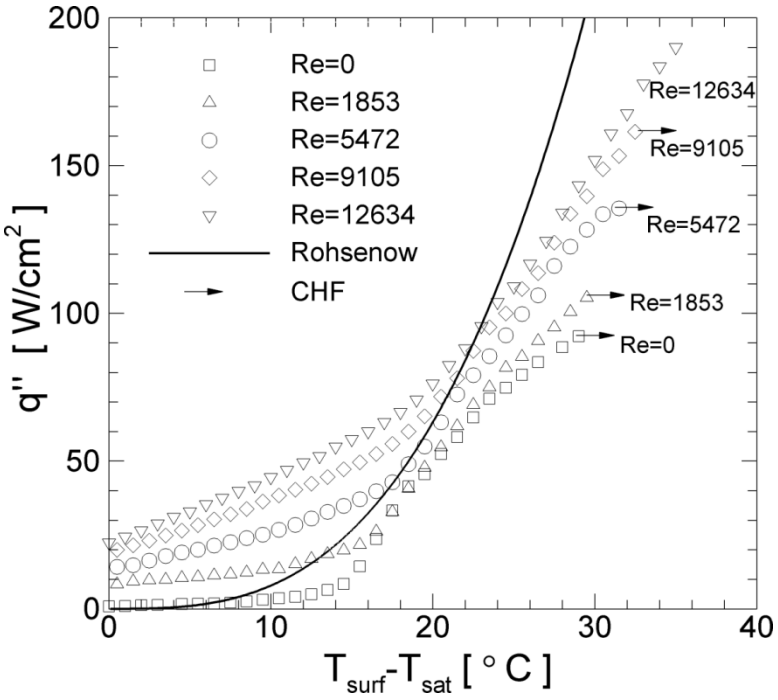

Figure 28: Saturated jet impingement boiling at P=0.478 bar on a 123 nm Ra surface

Past the “knee” of the boiling curves, for wall superheats approximately greater than 20 ^{o}C in Figs. 26-28, boiling curves for different Re tended toward a common boiling asymptote similar to that of fully developed nucleate pool boiling. Such conditions were visually represented in Figs. 25(b) and (c). These visual observations and the merging trend of the curves indicates that heat transfer rate in this region seems to be mainly governed by the two-phase heat transfer mechanism. As a result, heat transfer in the fully developed nucleate boiling region became less sensitive to jet Re. Invariance of the boiling curves with jet velocity in the fully developed nucleate boiling region has been reiterated in jet impingement boiling literature [4] and it is more apparent on a log-log boiling curve plot. This result allows, to a good approximation, the use of pool boiling correlations to predict the trend in the boiling curve for an impinging jet in the fully developed nucleate boiling region, so long as the estimated heat flux values are below that of jet impingement CHF at the given Re.

Figure 26 through Fig. 28 also indicate that larger jet Re had a more pronounced partial nucleate boiling regime compared with the pool boiling or low Re jet conditions. Also, the fully developed nucleate boiling regime occurred over a smaller extent at higher Re before reaching CHF. As is evident from these figures and as quantitatively indicated in Table 7, for a fixed roughness and pressure, CHF steadily increased with increasing Re. For a fixed Re, CHF increased with increasing pressure similar to the trend observed for pool boiling.

The qualitative behavior of the jet impingement boiling curves with varying pressures in Fig. 26 through Fig. 28 was similar in the partially developed and fully developed nucleate boiling regimes. Keeping in mind that lower pressures are associated with lower saturation temperatures, it is clear from these figures that jet impingement boiling curves for varying pressures had a similar behavior relative to the trend predicted by Rohsenow correlation (Eq. 8). However, it is to be noted that upon approaching CHF conditions, the saturated jet impingement boiling curves for the lowest pressure of 0.176 bar began to plateau in heat flux with increasing wall superheat. This behavior led towards higher wall superheats observed at critical heat flux in comparison to those seen at pressures of 0.276 bar and 0.478 bar. This flattening of the boiling curve as critical heat flux is approached at low pressure was also captured in Fig. 21 for saturated pool boiling and are accompanied by a corresponding reduction in heat transfer coefficient. Although the reason for this behavior at the lowest pressure is unclear, the trend suggests that fluid distribution on the surface remained relatively unchanged for a higher range of wall superheats near critical heat flux at the lowest pressure condition. Zuber's critical heat flux model, based on Kelvin-Helmholtz linear stability analysis [6], predicts that a higher surface tension tends to stabilize the vapor columns that occur at CHF conditions. Since surface tension is higher at lower pressures, it is possible that these vapor columns are more stable at lower pressures, leading to a fairly unchanged distribution of fluid within a wider range of wall superheats near CHF. However, further experiments near CHF under various pressures are needed to make conclusive statements.

To understand the effect of surface roughness on heat transfer performance, saturated jet impingement boiling experiments at pressures of 0.176 bar, 0.276 bar and 0.476 bar were also performed for varying Re on a 33 nm average roughness surface. Figure 29 through Fig. 31 show the saturated jet impingement boiling curves at these three respective pressures on the 33 nm Ra surface. Comparing these figures to their rougher surface analogs on Fig. 26 through Fig. 28 reveals, for a fixed pressure, that heat transfer trends in the partially developed and fully developed nucleate boiling region of the curve were similar for both surface roughnesses. However, it is clearly seen that the rougher 123 nm Ra surface sustained higher CHF values than the smoother 33 nm Ra surface. CHF for pool boiling has been shown to be dependent on surface finish because surface roughness can alter the wetting characteristics of the surface by the liquid, thereby affecting CHF [6]. Jones et al. [40] reported an increase in CHF with larger surface roughness for pool boiling of FC-77 on aluminum surfaces indicating that CHF dependence on surface roughness is important. The present results show that surface roughness continues to play an important role in CHF for a submerged impinging jet. Note that the higher jet impingement CHF values on the 123 nm Ra surface were in general also accompanied by larger wall superheats in comparison to the smoother 33 nm Ra surface.

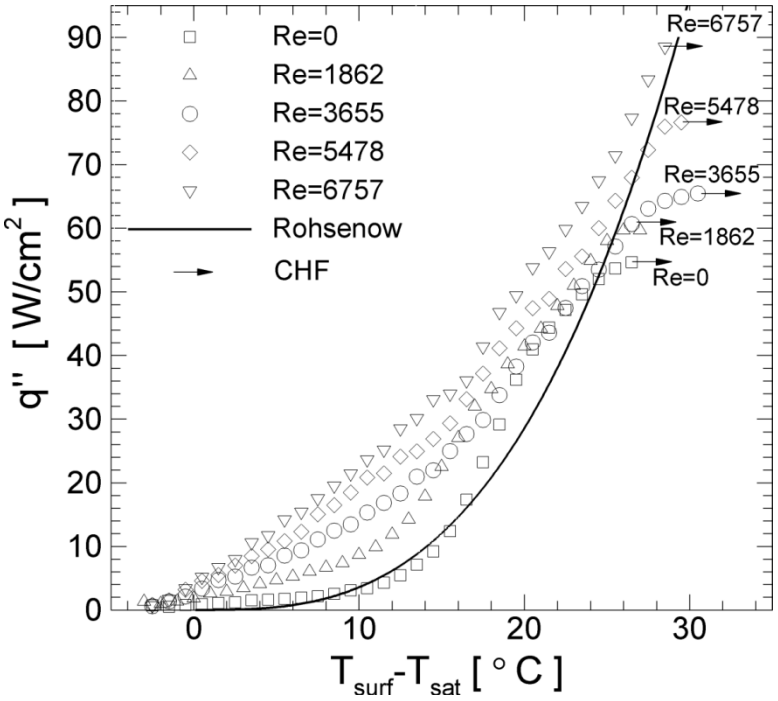

Figure 29: Saturated jet impingement boiling at P=0.176 bar on a 33 nm Ra surface

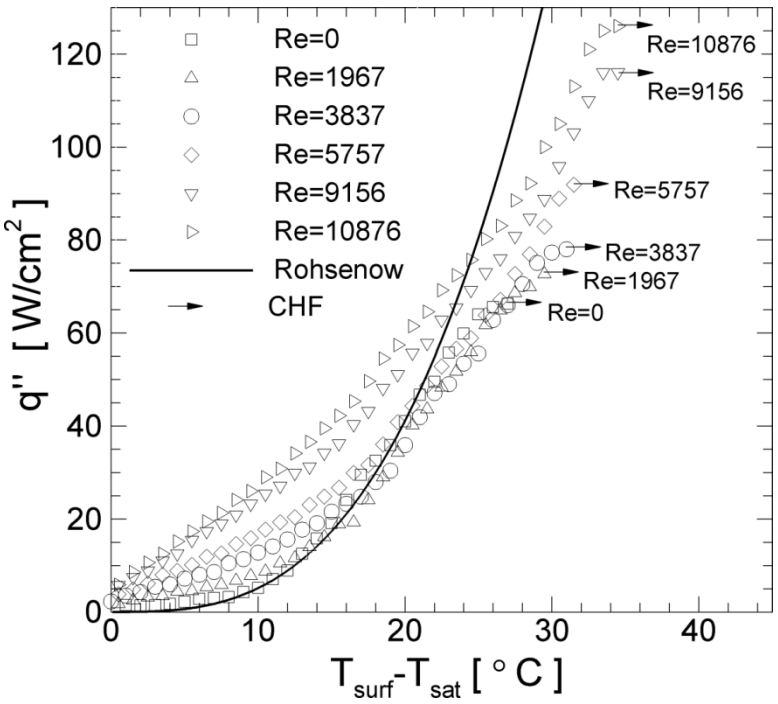

Figure 30: Saturated jet impingement boiling at P=0.276 bar on a 33 nm Ra surface

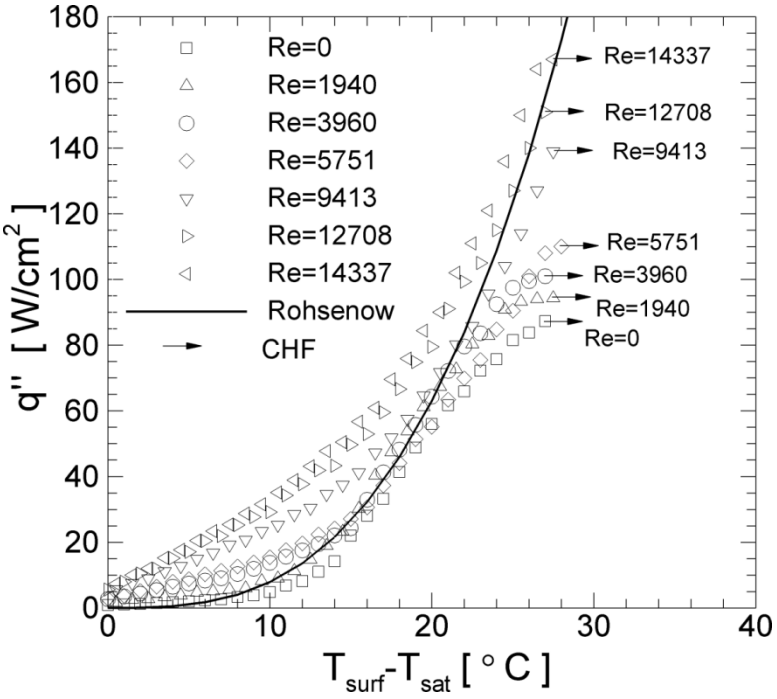

Figure 31: Saturated jet impingement boiling at P=0.476 bar on a 33 nm Ra surface

5.2.5 SUBCOOLED JET IMPINGEMENT BOILING

To determine the effect of fluid subcooling on jet impingement boiling, one subcooled fluid condition was studied at a system pressure of 0.176 bar. Figure 32 shows jet impingement boiling curves at a pressure of 0.176 bar on a 33 nm Ra surface for a 17 ^{o}C fluid subcooling. Critical heat flux for the highest Re=5966 was not attained owing to heater power limitations. However, visual observations indicated that the CHF condition was imminent. In accordance to prior literature findings [4], fluid subcooling increased heat transfer by shifting the boiling curves to the left (note the

shift relative to Rohsenow's correlation) and CHF limits were significantly enhanced when compared to the saturated case (Fig. 29 vs. Fig. 32).

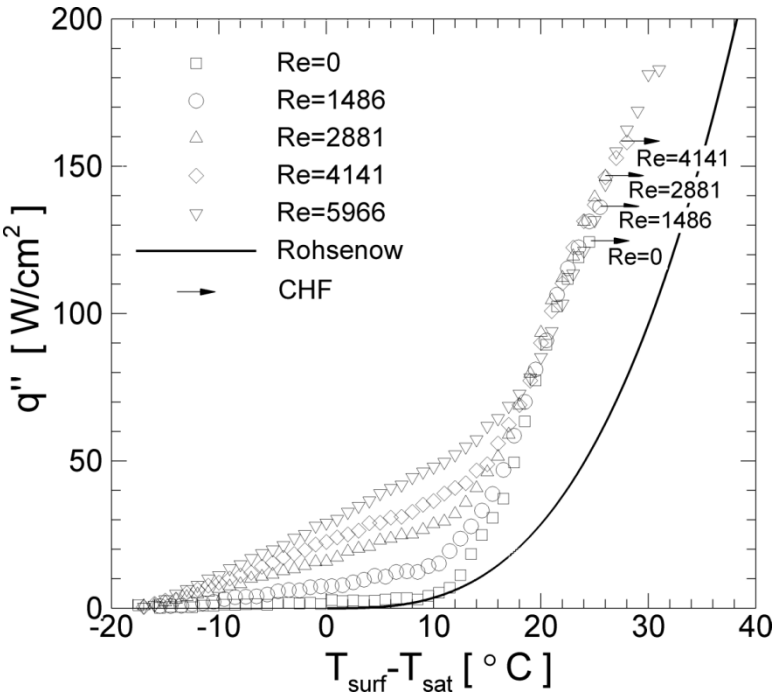

Figure 32: 17 ^{o}C Subcooled jet impingement boiling at P=0.176 bar on a 33 nm Ra surface

The merger of the boiling curves into a common boiling asymptote in the fully developed nucleate boiling region was more evident at subcooled conditions than at saturated conditions (Fig. 29 vs. Fig. 32). This trend is caused perhaps by the less chaotic and more repeatable flow boiling conditions during subcooled boiling due to the smaller vapor bubbles that quickly condensed as opposed to the large vapor slugs

seen in the saturated case. A particular difference between the saturated and subcooled conditions needs to be mentioned again. In the saturated boiling case, visual observations indicated that the entire surface was covered with bubbles when the boiling curves for different Re tended to merge (Fig. 25(b) and Fig. 29). However, in the subcooled condition, a comparison of the heat flux values in Fig. 32 with the visual observations in Fig. 25(d-f) clearly indicate that a significant portion of the surface was influenced by the single-phase jet following the merger of the boiling curves for different Re. It was only when the heat flux was close to the CHF limit, as seen in Fig. 25(f), that most of the surface was occupied with bubbles. The independence of surface heat flux with jet Re in the fully developed nucleate boiling regime (Fig. 32), despite the single-phase region under the jet influence visually observed in Fig. 25(d-e), corroborates the dominance of two-phase heat transfer in this region of the boiling curve. Thus, the saturated and subcooled data in the fully developed nucleate boiling region indicate that the influence of the jet in this boiling region is to enhance fluid supply to the surface compared with pool boiling, thereby enhancing the CHF limits.

5.3 FC-72: SUBMERGED ATMOSPHERIC BOILING

This section summarizes all the experimental results obtained for FC-72 under atmospheric conditions during pool boiling and submerged jet impingement boiling. For a detailed list of the experimental conditions considered, refer back to the

experimental test matrix in Table 8 Chap.4. Recall that this fluid has significantly different thermo-physical properties than water (Table 6) which led to different heat transfer characteristics. Data indicated considerable hysteresis near boiling inception on the resultant boiling curves for this fluid. Therefore, boiling curves for this fluid have been generated under increasing as well as decreasing heat flux conditions. All FC-72 experiments were performed at a fixed average surface roughness finish of 33 nm.

5.3.1 BOILING HYSTERESIS AND INCIPIENCE

Highly wetting fluids in contact with smooth heated surfaces often require wall temperatures much higher than the fluid saturation temperature to initiate boiling. These high surface temperatures are necessary to activate the cavities on the heated surface which have been wetted by the fluid due to its low surface tension. However, once a cavity becomes active, the wall superheat needed to sustain nucleation drops to a lower value leading to a temperature drop on the surface. For a heat flux controlled surface under increasing heat flux conditions, once boiling is initiated, the surface temperature drops leading to a boiling incipience phenomena referred to as temperature overshoot. Temperature overshoot is only experienced during increasing heat flux conditions and thus, highly wetting fluids often show significant boiling curve hysteresis near boiling incipience. Boiling curve hysteresis was studied by

performing boiling experiments for increasing and decreasing heat flux conditions. The decreasing heat flux experiment was performed immediately after completing the corresponding equivalent increasing heat flux experiment.

Figure 33(a-d) show the resultant boiling curve hysteresis for Re=0, Re=2133, Re=7162, and Re=14256 respectively using a 1.16 mm diameter nozzle. Note that similar pairs of experiments were performed for almost all flow conditions for FC-72. However, only a few experimental pairs are shown here for brevity since similar results were observed in all cases. Note that with the exception of the boiling curve region near boiling incipience, the boiling curves for increasing and decreasing heat flux conditions are nearly identical. This result indicates that boiling hysteresis only occurred as a result of the delay in boiling incipience for increasing heat flux conditions and highlights the good experimental practices adopted for data collection. As suggested by Zhou and Ma [12], boiling hysteresis is likely to have been caused by the deactivation of vapor embryos on the heater surface as a result of the low surface tension of the working fluid. Therefore, the main difference on the boiling curve between increasing and decreasing heat flux conditions is the absence of a temperature overshoot in the latter case.

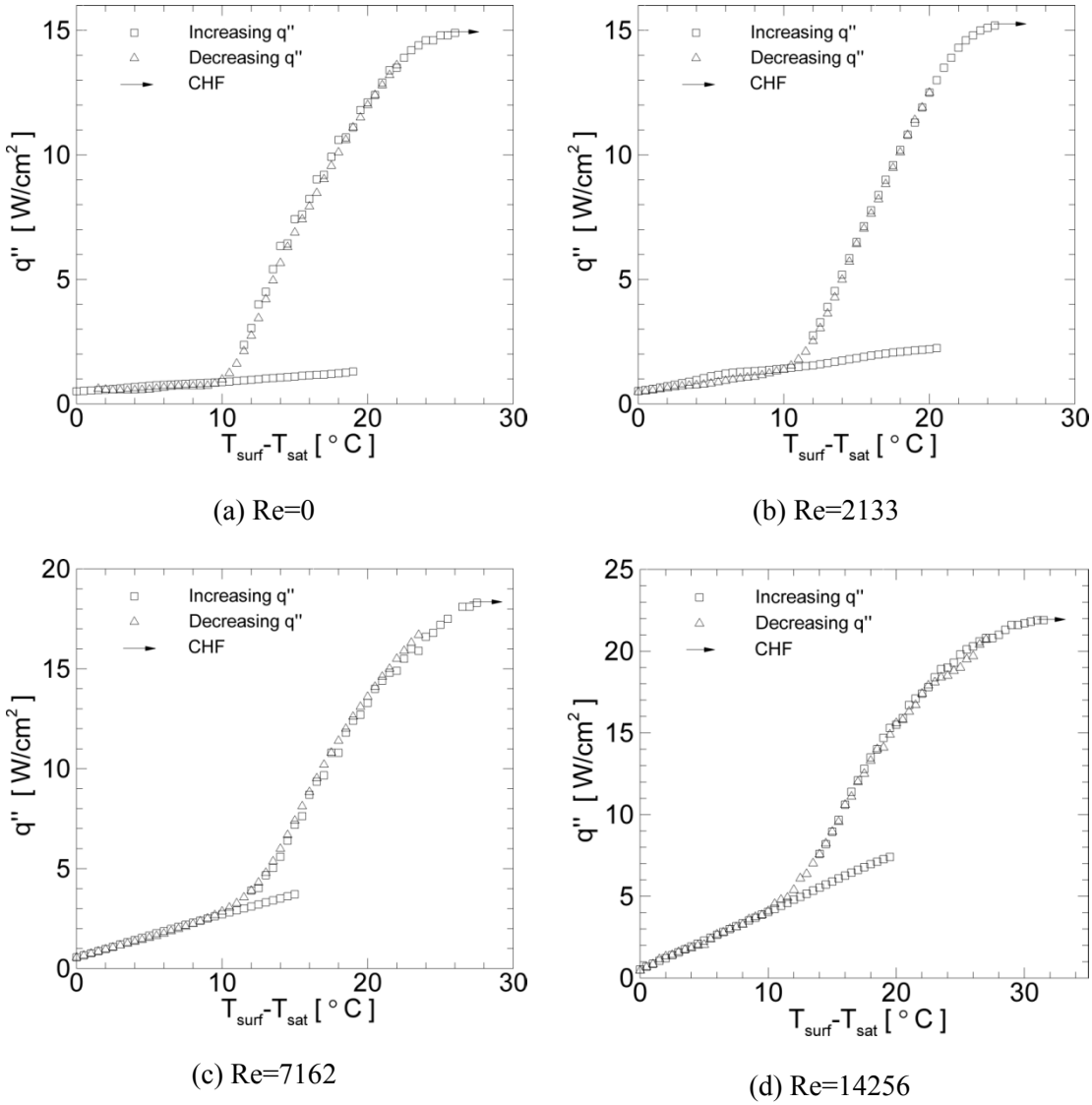

Figure 33: FC-72 boiling curve hysteresis for d_j=1.16 mm on a 33 nm Ra surface

As a result of the large wall superheats experienced prior to boiling incipience, once boiling was initiated, the boiling activity quickly spread over the entire surface. Figure 34(a-f) and Fig. 35(a-f) show instantaneous high-speed photographs of the transient boiling progression at the moment of boiling incipience for Re=2133 (ΔT_i=20.5 ^oC)

and Re=12484 (ΔT_i=27.5^{o}C) respectively. Note from Fig. 34(a) and Fig. 35(a) that boiling was initiated at a single random location on the surface. This location, as seen from these images, was not fixed but varied randomly for different experiments. Upon the activation of a single cavity on the surface, the boiling activity rapidly extended over the rest of the surface within a few milliseconds at the same heat flux value. The time it took for the boiling to cover the entire surface decreased with increasing incipience temperature as seen by these figures.

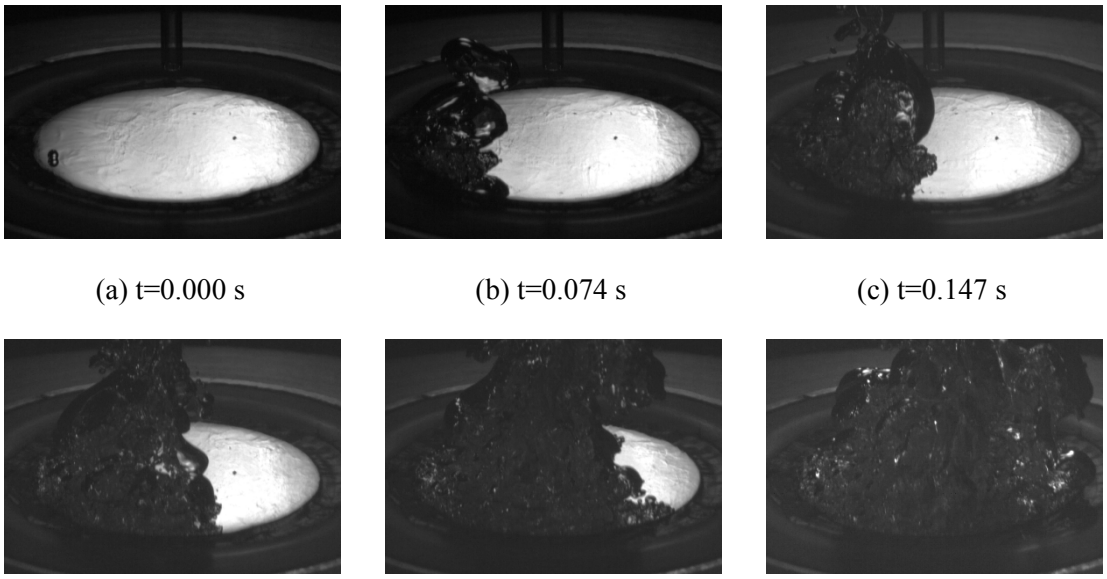

(a) t=0.000 s (b) t=0.074 s (c) t=0.147 s

(d) t=0.221 s (e) t=0.295 s (f) t=0.368 s

Figure 34: Boiling progression at boiling incipience for Re=2133 at ΔT_i=20.5 ^{o}C

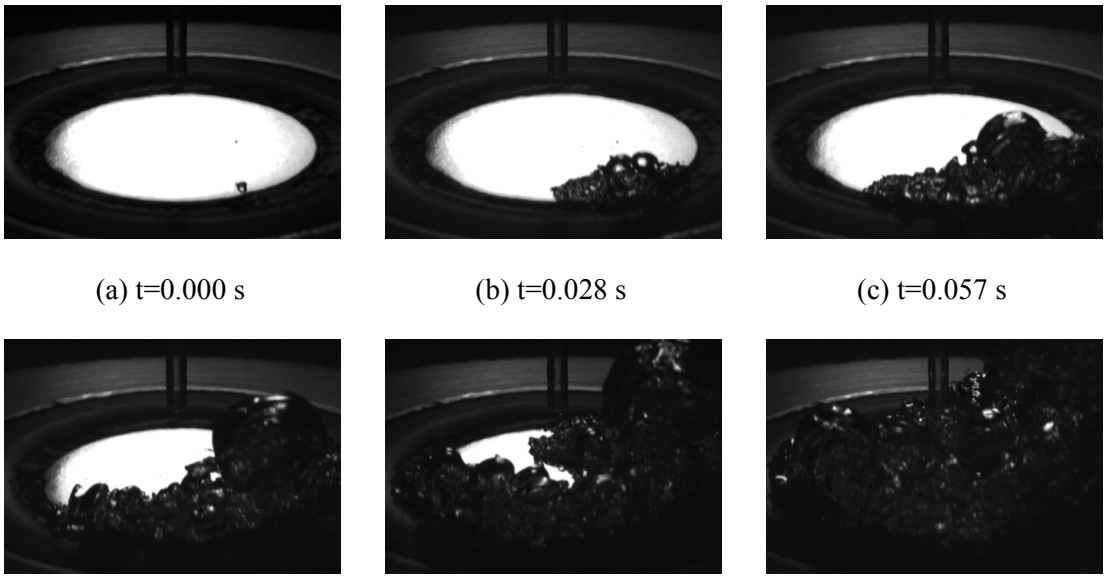

(a) t=0.000 s (b) t=0.028 s (c) t=0.057 s

(d) t=0.085 s (e) t=0.113 s (f) t=0.142 s

Figure 35: Boiling progression at boiling incipience for Re=12484 at ΔT_i=27.5 ^oC

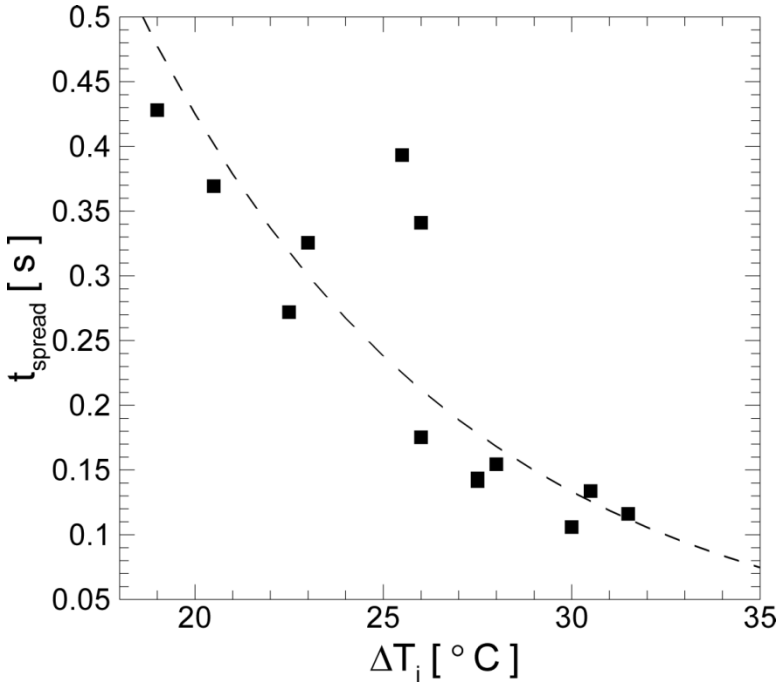

Figure 36: Time of boiling spread with superheat incipience temperature

Figure 36 shows the time required for the boiling activity to spread over the entire surface as a function of superheat incipience temperature. These times were determined by looking at high-speed footage taken exactly at the moment of boiling incipience similar to the images shown in Fig. 34 and Fig. 35. Since high-speed videos at the moment of boiling incipience were not obtained for all cases, only 13 data points are shown. Figure 36 indicates that the time of spread decreased exponentially with increasing wall superheat incipience temperature. Vapor generation at extremely rapid rates can potentially lead to a vapor explosion causing serious consequences. Vapor explosions are typically related with homogeneous nucleation [6] but they can also occur during heterogeneous nucleation on systems with very large superheat incipience temperatures.

Zhou and Ma [12] found that, for submerged jet impingement boiling of R-113 and L12378, the incipient boiling superheat was independent of jet parameters and only depended on fluid subcooling. Figure 37 shows the boiling incipience wall superheat with Re for three nozzle diameters for 24 experimental runs performed with FC-72 for increasing heat flux conditions. Note that no evident trend is observed from this data. As previously mentioned in Section 5.1.3, variations in incipience boiling superheat were observed even for identical test runs. A linear regression analysis was performed to test for a dependence of incipience boiling superheat on jet Re and jet diameter. Results indicated no statistically significant association of incipience boiling superheat with these jet parameters (P-value > 0.25).

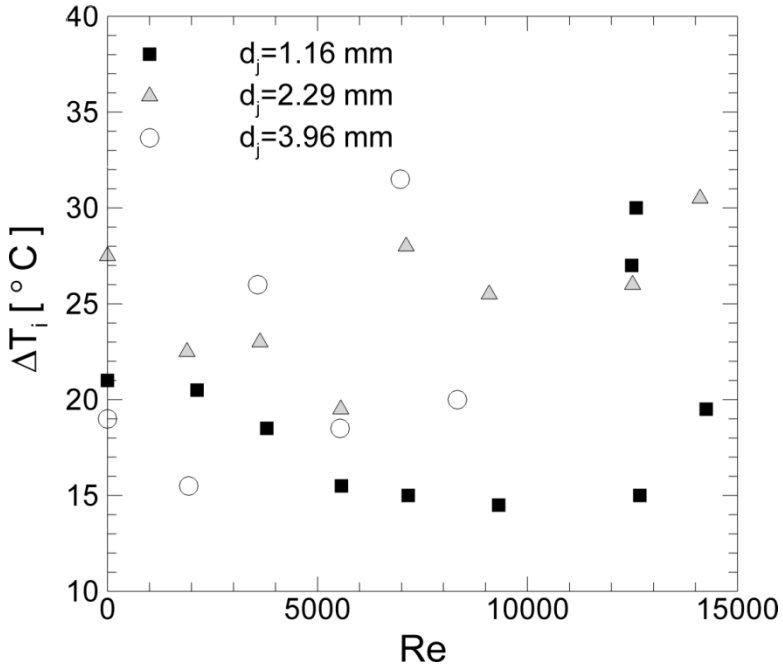

Figure 37: Boiling incipience wall superheat for varying jet parameters

You and Bar-Cohen [42] studied boiling incipience for pool boiling of FC-72 and R-113 on electronic material surfaces (Pt, SiO_2, Al_2O_3). Their studied revealed that incipience wall superheats were strongly dependent on the working fluid and weakly dependent on surface material. However, even for a fixed fluid/surface combination, wide variations in boiling incipience wall superheat values were reported from identical experimental runs. For this reason, You and Bar-Cohen [42] adopted a probabilistic representation of the incipience data. This method consisted of generating a plot of probability of boiling incipience as a function of wall superheat. A similar probabilistic representation of the incipience superheat data is adopted here. Figure 38 shows the probability of boiling incipience as a function of wall superheat for the

FC-72/Copper system studied. This plot was generated by creating a cumulative probability distribution function utilizing the boiling incipient superheats recorded for the 24 different FC-72 experiments conducted at increasing heat flux conditions. Note that the probability of boiling incipience increased almost linearly with increasing wall superheat from zero at 13.5 ^{o}C wall superheat to one (100 %) at 31.5 ^{o}C wall superheat. The 50 percent boiling incipience probability mark occurred around a wall superheat of 20 ^{o}C. For comparison, the probability of boiling incipience observed by You and Bar-Cohen [42] for FC-72 on electronic material surfaces varied between 0 at 17.9 ^{o}C wall superheat to 1 at 51.1 ^{o}C wall superheat with a 50 percent mark at around 24.7 ^{o}C wall superheat. However, in their case, the probability of boiling incipience did not vary linearly over the entire wall superheat range.

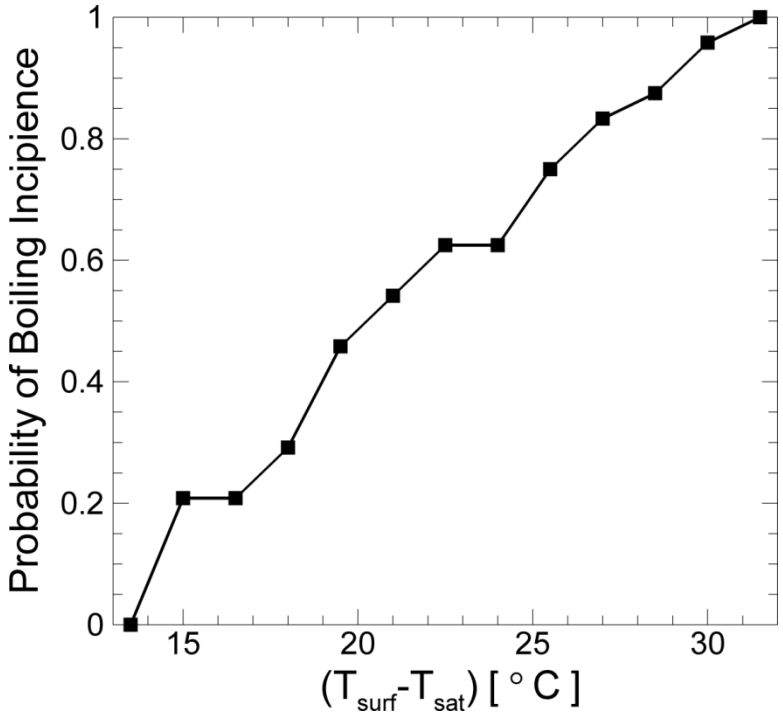

Figure 38: Probability of boiling incipience as a function of wall superheat

5.3.2 TEMPERATURE OVERSHOOT MITIGATION

Boiling incipience superheat temperatures can exceed the wall superheat temperature at CHF conditions. This was observed in this study in a few occasions for pool boiling as well as for submerged jet impingement boiling. In this study, boiling incipience superheat temperatures for FC-72 on copper of up to 31.5 ^{o}C were documented while the wall superheat temperatures at CHF conditions were normally around 30 ^{o}C. For pool boiling of FC-72 on electronic materials, boiling incipience wall superheat temperatures of up to 51 ^{o}C have been reported [42]. Failure to initiate boiling with highly-wetting fluids can result in significant damage to high flux and temperature

sensitive applications such as electronics cooling. For this reason, temperature overshoot mitigation has been the whole focus of several research studies. Techniques such as zero-angle cavities created by curved surfaces in contact with heated surfaces [50], bubble generation from nearby heaters [51, 52], and the use of mixed fluids with different saturation temperatures [53] among others have been recommended to reduce or eliminate temperature overshoot. In this study, a novel passive overshoot mitigation technique using a self-cavitating impinging jet is presented.

Self-oscillating jets, also known as the whistler nozzle phenomena, have been studied in the past [54] for submerged gas jets. This phenomenon occurs when a concentric collar is added at the end of a circular jet nozzle creating an expansion region, similar to a backward-facing step, around the exit periphery of the jet nozzle. Such geometry is illustrated in Fig. 39. For a gas flow, the addition of the collar generates oscillations in the system which can be detected by a particular audible frequency and thus the name of whistler nozzle. A mathematical expression for the resonance frequencies of a whistler nozzle have been given by Hasan and Hussain [54] based on a modification to the organ pipe resonance frequency relationship. Resonance characteristics of the whistler nozzle phenomena and their impact on boiling heat transfer performance for submerged liquid jets are currently being studied as part of the ongoing research in the lab. However, an additional phenomenon in these nozzles that was detected as a consequence of having a liquid medium was the appearance of cavitation in the expansion region of the collar. This phenomenon was observed using both water and FC-72 and generated very small vapor bubbles that appeared as a cavitation cloud as

these bubbles exited the collar. For a similar nozzle geometry, the flow rates required to generate cavitation were roughly seven times larger for water than for FC-72 which could be attributed to the lower surface tension and the higher vapor pressure of the later fluid. Preliminary testing using self-cavitating nozzles suggest that there exist a critical jet Re required to initiate cavitation which varies as a function of nozzle geometry and working fluid. However, the detail characterization of the cavitation phenomena on these types of nozzles is currently under investigation and has been left out of the scope of this document.

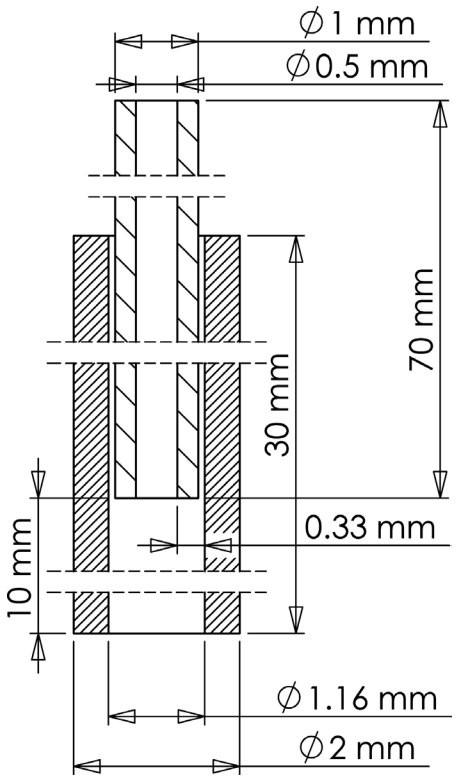

Figure 39: Dimensions of the self-cavitating jet used for overshoot mitigation

It was hypothesized that, for submerged jet impingement boiling, the small vapor bubbles generated using a self-cavitating jet would impinged on the heated surface and would generate artificial nucleation sites which would prevent temperature overshoot regardless of surface conditions. An experiment was performed to test the hypothesis that the use of a self-cavitating jet would serve as a passive means to mitigate temperature overshoot in submerged jet impingement boiling systems using FC-72. Figure 39 shows the geometry of the self-cavitating jet used for this experiment. A 1 mm outer diameter glass tube with an inner diameter of 0.5 mm was used as the jet nozzle. A 1.16 mm inner diameter glass tube was used as the jet collar resulting in a nominal 0.33 mm step height. Both glass tubes were glued together using aquarium grade silicone sealant with an overlap of 20 mm resulting in a 10 mm collar length. For this test, the exit of the jet collar was located roughly six jet nozzle inner diameters away from the heated surface and the jet Re based on the jet nozzle inner diameter was approximately 10450. Figure 40 shows high-speed images taken to visually demonstrate the cavitation exiting the jet collar and impinging on the heated surface at increasing heat flux conditions. Note from Fig. 40(a) that a large number of small vapor bubbles exited the nozzle while impinging and spreading over the heated surface serving as potential nucleation sites. As the heat flux was increased, boiling was initiated on the periphery of the heated surface (Fig. 40(b)) and progressed inwards with increasing heat flux (Fig. 40(c)). This behavior was unlike the sudden vapor generation over the entire surface that was observed at incipience boiling during temperature overshoot (Fig. 34 and Fig. 35).

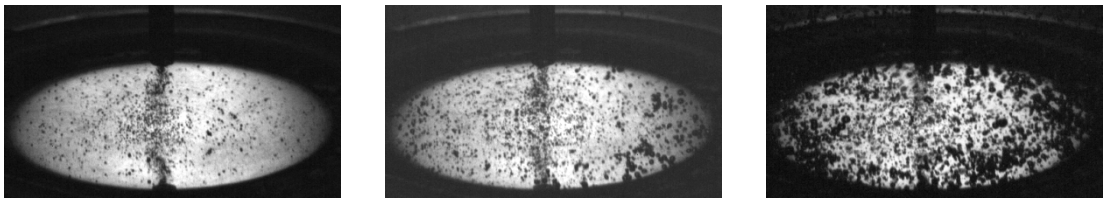

(a) q"=0 W/cm^2 (b) q"=2 W/cm^2 (c) q"=3W/cm^2

Figure 40: Self-cavitating jet phenomena with increasing heat flux, Re=10470

Figure 41 shows two boiling curves taken with the self-cavitating jet for increasing and decreasing heat flux conditions for Re=10445 based on the jet inner diameter. Figure 42 shows a repeat experiment of the same data set performed four days later after opening the test chamber to replace the nozzle-collar assembly by a new equivalent nozzle-collar assembly. This repeat experiment was performed to show repeatability of the self-oscillating jet phenomena and temperature overshoot mitigation. Note from these figures that the temperature overshoot region typically found for the increasing heat flux condition was completely eliminated. It is well known that the presence of a liquid-gas interface in trapped gas or vapor in surface cavities allow vaporization to occur at relative low surface temperatures [6]. Similarly, the small vapor bubbles created by the self-cavitating jet scattered over the heated surface providing a liquid-vapor interface for nucleation, and activated surface cavities at lower surface temperatures. This effect resulted in complete mitigation of the temperature overshoot.

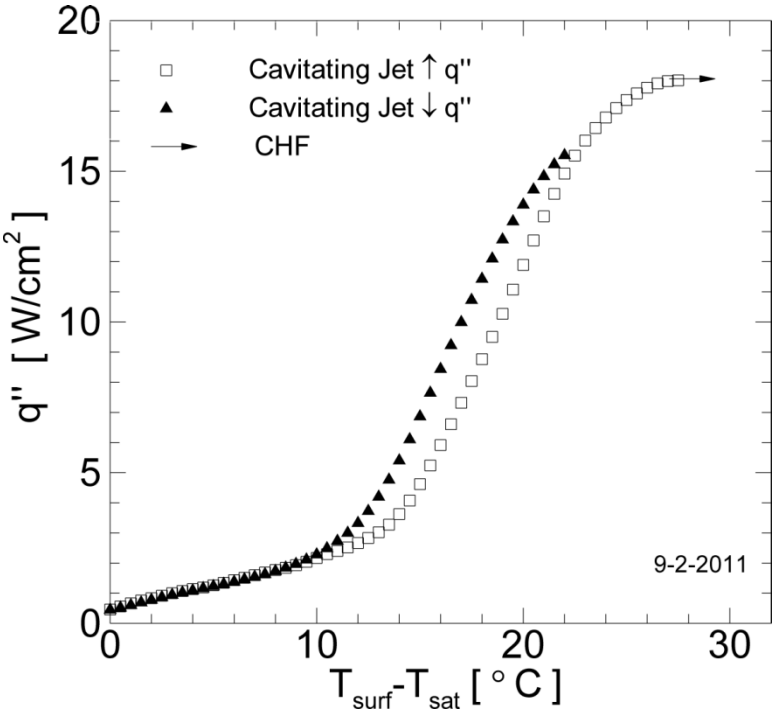

Figure 41: FC-72 temperature overshoot mitigation for Re=10445

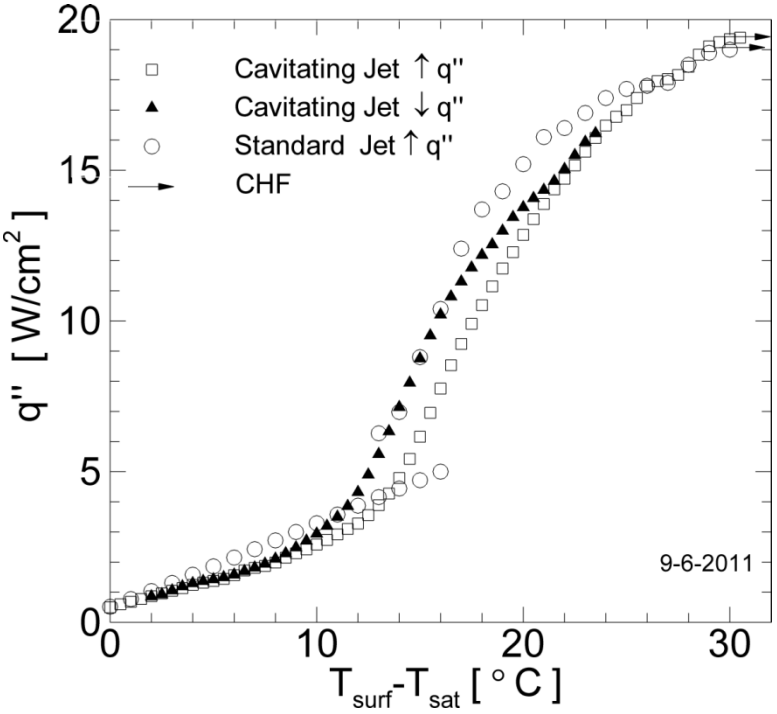

Figure 42: FC-72 temperature overshoot mitigation for Re=10470

Figure 41 and Fig. 42 also indicate that the decreasing heat flux boiling curve was slightly shifted towards the left in the boiling region of the boiling curve. This was not the case for the plots shown in Fig. 33 of increasing and decreasing heat flux conditions. Note that the decreasing boiling curve experiment in all cases was performed subsequent to the corresponding increasing boiling curve experiment. A potential explanation for this trend may be related to the temperature overshoot itself. When the surface achieved boiling inception through a temperature overshoot, the entire surface experienced temperatures significantly higher than the fluid saturation temperature. Once nucleation started, it quickly spread over the entire surface as seen in Fig. 34 and Fig. 35 activating most cavities on the surface all at once. With the self-cavitating jet, boiling initiated at the edges of the heated surface where the heat transport was lowest (highest surface temperature) and moved inwards with increasing heat flux as the local regions on the surface reached the necessary temperature for nucleation (Fig. 40). Therefore, potentially a similar number of active cavities were present for the increasing and decreasing heat flux conditions all through the boiling region of the boiling curve when temperature overshoot occurred. However, the number of active cavities in the case of utilizing a self-cavitating jet might not have been as many as in the decreasing heat flux condition case up until elevated values of heat flux. Figure 41 and Fig. 42 indicate that the hysteresis in the boiling curve disappeared at high heat flux values giving more validity to the aforementioned reasoning.

Critical heat flux values in Fig. 41 and Fig. 42 were on average approximately 18.7 W/cm^2 and differed by 6.7 percent. This difference in CHF is close to the repeatability uncertainty of these experiments. The effect of a self-cavitating jet in CHF values is still under investigation. However, preliminary data have indicated no difference between submerged jet impingement CHF with or without using a self-cavitating jet while keeping everything else constant (Fig. 42). A similar trend was observed over the fully developed and single-phase regions of the boiling curve (Fig. 42).

5.3.3 SATURATED POOL BOILING

To provide a baseline condition for comparison with jet impingement data, saturated pool boiling data of FC-72 were collected. Unfortunately, a direct comparison of the data with the standard form of Rohsenow's correlation (Eq. 8) cannot be performed since values of $C_{surf,l}$ for a copper/FC-72 system are not readily available in literature. Instead, the experimental data were utilized to approximate a value of $C_{surf,l}$ for FC-72 on emery polished copper. As recommended for all fluids except water [5, 6], a Prandtl number exponent of n=1.7 was utilized in the correlation. Figure 43 shows the resultant comparison of Rohsenow's correlation (Eq. 8) with 5 sets of pool boiling data for $C_{surf,l}$=0.00415. Note from this figure that by setting $C_{surf,l}$=0.00415, Rohsenow's correlation captures the fully developed nucleate boiling region of the boiling curves fairly well. The data only deviates from the correlation's predicted

values at high heat fluxes near CHF conditions. This deviation of the experimental data from the correlation predictions at high heat fluxes is to be expected since Rohsenow's correlation was developed based upon an inverted flow model for the isolated bubble regime. Therefore, this model does not properly account for the slugs and columns region of the boiling curve that occurs prior to CHF. It is also noted that a $C_{surf,l}$ value of 0.00415 is not unreasonable. A value of $C_{surf,l}$ of 0.0049 has been reported for n-Pentane on lapped copper and of 0.0070 for Carbon tetrachloride on emery polished copper [6].

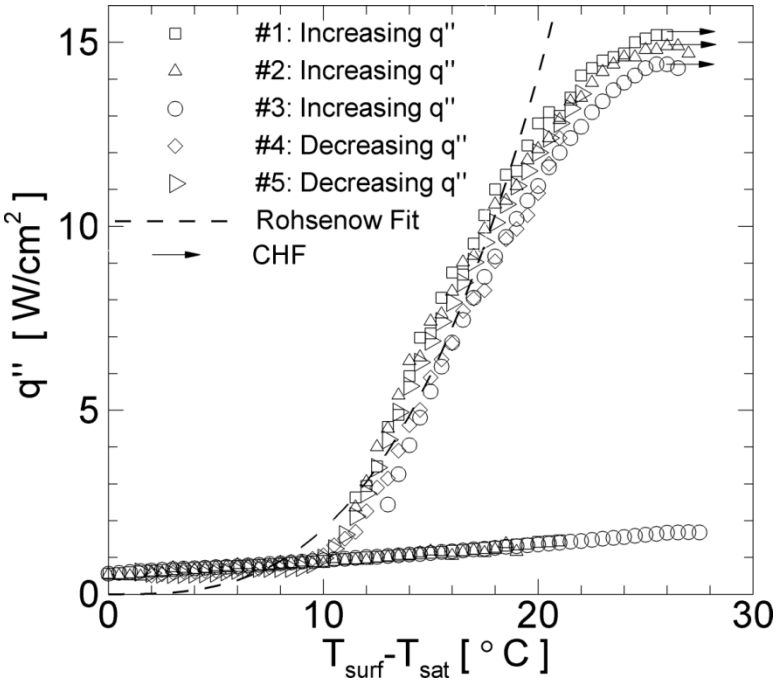

Figure 43: FC-72 saturated pool boiling comparison with Rohsenow correlation prediction: $C_{surf,l}$=0.00415 and n=1.7

Figure 43 indicates that the pool boiling CHF for FC-72 was on average approximately 14.8 W/cm^2. This value is within eight percent of the 16 W/cm^2 predicted by Kutateladze's pool boiling CHF correlation (Eq. 9), with C=0.149 as recommended for a large horizontal surface [5]. For comparison, reported pool boiling CHF values for saturated FC-72 on plain copper surfaces at atmospheric conditions have varied between 12.6 W/cm^2 [55] and 16 W/cm^2 [56]. These results indicate agreement of the FC-72 pool boiling CHF value obtained in this study with other literature studies and with theory.

Figure 44 shows photographs of the typical FC-72 vapor bubble sizes observed during saturated pool boiling. Note that although the nozzle is seen in these pictures, there is no jet flow. Comparison of Fig. 22 with Fig. 44 indicate that the typical bubble size observed for saturated water was much larger than for saturated FC-72. Note that while these figures for the distinct fluids are given at different heat flux levels, the percent heat flux in relationship to CHF is similar between FC-72 and water at P=0.476 bar. Smaller bubble departure diameters are to be expected for FC-72 in comparison to water since this parameter have been found to be inversely proportional to the surface tension of the working fluid (several correlations indicating this trend are given by Carey [6]).

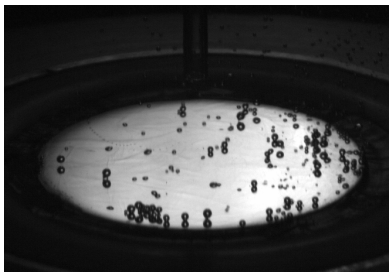

(a) q"<1 W/cm^2

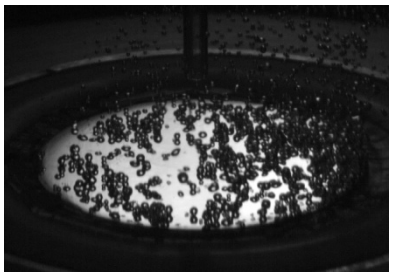

(b) q" ~ 1.5 W/cm^2

Figure 44: Typical FC-72 bubble sizes during decreasing heat flux saturated pool boiling conditions

5.3.4 JET IMPINGEMENT FLOW VISUALIZATION

Figure 45 shows photographs of saturated FC-72 jet impingement boiling at different heat flux levels for Re=9316. Note that these photographs were taken under decreasing heat flux conditions in order to capture the boiling activity on the surface at low heat flux levels. Figure 45(a) and (b) show that at elevated values of wall heat fluxes, near CHF conditions, all generated vapor escapes the surface as large vapor slugs which decreased in size with decreases in heat flux. As the heat flux was decreased further, the vapor slugs started to become individual vapor bubbles (Fig. 45(c)) and eventually led to a large population density of small vapor bubbles departing from the surface (Fig. 45(d)). Figure 45(e) and (f) show that at relatively low values of surface heat flux, several small vapor bubbles were generated on the surface and were pushed away by jet flow. Figure 45(e) also shows the boiling front for FC-72 jet impingement during partially developed nucleate boiling.

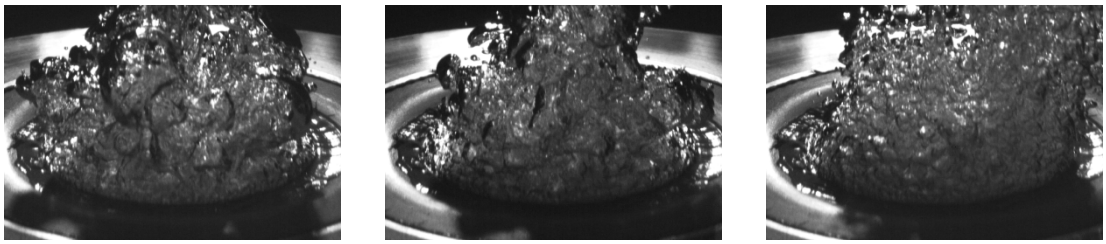

(a) q"=17.5 W/cm^2 (93.1 % CHF)

(b) q"=13.5 W/cm^2 (71.8 % CHF)

(c) q"=10 W/cm^2 (53.2 % CHF)

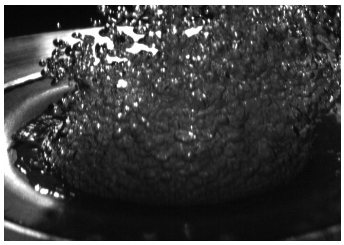

(d) q"=7 W/cm^2 (37.3 % CHF)

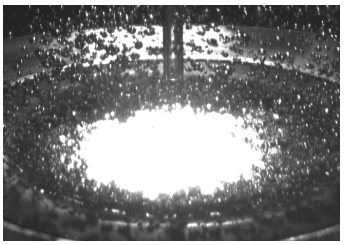

(e) q"=4 W/cm^2 (21.3 % CHF)

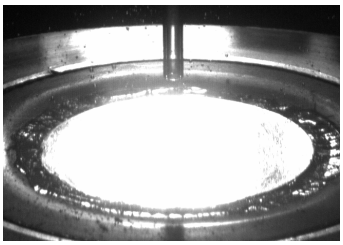

(f) q"=2.5 W/cm^2 (13.3 % CHF)

Figure 45: FC-72 saturated jet impingement flow visualization for Re=9316 on a 33 nm Ra surface

Comparison of Fig. 25(a-c) and Fig. 45 for water and FC-72 jet impingement respectively at saturated conditions reveal that vapor bubbles and vapor slugs were larger for the water case. For water, it appears that only one large vapor slug covered the surface near CHF conditions while for FC-72, several independent vapor column structures are observed near these same conditions. Such a behavior would be expected from a stability analysis perspective since the most dangerous wavelength for instability is of approximately the same dimension as the heated surface for water, but 3.5 times smaller than the heated surface diameter for FC-72.

5.3.5 SATURATED JET IMPINGEMENT BOILING

Figure 46 through Fig. 48 show saturated jet impingement boiling curves on a 33 nm Ra surface for jet diameters of 1.16 mm, 2.29 mm, and 3.96 mm respectively. The axes of these figures are given over an equivalent range of wall superheat and wall heat flux to ease the comparison among them. The corresponding surface-to-nozzle diameter ratios (d_{surf}/d_j) for these three cases were 23.8, 12.1, and 7.0 and the surface-to-nozzle spacing was kept fixed at six jet diameters. Note that all of the boiling curves shown in these figures were collected for increasing heat flux conditions and thus show temperature overshoot. A distinct feature of boiling curves showing temperature overshoot is that the single-phase region of the boiling curve is clearly separated from the two-phase region. As expected from single-phase jet impingement theory, all of the boiling curves collected for FC-72 consistently show increasing heat transfer rates with increasing jet Re for a fixed wall superheat in the single-phase region of the boiling curves. The extent of the single-phase region of the boiling curve varied widely for all experiments as a result of the randomly varying boiling incipience wall superheat.

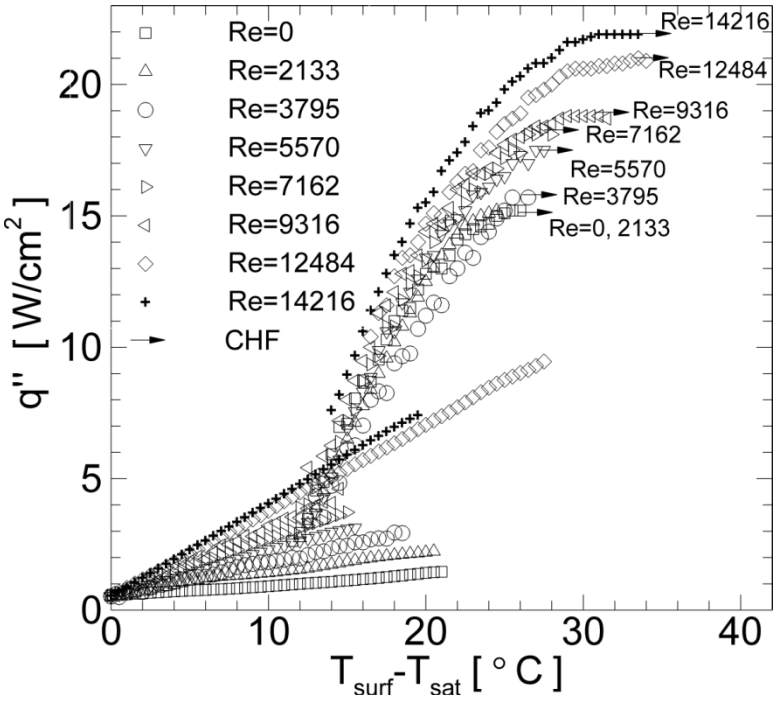

Figure 46: FC-72 jet impingement boiling curves for d_j=1.16 mm (d_{surf}/d_j=23.8)

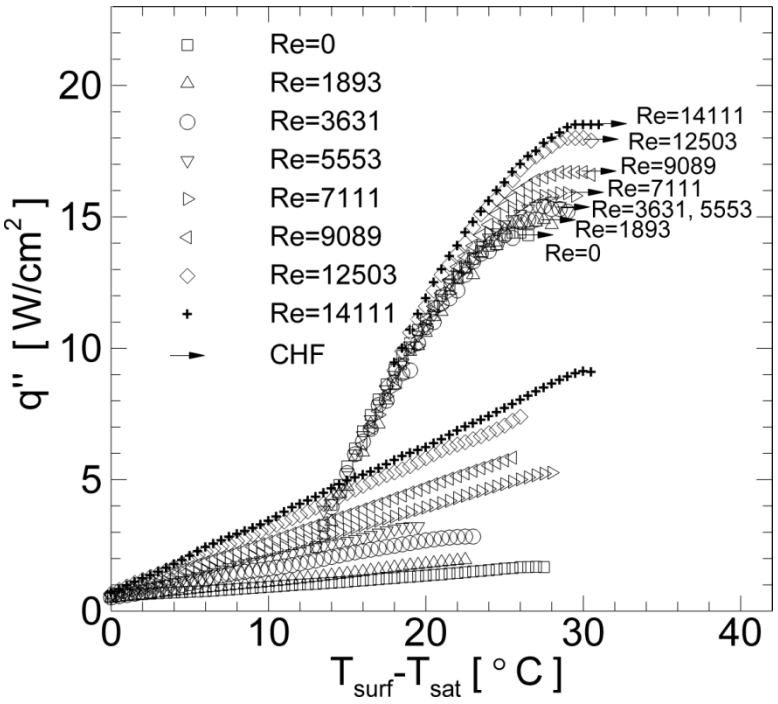

Figure 47: FC-72 jet impingement boiling curves for d_j=2.29 mm (d_{surf}/d_j=12.1)

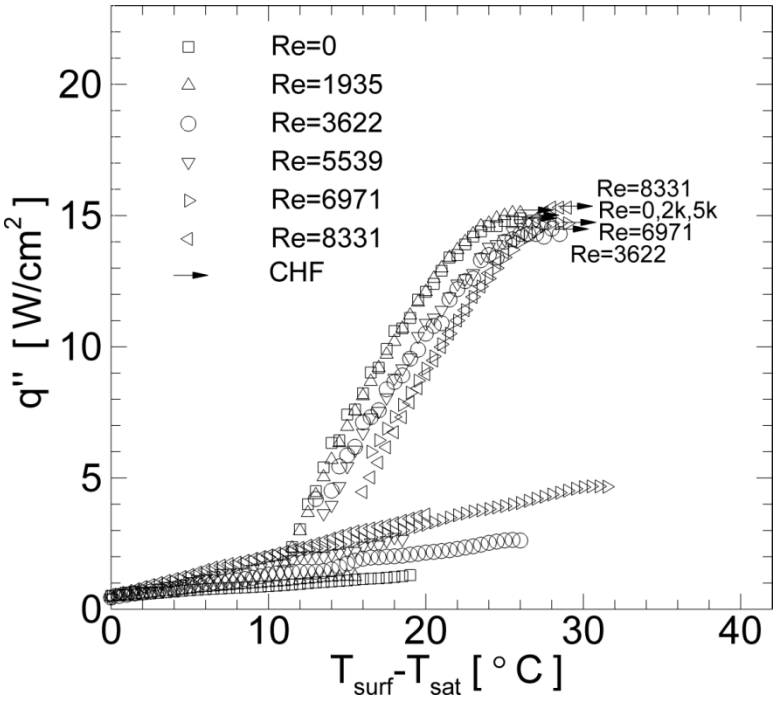

Figure 48: FC-72 jet impingement boiling curves for d_j=3.96 mm (d_{surf}/d_j=7.0)

In the two-phase region of the boiling curves, for any particular jet diameter, curves for distinct Re can be approximated as following a common boiling asymptote. However, an interesting trend seems to govern the general behavior of the boiling curves for varying jet diameters. Figure 46 indicates that, for d_j=1.16 mm, the fully developed nucleate boiling region of the boiling curve was slightly shifted toward the left with increasing jet Re corresponding to enhanced heat transfer performance. Figure 47 shows almost no variations in the fully developed nucleate boiling region of the boiling curve with jet Re for d_j=2.29 mm. For d_j=3.96 mm, Fig. 48 indicates that fully developed nucleate boiling curve was shifting to the right with increasing jet Re indicating diminished heat transfer performance with Re. Since the surface diameter

was fixed, this particular trend could be associated with the distinct surface-to-nozzle area ratios that were considered. The downward drag force that the flow imposes in the impingement zone on the vapor bubbles is experienced over a larger region of the surface for large jet diameters in comparison to small jet diameters. It is possible that for the large jet diameter considered, the downward drag force experienced over a significant portion of the surface was sufficient to significantly retard bubble departure and thereby reducing heat transfer rates with increasing Re for a fixed wall superheat. For the small jet diameter, the region of the surface affected by the downward drag force is small and it is possible that the wall jet created along the surface actually assisted in shearing off vapor bubbles and thus increase heat transfer rates for increasing Re. Under this hypothesis is it possible that for some middle range of jet diameters, the resultant trend is neither to increase nor to decrease the heat transfer rate at a fixed wall superheat, which was the case for d_j=2.29 mm. It is important to point out that the aforementioned trend would be expected to be more evident in fluids with low surface tension since this causes smaller vapor bubbles in relationship with the jet diameter, which was the case for FC-72.

Critical heat flux also varied as a function of jet Re and jet diameter. Figure 46 and Fig. 47 show almost consistent enhancements in CHF with increasing jet Re for jet diameters of 1.16 mm and 2.29 mm respectively. However, note that the enhancements in CHF were more significant for the 1.16 mm jet diameter case than for the 2.29 mm case. For the 3.96 mm jet diameter case, Fig. 48 shows no consistent or significant variation of CHF with increasing jet Re since the variability of the data

was within the repeatability uncertainty of the measurement. Figure 49 shows saturated jet impingement boiling data for the three jet diameters considered at the common highest jet average Re of 7081. This figure indicates that both single-phase and two-phase heat transfer as well as the CHF limit was enhanced for the smaller diameter jet despite of the nearly constant initial jet exit momentum. For a fixed Re and surface diameter under the conditions considered in this study, Martin's correlation for an average single-phase jet impingement heat transfer coefficient from a single round nozzle, predicts larger heat transfer coefficients for smaller jet diameters [5], consistent with the trends observed in the data. Single-phase heat transfer coefficients for all three jet diameters estimated from the data in Fig. 49 are on average within 5.4 percent from the predicted values given by Martin's correlation.

At first, the trend of higher CHF with smaller jet diameters for a fixed Re and surface dimension may seem counterintuitive because, by keeping the Re constant, the initial momentum of the jet is constant for all jet diameter cases. However, for a fixed Re, higher jet velocities are associated with smaller jet diameters. These higher jet velocities result in higher initial jet kinetic energies for Re cases with smaller jet diameters. The results in Fig. 49 indicate that it is this higher initial flow kinetic energy at the jet exit that is responsible for enhancing fluid supply to the surface under elevated heat flux conditions, thereby enhancing CHF.

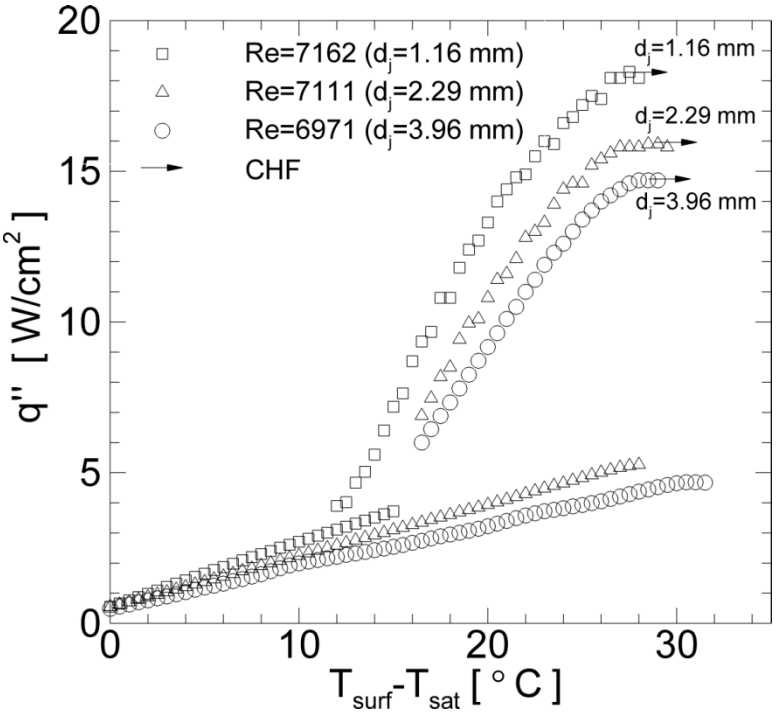

Figure 49: Saturated jet impingement boiling of FC-72 an average Re=7081

5.3.6 Comparison Between Water and FC-72 Data

Submerged jet impingement boiling experiments were performed for two fluids with distinct thermo-physical properties. The reader is referred back to Table 6 in Chapter 4 for a detailed comparison of saturated fluid properties between water and FC-72. Water was used as one of the working fluids because of its attractive heat transfer properties for high flux applications. However, to reduce the saturation temperature of this fluid to temperatures below its normal boiling point, which are required for high flux low temperature applications, experiments were performed at sub-atmospheric conditions. FC-72 was used as the second working fluid because of its popularity for

electronics cooling applications owing its low normal boiling point and its dielectric properties. Note that at a pressure of 0.176 bar, the saturation temperature of water is about 57.3 ^{o}C which is within less than a degree of the normal boiling point of FC-72 of 56.6 ^{o}C. Therefore, it is possible with the current data set to compare the boiling heat transfer characteristics of water against FC-72 for an approximately equivalent saturation temperature. Such a comparison between these two popular heat transfer fluids has not been previously reported in the literature and is of great interest to the electronics cooling community.

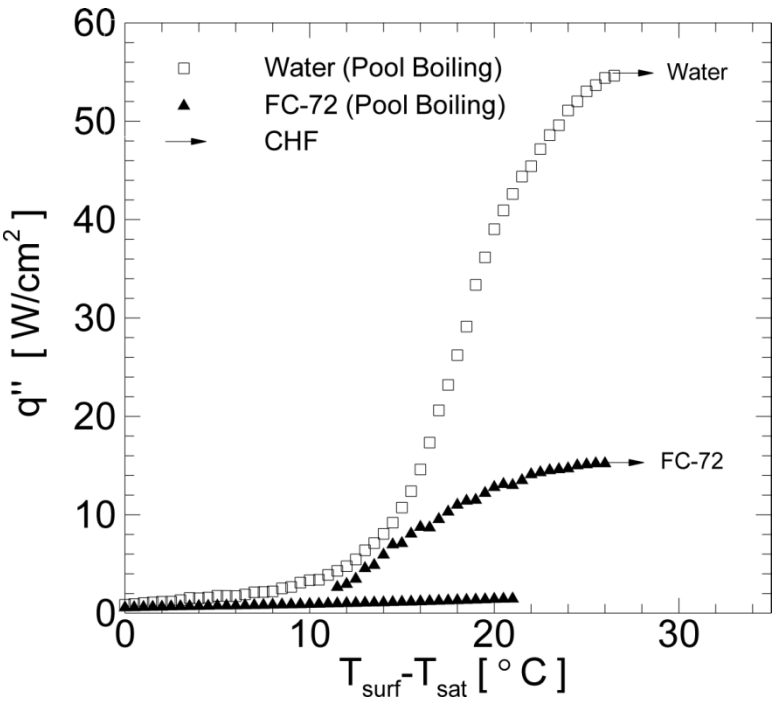

Figure 50: Pool boiling comparison for water at P=0.176 bar and FC-72 on a 33 nm Ra surface

Figure 50 shows the saturated pool boiling comparison of water and FC-72 for an almost equivalent fluid saturation temperature of roughly 57 ^{o}C. Note that at any fixed wall superheat, the heat transfer rates from the surface are larger for water than for FC-72. This trend is evident over the entire boiling curve but it is much more significant in the fully developed nucleate boiling region. Note that the boiling curves for both fluids were similar immediately after the incipience boiling of FC-72. However, the heat transfer rates were diminished much faster for FC-72 than for water allowing the second fluid to reach significantly much higher CHF magnitudes. Therefore, despite the penalty paid in lower heat transfer rates with decreasing pressure, the boiling heat transfer characteristics for water remain much superior to FC-72 for an equivalent saturation temperature.

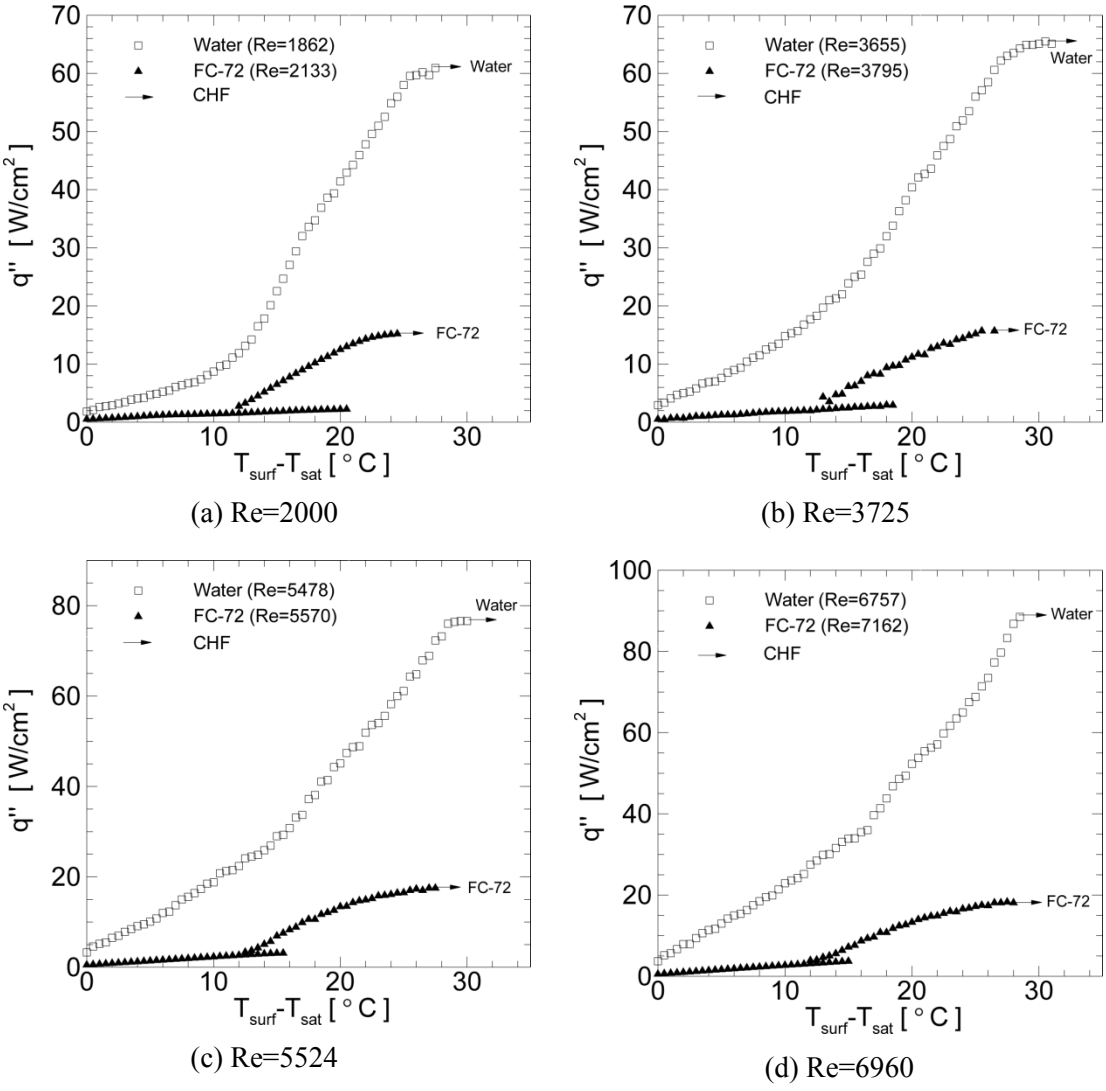

Figure 51: Jet impingement boiling comparison for water at P=0.176 bar and FC-72 on a 33 nm Ra surface

Figure 51(a-d) show jet impingement boiling curves for saturated water and saturated FC-72 for an almost equivalent fluid saturation temperature of roughly 57 ^{o}C. Similar trends as those seen for the pool boiling case in Fig. 50 are seen in Fig. 51 for the submerged jet impingement data. Note that enhancements in the single-phase region

of the boiling curves with Re for water (T_{surf} - T_{sat}< 10^{o}C approximately) are much more significant than for FC-72 owing the superior thermo-physical properties of the former fluid. For a fixed wall superheat, the wall heat flux difference between water and FC-72 increases with increasing jet Re. This trend indicates that the benefit of increasing the jet Re is greater for water than it is for FC-72. Therefore, potentially greater heat transfer enhancements using submerged jet impingement boiling are expected for water in comparison to FC-72. Table 10 shows a summary of CHF between water and FC-72 for an equivalent fluid saturation temperature and fixed system parameters. Water CHF limits were between 3.6 and 4.8 times larger than equivalent CHF limits for FC-72. Table 10 also tabulates the enhancement ratios observed for varying Re with these two fluids. Note that enhancement ratios for water were greater than for FC-72 at any given Re. This trend indicates once again that greater benefits are obtained by using submerged jet impingement boiling for water than for FC-72.

Table 10: Summary of CHF between water and FC-72 for an equivalent saturation temperature and system parameters

Re_{avg}	Test Fluid	Re	CHF [W/cm^2]	CHF/CHF_{pool}
0	Water	0	54.6	1.00
	FC-72	0	15.2	1.00
1998	Water	1862	60.9	1.12
	FC-72	2133	15.2	1.00
3725	Water	3655	65.3	1.20
	FC-72	3795	15.7	1.03
5524	Water	5478	76.6	1.40
	FC-72	5570	17.5	1.15
6960	Water	6757	88.5	1.62
	FC-72	7162	18.3	1.20

The trends illustrated in Fig. 50 and Fig. 51 indicate that water at sub-atmospheric conditions is the fluid of choice for heat transfer applications requiring both low surface temperatures and high levels of heat flux. The electronics cooling industry is in need of such potential. However, the hesitation to use water for electronic cooling comes from the difficulty to keep this fluid dielectric which could potentially caused electrical damage. Pure deionized water has good dielectric properties (appendix1), but keeping this fluid free of ions is a practical challenge. The polarity of the water molecule makes this fluid a good solvent capable of easily accepting and transporting ions. This practical issue remains as a barrier to adopt water as the working fluid on electronics cooling applications. One possible solution is to developed systems which can keep the water pure and deionized. One can also compromise and use a third high

thermal conductivity interface material (thermal spreader) which prevents the water from coming in direct contact with electrical devices. The heat transfer penalty associated with the interface thermal resistance in such systems might be less than the benefits realized by using water as the working fluid, resulting in a net increase in heat transfer rate in comparison to using direct cooling with a dielectric fluid. These issues need to be explored further. However, given the significant benefit in heat transfer rates, it would be worthwhile estimating this penalty.

5.4 CRITICAL HEAT FLUX

Critical heat flux is an important point on a boiling curve since its magnitude corresponds to the maximum heat transfer rate in phase-change cooling. Even though it may be desirable for many high flux cooling applications to operate near this upper limit, it is important to recognize the danger that is accompanied with the catastrophic surface temperature overrun that occurs at CHF for heat flux controlled surfaces. For this reason, it is very important to be able to correctly predict CHF limits. This section discusses in detail the CHF trends observed for the varying flow conditions during submerged jet impingement boiling. For a detailed list of the experimental test conditions refer to Table 7 for water experiments and Table 8 for FC-72 experiments.

5.4.1 SATURATED POOL BOILING CHF

Figure 52 shows the comparison of critical heat flux data for saturated pool boiling of water and FC-72 with the trend predicted by the saturated pool boiling CHF correlation (Eq. 9) originally developed by Kutateladze [5]. Note that the x-axis of this figure is equivalent to the right hand side of Eq. 9 with C=1 and in units of W/cm^2. A C value of 0.149, as recommended by Lienhard and Dhir [6], for a large horizontal heated plate was used in the solid line trend for this correlation. Note that the correlation predicts the experimentally determined CHF values for both fluids reasonably well within ±6.4 percent error on average and with a maximum error of 10.6 percent. For water, the correlation properly predicts the changes in CHF with varying pressure. Although pressure is not directly included in the correlation, its effect is implicitly captured by the change in vapor density. Note that for a fixed set of conditions, the 123 nm Ra surface CHF was consistently higher than that of the 33 nm Ra surface. Although Kutateladze's correlation does not capture the effect of surface roughness, CHF for pool boiling has been shown to be dependent on surface finish because, as already seen in Fig.12 and Fig. 13, roughness can alter the wetting characteristics of the liquid on the surface, directly affecting CHF [6]. Jones et al. [40] noticed an increase in CHF with larger surface roughness for pool boiling of FC-77 on aluminum surfaces. For water, their study showed improvements in heat flux for a fixed wall superheat with increasing surface roughness; however, CHF was not achieved in their water experiments.

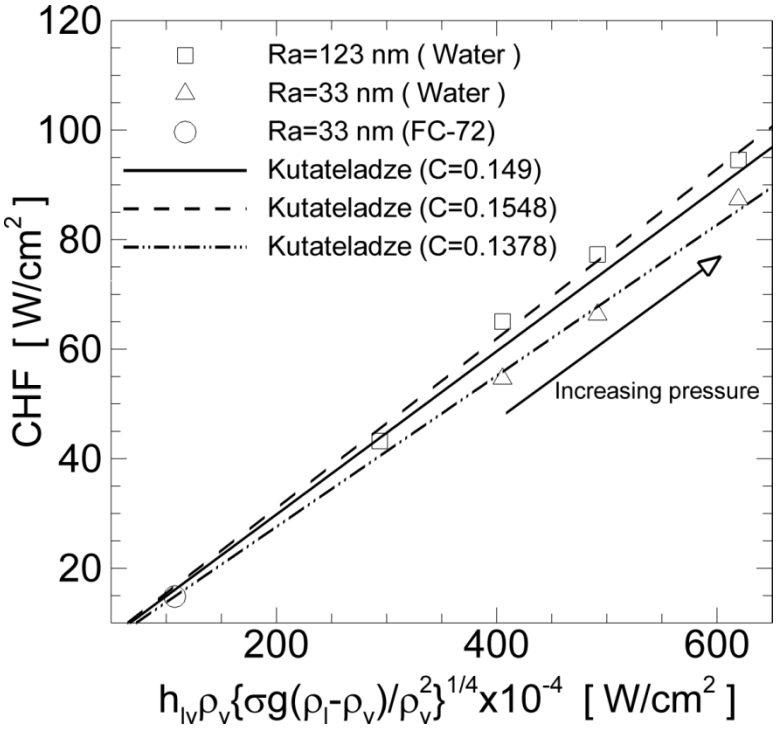

Figure 52: Comparison of saturated pool boiling CHF with Kutateladze's correlation

Table 11: Summary output of regression analysis for saturated pool boiling data fit

	Ra= 123 nm	Ra=33 nm
Estimated Value of C	0.1548	0.1378
P-value	7.0×10^{-6}	4.6×10^{-6}
R^2	0.99935	0.999501
95% Confidence Interval	[0.1476 0.1621]	[0.1322 0.1434]

A least-square regression of the experimental data to Kutateladze's correlation for CHF was performed to modify the leading constant C in Eq. 9 that best represents the effect of surface roughness on the data. No fluid dependency on this constant was assumed, and both water and FC-72 pool boiling CHF data for the 33 nm Ra surface were used for the analysis. This assumption is in accordance to the statement in [5] which says that the constant C in Eq. 9 is independent of surface material and only weakly dependent on geometrical considerations. Table 11 show a summary of the regression output obtained. Independent of working fluid, values of C of 0.1548 and 0.1378 were found for the 123 nm Ra surface and the 33 nm Ra surface respectively. Note that the 95 percent confidence intervals for these estimated quantities do not overlap, indicating that the higher CHF values measured for the rougher surface in comparison to the smoother surface were statistically significant despite the limited sample size. The values of the leading constant C obtained for Eq. 9 are within previously reported values. Kutateladze originally found C to be 0.17 [48] while Zuber's hydrodynamic stability model suggested that C≈ 0.131 [49]. Lienhard and Dhir [6] later proposed a value of C=0.149 for a large horizontal plate. With the modified C values to account for the effect of surface roughness, Kutateladze's CHF correlation (Eq. 9) captures the entire saturated pool boiling data set with an average error of 2.3 percent and a maximum error of 5.2 percent. These errors are within the experimental repeatability variations of up to six percent seen for these experiments. Table 12 summarizes the findings for properly predicting critical heat flux for saturated pool boiling conditions based on the experimental data.

Table 12: Summary of findings for pool boiling CHF predictions

Pool Boiling CHF Model	$q''_{CHF,pool} = Ch_{lv}\rho_v\left[\frac{\sigma g(\rho_l-\rho_v)}{\rho_v^2}\right]^{1/4}$
Horizontal plate [5, 6]	C=0.1490
123 nm Ra surface	C= 0.1548
33 nm Ra surface	C= 0.1378

5.4.2 SATURATED JET IMPINGEMENT BOILING CHF

Figure 53 and Fig. 54 show variations in critical heat flux with Re for water on the 123 nm Ra surface and the 33 nm Ra surface respectively. In both of these figures, trends of CHF with Re are presented for three sub-atmospheric pressures of 0.176 bar, 0.276 bar, and 0.477 bar. For a constant Re, an increase in CHF with increasing pressure is observed, consistent with the CHF trend in pool boiling data shown in Fig. 52. Also consistent with the pool boiling trends, for a fixed pressure and Re, higher CHF values were obtained for the 123 nm Ra surface (Fig. 53) compared to the 33 nm Ra surface (Fig. 54) indicating that surface roughness substantially affects jet impingement CHF. At a fixed pressure, a consistent increase in CHF above that of pool boiling with increasing Re is noted. This trend confirms the effectiveness of using jet impingement boiling to extend the upper limits of heat flux in two-phase cooling to higher bounds.

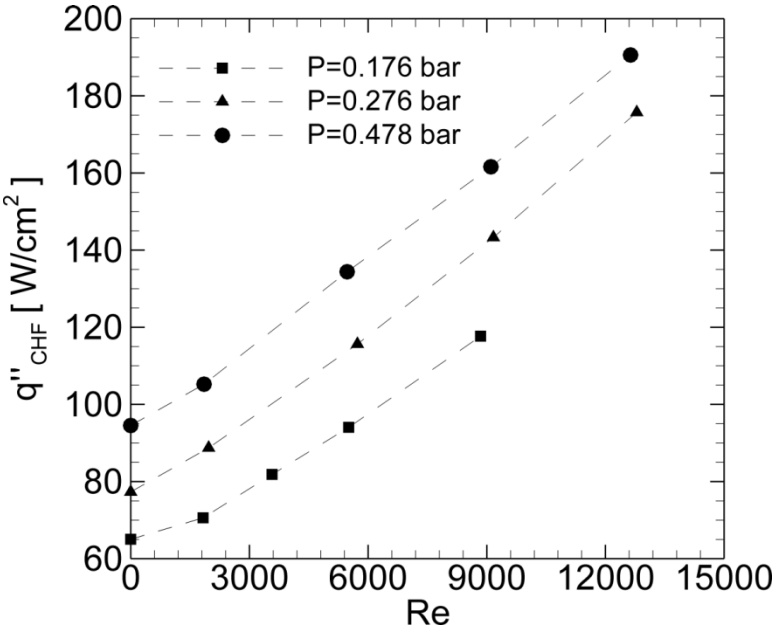

Figure 53: Water jet impingement CHF data for the 123 nm Ra surface

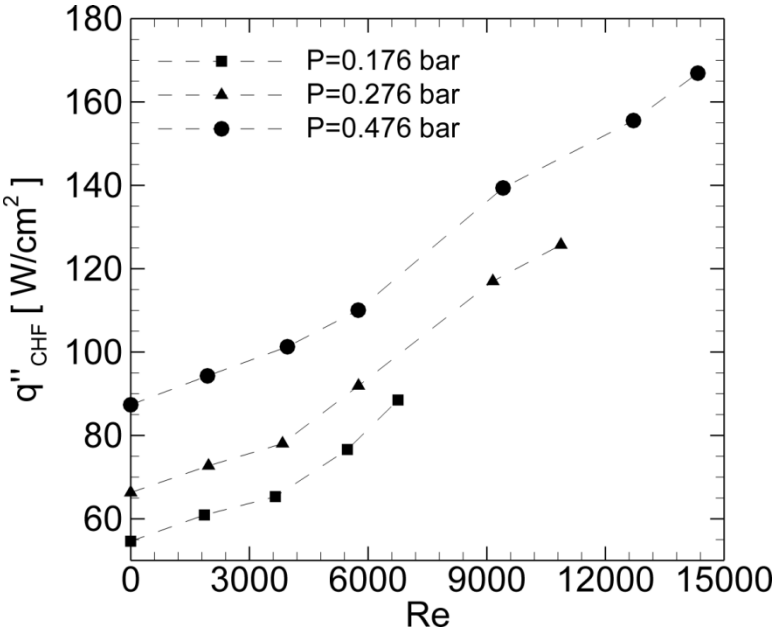

Figure 54: Water jet impingement CHF data for the 33 nm Ra surface

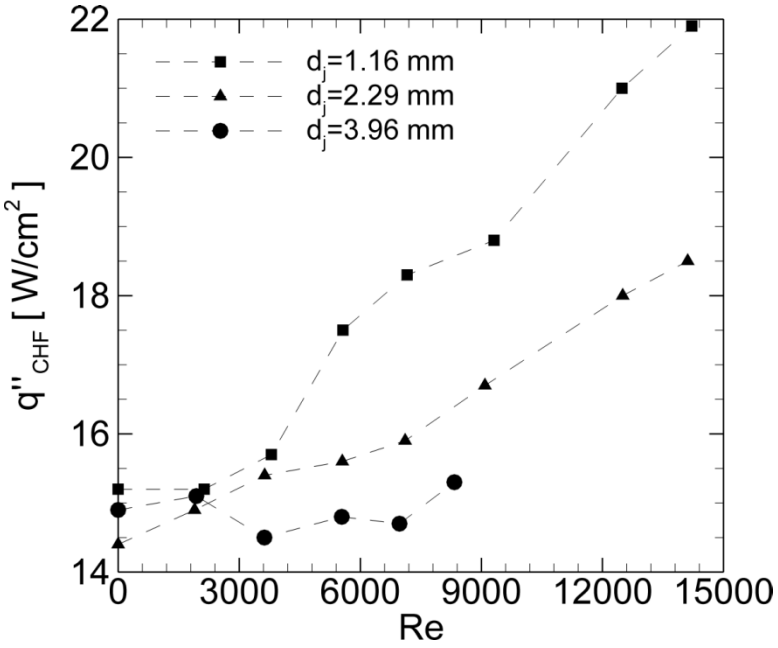

Figure 55: FC-72 jet impingement CHF data for the 33 nm Ra surface

Figure 55 show variations in CHF with Re for FC-72 on the 33 nm Ra surface. Trends of CHF with Re are presented for three jet inner diameters of 1.16 mm, 2.29 mm, and 3.96 mm. Note that the magnitudes of CHF for FC-72 were significantly less than those recorded for water, owing the distinct fluid properties of these two fluids. Similarly to the water case, consistent enhancements in CHF were observed with increasing jet Re for jet diameters of 1.16 mm and 2.29 mm. However, for the larger jet diameter of 3.96 mm, no significant enhancement of CHF over the pool boiling case was seen for any jet Re. For this particular jet diameter, all variations in CHF with Re were within the repeatability uncertainty of the measurement. The trend shown in Fig. 55 for different jet diameters indicates, within the particular range of (d_{surf}/d_j) tested, that higher CHF values for any fixed Re are obtained with a smaller

diameter jet. Note that despite the variations in jet diameter, the jet exit momentum is constant for a fixed jet Re. However, for a fixed Re, higher velocities are required at smaller jet diameters resulting in a higher jet kinetic energy for the smaller jet diameter cases. This trend suggests that the enhancements in CHF with increasing jet flow are perhaps better correlated to the initial jet kinetic energy. It is important to note that the trend of increasing CHF with decreasing jet diameter at a fixed Re is not expected to continue indefinitely. For very large surface-to-nozzle diameter ratios, (d_{surf}/d_j), the jet flow will not be able to spread on the entire surface or provide sufficient liquid mass flow rate to the surface to cause a significant enhancement. Preliminary data has been collected as a continuation of this project that indicated this behavior, and thus, suggests the existence of an optimal (d_{surf}/d_j) ratio to maximize CHF for a fixed jet Re. If such a relationship exist, it would be possible to minimize the pumping power required to operate the jet flow for a fixed surface diameter and heat flux load.

The CHF data in Fig. 53, Fig. 54, and Fig. 55 are re-plotted in Fig. 56, Fig. 57, and Fig. 58 respectively as the enhancement ratio between jet impingement CHF and pool boiling CHF. The enhancement ratio is a very useful quantity because for any fixed Re, this quantity provides the magnitude of the CHF enhancement above pool boiling CHF that is gained by using the impinging jet. If we assume that all the energy goes into latent heat at CHF conditions, the CHF enhancement ratio is independent of the enthalpy of vaporization of the working fluid, and is equivalent to the ratio of how much fluid effectively reaches the surface at CHF for jet impingement cases in

comparison to how much fluid reaches the surface under the conventional pool boiling CHF condition.

CHF enhancement ratio plots in Fig. 56 through Fig. 58 show that CHF was consistently enhanced by using a submerged impinging jet compared to pool boiling CHF, except for the largest diameter nozzle case in FC-72. In water, enhancements up to 2.27 times pool boiling CHF were measured for the 123 nm Ra surface (Fig. 56), and up to 1.91 times for the 33 nm Ra surface (Fig. 57). For FC-72, enhancement ratios up to 1.44 times pool boiling CHF were obtained (Fig. 58). These results indicate that enhancement ratios have a small dependency on surface roughness and a significant dependence on the working fluid. The CHF water data in Fig. 56 and Fig. 57 indicate that for Re > 6000, at a fixed Re, the enhancement ratio is noticeably higher for lower pressures. Since bubble size varied inversely proportional to pressure, fluid supply to the surface through the jet flow above the pool boiling condition could have a more significant influence on CHF at lower operating pressures. This trend indicates that the benefit of using a submerged impinging jet is greater at lower system pressures. At low Re (approx. <4000) the enhancement ratios in the water data varied almost linearly with Re and the variations with pressure almost disappeared. Figure 58 shows that for FC-72 at a fixed Re, higher CHF enhancement ratios were observed for smaller jet diameters. The difference between the enhancement ratios for different jet diameters increased with increasing jet Re. This trend indicates that the benefits of using a smaller diameter jet are greater at higher Re. This particular tendency could be associated with the rapid increases in jet kinetic energy with increasing Re for smaller

jet nozzle diameters. Note that at the largest jet diameter of 3.96 mm, the enhancement ratio became independent of Re within the repeatability uncertainty of the data.

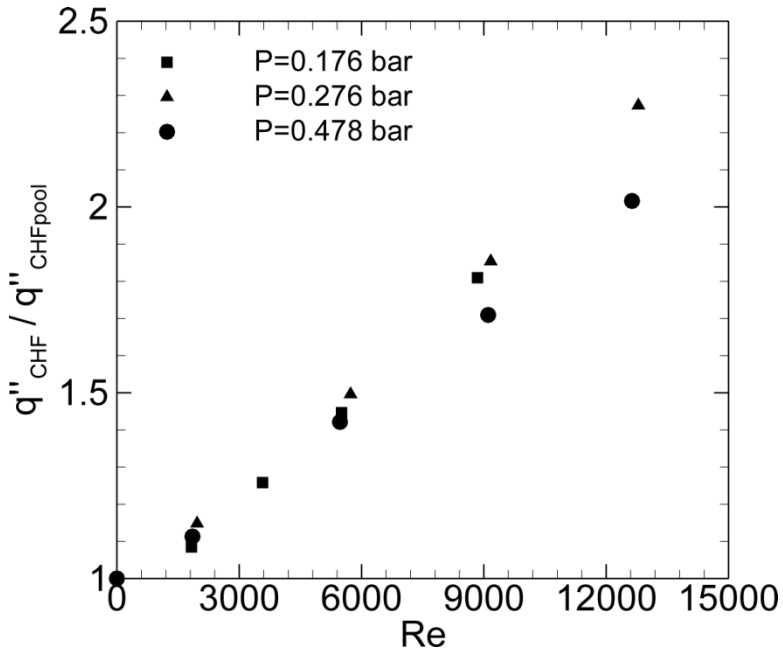

Figure 56: CHF enhancement ratio for water on a 123 nm Ra surface

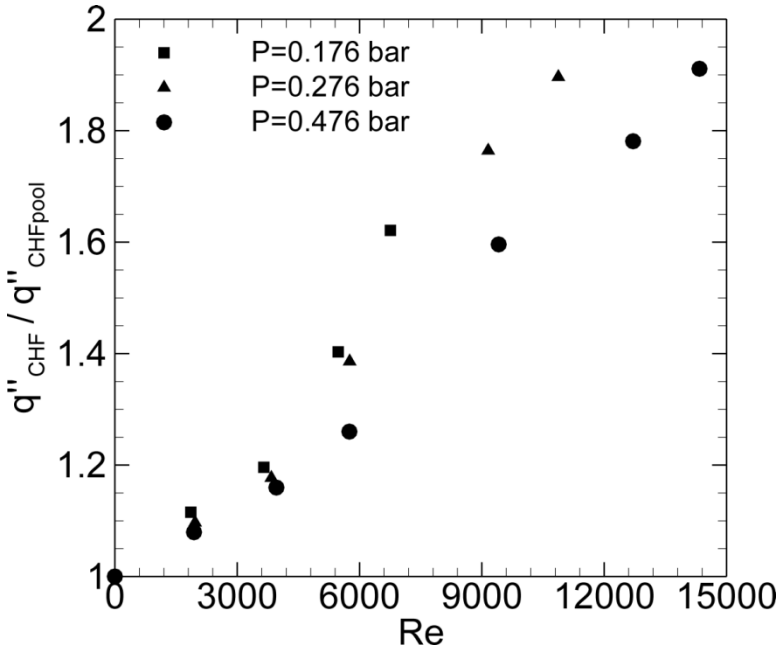

Figure 57: CHF enhancement ratio for water on a 33 nm Ra surface

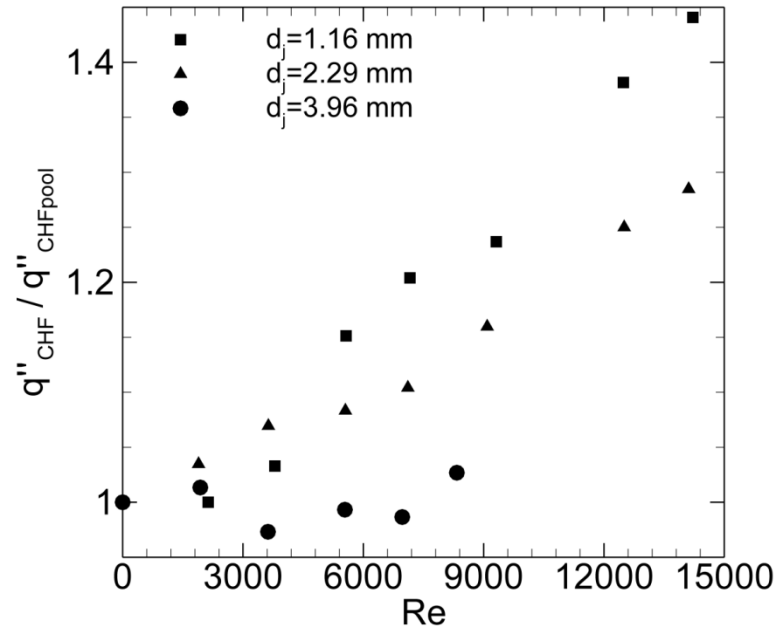

Figure 58: CHF enhancement ratio for FC-72 on a 33 nm Ra surface

Comparison of the water CHF enhancement ratio (Fig. 57) and the FC-72 CHF enhancement ratio (Fig. 58) for the same surface roughness and jet diameter clearly indicate significantly smaller ratios for FC-72 than for water. Since surface tension varies significantly between these two fluids, it is possible that the evident decrease in CHF enhancement ratio is related to the significantly decreased surface tension of this working fluid. This trend of higher jet CHF enhancement ratios with higher surface tension could also explain the higher enhancement ratios observed for water at lower pressures, because the surface tension of water was highest at the lowest temperature owing the temperature dependency of surface tension. However, such a trend in enhancement ratio with variations in fluid as well as pressure could also be mathematically explained by the variations in liquid-to-vapor density ratio which was highest for water at the lowest pressure and lowest for FC-72. A more physical explanation for the variations in enhancement ratio could be the trend of CHF enhancement ratio with observed bubble sizes. Higher enhancement ratios were observed for systems having larger bubble sizes. Since FC-72 had the smaller bubble departure diameters, the enhancement ratio for FC-72 was also the smallest. Everything else being equal, a system having larger bubble sizes is more likely to reach pool boiling CHF conditions at lower heat flux magnitudes in comparison to an equivalent system with smaller bubbles sizes, because larger bubbles are more likely to coalesce to form even larger bubbles and to prevent fluid from the pool to reach the surface. The enhancement ratio trends suggest that is possible, in comparison to the pool boiling CHF for a particular bubble size system, that the additional fluid supplied

by the jet flow to the surface at a fixed Re will become more substantial in systems with larger bubble sizes.

5.4.3 SUBMERGED JET IMPINGEMENT CHF MAP

CHF data from the previous section is presented in this section in a non-dimensional form. In the context of jet impingement boiling, correlations typically present CHF as a grouping of terms representative of the Boiling number, Bo,

$$Bo = \frac{q''_{CHF,sat}}{\rho V_j h_{lv}} \tag{10}$$

The Bo has been reported using either the liquid [16, 32, 34] or vapor density [24, 29-31, 33, 35, 37]. In the present study, Bo is defined using the liquid density since it would then represent the ratio between CHF and the jet latent heat flux capacity. Furthermore, based on the Bo definition, a boiling effectiveness, ε, is introduced,

$$\varepsilon = \left(\frac{q''_{CHF,sat}}{\rho_l V_j h_{lv}}\right)\left(\frac{A_{surf}}{A_j}\right) = Bo \times \left(\frac{A_{surf}}{A_j}\right) \tag{11}$$

This term represents the ratio between the actual surface heat rate and the potential jet latent heat capacity rate. A boiling effectiveness of unity corresponds to the situation where the net heat transfer rate from the surface equals the net potential latent heat capacity rate provided by the jet flow. A large boiling effectiveness utilizes lower jet

mass flow rates to achieve a fixed CHF value. For a free surface jet, the highest possible ε is unity, a condition that would correspond to the entire jet flow undergoing phase-change, such that fluid distribution on the surface is assumed to be uniform. For submerged jets, because of the presence of the pool, it is possible to have ε greater than unity.

Figure 59 and Fig. 60 show the variation of inverse boiling effectiveness, 1/ε, with Re for water with varying pressures on the 123 nm Ra surface and the 33 nm Ra surface respectively. Figure 61 shows the same trends for FC-72 data with varying jet diameters on the 33 nm Ra surface. The inverse of ε is plotted to better distinguish the CHF trends with Re, pressure, and jet diameter. A value of 1/ε of unity corresponds to the condition of complete evaporation of jet flow. Dotted lines on these plots represent the pool boiling CHF limit determined by using pool boiling CHF values from experiments at the corresponding experimental conditions in Eq.11, while varying the jet velocity. Since pool boiling CHF is fixed at a fixed experimental condition, these lines appear as a straight line in the 1/ε vs. Re figures. For a fixed Re, the vertical distance on these plots between the experimental data and the corresponding pool boiling CHF limit represents the realized enhancement in CHF by using the jet, while the vertical distance from the data to 1/ε of unity represents the unrealized jet flow enhancement potential for the given experimental conditions.

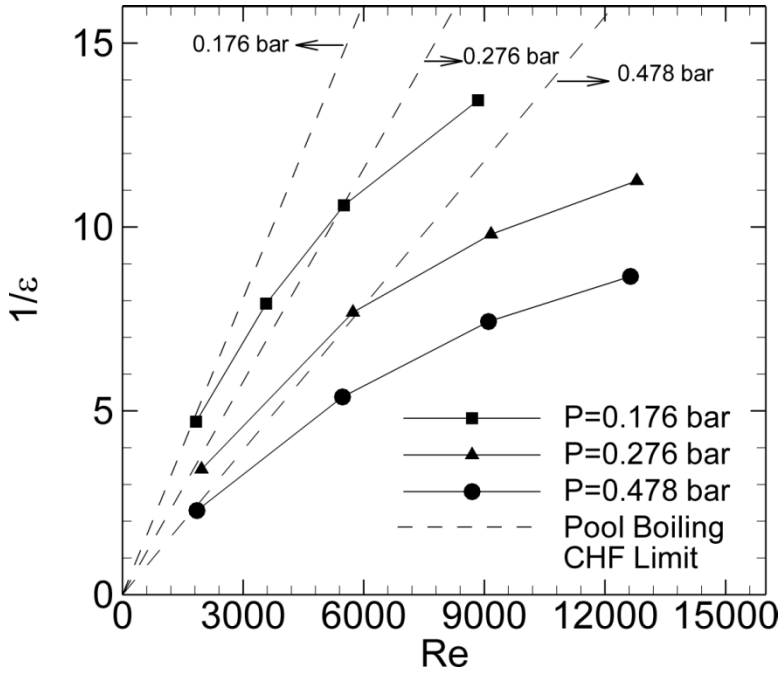

Figure 59: Jet impingement boiling effectiveness for water on a 123 nm Ra surface

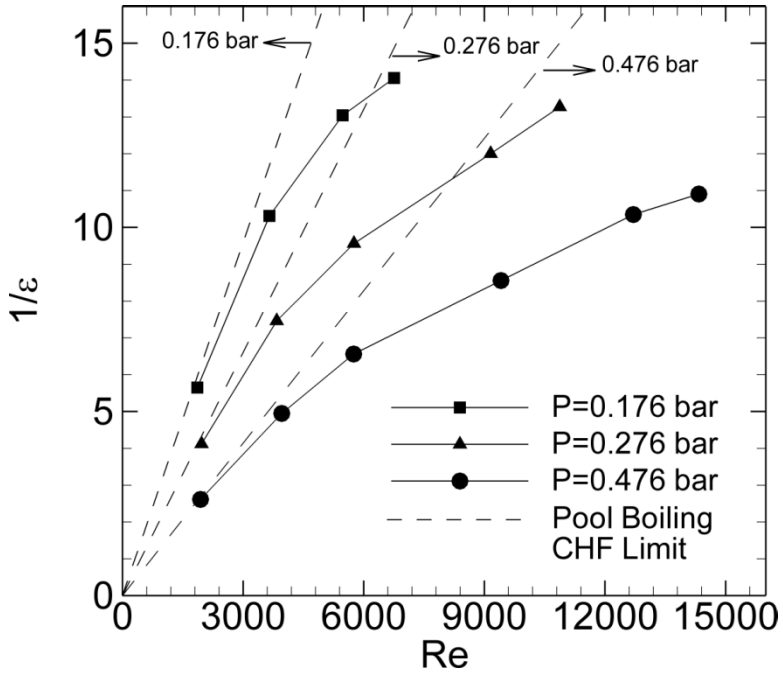

Figure 60: Jet impingement boiling effectiveness for water on a 33 nm Ra surface

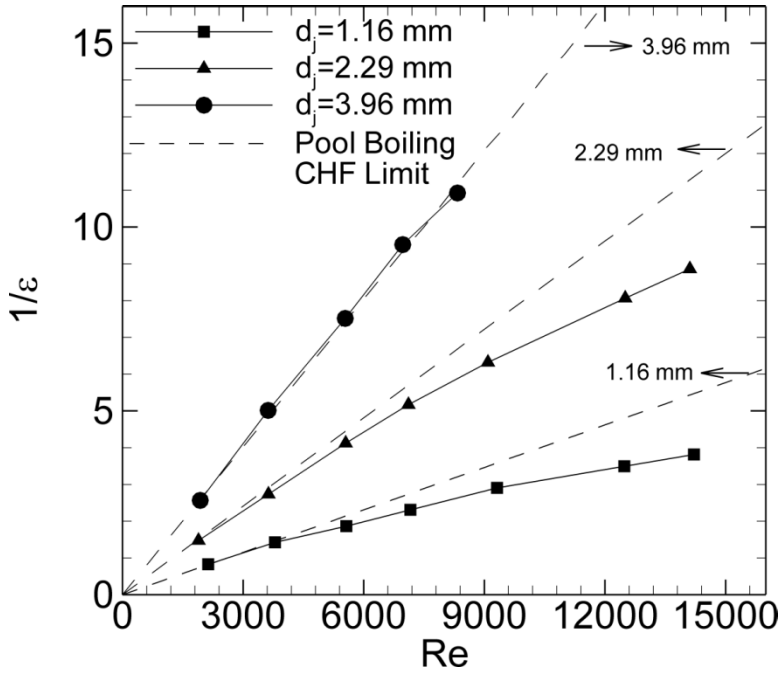

Figure 61: Jet impingement boiling effectiveness for FC-72 on a 33 nm Ra surface

For the data shown in Fig. 59, Fig. 60, and Fig. 61, the jet latent heat capacity rate was almost always higher than the actual surface heat rate at CHF as indicated by 1/ε magnitudes in excess of unity. This trend is with the exception of the lowest Re data point for FC-72 using a 1.16 mm diameter jet. This value of 1/ε less than unity (ε > 1) implies that the net heat transfer rate from the surface at CHF was greater than the net potential latent heat capacity rate provided by the jet flow. This condition can be encountered in submerged jet configurations because at low jet mass flow rates the CHF reverts back to pool boiling CHF. Therefore, with the exception of this data point, all the data collected in this study fall under the CHF condition where the heat transfer rate from the surface is only a fraction of the jet latent heat capacity rate [4].

For an equivalent surface Ra and jet diameter, comparison of the pool boiling CHF limit between water (Fig. 60) and FC-72 data (Fig. 61) indicate that the slope of the pool boiling limit line is smaller for the FC-72 case. This trend simply implies that, in comparison with the jet flow, pool boiling alone more effectively brings fluid to the surface for FC-72 than for water. However, owing the significantly larger latent heat of vaporization of water, pool boiling CHF magnitudes for water were always much greater than for FC-72. Note that for a fixed set of conditions, as the Re approaches zero, the experimental data approaches the pool boiling CHF limit as expected. However, with increasing Re, the experimental data deviates from the pool boiling CHF limit towards a $1/\varepsilon$ value closer to unity.

The benefit of using a submerged impinging jet in comparison to pool boiling is better described by the magnitude of the realized jet CHF enhancement relative to the total jet enhancement potential. Figure 62 and Fig. 63 show the ratio of the realized jet CHF enhancement (ϕ_j) over the total jet enhancement potential (ϕ_{Total}) with Re for water on a 123 nm and 33 nm Ra surface respectively. Figure 64 shows the same trends for FC-72 on a 33 nm Ra surface. In general, these figures indicate that for large Re, the benefit of using a submerged impinging jet over pool boiling alone is greater with higher surface roughness, lower system pressures, and smaller jet diameters. Also note from these figures that sub-atmospheric boiling of water benefits more from the submerged impinging jet than atmospheric boiling of FC-72.

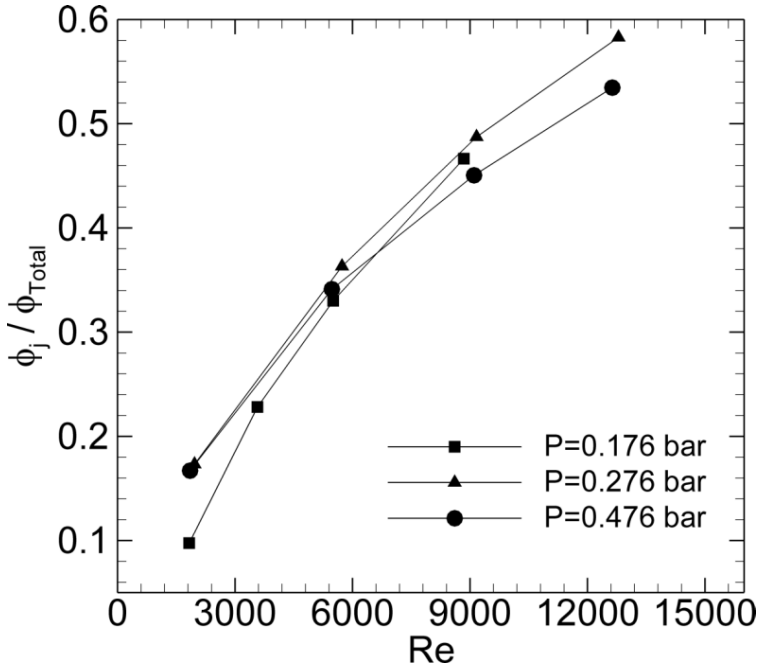

Figure 62: Realized jet enhancement over the total enhancement potential for water on a 123 nm Ra surface

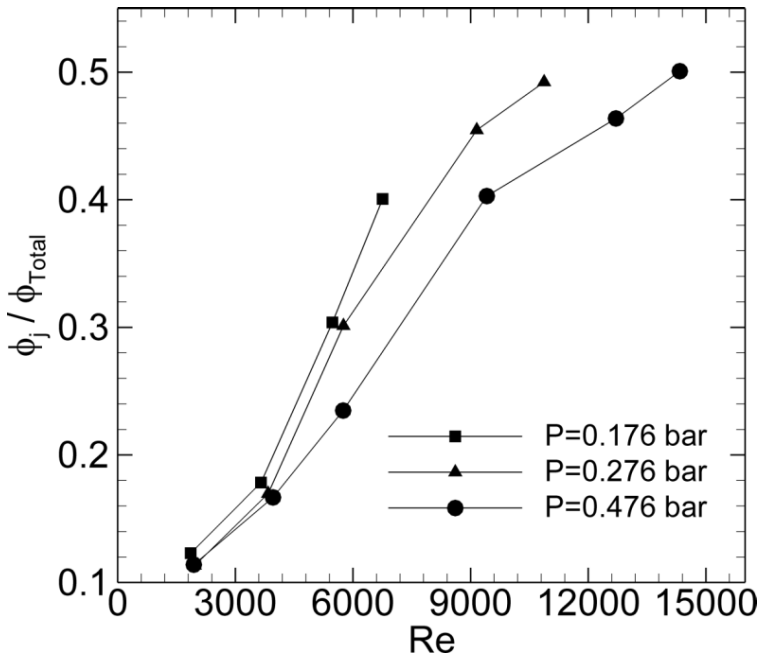

Figure 63: Realized jet enhancement over the total enhancement potential for water on a 33 nm Ra surface

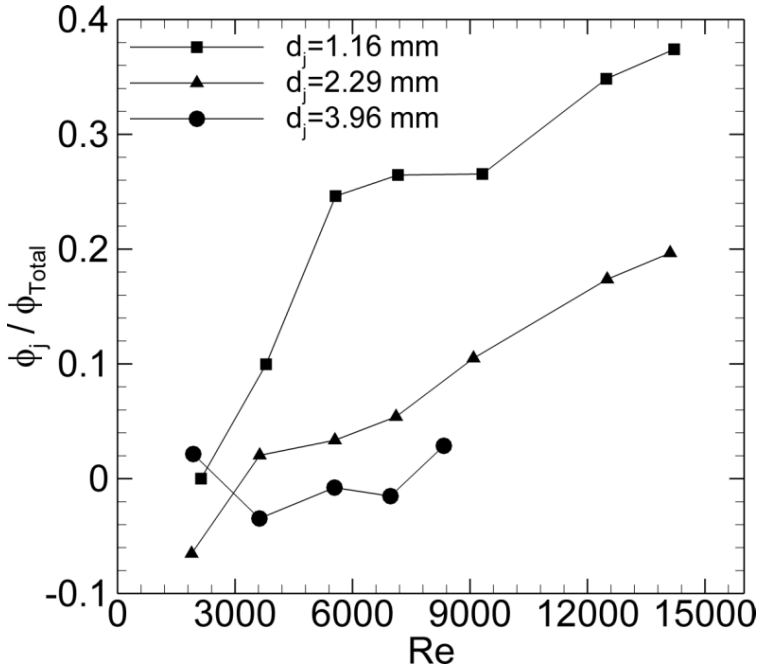

Figure 64: Realized jet enhancement over the total enhancement potential for FC-72 on a 33 nm Ra surface

The experimental data trends shown in Fig. 59 through Fig. 61 are summarized in a CHF map given in Fig. 65. Two theoretical boundaries based on pool boiling CHF and jet vaporization enthalpy rate are delineated on this figure. The shaded region on the map represents possible operating conditions for submerged jet impingement boiling. The jet CHF boundary marks the upper heat flux limit when using an impinging jet. As previously mentioned, the distance between the jet CHF boundary and the CHF boundary based on pool boiling represents the realized jet CHF enhancement, while the distance between the jet CHF boundary and the CHF boundary based on jet vaporization enthalpy rate ($1/\varepsilon=1$) represents the unrealized jet enhancement potential for the particular experimental conditions. A lever rule, based on the magnitude of the

realized jet CHF enhancement and the total jet enhancement potential, can be used to compute the benefit gained, in comparison to pool boiling CHF, by using the submerged impinging jet for a given set of experimental conditions at any fixed Re .

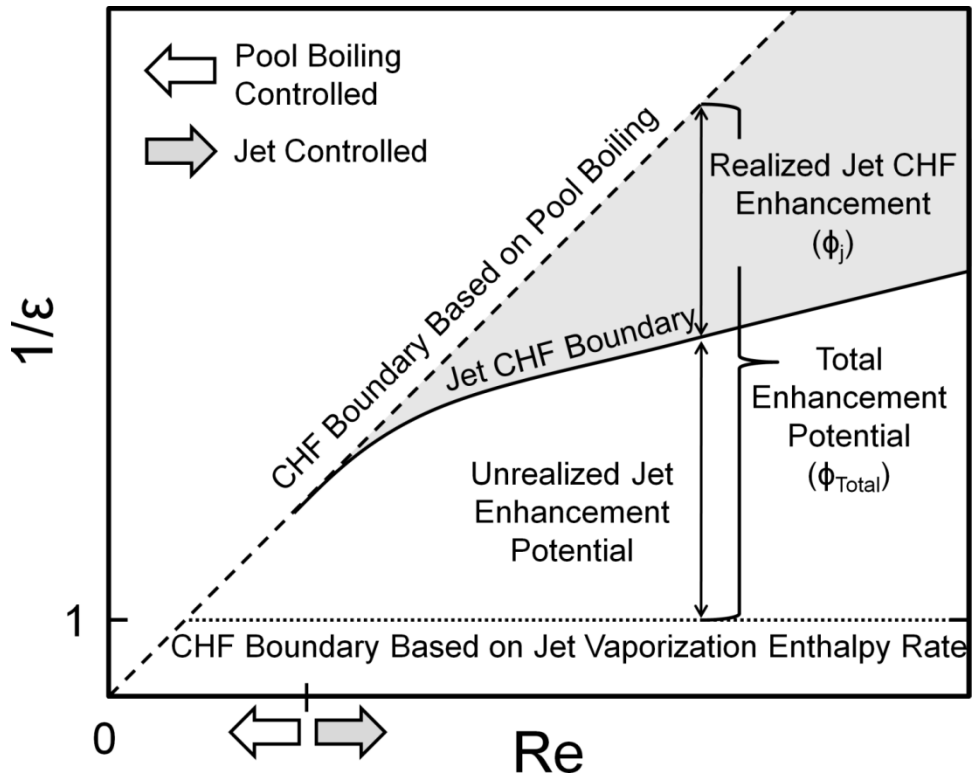

Figure 65: CHF map for submerged jet impingement boiling

In Fig. 65, the Re at which the jet CHF boundary meets the theoretical CHF boundary based on pool boiling on the lower left corner marks the limit between pool boiling controlled CHF and jet controlled CHF. Conditions to the left of this Re do not show any CHF enhancement despite the jet flow, and CHF in this region is controlled by

pool boiling (this was the case for FC-72 at d_j=3.96 mm as seen in Fig. 61). Conditions to the right of this Re show realized jet CHF enhancement and are thus of practical interest. In the pool boiling controlled region, CHF is fixed and equal to that of pool boiling. Therefore, as the Re approaches zero, values of $1/\varepsilon$ less than unity are possible for the submerged jet configuration such as the data point for FC-72 at the lowest Re for d_j=1.16 mm. However, these conditions are not of practical interest in submerged jet impingement boiling.

The experimental data showed that increased surface roughness and pool pressures as well as smaller jet diameters caused the pool and jet CHF boundaries to be further pushed down towards the lower jet vaporization enthalpy limit of unity. This occurs because all of the changes mentioned above make the pool boiling heat transfer action more effective into bringing fluid to the surface at CHF conditions, in comparison to the jet flow. However, to identify and isolate the benefit gained by using the submerged jet, it is necessary to look at the realized jet CHF enhancement region. As previously mentioned, for a fixed Re, the jet enhancement over pool boiling is measured by the relative size of the realized jet CHF enhancement to the total jet enhancement potential. The experimental data showed that these enhancements were greater with higher surface roughness, at lower system pressures, and with smaller jet diameters. In addition, higher improvements in CHF beyond the pool boiling limit were possible using water in comparison to FC-72.

5.4.4 Comparison of CHF Data with Correlations

The experimental CHF data obtained for submerged jet impingement boiling were compared against 12 jet CHF correlations available in literature, evaluated at the particular experimental conditions. Table 13 provides a summary of these correlations and the conditions for which they were developed. Since existing CHF correlations for submerged jet impingement boiling are limited, most correlations are those developed for free surface jet configurations. Note from Table 13 that the liquid-to-vapor density ratio is an important factor which appears in most of the correlations. While the range of conditions represented in the existing correlations is large, the range of density ratio ρ_l/ρ_v currently represented in all these correlations is well below the experimental conditions for the sub-atmospheric water cases. At the considered sub-atmospheric pressures of 0.176 bar, 0.276 bar, and 0.477 bar, the corresponding liquid-to-vapor density ratios for water were 8502, 5544, and 3295 respectively. The correlations presented in Table 13 only cover liquid-to-vapor density ratios of up to approximately 1626. However, for the FC-72 experiments, the liquid-to-vapor density ratio of 119 falls within the range of some of these correlations.

Table 13: Jet CHF correlations

C.#	Configuration	Correlation	Conditions
C.1 [24]	Free-Surface	$\frac{q''_{CHF}}{\rho_v V_j h_{lv}} = 7.45\times10^{-2}\left(\frac{\rho_l}{\rho_v}\right)^{0.725}\left(\frac{\sigma}{\rho_l V_j^{\,2} d_{surf}}\right)^{\frac{1}{3}}\left(1+\varepsilon_{sub}\right)$	Fluids: Water, R-113 ρ_l/ρ_v =1626, 204.7 ΔT_{sub}=0-30 ˚C d_{surf} =11.2- 21 [mm] d_{surf}/d_j= 5.6-10.5 V_j=2.04-26 [m/s] Upward & Downward facing surface
C.2 [29]	Free-Surface	$\frac{q''_{CHF,sat}}{\rho_v V_j h_{lv}} = 0.188\left(\frac{\rho_l}{\rho_v}\right)^{0.614}\left(\frac{\sigma}{\rho_l V_j^{\,2} d_{surf}}\right)^{\frac{1}{3}}$	Fluids: R-12, R-113 ρ_l/ρ_v=205, 5.2<ρ_l/ρ_v<39 ΔT_{sub}=0 ˚C d_{surf} =10 [mm] d_{surf}/d_j= 5 V_j< 20 [m/s] Downward-facing surface
C.3 [31]	Free-Surface	$\frac{q''_{CHF,sat}}{\rho_v V_j h_{lv}}\frac{d_{surf}}{d_j} = f(r)\left(\frac{\sigma}{\rho_l V_j^{\,2} d_{surf}}\left(\frac{d_{surf}}{d_j}\right)^3\right)^{A(r)}$, $f(r)=0.744+0.0084r$ $r=\frac{\rho_l}{\rho_v}$, $A(r)=0.4346+0.1027\ln r-0.0474(\ln r)^2+0.00426(\ln r)^3$	Fluids: Water, R-113, R-12 ρ_l/ρ_v = 5-1622 ΔT_{sub}=0 ˚C Horizontal Surface Includes data from: [24, 29] Accuracy: ±20% for 95% of data used
C.4 [37]	Free-Surface	$\frac{q''_{CHF,sat}}{\rho_v V_j h_{lv}} = \frac{0.0601\left(\frac{\rho_l}{\rho_v}\right)^{0.725}\left(\frac{2\sigma}{\rho_l V_j^{\,2} d_{surf}}\right)^{\frac{1}{3}}}{\left(1+0.00113\left(d_{surf}/d_j\right)^2\right)}$	Fluids: Water, R-113* ρ_l/ρ_v =100-1603 ΔT_{sub}=0 ˚C d_{surf} =11.9- 25.5 [mm] d_{surf}/d_j= 5-36.4 V_j=0.3-15 [m/s] Upward-facing surface Includes data from: [24]

* Data from reference sources

Table 13: Jet CHF correlations (Continued)

C.#	Configuration	Correlation	Conditions
C.5 [30]	Free-Surface	$\frac{q''_{CHF,sat}}{\rho_v V_j h_{lv}} = 0.221\left(\frac{\rho_l}{\rho_v}\right)^{0.645}\left(\frac{2\sigma}{\rho_l V_j^2\left(d_{surf}-d_j\right)}\right)^{0.343}\left(1+\frac{d_{surf}}{d_j}\right)^{-0.364}$	Fluids: Water*, R-113*, R-12* ρ_l/ρ_v =5.3-1603 ΔT_{sub}=0 ˚C d_{surf} =10- 60.1 [mm] d_{surf}/d_j= 2.25-57.1 V_j=0.21-60 [m/s] Horizontal Surface Includes data from: [24, 29, 37] Accuracy: ±20%
C.6 [32]	Free-Surface	$\frac{q''_{CHF,sat}}{Gh_{lv}} = 0.278\left(\frac{\rho_v}{\rho_l}\right)^{0.467}\left(1+\frac{\rho_v}{\rho_l}\right)^{\frac{1}{3}}\left(\frac{\sigma\rho_l}{G^2\left(d_{surf}-d_j\right)}\right)^{\frac{1}{3}}\left(1+\frac{d_{surf}}{d_j}\right)^{\frac{-1}{3}}$	ΔT_{sub}=0 ˚C d_{surf}/d_j>1 Derived using Liquid Sub-film Model
C.7 [33]	Free-Surface	$\frac{q''_{CHF,sat}}{\rho_v V_j h_{lv}} = \left(0.21+0.00171\gamma\right)\left(\frac{d_j}{d_{surf}}\right)^{1/3}\left(\frac{1000}{We}\right)^{A}$, $We=\frac{\rho_l V_j^2 d_{surf}}{\sigma}$ $\gamma=\frac{\rho_l}{\rho_v}$, $A=0.486+0.06052\ln\gamma-0.0378\left(\ln\gamma\right)^2+0.00362\left(\ln\gamma\right)^3$	Fluids: Water*, R-113*, R-12* ρ_l/ρ_v =5.2-1604 ΔT_{sub}=0 ˚C Accuracy: 8.6% standard deviation error Includes data from:[24, 29, 37]
C.8 [34]	Free-Surface	$\frac{q''_{CHF,sat}}{Gh_{lv}} = K\left[\frac{\sigma\rho_l}{G^2\left(d_{surf}-d_j\right)}\left(\frac{1}{1+d_{surf}/d_j}\right)\right]^m$, $K=0.0166+7\left(\frac{\rho_v}{\rho_l}\right)^{1.12}$ $m=0.374\left(\frac{\rho_v}{\rho_l}\right)^{0.0155}$ $for\ \frac{\rho_v}{\rho_l}\le 0.00403$ or $m=0.532\left(\frac{\rho_v}{\rho_l}\right)^{0.0794}$ $for\ \frac{\rho_v}{\rho_l}\ge 0.00403$	Fluids: Water*, R-113*, R-12* ρ_l/ρ_v =5.3-1604 ΔT_{sub}=0 ˚C d_{surf} =10-60.1 [mm] d_{surf}/d_j= 3.9-53.9 V_j=0.3-60 [m/s] Upward and Downward-facing surface Includes data from:[24, 29, 30, 37] Accuracy: 16% RMS error

* Data from reference sources

Table 13: Jet CHF correlations (Continued)

C.#	Configuration	Correlation	Conditions
C.9 [35]	Confined	$\frac{q''_{CHF,sat}}{\rho_v V_j h_{lv}} = 0.0786\left(\frac{\rho_l}{\rho_v}\right)^{\frac{2}{3}}\left(\frac{\sigma}{\rho_l V_j^{\,2}\left(d_{surf}-d_j\right)}\right)^{0.149}\left(\frac{d_j}{d_{surf}-d_j}\right)^{0.396}$	Fluids: FC-72 ρ_l/ρ_v =93-102 ΔT_{sub}=0-40 ˚C d_{surf} =17.96 [mm] d_{surf}/d_j= 35.35-141.42 V_j= 1-13 [m/s] Upward-facing surface Accuracy: ±18.2% max, ±7.4% average
C.10 [4]	Submerged	$q''_{CHF} = q''_{CHF,sat\,pool}\left(1+0.92V_j^{\,0.44}\right)\left(1+\varepsilon_{sub}\right)$ $q''_{CHF,sat\,pool} = 0.16\rho_v h_{lv}\left(\frac{\sigma g\left(\rho_l-\rho_v\right)}{\rho_v^{\,2}}\right)^{\frac{1}{4}} \rightarrow Kutateladze$	Fluid: Water ΔT_{sub}=85-151 ˚C V_j= 1-35 [m/s] d_{surf} =9 [mm] d_{surf}/d_j= 0.44
C.11 [16]	Free-Surface	$\frac{q''_{CHF,sat}}{Gh_{lv}} = 0.132\left(1+\frac{\rho_v}{\rho_l}\right)^{\frac{1}{3}}\left(\frac{\sigma\rho_l}{G^2 d}\right)^{\frac{1}{3}}\left(\frac{\rho_v}{\rho_l}\right)^{\frac{1.4}{3}}$ $d = d_{surf} = d_j$	Fluids: Water ρ_l/ρ_v =1603 ΔT_{sub}=0˚C d_{surf} =2-10 [mm] d_{surf}/d_j= 1 V_j= 0.5-6 [m/s] Upward-facing surface Accuracy: ±20% relative error
C.12 [16]	Free-Surface	$\frac{q''_{CHF,sat}}{Gh_{lv}} = 0.278\left(\frac{\rho_v}{\rho_l}\right)^{0.645}\left(\frac{\sigma\rho_l}{G^2\left(d_{surf}-d_j\right)}\right)^{0.343}\left(1+\frac{d_{surf}}{d_j}\right)^{-0.343}$	$d_{surf}/d_j > 1$

* Data from reference sources

Figure 66(a-c) show the comparison between the experimental water CHF data and the CHF correlations from literature at pressures of 0.176 bar, 0.276 bar, and 0.477 bar respectively. In general, poor agreement of the CHF correlations with each other and with the experimental data is observed. Correlation C.11, which appears to best agree with experimental data at all pressures (up to 30% difference), was developed for the specific case where the heated surface diameter is equal to the jet nozzle diameter. For the water data in this dissertation, the ratio d_{surf}/d_{jet} was about 23.8. Therefore, for the correlation C.11 trendline shown in Fig. 66, the surface diameter was used to compute CHF. If the jet diameter would have been used instead, predicted CHF values would have been about three times higher than those shown, resulting in a far worse prediction of the present experimental data. Note that correlations C.3 and C.7 in Figs. 66(a) and (b) do not capture the trend of CHF with Re properly. At pressures of 0.176 bar (Fig. 66(a)) and 0.276 bar (Fig. 66(b)), both correlations erroneously predict a decreasing CHF with increasing jet Re. However, once the pressure is increased to 0.477 bar (Fig. 66(c)), the trend reverses and CHF is predicted to increase with Re.

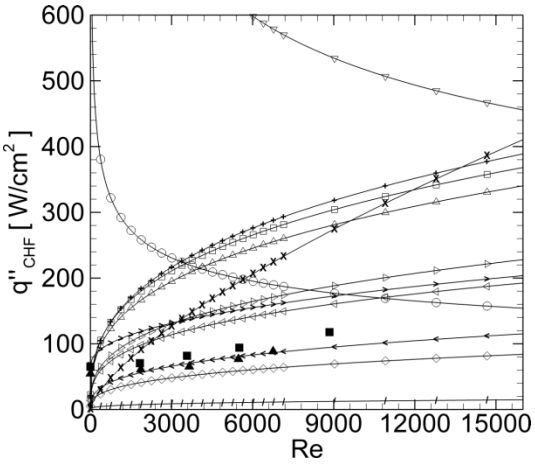

(a) P=0.176 bar

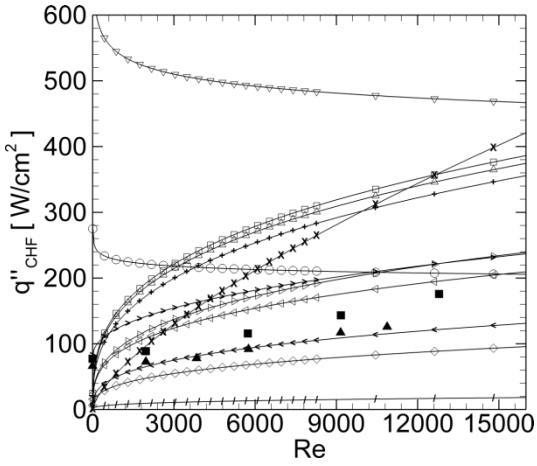

(b) P=0.276 bar

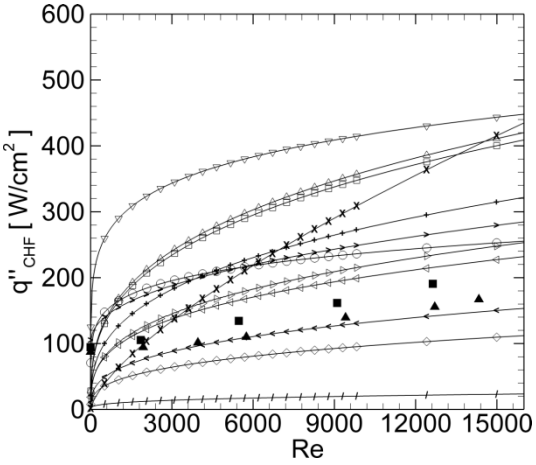

(c) P=0.477 bar

Figure 66: Comparison of water CHF jet impingement data with correlations: □ C.1, △ C.2, ▽ C.3, ▷ C.4, ◁ C.5, ◇ C.6, ○ C.7, + C.8, x C.9, > C.10, < C.11, / C.12, ■ 123 nm Ra surface, ▲ 33 nm Ra surface

Figure 67(a-c) show the comparison between the experimental FC-72 CHF data and the CHF correlations from literature for a jet diameter of 1.16 mm, 2.29 mm, and 3.96 mm respectively. Once again, the comparison of the experimental data with the correlations is poor. Correlation C.9, which is the only correlation in Table 13 developed for FC-72, seems to over predict the growth rate of CHF with Re. This over prediction of CHF with Re from correlation C.9 could be associated with the difference in jet configuration since correlation C.9 was developed for a confined jet configuration. Correlation C.1 agrees with the FC-72 CHF data for d_j=1.16 mm (Fig. 67(a)) and d_j=2.29 mm (Fig. 67(b)) within 10 percent for Re > 4000. For d_j=3.96 mm (Fig. 67(c)), the discrepancy can be up to 20 percent over the same Re range. Note from Table 13 that correlation C.1 does not directly depend on jet diameter except through the jet diameter dependency of the exit jet velocity for a fixed Re. However, the predictions from correlation C.1 worsen at low Re and with increasing jet diameter. In general, at large Re and small jet diameters, the majority of the correlations are in better agreement with each other, and the discrepancy with the experimental data is lower. Perhaps this better agreement of the correlations with each other and with the experimental data is because the experimental conditions considered fall under the range of validity of these correlations which considered liquid-to-vapor density ratios of less than 1626 as well as highly wetting fluids like R-113, R-12.

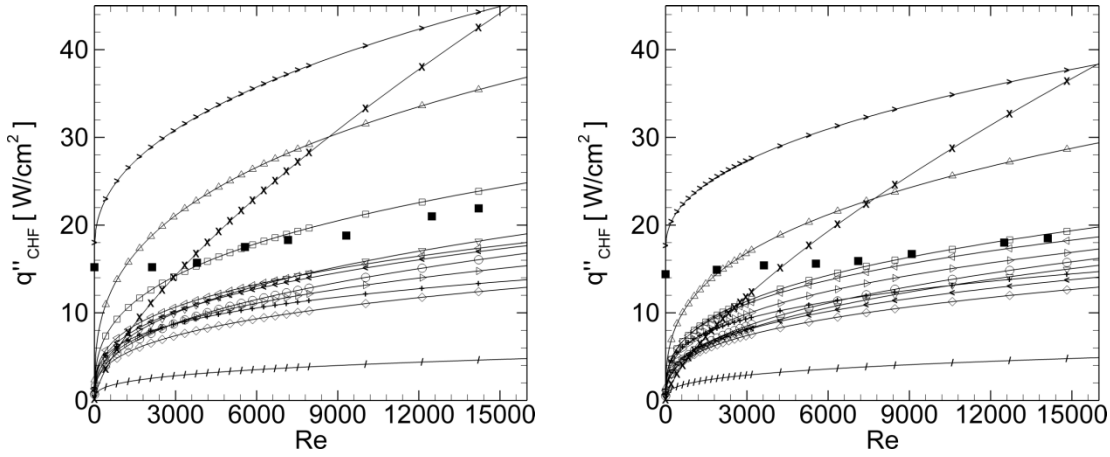

(a) d_j=1.16 mm (b) d_j=2.29 mm

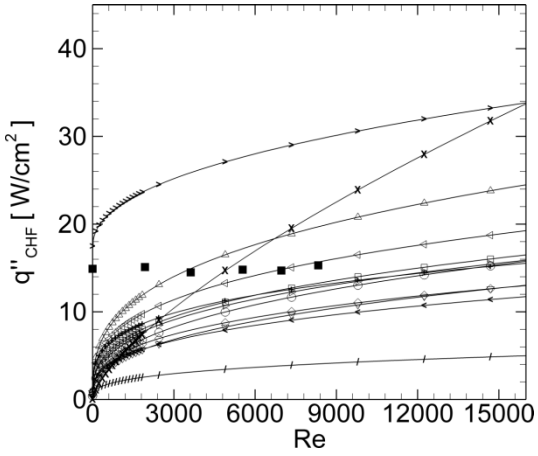

(c) d_j=3.96 mm

Figure 67: Comparison of FC-72 CHF jet impingement data with correlations: □ C.1, △ C.2, ▽ C.3, ▷ C.4, ◁ C.5, ◇ C.6, ○ C.7, + C.8, x C.9, > C.10, < C.11, / C.12, ■ 33 nm Ra surface

It is evident from Fig. 66 and Fig. 67 that existing CHF correlations in literature for jet impingement boiling cannot reliably predict CHF at all the experimental conditions considered in this study. Note that all of the CHF correlations developed so far, with the exception of correlation C.10, do not approach pool boiling CHF as the Re goes to zero but instead the CHF goes to zero. This might be the case in free surface jet impingement but should not be the case for a submerged jet configuration. For FC-72 at large Re, the majority of the existing correlations, with the exception of correlations C.2, C.9, C.10, and C.12, do provide fairly reasonable and conservative CHF estimates. For water, the predictions vary widely. One likely cause for such a discrepancy between the experimental data for water and the correlations, besides the jet configuration itself, could be the liquid-to-vapor density ratios, ρ_l/ρ_v, being considered. Therefore, there is a need of a general submerged jet impingement CHF correlation that can properly capture the pool boiling CHF limit as well as the jet impingement CHF trends for varying fluid properties, Re, and nozzle diameter for the conditions considered in this study.

5.4.5 Submerged Jet Impingement CHF Model

Poor agreement was seen between the experimentally determined jet impingement CHF data and the predictions from existing literature correlations discussed in Section 5.4.4. In addition, a major drawback of most correlations available in literature for jet impingement boiling, is that they do not properly converge to pool boiling CHF as the

jet flow goes to zero. This behavior must be enforced in a proper CHF correlation for submerged jet impingement boiling. This section develops a CHF correlation for submerged jet impingement boiling based upon an extension of a hydrodynamic stability CHF model to best represent the CHF jet impingement data while properly capturing the pool boiling CHF limit.

In 1983, Haramura and Katto [26] presented a new hydrodynamic CHF model based on hydrodynamic stability principles. The use of hydrodynamic stability analysis to develop pool boiling CHF models dates back to Zuber [49] in 1959. However, the novelty of the model presented by Haramura and Katto [26] was its applicability not only to pool boiling systems but also to forced convection boiling of saturated liquids in submerged environments. Figure 68 illustrates the postulated idea behind Haramura and Katto [26] CHF model. The premise of their model was the existence of a thin and stable liquid film which nourishes the large vapor bubbles that hover over the heated surface through underlying vapor stems. This thin liquid film does not get replenished until the large vapor bubbles hovering over the surface depart. To find the upward velocity of the vapor stems (V_v) needed in the stability analysis, an energy balance was used while assuming that all of the heat is converted into latent heat at CHF conditions. The downward liquid velocity (V_l) towards the surface was found by a mass conservation equation between the vapor and liquid phases. Using these velocities, the Helmholtz wavelength (λ_H) for instability was computed, and to ensure that the thin liquid film remained stable, a film thickness of ¼ the Helmholtz wavelength for instability was assigned. For a large heater surface, the interval

between adjacent vapor bubbles was given as the most dangerous wavelength (λ_D) based on Taylor instability analysis. From the intervals between vapor bubbles, a volumetric bubble growth rate and a corresponding hovering time were computed based upon relationships from literature. The authors assumed that the CHF condition was reached when the hovering time of the vapor bubbles was exactly equal to the amount of time the thin liquid film can sustain the heat load on the surface through evaporation. Therefore, using energy conservation principles at CHF conditions, and the geometry of the thin liquid film, Haramura and Katto [26] first developed a CHF model for the basic case of pool boiling. However, in their model, the ratio of the surface area covered by vapor to the total surface area for heat transfer was unknown. To find an expression for this unknown quantity, Haramura and Katto [26] equated their models to Zuber's pool boiling critical heat flux model (which is equivalent to Kutateladze's correlation in Eq. 9) since this model had shown great success in predicting pool boiling CHF.

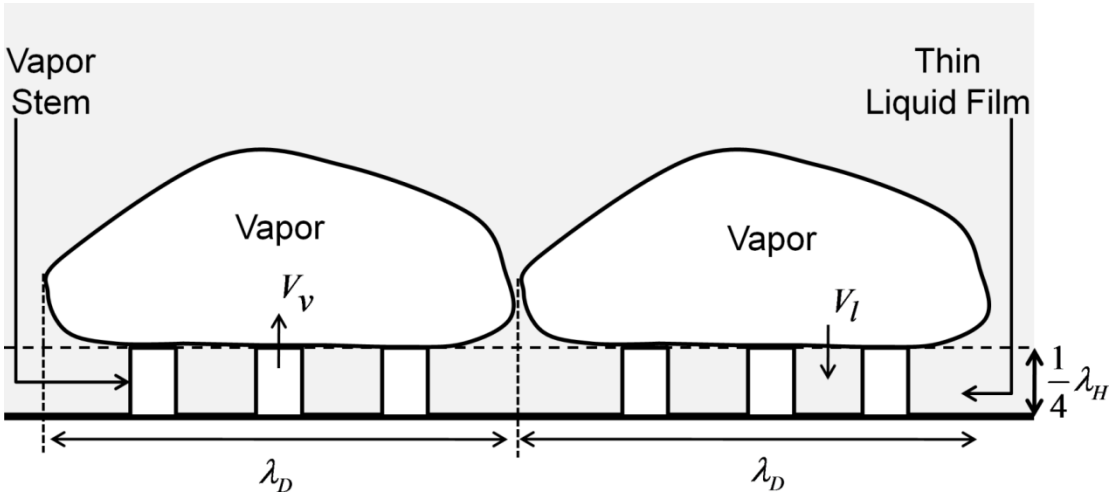

Figure 68: Haramura and Katto [26] pool boiling CHF model

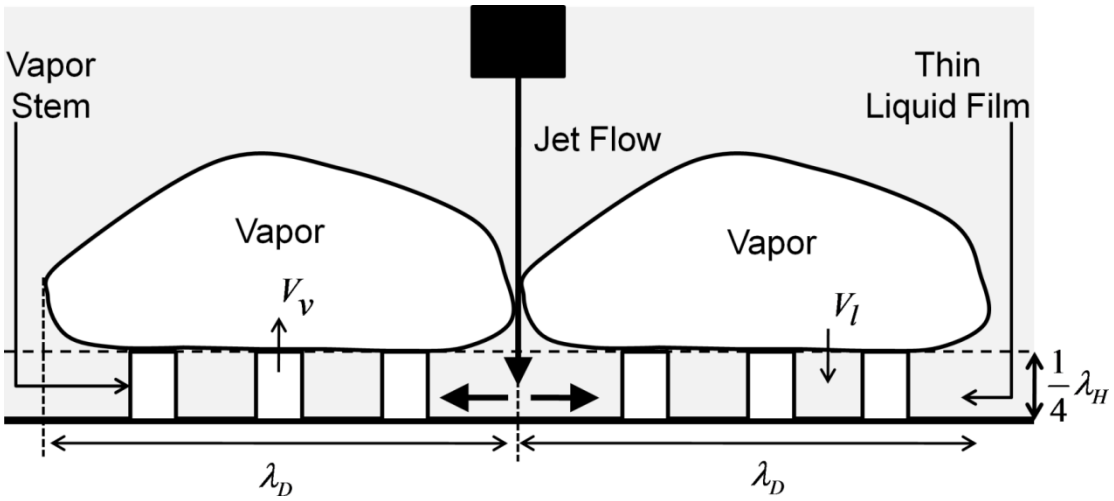

Figure 69: Extension of Haramura and Katto [26] CHF model to submerged jet impingement boiling

After deriving a pool boiling CHF model equivalent to Eq. 9, Haramura and Katto [26] proceeded to apply their model to other forced convection boiling systems. The

authors worked out a simple equation from their model that takes into account the artificial supply of liquid to the heated surface through other means different than the conventional pool boiling action itself. Haramura and Katto [26] suggested that this artificial supply of fluid could come from an impinging jet flow while citing the work by Katto and Kunihiro [23] on submerged jet impingement boiling. However, the authors did not elaborate further on the particular application of submerged jet impingement boiling. Figure 69 graphically illustrates the extension of Haramura and Katto [26] CHF model to submerged jet impingement. The simple equation, that was derived to account for a forced convective fluid supply to the surface, can be written for the present impinging jet configuration as

$$\frac{q''_{CHF,j}}{q''_{CHF,pool}} = (1+k)^{5/16} \tag{12}$$

where the factor k takes into account the impact of the forced convective inflow. Note that the analogous equation to Eq. 12 presented by Haramura and Katto [26] includes an additional term to account for the case when the heated surface diameter is much smaller than the most dangerous wavelength for instability. However, for the collected data record in this report, this term is not significant for the water data and not applicable to the FC-72 data and hence, has been neglected.

In the present study, Eq. 12 is utilized as the initial CHF model for submerged jet impingement. The factor k in the model can in general be a function of all the relevant

parameters varied in the study which can be represented using standard dimensionless groups and the surface roughness parameter,

$$k = f\left(\mathrm{Re}, \frac{\rho_l}{\rho_v}, \mathrm{Pr}, Bond, \frac{d_{surf}}{d_j}, Ra \right) \tag{13}$$

The choice of parameters in Eq. 13 was based upon the physics of the phenomena being considered, as well as the knowledge gained from the CHF enhancement ratio plots in Fig. 56, Fig. 57, and Fig. 58. These plots showed that the enhancement ratio varied with Re, density ratio, working fluid, diameter ratio, and surface roughness. In addition, the Prandtl number was considered since this non-dimensional quantity gives the ratio of momentum to thermal diffusivity for the submerged jet flow and it is of significant importance in single-phase jet impingement cooling [5]. A possible mathematical expression for k can be given as

$$k = \kappa \left(\mathrm{Re}\right)^{\beta_1} \left(\frac{\rho_l}{\rho_v} \right)^{\beta_2} \left(\mathrm{Pr}\right)^{\beta_3} \left(Bond\right)^{\beta_4} \left(\frac{d_{surf}}{d_j} \right)^{\beta_5} \left(Ra\right)^{\beta_6} \tag{14}$$

where the leading constant κ (units of Ra $^{-\beta 6}$) and the powers β_1, β_2, β_3, β_4, β_5, and β_6 are to be determined. Note that Eq. 14 is non-linear and difficult to optimize. However, one can make Eq. 14 linear by taking the natural logarithm of both sides,

$$\ln\left(k\right) = \ln\left(\kappa\right) + \beta_1 \ln\left(\mathrm{Re}\right) + \beta_2 \ln\left(\frac{\rho_l}{\rho_v} \right) + \beta_3 \ln\left(\mathrm{Pr}\right) + \beta_4 \ln\left(Bond\right) + \beta_5 \ln\left(\frac{d_{surf}}{d_j} \right) + \beta_6 \ln\left(Ra\right) \tag{15}$$

Equation 15 above can more easily be written in standard linear form as

$$\ln(k) = \beta_0 + \beta_1 x_1 + \beta_2 x_2 + \beta_3 x_3 + \beta_4 x_4 + \beta_5 x_5 + \beta_6 x_6 \tag{16}$$

with the x variables being the natural logarithm of the corresponding original variables. Similarly, Eq.12 can be rewritten in the form

$$ln\left[\left(\frac{q''_{CHF,j}}{q''_{CHF,pool}}\right)^{16/5} - 1\right] = \ln(k) = y \tag{17}$$

Using Eq.16 and Eq. 17, the following standard linear equation is obtained

$$y = \beta_0 + \beta_1 x_1 + \beta_2 x_2 + \beta_3 x_3 + \beta_4 x_4 + \beta_5 x_5 + \beta_6 x_6 \tag{18}$$

It is now possible to use statistical considerations to determine which of the six variables included in the model for the factor k are significant and which ones are not. Since Eq.18 is linear, one can use an analysis of variances (ANOVA) with multiple linear regressions to determine the best regression model. This approach is known as the all possible models approach [57]. In general, this method can be performed in two different ways which can potentially lead to two different answers. The first way is the forward selection [57], in which a new variable is introduced one at a time into the model. The variables are introduced by selecting the variable that maximizes the R^2 value of the regression the most at each step. The second way is the backward elimination [57] which begins with the full model and eliminates the variable that reduces the R^2 value the least at each step. If features of both forward selection and

backward elimination are used, the method is called stepwise selection [57]. A stepwise selection method can begin as a forward or backward process but at each step, all included variables are checked forward and/or backwards to ensure that they maintain their statistical significance. At the end, only those variables that are of statistical significance (P-value < 0.05) to the data will remain.

Using Eq.18 as a model, a stepwise forward selection and a stepwise backward elimination was performed on 42 distinct experimental observations of jet impingement CHF using the data analysis and statistical software Stata. Table 14 summarizes the regression analysis output for these two methods. An important assumption of linear regression analysis is homoscedasticity [57] meaning that the standard deviation of the predicted value y does not vary with the predictor variable x. This assumption was checked for after completing the regression analysis. Note from Table 14 that two distinct solutions were found. The stepwise forward selection resulted in a three-parameter model that found that most of the data can be statistically explained by the variables x_1 (Re), x_4 (Bond), and x_6 (Ra). The stepwise backward elimination resulted in a four-parameter model, which had a slightly larger R^2 value, that found that the data can be statistically explained by the variables x_1 (Re), x_2 (ρ_l/ρ_v), x_5 (d_{surf}/d_j), and x_6 (Ra). While there is no statistical difference between these two models, the fundamental physical quantities involved are different. Both models agree that the jet Re is an important parameter and that higher Re lead to a higher k value which eventually lead to higher jet CHF values. Both models also agree that the average surface roughness and jet diameter are important. In the three-parameter

model, the jet diameter effect is included in the Bond number while in the four-parameter model a separate diameter ratio takes its effect into account. However, the main difference between these two models is that the three-parameter model includes the surface tension forces which are quite different for water and FC-72 but does not include the density ratio. Meanwhile, the four-parameter model includes the liquid-to-vapor density ratio, which also varied widely, but does not include surface tension forces. One can quickly reason why both models work mathematically. Note that the liquid-to-vapor density ratio is largest for water at the lowest pressure, decreases with pressure for this fluid and significantly drops for FC-72. Surface tension exhibits the same behavior. It is largest for water at the lowest pressure, decreases with increasing pressure for this same fluid and significantly drops for FC-72. The inverse of the Bond number in the three-parameter model and the liquid-to-vapor density ratio in the four-parameter model change in the same direction and hence, one cannot statistically decide which model is correct as they are both statistically significant and correctly capture the behavior of the experimental data.

Table 14: Summary output of regression analysis for stepwise forward selection and stepwise backward elimination

Stepwise Forward Selection (R^2=0.9328)				
	β_n	P-value	95 % Confidence Interval	
$\ln(\mathrm{Re})$: x_1	1.540295	0.000	[1.366739	1.71385]
$\ln(Bond)$: x_4	-0.465786	0.000	[-0.5388778	-0.3926942]
$\ln(Ra)$: x_6	0.2804515	0.013	[0.063422	0.4974811]
$\ln(\kappa)$	-8.692145	0.000	[-12.60619	-4.778102]
Stepwise Backward Elimination (R^2=0.9359)				
	β_n	P-value	95 % Confidence Interval	
$\ln(\mathrm{Re})$: x_1	1.569548	0.000	[1.391616	1.747479]
$\ln(\rho_l/\rho_v)$: x_2	0.3219596	0.000	[0.2299381	0.4139811]
$\ln(d_{surf}/d_j)$: x_5	0.9080657	0.000	[0.4603275	1.355804]
$\ln(Ra)$: x_6	0.2680388	0.017	[0.0499635	0.4861141]
$\ln(\kappa)$	-14.03438	0.000	[-18.3469	-9.721862]

The answer to which model is correct depends on which fluid property is actually causing the jet flow to reach the surface more effectively in comparison to pool boiling. According to the three-parameter model, the amount of fluid that reaches the surface at CHF conditions, in comparison to pool boiling, is larger for higher surface

tension fluids in comparison to lower surface tension fluids. On the other hand, the four-parameter model indicates that jet impingement enhancements are greater for fluids with lower vapor densities, regardless of surface tension. Both of these effects physically suggest that if the pool boiling system has smaller bubbles at departure, the additional CHF enhancement with an impinging jet flow is lower than in the case of larger bubbles at departure. A similar conclusion was made in Section 5.4.2 by looking at the plots of CHF enhancement ratio. Recall from Table 6 that in the present study, surface tension varied between 66.7 mN/m to 62.64 mN/m for water and 8.02 mN/m for FC-72 while the vapor density varied between 0.1158 kg/m^3 to 0.2949 kg/m^3 for water and 13.43 kg/m^3 for FC-72.

There is no evidence in the experimental data which could help distinguish which of the two model predictions is correct. In fact, it might be difficult to distinguish between the surface tension effect and the density ratio effect as most common heat transfer fluids which have low surface tension in comparison to water, also have lower liquid-to-vapor density ratios (FC-40, FC-43, FC-72, FC-77, FC-84, FC-87, PF-5052, R-113, and R-11 among others). Once can envision an experiment using a surfactant to clarify this question. For example, a mixture of water/2-propanol at a bulk mole fraction of 0.03 has a surface tension of about 30 percent that of pure water while the other fluid properties remain practically unchanged [6]. Comparing jet impingement CHF data of such a solution with that of pure water could help identify if the lower surface tension is responsible for the aforementioned trends.

Since a conclusive decision cannot be made regarding which of the two models is more appropriate for submerged jet impingement boiling CHF, both models are left as plausible options. Table 15 summarizes the critical heat flux model used for submerged jet impingement, as well as the two plausible models for the k factor in the CHF model which were obtained from the linear regression output in Table 14. Table 16 summarizes the range of the model parameters considered in the experimental data utilized to develop the model.

Table 15: Submerged jet impingement CHF model summary

CHF Model	$\frac{q''_{CHF,j}}{q''_{CHF,pool}} = (1+k)^{5/16}$						
k-factor model	$k = \kappa(\mathrm{Re})^{\beta_1}\left(\frac{\rho_l}{\rho_v}\right)^{\beta_2}(\mathrm{Pr})^{\beta_3}(Bond)^{\beta_4}\left(\frac{d_{surf}}{d_j}\right)^{\beta_5}(Ra)^{\beta_6}$						
	κ [$m^{-\beta 6}$]	β_1	β_2	β_3	β_4	β_5	β_6
3-parameter model	1.679×10^{-4}	1.5403	0	0	-0.4658	0	0.28045
4-parameter model	8.034×10^{-7}	1.5695	0.32196	0	0	0.9081	0.26804

Table 16: Range of parameters considered for CHF model development

	Values Tested	Range
Re	0, 1900, 3600, 5555, 7100, 9100, 12600, 14300	0 – 14300
ρ_l/ρ_v	119, 3295, 5545, 8502	119 – 8502
Pr	2.3, 2.7, 3.2, 9.0	2.3 – 9.0
Bond	0.195, 0.199, 0.205, 2.600, 10.134, 30.303	0.195 – 30.303
d_{surf}/d_j	7.0, 12.1, 23.8	7.0 – 23.8
Ra	33 nm, 123 nm	33 - 123

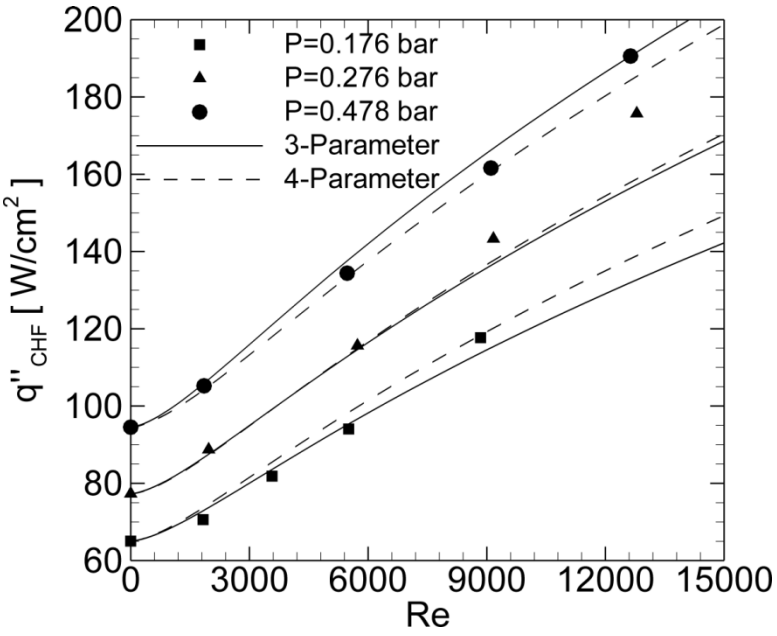

Figure 70: Comparison of developed submerged jet impingement CHF correlation with experimental data for water on the 123 nm Ra surface

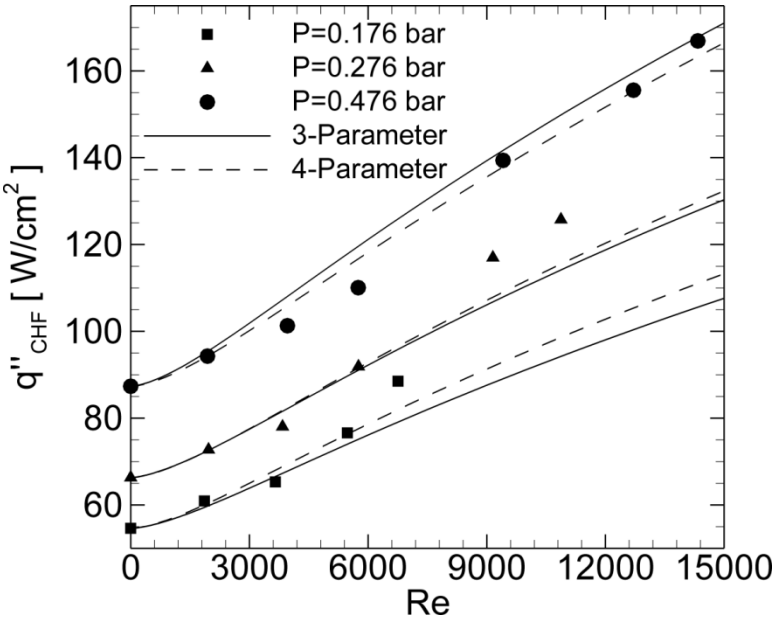

Figure 71: Comparison of developed submerged jet impingement CHF correlation with experimental data for water on the 33 nm Ra surface

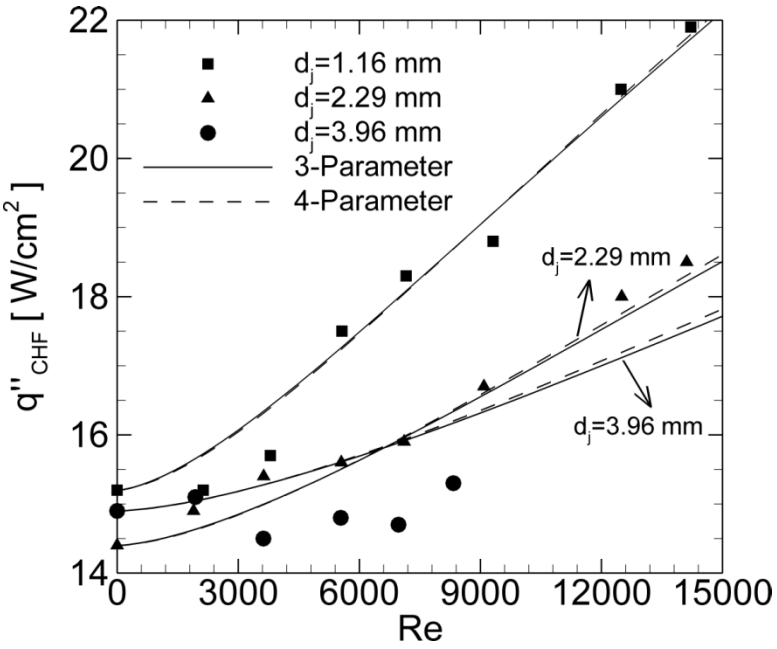

Figure 72: Comparison of developed submerged jet impingement CHF correlation with experimental data for FC-72 on the 33 nm Ra surface

Figure 70 and Fig. 71 show the comparison between both CHF jet impingement models with the experimental jet impingement CHF data for water on a 123 nm Ra surface and a 33 nm Ra surface respectively for varying system pressure. Figure 72 shows the same comparison for FC-72 jet impingement data on a 33 nm Ra surface for varying jet diameters. In general, the predicted CHF magnitudes and the general functional trend predicted by both of the CHF models agree reasonably well with the experimental data. Note that the predictions from these two models are almost equivalent everywhere. The three-parameter model predicts the entire jet impingement data set with a maximum error of 10.6 percent and an average error of 2.6 percent. The four-parameter model does slightly better (owing the slightly larger R^2 value of the regression model) and predicts the entire data set with a maximum error of 9.6 percent and an average error of 2.4 percent. Perhaps the worst agreement of the experimental data with the models occurs for the larger jet diameter in the FC-72 data. Such a discrepancy was expected, as most of the CHF data for this jet diameter was independent of Re and only showed random variations within the repetition uncertainty of the CHF data. More importantly, note that the proposed CHF models properly predict the pool boiling CHF limit as $Re \rightarrow 0$ as well as the general trend of the CHF data for increasing Re. Figure 73 shows a summary of the comparison between the predicted CHF values by both models with the experimentally determined quantities. This figure is plotted on a log-log scale to be able to distinguish the FC-72 data points, since such distinction is not possible on a linear-linear scale owing the much larger CHF values of water. Note that most of the data predictions fall within a

10 percent uncertainty bracket for all conditions considered. Also note that predicted CHF values are more or less randomly distributed over the upper 10 percent and the lower 10 percent uncertainty bracket. This trend of no evident pattern for the errors of the predicted values confirms the assumption of homoscedasticity of the regression model.

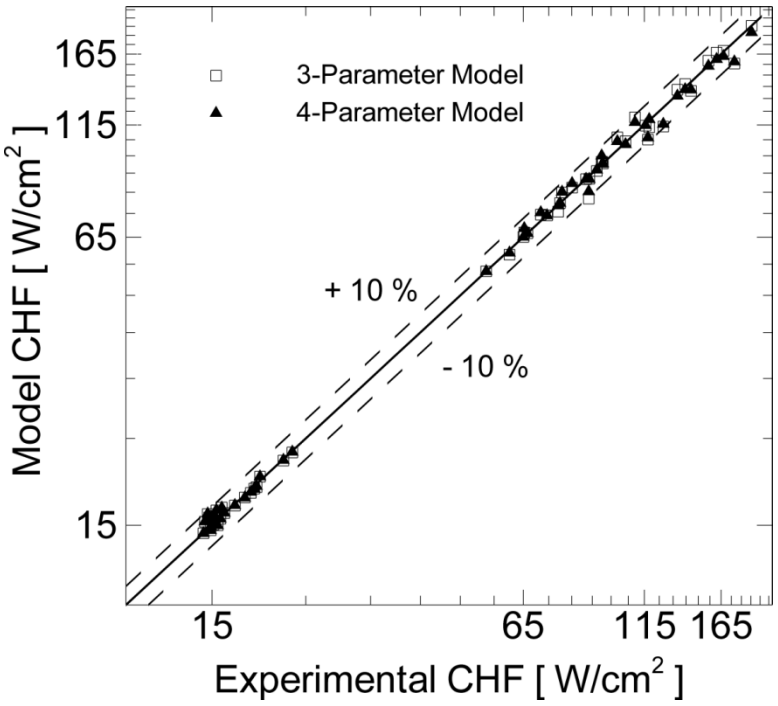

Figure 73: Summary of model comparison with experimental data on a log-log plot

Another approach to develop a model for the factor k in Eq.12 is to define a single variable composed of the interaction between the two equally important but different

physical properties which are present in each of the models above. Instead of explaining the lower enhancement ratios with either lower surface tension or lower density ratios, one can explain this result by the ratio between surface tension to vapor density (σ/ρ_v). Note that the enhancement ratios decreased as the ratio (σ/ρ_v) decreased since the variations of surface tension were inversely proportional to the variations in vapor density in the current data set. Therefore, one can combine the liquid-to-vapor density variable to the Bond number variable such that they work together by dividing the former by the later. Table 17 summarizes the results from the joint CHF correlation regression output. For brevity, the comparison of this joint model with the experimental data is shown in appendix6 of this document. The statistical significance of the joint model was equivalent to the three-parameter or the four-parameter model presented, and captured the entire data set with equivalent success (maximum error of 10.4 percent and average error of 2.6 percent).

Table 17: Joint jet impingement CHF correlation summary

CHF Model	$\frac{q''_{CHF,j}}{q''_{CHF,pool}} = (1+k)^{5/16}$			
k-factor model	$k = \kappa(\mathrm{Re})^{\beta_1}\left[\left(\frac{\rho_l}{\rho_v}\right)\left(\frac{\sigma}{g\{\rho_l-\rho_v\}d_j^2}\right)\right]^{\beta_2}(Ra)^{\beta_3}$			
Regression Output (R^2=0.92911)				
	κ [$m^{-\beta 3}$]	β_1	β_2	β_3
Coefficient	1.2592×10^{-5}	1.5987	0.23396	0.25197
P-value	0.000	0.000	0.000	0.0293

5.4.6 Effect of Subcooling on Submerged Jet Impingement CHF

The effect of fluid subcooling on submerged jet impingement CHF was investigated using water at the lowest pressure of 0.176 bar by maintaining the pool and jet temperatures at 17 ^{o}C below the fluid saturation temperature. The pool and jet temperatures were maintained at the same subcooling in order to ensure that thermal entrainment effects were negligible. CHF values for subcooled fluid temperatures are expected to be higher than for the saturated case, not only due to the additional

sensible heat available, but also due to the significantly smaller vapor bubbles observed in subcooled boiling conditions. Figure 74 shows the comparison between saturated and subcooled jet CHF with Re for water at the fixed pressure of 0.176 bar for a 33 nm Ra surface. As expected, for a fixed Re, CHF was consistently higher for the subcooled condition compared to the saturated case. Note that the general functional behavior of CHF with Re was nearly identical for both saturated and subcooled conditions. This result suggests that fluid subcooling does not significantly affect the Re dependency of CHF, but only shifts the data toward higher CHF values. Hence, the increase in subcooled jet CHF was compared to its saturated values using a subcooled pool boiling CHF correlation.

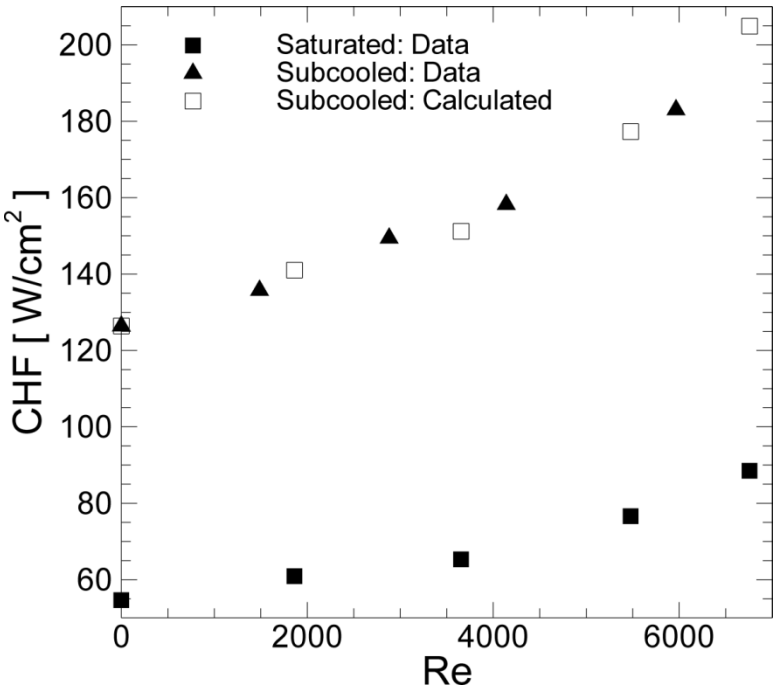

Figure 74: Effect of 17 ^{o}C fluid subcooling on submerged jet CHF for water on a 33 nm Ra surface for P=0.176 bar

The effect of fluid subcooling on pool boiling CHF has been previously investigated by several researchers [36] and correlations have been developed to relate subcooled pool boiling CHF to its corresponding saturated value. These types of correlations often include the degree of fluid subcooling using the non-dimensional Jakob number (Ja) which gives the ratio of sensible to latent heat absorbed during liquid-to-vapor phase-change. Figure 74 shows the estimated values for subcooled jet CHF based on saturated jet impingement data. The estimation was based on a subcooled pool boiling CHF correlation by Inoue et al. [36],

$$\frac{q''_{CHF,sub}}{q''_{CHF,sat}} = 1 + C_{sub}\left(\frac{\rho_l}{\rho_v}\right)^m Pe^n Ja \tag{19}$$

where

$$Pe = \frac{\sigma^{3/4}}{\alpha \rho_v^{1/2}\left[g\left(\rho_l - \rho_v\right)\right]^{1/4}} \tag{20}$$

Values of m and n in Eq.19 were taken to be -0.156 and -0.385 respectively based on Inoue et al [36]. A value for C_{sub} of 2.528 (as opposed to 3.318 in [36]) was found from the present experimental data on pool boiling, since data by Inoue et al. [36] were performed on a horizontal heater thin wire, as opposed to a high thermal capacity surface such as the one used in the present experiment. An excellent agreement is observed between trend of the estimated CHF for subcooled jet impingement and experimental data, confirming that one can use the same relations to extrapolate CHF

of jet impingement data from saturated to subcooled conditions as those used for pool boiling.

5.5 WATER: FREE SURFACE SUB-ATMOSPHERIC BOILING

The focus of the present study was to investigate the heat transfer characteristics of submerged jet impingement boiling. However, after seeing the poor agreement between the submerged jet impingement CHF data for water in particular with existing literature correlations presented in Section 5.4.4, it is natural to ask whether the jet configuration itself could have lead to this discrepancy. Although the free surface jet configuration was not within the original scope of this study, a few preliminary experiments were performed to better understand the effect of jet configuration in jet impingement boiling. Table 9 summarizes the experimental conditions considered. Experiments were performed for water at pressure of 0.176 bar and 0.276 bar on a 33 nm Ra surface.

5.5.1 FREE SURFACE JET IMPINGEMENT VISUALIZATION

The intent of using free surface jet impingement boiling may appear analogous to that of using submerged jet impingement boiling. However, major differences between these two jet configurations were seen through qualitative flow visualization. Figure

75 shows photographs of free surface jet impingement boiling for a system pressure of 0.176 bar and Re=10196. Note that blurry images for the boiling cases were caused by vapor condensation on the visualization window on the inside of the chamber. Figure 75(a) shows that at low heat fluxes, the surface was cooled by the single-phase liquid film which spread all throughout the surface providing that the jet flow rate was enough to completely wet the surface. As the heat flux was increased, boiling first occurred on the edges of the surface and began to expand to the rest of the surface with increasing heat fluxes. At moderate heat fluxes, as seen in Fig. 75(b), several liquid droplets were ejected upwards from the surface as the liquid film boiled and then fell back onto the surface. At relatively high heat fluxes, partial sections of the surface were observed to dry up periodically but were quickly re-wetted by the jet flow. Figure 75(c) shows that at critical heat flux conditions, the jet flow was completely splashed away from the surface near the stagnation region and most of the heat transfer surface became dry leading to very large and much sudden temperature excursions in comparison to the submerged jet configuration. Figure 75(c) was taken at the expense of burning the seal that made the surface vacuum tight and repairs were required.

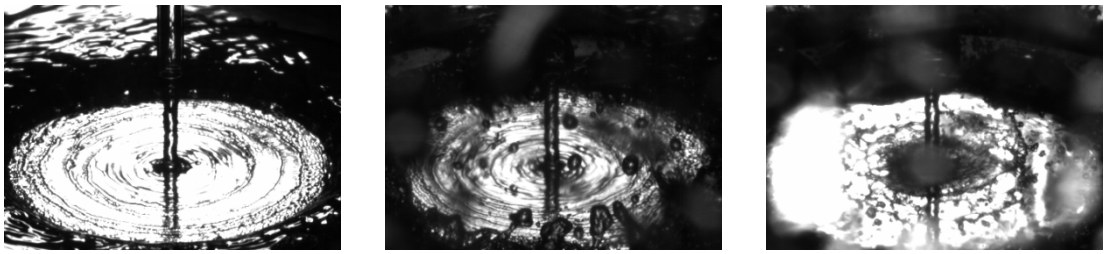

(a) q"=0 W/cm^2 (b) q"=53 W/cm^2 (c) q"= 130 W/cm^2 (CHF)

Figure 75: Free surface jet impingement visualization for P=0.176 bar and Re=10196

5.5.2 FREE SURFACE JET IMPINGEMENT BOILING

Figure 76 and Fig. 77 show free surface jet impingement boiling curves for saturated water at P=0.176 bar and P=0.276 bar respectively on a 33 nm Ra surface. The solid line on these plots provides the experimentally collected pool boiling data curve at the corresponding system pressure. For a system pressure of 0.276 bar, the lowest Re tested was 6078. Lower jet Re conditions could not be kept at saturated temperatures providing the limitation of the test facility under free surface jet impingement boiling. For Re < 1641, the jet flow could not properly wet the surface even under no heat flux conditions. Note from Fig. 76 that the two lower jet Re of 1641 and 3709 at the lowest system pressure of 0.176 bar reached similar CHF values which were much below pool boiling CHF. At these Re, visual observations indicated that as soon as the surface started to significantly boil, considerably large dry patches appeared on the surface which the jet could not rewet. These conditions led to a rising surface

temperature without improvements in heat flux, and thus were considered as the CHF limit for these low jet Re. As the Re was increased, better heat transfer performance was observed.

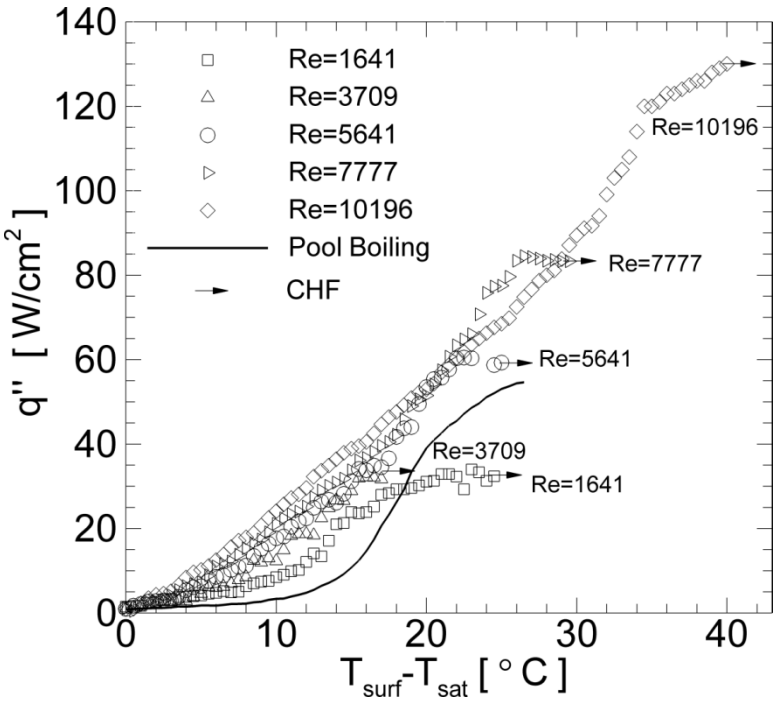

Figure 76: Free surface jet impingement boiling for saturated water at P=0.176 bar on a 33 nm Ra surface

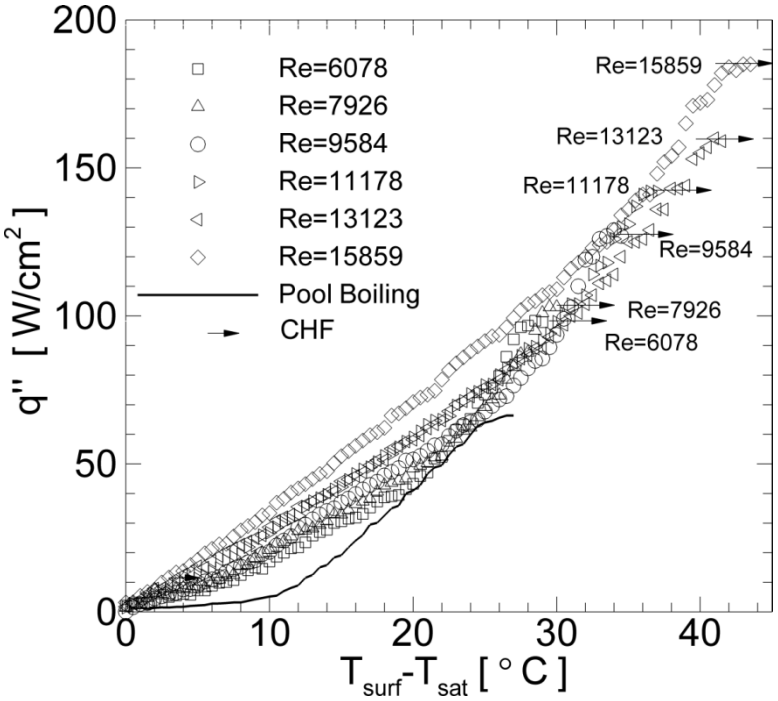

Figure 77: Free surface jet impingement boiling for saturated water at P=0.276 bar on a 33 nm Ra surface

Figure 76 and Fig. 77 indicate that large Re boiling curves for free surface jet impingement boiling look more like straight lines as opposed to the distinct "knee" of the boiling curve seen for submerged jet cases. At a fixed pressure, all free surface jet impingement boiling curves seem to also follow a common boiling asymptote which is roughly equivalent to the fully developed nucleate boiling asymptote established by the pool boiling curve. Also note from these figures that CHF conditions occurred at higher surface temperatures for the free surface jet configuration compared with pool boiling. However, surface temperatures at CHF in free surface jet impingement boiling were similar to those for the submerged jet configuration in the same Re range.

It is important to remember that in the present study, the surface temperature was measured at a center location just below the impingement region on the boiling surface. For the submerged jet configuration, other studies have reported that in the fully developed nucleate boiling region of the boiling curve, surface temperature becomes uniform and no significant differences in heat transfer rate are seen as a function of radial location [9]. However, this is not likely the case for the free surface jet configuration, since high-speed visualization indicated the periodic appearance and disappearance of dry patches on the surface which can lead to significant temperature gradients on the surface. At low Re, dry patches appeared on the surface even at low heat fluxes as a result of the insufficient supply of fluid by the jet flow to wet the surface. At high Re, dry patches appeared at elevated values of heat flux due to excessive boiling on the surface.

5.5.3 Free Surface Jet Impingement Boiling CHF

Figure 78 shows the free surface jet impingement CHF data in comparison to the submerged jet configuration. CHF trends with Re from the three-parameter submerged jet impingement correlation are also plotted for comparison. Unfortunately, the Re range of both data sets could not be kept equivalent since the submerged jet configuration was limited at high Re by the pump and the free surface jet configuration was limited at low Re by the inability to maintain the fluid at saturation

conditions and/or the surface fully wetted. Nevertheless, the data indicates that at low Re, the submerged jet CHF is higher than the free surface jet CHF. However, at a Re of about 8000, the CHF for both jet configurations is approximately equivalent. Note that for Re greater than about 8000, the data in Fig. 78 seem to indicate higher CHF values for the free surface configuration in comparison to the submerged configuration. However, insufficient data is available in this upper range of Re for the submerged jet configuration to make a clear distinction. Comparing the trend of CHF with Re for the free surface jet configuration, and the expected trend from extrapolation of the three-parameter model to higher Re, reveals that higher rates of increase in CHF with Re are observed in the free surface jet configuration. This trend may be associated in part by the continuing liquid droplets falling back onto the surface and enhancing heat transfer.

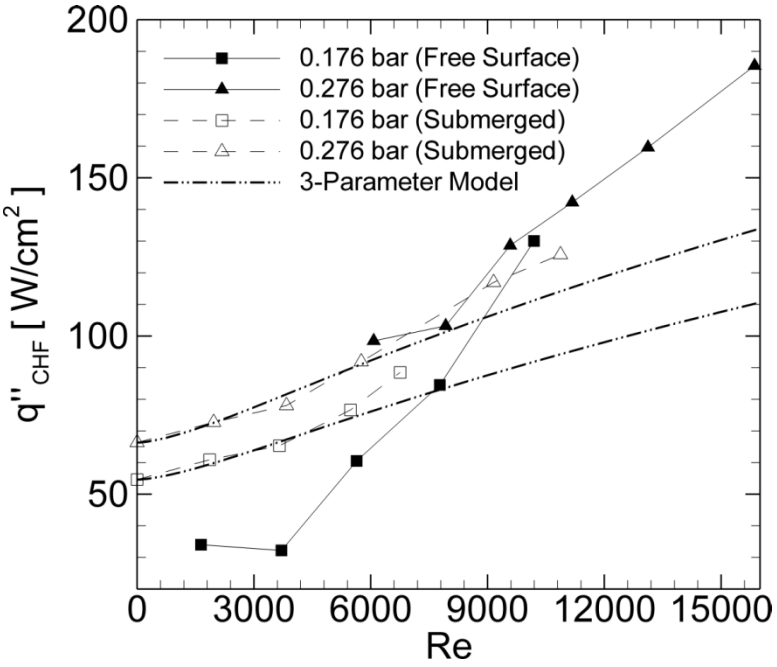

Figure 78: Free surface jet impingement CHF data in comparison the submerged jet configuration on a 33 nm Ra surface

Regardless of the higher CHF enhancements seen in Fig. 78 for the free surface jet configuration at large Re in comparison to the submerged jet configuration, it is reiterated once more that surface temperature and heat flux at elevated heat flux values may vary widely over the surface for the free surface jet configuration. High-speed imaging indicated that for large values of heat flux, sporadic dry patches appeared on the surface. This behavior continued until the heat flux was large enough to splash away all flow exiting the nozzle and leading to the globally determined CHF condition. Therefore, for high flux cooling applications, such as electronics cooling, where surface temperature uniformity is very important, single free surface jet impingement boiling is not recommended.

5.5.4 Comparison of Free Surface Jet CHF with Correlations

Figure 79 shows the comparison of free surface jet impingement CHF data for water with the CHF jet impingement correlations in Table 13, evaluated at the corresponding pressures. Note that while some correlations intersect the data, the general CHF trend with Re given by the data does not follow the trend predicted by the correlations over the Re range considered. This result, along with those of submerged jet data vs. literature correlations, indicate that the much larger liquid-to-vapor density ratios considered in this study for sub-atmospheric water testing, in comparison to the range covered by the correlations, played a significant role in the discrepancy observed not only of the correlations with the data, but also among the correlations themselves. This result is reasonable, since careful observation of the correlations given in Table 13 indicate that the liquid-to-vapor density ratio is an important parameter in most of these correlations.

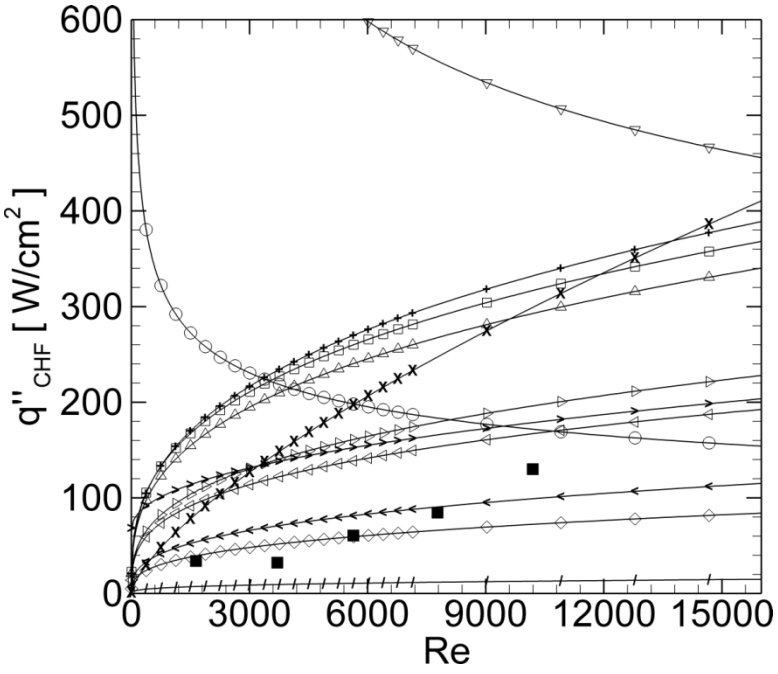

(a) P=0.176 bar

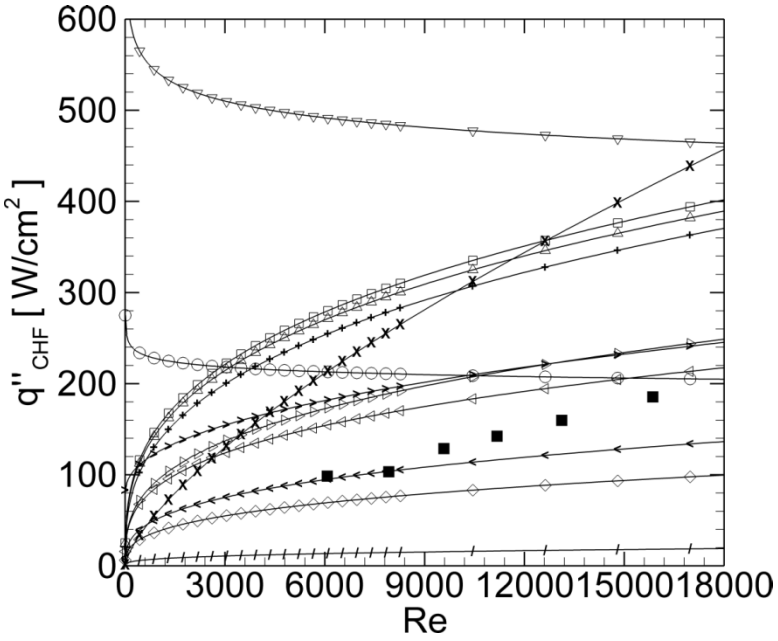

(b) P=0.276 bar

Figure 79: Comparison of water CHF free surface jet impingement data with correlations on a 33 nm Ra surface: □ C.1, △ C.2, ▽ C.3, ▷ C.4, ◁ C.5, ◇ C.6, ○ C.7, + C.8, x C.9, > C.10, < C.11, / C.12, ■ Experimental data

6 CONCLUSIONS AND FINAL REMARKS

This chapter summarizes the salient results of this study. A list of the major scientific and technological contributions is provided, followed by recommendations for future work.

6.1 SUMMARY

An experimental study characterizing submerged jet impingement boiling thermal management was presented. This work was inspired by the practical application of high power electronic devices that necessitate the removal of heat at elevated heat flux values while maintaining surface temperatures usually lower than 85 ^{o}C. Global heat transfer characteristics were determined by measuring bulk fluid temperatures, jet flow rate, and the axial temperature profile of the heated surface. Flow visualization was performed through high-speed imaging for qualitative flow comparison. Varied geometrical parameters included the surface roughness, the surface-to-nozzle diameter ratio, and the jet configuration. Varied fluidic parameters included pressure, jet exit Reynolds number, fluid subcooling, and fluid properties. Heat transfer characteristics were captured using boiling curves and critical heat flux limits.

Experiments were performed with two fluids having distinct thermo-physical properties, namely water and FC-72, on a fixed copper surface diameter of 27.64 mm

corresponding to a six square centimeters heat transfer area. The repeatability of the experimental results was tested under experimental repetition and replication and showed acceptable levels with CHF variations within six percent. For water, no boiling hysteresis was observed. However, a significant boiling curve hysteresis in terms of a temperature overshoot was detected for FC-72 owing its low surface tension. The boiling incipience wall superheat that led to a temperature overshoot varied randomly with varying experimental conditions and no statistically significant relationship was found between wall superheat at boiling incipience and jet parameters. A cumulative probability distribution function of boiling incipience varied almost linearly from zero percent at a wall superheat of about 14 ^{o}C to 100 percent at 31.5 ^{o}C wall superheat. The time required for nucleation to spread over the heated surface at boiling incipience decreased exponentially with increasing boiling incipience superheat temperatures. A novel passive means to prevent temperature overshoot in submerged jet impingement boiling using a self-cavitating jet was demonstrated.

Pool boiling curves for water under saturated conditions for all system pressures were found to agree well with the predictions from Rohsenow's fully developed nucleate boiling correlation using the recommended surface-fluid constant for water on polished copper. However, since an equivalent surface-fluid constant is not readily available for FC-72 on polished copper, a value for this constant based on the experimental data was suggested. Variations in pool boiling critical heat flux with varying system pressure and fluid properties were found to be properly predicted by

Kutateladze's pool boiling critical heat flux correlation, by using the leading constant recommended for a large horizontal surface. However, the data showed a statistically significant trend of larger CHF magnitudes on the 123 nm Ra surface in comparison to the 33 nm Ra surface owing the different wetting characteristics of these two surfaces. Appropriate modifications to the leading constant in this correlation were suggested which can be used to predict the entire pool boiling CHF values determined in this study with a maximum error of five percent and an average error of 2.3 percent.

For a fixed wall superheat in the single-phase region and in the partially developed nucleate boiling region, submerged jet impingement data showed consistent heat transfer enhancements through higher heat transfer rates with Re for both fluids. In the fully developed nucleate boiling region, jet impingement boiling curves roughly merged into a common boiling asymptote which can be approximated by extending the fully developed nucleate boiling region of a pool boiling curve to higher heat flux values. This observation, which has also been reported by several researchers, allows for the use of standard pool boiling correlations, such as Rohsenow's correlation, to estimate the heat transfer characteristics of a submerged impinging jet in the fully developed nucleate boiling region. For a fixed saturation temperature, much higher heat transfer rates were obtained using water than FC-72 over the entire wall superheat range. This result emphasizes the need for using deionized water for high flux thermal management.

A general trend of increase in jet impingement CHF with increasing Re was observed. For water, enhancements in CHF above the pool boiling CHF magnitude for a fixed Re were more significant at lower system pressures. This trend indicated that the benefit of using a submerged impinging jet is greater at lower pressures in comparison to higher pressures. For FC-72, at any fixed Re, higher CHF enhancements were recorded with smaller jet diameters. This trend indicated that enhancements in CHF are not only dependent on initial jet exit momentum, but also initial jet exit kinetic energy. A comparison between the two fluids showed that jet impingement CHF enhancements above pool boiling CHF were more significant for water than for FC-72. This trend suggested that submerged jet impingement enhancements in CHF above pool boiling CHF are dependent on fluid properties. Higher surface roughness was found to improve the benefits of submerged jet impingement boiling. Based on the experimental data, a non-dimensional jet impingement CHF map was developed to explain the heat transfer characteristics of submerged jet impingement boiling.

CHF trends with Re from 12 jet impingement CHF correlations available in literature were found to poorly agree with each other and with the experimental data for the test conditions considered, indicating a need of a proper predictive tool for submerged jet impingement boiling CHF. For this reason, a CHF model applicable to submerged convection boiling systems developed by Haramura and Katto [26] was used to form a predictive jet impingement CHF correlation. The correlation was developed taking into account all the varied parameters in the experimental data that were statistically significant to the variability of CHF by using standard model selection techniques

through multiple linear regression. Physically, it was determined that systems having larger bubble departure diameters benefited more from the jet flow at CHF conditions. Statistically, two different models were found to properly predict the CHF data with equivalent significance. Using either of these models, the entire jet impingement boiling CHF data set was predicted with a maximum error of less than 10.6 percent and an average error of less than 2.6 percent. An important advantage of using Haramura and Katto CHF model is that the correlation converges to pool boiling CHF at zero Re.

Fluid subcooling caused a leftward shift in the boiling curve leading to enhanced heat transfer performance in comparison to the saturated case. Critical heat flux was found to significantly increase with increasing fluid subcooling for pool and jet impingement boiling. Trends of CHF with Re for subcooled conditions were found to be well predicted from the analogous saturated trends by using a subcooled pool boiling CHF correction. This is an advantageous finding since corrections for subcooled pool boiling CHF, in terms of a Jakob number, are readily available in literature for a wide range of conditions. Therefore, for submerged subcooled jet impingement CHF predictions, one can use the jet impingement CHF correlations developed in this study for the saturated case together with a subcooled pool boiling CHF correction.

Preliminary free surface jet impingement data was collected to compare its heat transfer characteristics against submerged jet impingement boiling. At low Re, the CHF for a free surface jet was lower than for the submerged jet configuration. At large

Re, higher CHF values seemed possible for the free surface jet configuration in comparison to the submerged jet configuration. However, the practicality of using free surface jet impingement boiling for temperature sensitive applications is questionable since high-speed imaging showed periodic dry patches on the heated surface prior to reaching a global CHF condition over the entire surface.

6.2 MAJOR CONTRIBUTIONS

The major scientific and technological contributions unique to this study are listed below:

→Characterization of the effect of varying sub-atmospheric pressures on submerged jet impingement boiling of water

→Comparison of the boiling heat transfer capabilities of water and FC-72 at an equivalent fluid saturation temperature

→Introduction of a CHF map for submerged jet impingement boiling

→Development of a general CHF correlation for submerged jet impingement boiling

→Demonstration of a passive means to mitigate temperature overshoot for highly wetting fluids using a self-cavitating jet

6.3 FUTURE WORK

Continued work is required to expand upon the work presented in this dissertation to further understand and improve the heat transfer characteristics of submerged jet impingement boiling. Boiling curves were in general independent of jet parameters in the fully developed nucleate boiling region. However, small consistent shifts in this region of the boiling curve were seen with varying jet diameters for FC-72. This result needs to be investigated further using a broader range of jet diameters. In addition, to incorporate the effect of bubble size, which could be a determining factor in these observations, experiments with varying jet diameters using water are also needed.

Surface tension and liquid-to-vapor density ratio consistently varied in the same manner for the different experimental conditions considered. This trend made it difficult to distinguish between the effects of these quantities on CHF enhancement. A CHF jet impingement boiling experiment using water with a surfactant is needed to better distinguish between the effect of surface tension and density ratio on CHF enhancements with Re.

For a fixed Re, higher CHF values were obtained with smaller jet diameters for the range of jet diameters tested. However, recent preliminary data showed that this trend reverses as the jet diameter was decreased further. Additional investigation is needed to find the optimum surface-to-nozzle diameter ratio that maximizes CHF for a fixed

Re. Such a relationship could be used to optimize heat transfer rate while minimizing pumping power and system weight.

Significantly higher heat transfer rates and CHF limits were found for water in comparison to FC-72 for an equivalent fluid saturation temperature. Therefore, it would be worthwhile quantifying the heat transfer penalty associated with common thermal interface materials to be used in electronic cooling applications using water as the working fluid. For a fixed wall temperature, this analysis will reveal if there is a net gain in heat transfer rate by using indirect two-phase cooling with water in comparison to direct two-phase cooling with a dielectric fluid.

CHF trends with Re have been documented up to Re =14500. Additional experiments at Re > 14500 would be required to extend the results of this study into this higher Re range. These experiments can be performed with the current experimental facility with the addition of a new pump. All experiments in this study were conducted at a fixed surface-to-nozzle spacing of six jet diameters which is roughly the optimum spacing for average single-phase jet impingement heat transfer coefficient. Additional experiments are required to investigate the effect of surface-to-nozzle distance on submerged jet impingement boiling.

Preliminary CHF data for free surface jet impingement indicated possible higher CHF magnitudes in comparison to the submerged jet configuration at high Re. However, more experiments with the free surface jet configuration are required to fully understand the heat transfer characteristics of this jet configuration. Comparing local

surface temperature measurements between free surface and submerged jet impingement boiling using infrared thermography would reveal the potential benefits and limitations of these jet configurations for temperature sensitive heat transfer applications.

Although the use of a self-cavitating jet to prevent temperature overshoot was demonstrated, further work is needed to characterize the hydrodynamics of this phenomenon. If the self-cavitating action of the jet can be tuned with a resonance frequency of self-sustained jet oscillations, additional enhancements in heat transfer performance are expected and need to be explored.

BIBLIOGRAPHY

[1] Kandlikar, S., and Bapat, A., 2007, "Evaluation of Jet Impingement, Spray and Microchannel Chip Cooling Options for High Heat Flux Removal," Heat Transfer Engineering, 28(11), pp. 911-923.

[2] Bar-Cohen, A., and Geisler, K., 2011, "Cooling the Electronic Brain," ASME.

[3] Mudawar, I., 2001, "Assessment of High-Heat-Flux Thermal Management Schemes," Ieee Transactions on Components and Packaging Technologies, 24(2), pp. 122-141.

[4] Wolf, D. H., Incropera, F. P., and Viskanta, R., 1993, Advances in Heat Transfer, Elsevier.

[5] Incropera, F. P., 2007, Fundamentals of Heat and Mass Transfer, John Wiley, Hoboken, NJ.

[6] Carey, V. P., 2008, Liquid-Vapor Phase-Change Phenomena : An Introduction to the Thermophysics of Vaporization and Condensation Processes in Heat Transfer Equipment, Taylor and Francis, New York.

[7] Martin, H., 1977, Advances in Heat Transfer, Elsevier.

[8] Viskanta, R., 1993, "Heat-Transfer to Impinging Isothermal Gas and Flame Jets," Experimental Thermal and Fluid Science, 6(2), pp. 111-134.

[9] Wolf, D., Incropera, F., and Viskanta, R., 1996, "Local Jet Impingement Boiling Heat Transfer," International Journal of Heat and Mass Transfer, 39(7), pp. 1395-1406.

[10] Ma, C. F., and Bergles, A. E., 1986, "Jet Impingement Nucleate Boiling," International Journal of Heat and Mass Transfer, 29(8), pp. 1095-1101.

[11] Bergles, A. E., and Rohsenow, W. M., 1964, "The Determination of Forced-Convection Surface-Boiling Heat Transfer," Journal Name: Journal of Heat Transfer (U.S.); Journal Volume: Vol: 86; Other Information: Orig. Receipt Date: 31-DEC-65, pp. Medium: X; Size: Pages: 365-72.

[12] Zhou, D. W., Ma, C. F., and Yu, J., 2004, "Boiling Hysteresis of Impinging Circular Submerged Jets with Highly Wetting Liquids," International Journal of Heat and Fluid Flow, 25(1), pp. 81-90.

[13] You, S., Simon, T., Bar-Cohen, A., and Tong, W., 1990, "Experimental Investigation of Nucleate Boiling Incipience with a Highly-Wetting Dielectric Fluid (R-113)," International Journal of Heat and Mass Transfer, 33(1), pp. 105-117.

[14] Liu, Z., and Qiu, Y., 2006, "Critical Heat Flux of Steady Boiling for Water Jet Impingement in Flat Stagnation Zone on Superhydrophilic Surface," Journal of Heat Transfer-Transactions of the Asme, 128(7), pp. 726-729.

[15] Qiu, Y., and Liu, Z., 2008, "Nucleate Boiling on the Superhydrophilic Surface with a Small Water Impingement Jet," International Journal of Heat and Mass Transfer, 51(7-8), pp. 1683-1690.

[16] Liu, Z., and Zhu, Q., 2002, "Prediction of Critical Heat Flux for Convective Boiling of Saturated Water Jet Impinging on the Stagnation Zone," Journal of Heat Transfer-Transactions of the Asme, 124(6), pp. 1125-1130.

[17] Liu, Z., Tong, T., and Qiu, Y., 2004, "Critical Heat Flux of Steady Boiling for Subcooled Water Jet Impingement on the Flat Stagnation Zone," Journal of Heat Transfer-Transactions of the Asme, 126(2), pp. 179-183.

[18] Dukle, N. M., and Hollingsworth, D. K., 1996, "Liquid Crystal Images of the Transition from Jet Impingement Convection to Nucleate Boiling Part I: Monotonic Distribution of the Convection Coefficient," Experimental Thermal and Fluid Science, 12(3), pp. 274-287.

[19] Nakayama, W., Behnia, M., and Mishima, H., 2000, "Impinging Jet Boiling of a Fluorinert Liquid on a Foil Heater Array," Journal of Electronic Packaging, 122(2), pp. 132-137.

[20] Dukle, N. M., and Hollingsworth, D. K., 1996, "Liquid Crystal Images of the Transition from Jet Impingement Convection to Nucleate Boiling Part Ii: Nonmonotonic Distribution of the Convection Coefficient," Experimental Thermal and Fluid Science, 12(3), pp. 288-297.

[21] Qiu, Y., and Liu, Z., 2005, "Critical Heat Flux of Steady Boiling for Saturated Liquids Jet Impinging on the Stagnation Zone," International Journal of Heat and Mass Transfer, 48(21-22), pp. 4590-4597.

[22] Zhou, D., and Ma, C., 2004, "Local Jet Impingement Boiling Heat Transfer with R113," Heat and Mass Transfer, 40(6-7), pp. 539-549.

[23] Katto, Y., and Kunihiro, M., 1973, "Study of the Mechanism of Burn-out in Boiling System of High Burn-out Heat Flux," Bull. Jap. Soc. Mech. Engrs, 16(pp. 1357-1366.

[24] Monde, M., and Katto, Y., 1978, "Burnout in a High Heat-Flux Boiling System with an Impinging Jet," International Journal of Heat and Mass Transfer, 21(3), pp. 295-305.

[25] Tillery, S., Heffington, S., Smith, M., and Glezer, A., 2006, "Boiling Heat Transfer Enhancement Using, a Submerged, Vibration-Induced Jet," Journal of Electronic Packaging, 128(2), pp. 145-149.

[26] Haramura, Y., and Katto, Y., 1983, "A New Hydrodynamic Model of Critical Heat-Flux, Applicable Widely to Both Pool and Forced-Convection Boiling on Submerged Bodies in Saturated Liquids," International Journal of Heat and Mass Transfer, 26(3), pp. 389-399.

[27] Gambill, W., and Lienhard, J., 1989, "An Upper Bound for the Critical Boiling Heat Flux," Journal of Heat Transfer-Transactions of the Asme, 111(1-4), pp. 815-818.

[28] Mitsutake, Y., and Monde, M., 2003, "Ultra High Critical Heat Flux During Forced Flow Boiling Heat Transfer with an Impinging Jet," Journal of Heat Transfer-Transactions of the Asme, 125(6), pp. 1038-1045.

[29] Katto, Y., and Shimizu, M., 1979, "Upper Limit of Chf in the Saturated Forced-Convection Boiling on a Heated Disk with a Small Impinging Jet," Journal of Heat Transfer-Transactions of the Asme, 101(2), pp. 265-269.

[30] Monde, M., 1985, "Critical Heat Flux in Saturated Force Convective Boiling on a Heated Disk with an Impinging Jet," Wärme- und Stoffübertragung, 19(pp. 205-209.

[31] Lienhard, J., and Hasan, M., 1979, "Correlation of Burnout Data for Disk Heaters Cooled by Liquid Jets," Journal of Heat Transfer-Transactions of the Asme, 101(2), pp. 383-384.

[32] Katto, Y., 1985, Advances in Heat Transfer, Orland, Chap. CHF in External Flow under Other Conditions.

[33] Sharan, A., and Lienhard, J., 1985, "On Predicting Burnout in the Jet-Disk Configuration," Journal of Heat Transfer-Transactions of the Asme, 107(2), pp. 398-401.

[34] Katto, Y., and Yokoya, S., 1988, "Critical Heat-Flux on a Disk Heater Cooled by a Circular Jet of Saturated Liquid Impinging at the Center," International Journal of Heat and Mass Transfer, 31(2), pp. 219-227.

[35] Mudawar, I., and Wadsworth, D., 1991, "Critical Heat-Flux from a Simulated Chip to a Confined Rectangular Impinging Jet of Dielectric Liquid," International Journal of Heat and Mass Transfer, 34(6), pp. 1465-1479.

[36] Inoue, T., Kawae, N., and Monde, M., 1998, "Effect of Subcooling on Critical Heat Flux During Pool Boiling on a Horizontal Heated Wire," Heat and Mass Transfer, 33(5-6), pp. 481-488.

[37] Monde, M., 1980, "Burnout Heat Flux in Saturated Forced Convection Boiling with an Impinging Jet," Heat Transfer-Japanese Research, 9(pp. 31-41.

[38] Han, C.-Y., and Griffith, P., 1965, "The Mechanism of Heat Transfer in Nucleate Pool Boiling - Part I," International Journal Heat Mass Transfer, 8(pp. 887-904.

[39] Asme, 1995, "Surface Texture, Surface Roughness Waviness and Lay."

[40] Jones, B., Mchale, J., and Garimella, S., 2009, "The Influence of Surface Roughness on Nucleate Pool Boiling Heat Transfer," Journal of Heat Transfer-Transactions of the Asme, 131(12), pp. -.

[41] Kandlikar, S. G., 2001, "A Theoretical Model to Predict Pool Boiling Chf Incorporating Effects of Contact Angle and Orientation," Journal of Heat Transfer-Transactions of the Asme, 123(6), pp. 1071-1079.

[42] You, S. M., Barcohen, A., and Simon, T. W., 1990, "Boiling Incipience and Nucleate Boiling Heat-Transfer of Highly Wetting Dielectric Fluids from Electronic Materials," Ieee Transactions on Components Hybrids and Manufacturing Technology, 13(4), pp. 1032-1039.

[43] Klein, S., A., 2010, "Engineering Equation Solver," F-Chart Software.

[44] 3m, 2000, "Fluorinert Electronic Liquid Fc-72," 3M Specialty Materials.

[45] Moffat, R., 1988, "Describing the Uncertainties in Experimental Results," Experimental Thermal and Fluid Science, 1(1), pp. 3-17.

[46] Cleveland, W., and Devlin, S., 1988, "Locally Weighted Regression - an Approach to Regression-Analysis by Local Fitting," Journal of the American Statistical Association, 83(403), pp. 596-610.

[47] Schlax, M., and Chelton, D., 1992, "Frequency-Domain Diagnostics for Linear Smoothers," Journal of the American Statistical Association, 87(420), pp. 1070-1081.

[48] Kutateladze, S. S., 1948, "On the Transition to Film Boiling under Natural Convection," Kotloturbostroenie, 3(pp. 10-12.

[49] Zuber, N., 1959, "Hydrodynamic Aspects of Boiling Heat Transfer," University of California, Los Angeles.

[50] Reed, S. J., and Mudawar, I., 1999, "Elimination of Boiling Incipience Temperature Drop in Highly Wetting Fluids Using Spherical Contact with a Flat Surface," International Journal of Heat and Mass Transfer, 42(13), pp. 2439-2454.

[51] Bergles, A. E., and Kim, C. J., 1988, "A Method to Reduce Temperature Overshoots in Immersion Cooling of Microelectronic Devices," Proc. Thermal Phenomena in the Fabrication and Operation of Electronic Components: I-THERM '88, InterSociety Conference on, pp. 100-105.

[52] Bhavnani, S. H., Balch, S. E., and Jaeger, R. C., 1999, "Control of Incipience Hysteresis Effects in Liquid Cooled Electronics Heat Sinks," Journal of Electronics Manufacturing, 9(2), pp. 179-190.

[53] Normington, P. J. C., Mahalingam, M., and Lee, T. Y. T., 1992, "Thermal Management Control without Overshoot Using Combinations of Boiling Liquids," Components, Hybrids, and Manufacturing Technology, IEEE Transactions on, 15(5), pp. 806-814.

[54] Hasan, M. A. Z., and Hussain, A. K. M. F., 1979, A Formula for Resonance Frequencies of a Whistler Nozzle, ASA.

[55] Rainey, K. N., and You, S. M., 2001, "Effects of Heater Size and Orientation on Pool Boiling Heat Transfer from Microporous Coated Surfaces," International Journal of Heat and Mass Transfer, 44(14), pp. 2589-2599.

[56] Rainey, K. N., You, S. M., and Lee, S., 2003, "Effect of Pressure, Subcooling, and Dissolved Gas on Pool Boiling Heat Transfer from Microporous, Square Pin-Finned Surfaces in Fc-72," International Journal of Heat and Mass Transfer, 46(1), pp. 23-35.

[57] Pagano, M., and Gauvreau, K., 2000, Principles of Biostatistics, Duxbury, Australia ; Pacific Grove, CA.

[58] Chemical Rubber Company., 2004, Handbook of Chemistry and Physics, CRC Press, Cleveland, Ohio.

APPENDICES

APPENDIX

1. PROPERTIES OF SELECTED FLUIDS

Table A 1: Thermo-Physical properties of selected fluids at 1 atm

	Water	**FC-40**	**FC-43**	**FC-72**	**FC-77**	**FC-84**	**FC-87**	**PF-5052/ L12378**	**R113**	**R11**
T_{sat} [˚C]	100[A]	155[C]	174[C]	56.6[C]	97[C]	80[C]	30[C,2]	50[C]	47.61[E]	23.83
ρ_l [kg/m^3]	998.2[A,1]	1870[C,2]	1880[C,2]	1680[C,2]	1780[C,2]	1730[C,2]	1650[C,2]	1700[C,2]	1561[E,2]	1488[E,1]
ρ_v [kg/m^3]	0.5956[B,3,*]	26.37[C]	27.68[c]	13.43[D,*]	16.63[C]	15.92[C]	13.65[D]	11.98[D,*]	7.456[E,*]	5.867
μ_l [mg/m-s]	1.002[A,1]	4.114[C,2]	5.264[C,2]	0.672[C,2]	1.424[C,2]	0.9515[C,2]	0.45[C,2]	0.68[C,2]	0.6966[E,2]	0.418[E,1]
$C_{p,l}$ [J/kg-K]	4181.8[A,1]	1046[C,2]	1046[C,2]	1046[C,2]	1046[C,2]	1046[C,2]	1100[C]	1050[C,2]	913.7[E,2]	864.9[E,1]
h_{lv} [kJ/kg]	2256.806[A]	71.128[C]	71.128[C]	87.864[C]	83.680[C]	79.496[C]	103[C]	105[C]	144.43[E]	180.29[E]
k_l [W/m-k]	0.5984[A,1]	0.066[C,2]	0.066[C,2]	0.057[C,2]	0.063[C,2]	0.060[C,2]	0.056[C]	0.062[C,2]	0.07474	0.08946
σ [mN/m]	72.75[A,1]	16[C,2]	16[C,2]	12[C,2]	15[C,2]	13[C,2]	9[C]	13[C,2]	17.5	26.3
Dielectric Strength [kV/mm]	67-70[A]	18.1[C]	16.5[C]	14.96[C]	15.75[C]	16.535[C]	18.9[C]	----	----	----
Dielectric Constant	80.20[A,1]	1.89[C,+]	1.90[C,+]	1.76[C,+]	1.86[C,+]	1.81[C,+]	1.73[C]	----	----	----
Vapor Pressure [kPa]	2.3388[A,1]	0.4[C,2]	0.1733[C,2]	30.931[C,2]	5.6[C,2]	10.53[C,2]	81.1[C,2]	36.4[C,2]	----	----
$q''_{CHF,pool,sat}$ [W/cm^2]	134[4]	23[4]	23[4]	21[4]	22[4]	20[4]	20[4]	21[4]	24[4]	29[4]

A. Ref. [58]
B. Ref. [5]
C. Ref. [44]
D. Ref. [3]
E. Ref. [43]

1. Evaluated at 20 ˚C
2. Evaluated at 25 ˚C
3. Evaluated at 100 ˚C
4. Eq. 9

* Saturated Condition
\+ At 1 kHz

APPENDIX:

2. O-RINGS AND FASTENERS

Table A 2: O-ring location, type, and material

O-ring Location	AS568A Dash No.	Material	
		O-ring	Backup Ring
Top Plate	277	Viton	Buna-N
Inner Reservoir Bottom	224	Viton	N/A
Inner Reservoir Top Inside	29	Viton	N/A
Inner Reservoir Top Outside	37	Viton	N/A
Bottom Plate	156	Viton	Buna-N
Windows	159	Viton	Buna-N
Heated Copper Section	25	Silicon	N/A

Table A 3: List of screw fasteners used

Location	Type	Length [in]	Material
Top Plate	1/4-20	1	Stainless Steel
Inner Reservoir	10-32	3/4	Stainless Steel
Windows	1/4-20	3/4	Stainless Steel
Bottom Plate	1/4-20	1-1/8	Stainless Steel

APPENDIX:

3. DETAILED PART DRAWINGS

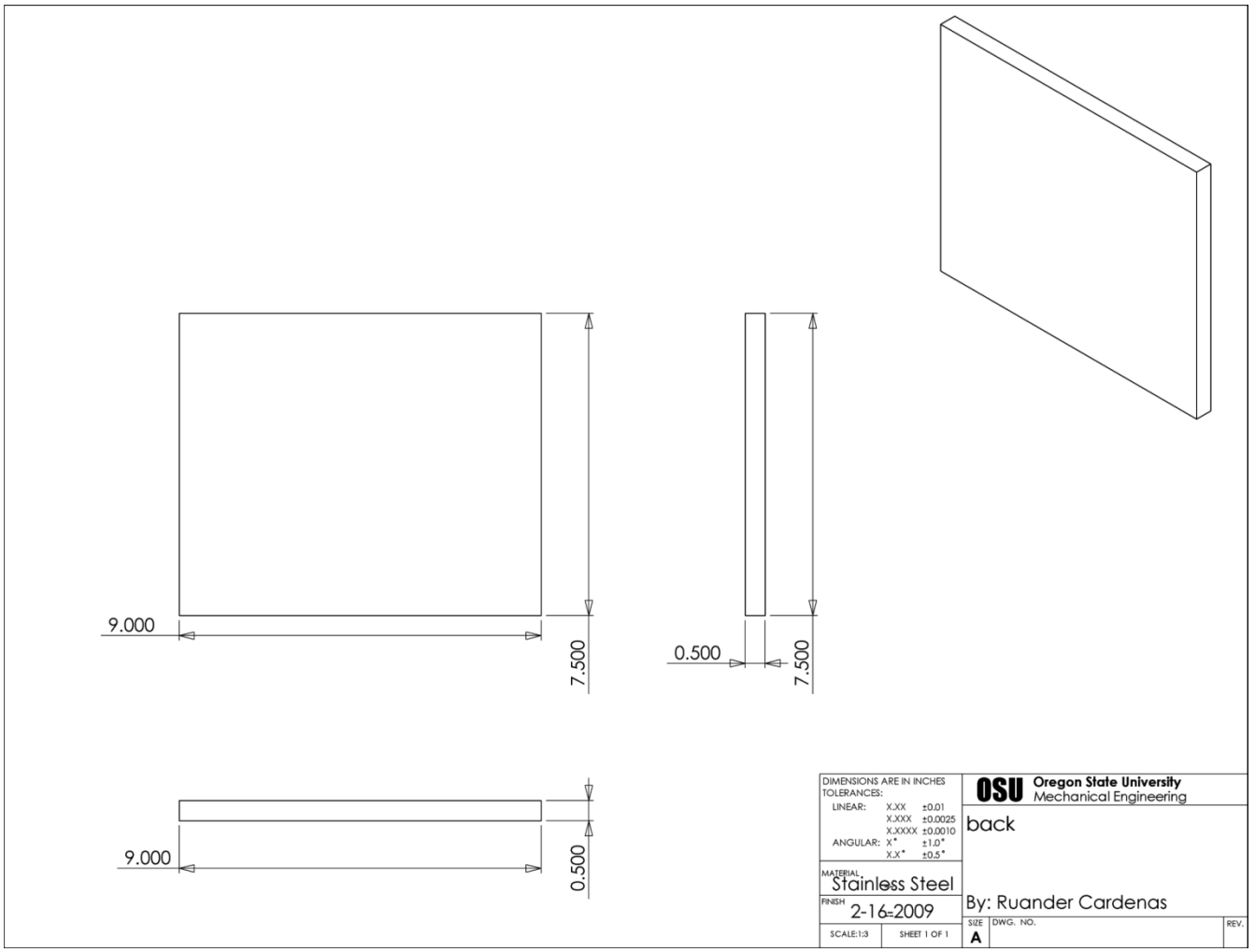

Figure A 1: Test chamber back wall

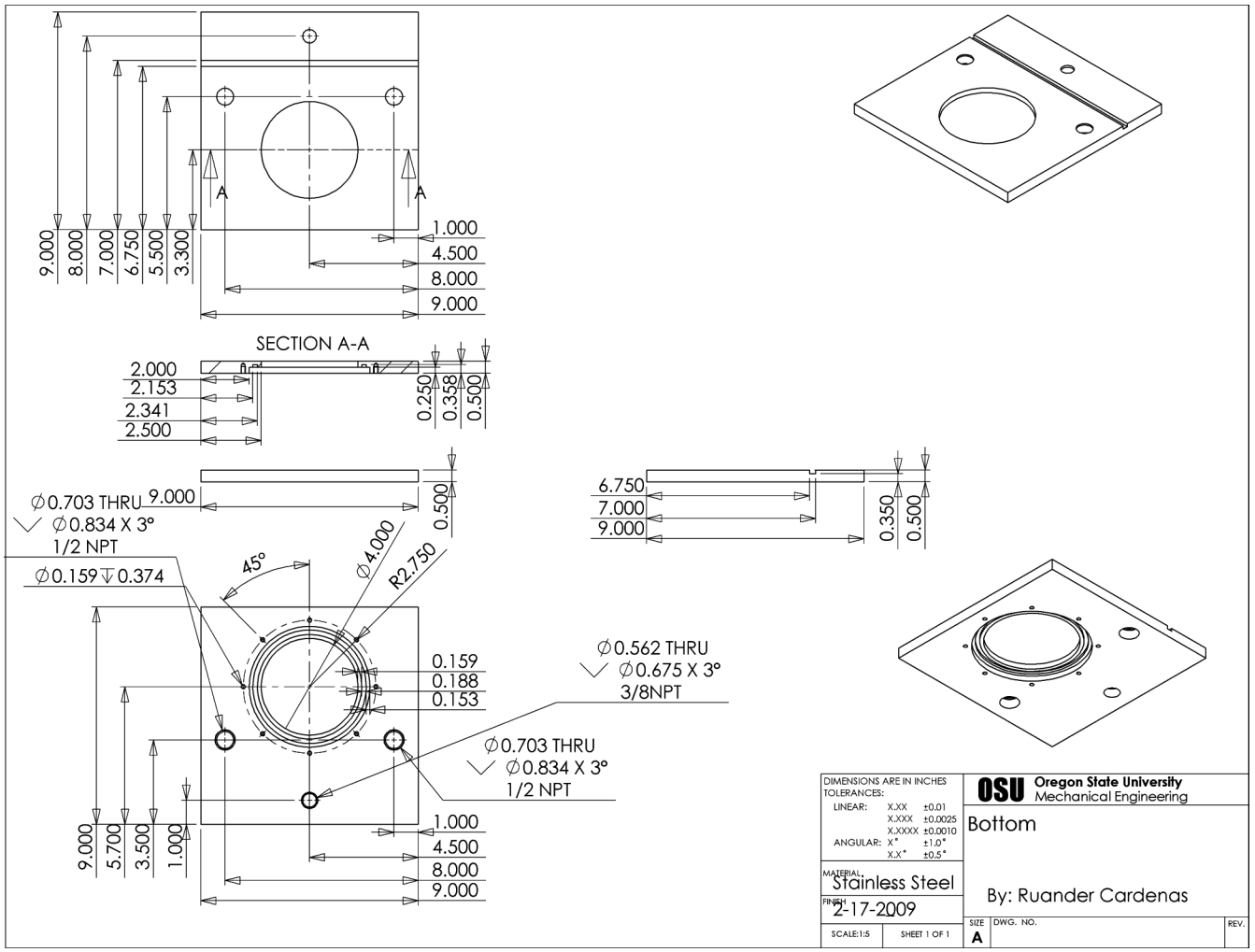

Figure A 2: Test chamber bottom wall

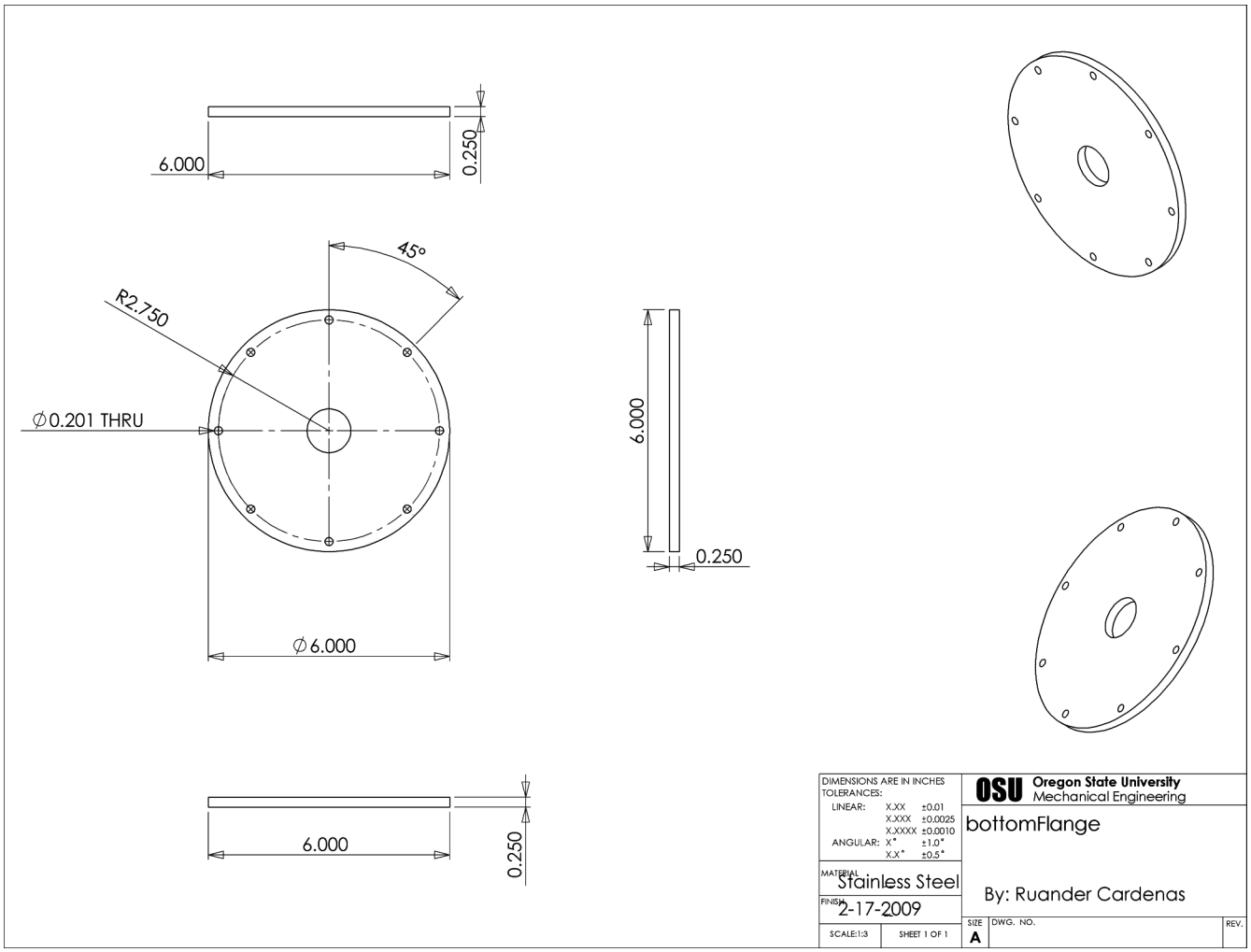

Figure A 3: Test section metal flange

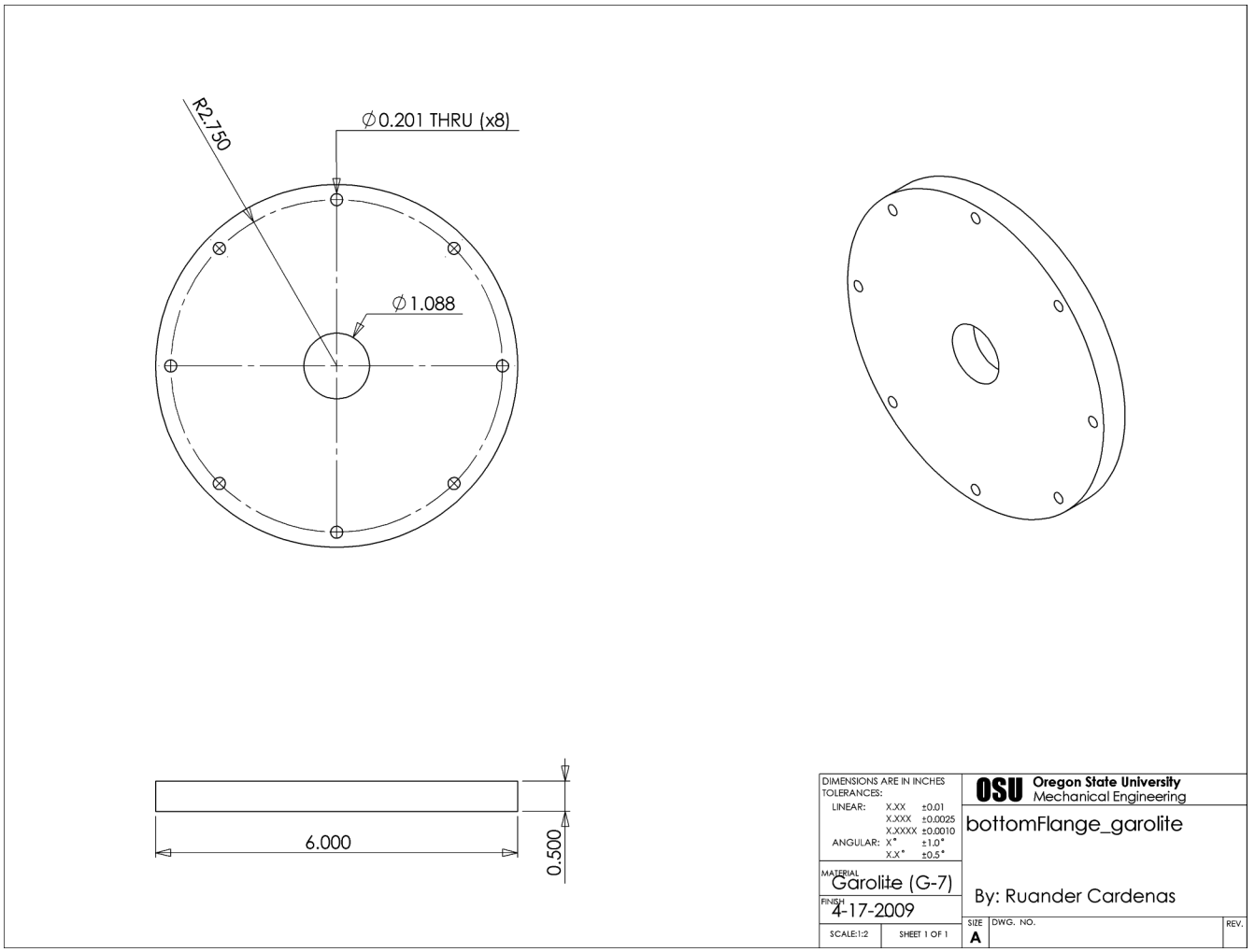

Figure A 4: Test section Garolite flange

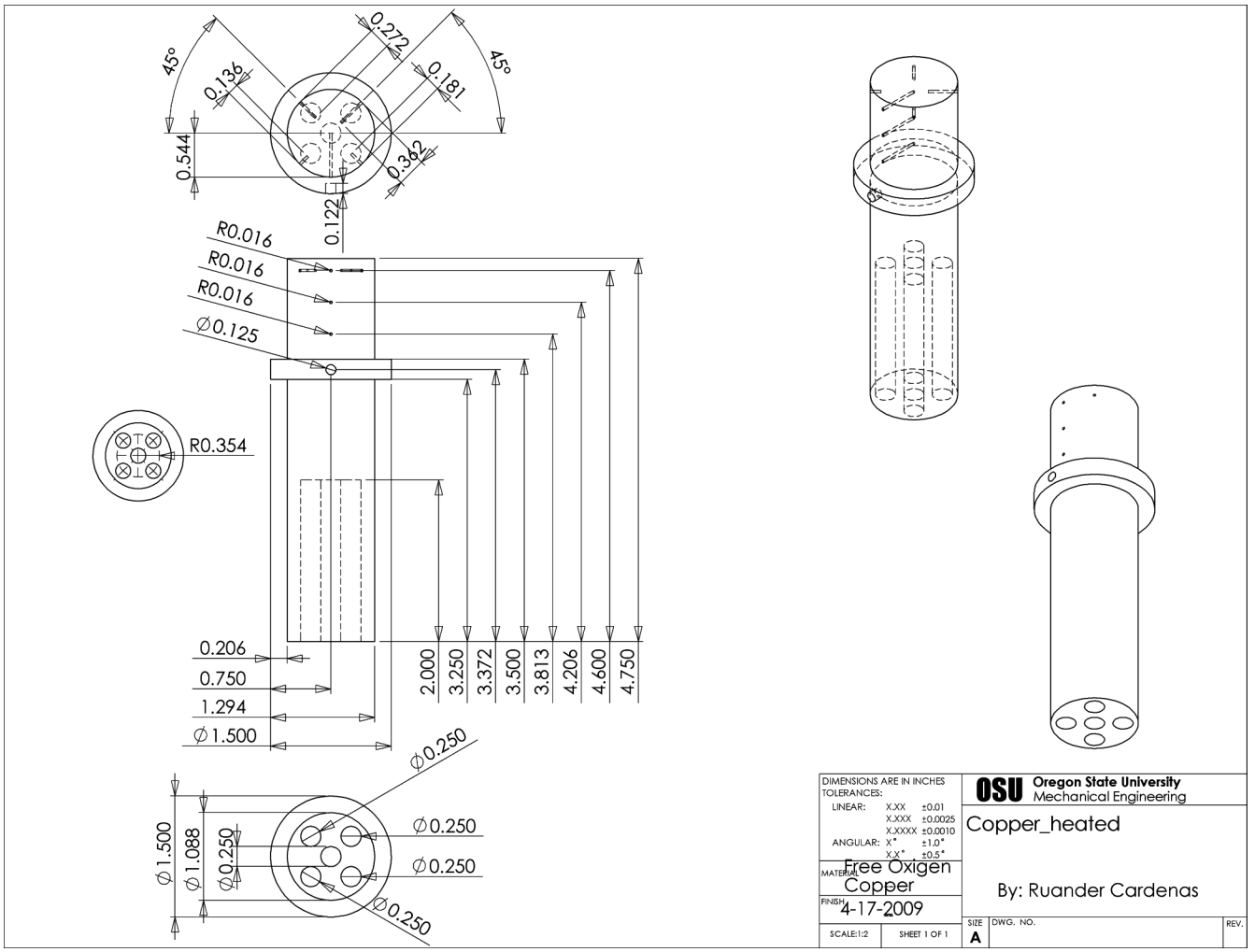

Figure A 5: Copper test section

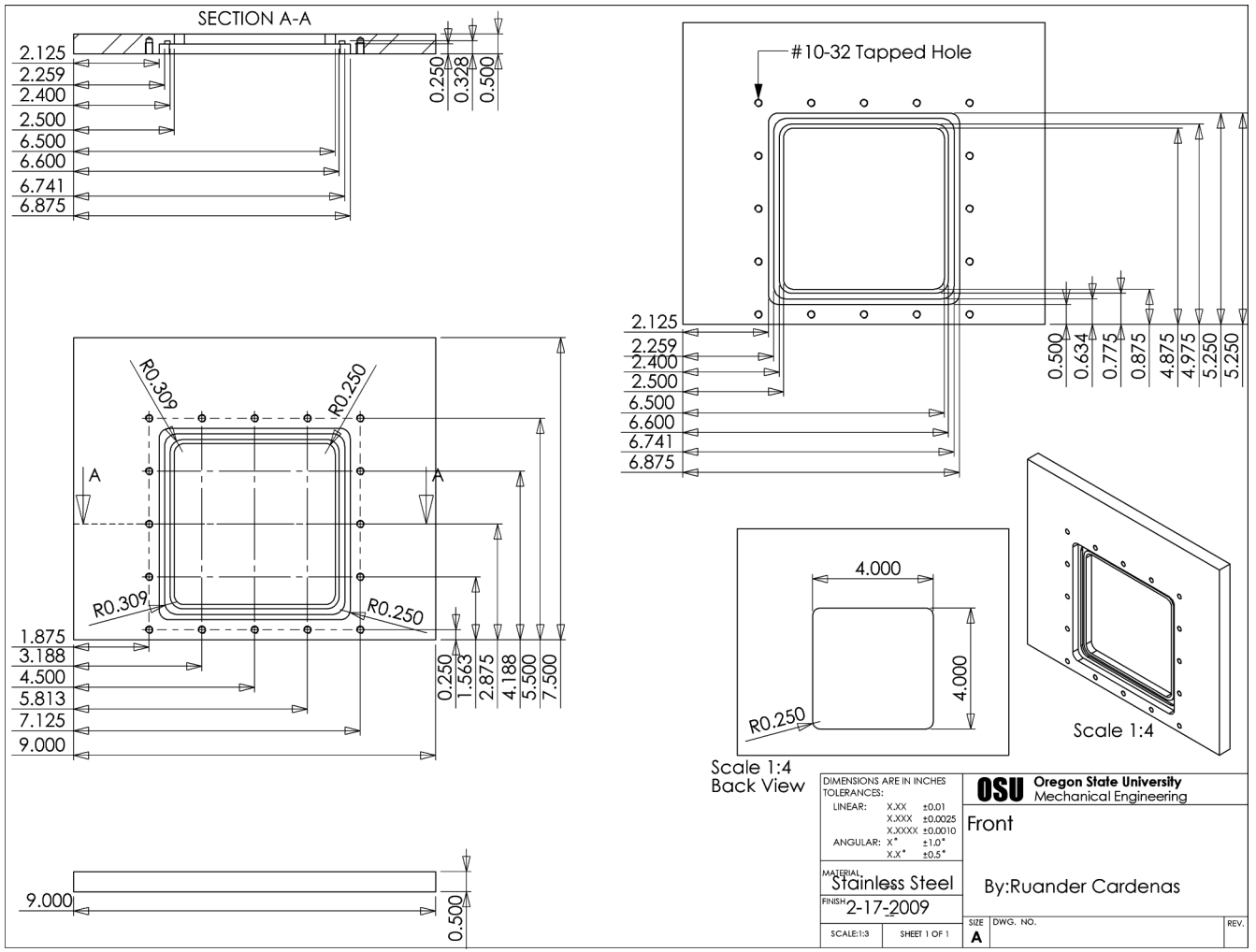

Figure A 6: Test chamber front wall

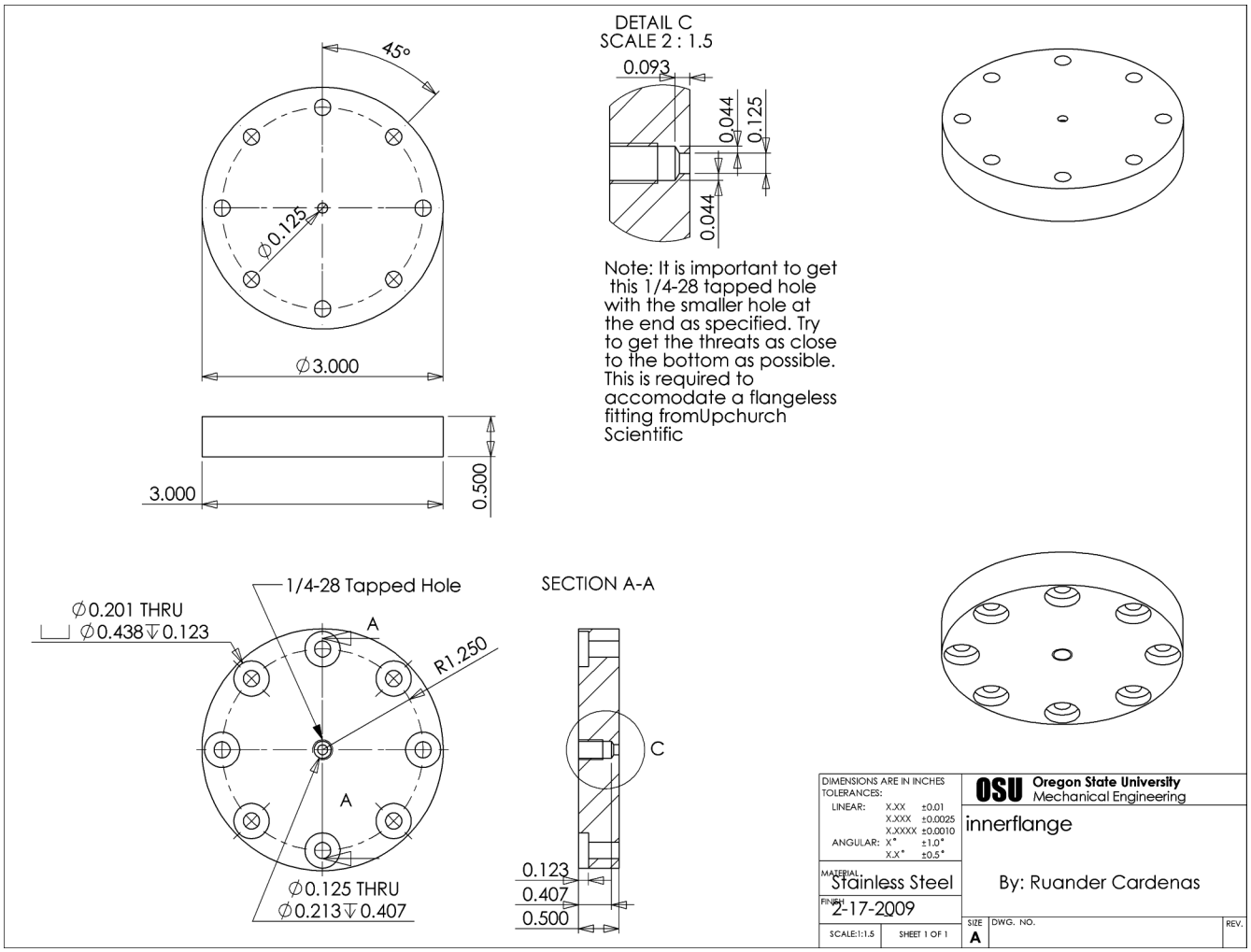

Figure A 7: Inner reservoir bottom attachment for 1/4-28 Upchurch fitting

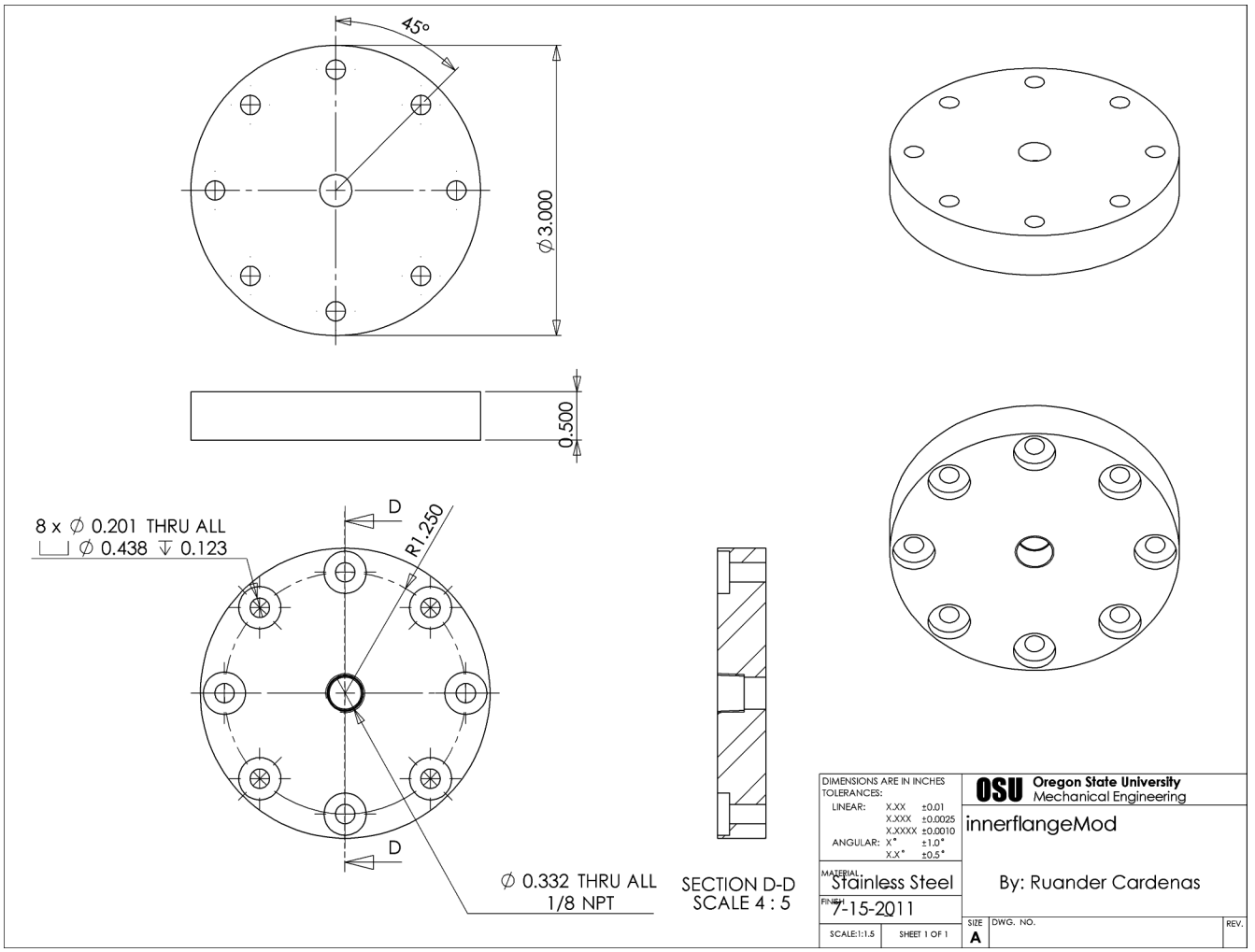

Figure A 8: Inner reservoir bottom attachment for standard 1/8 NPT fitting

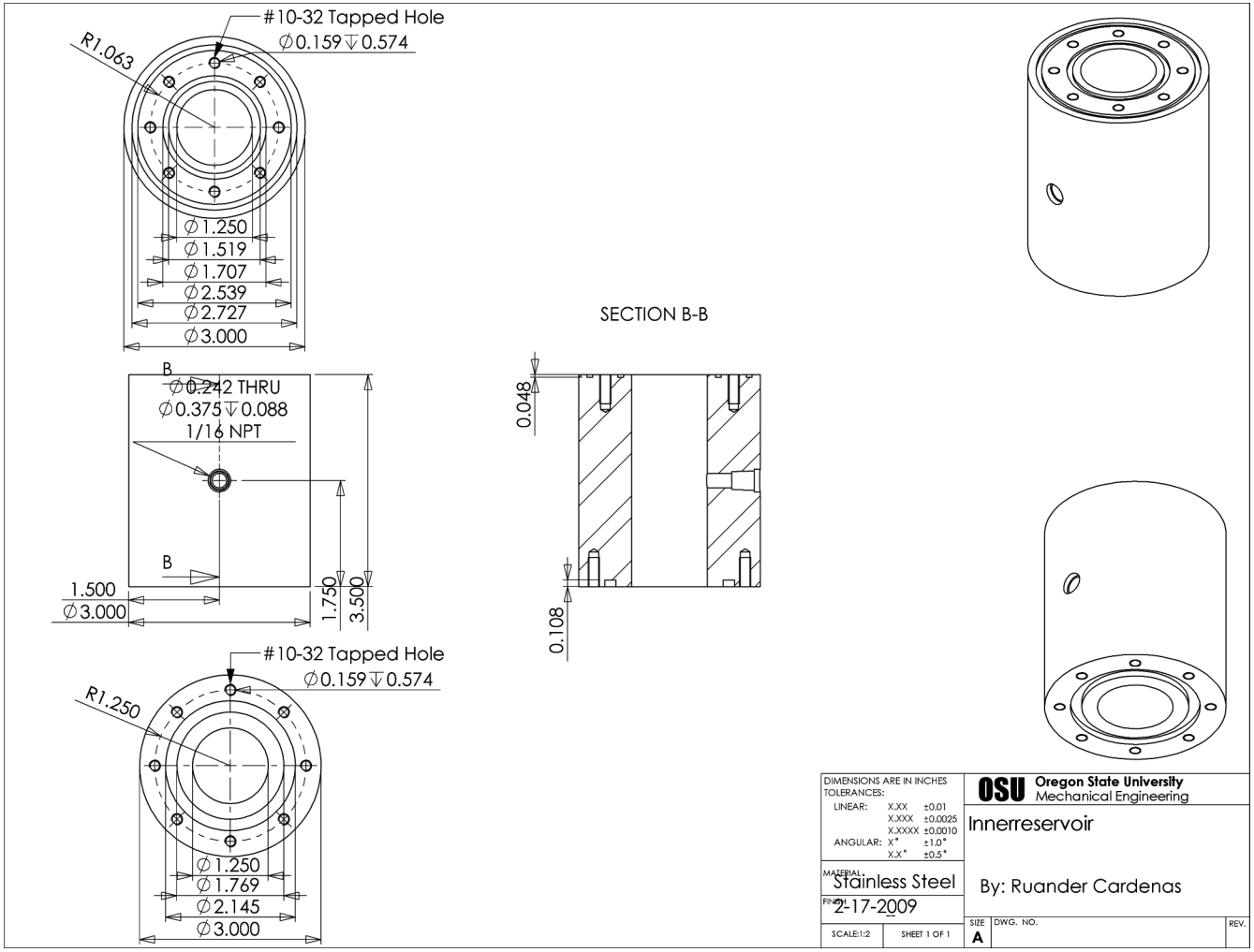

Figure A 9: Test chamber inner jet reservoir

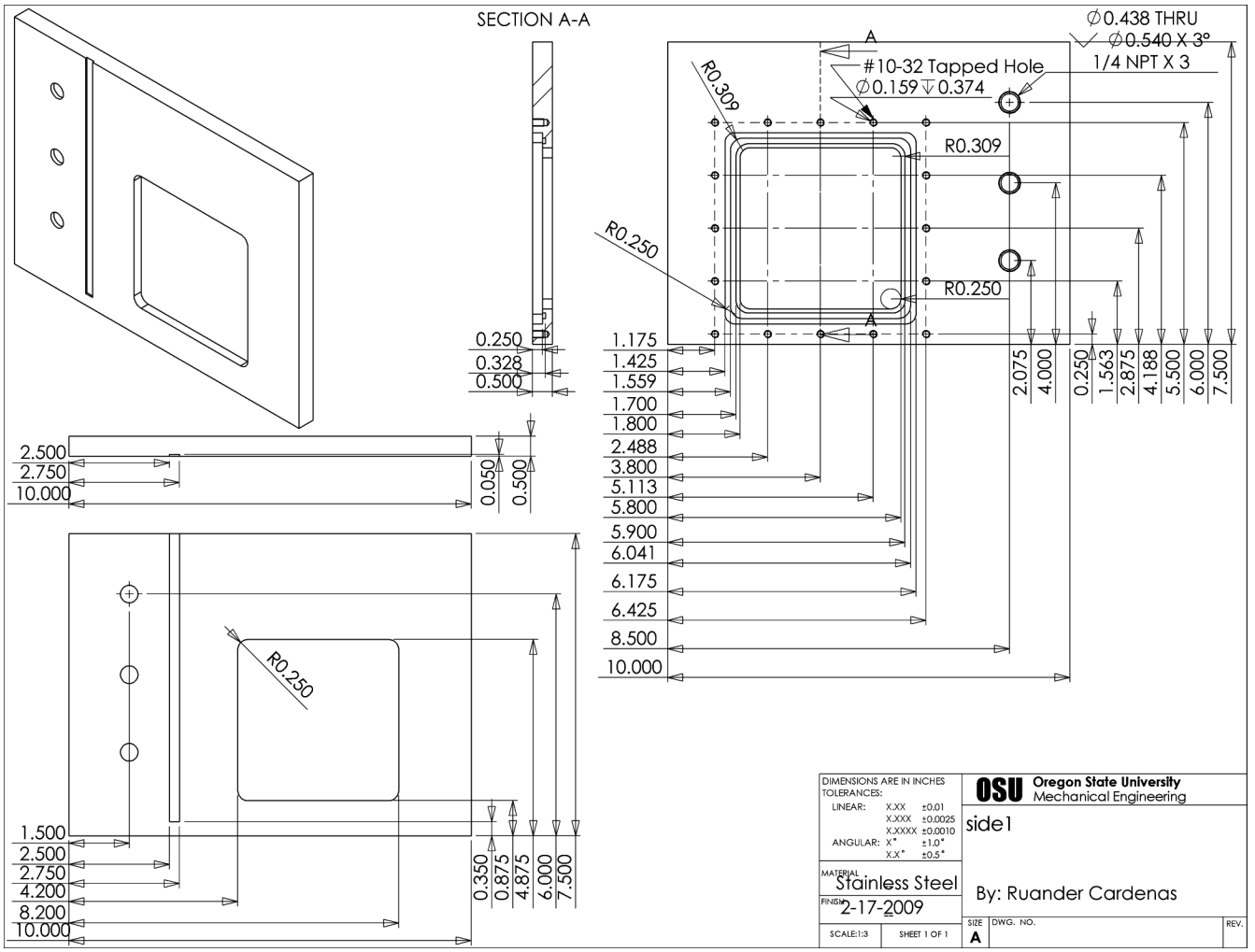

Figure A 10: Test chamber left wall

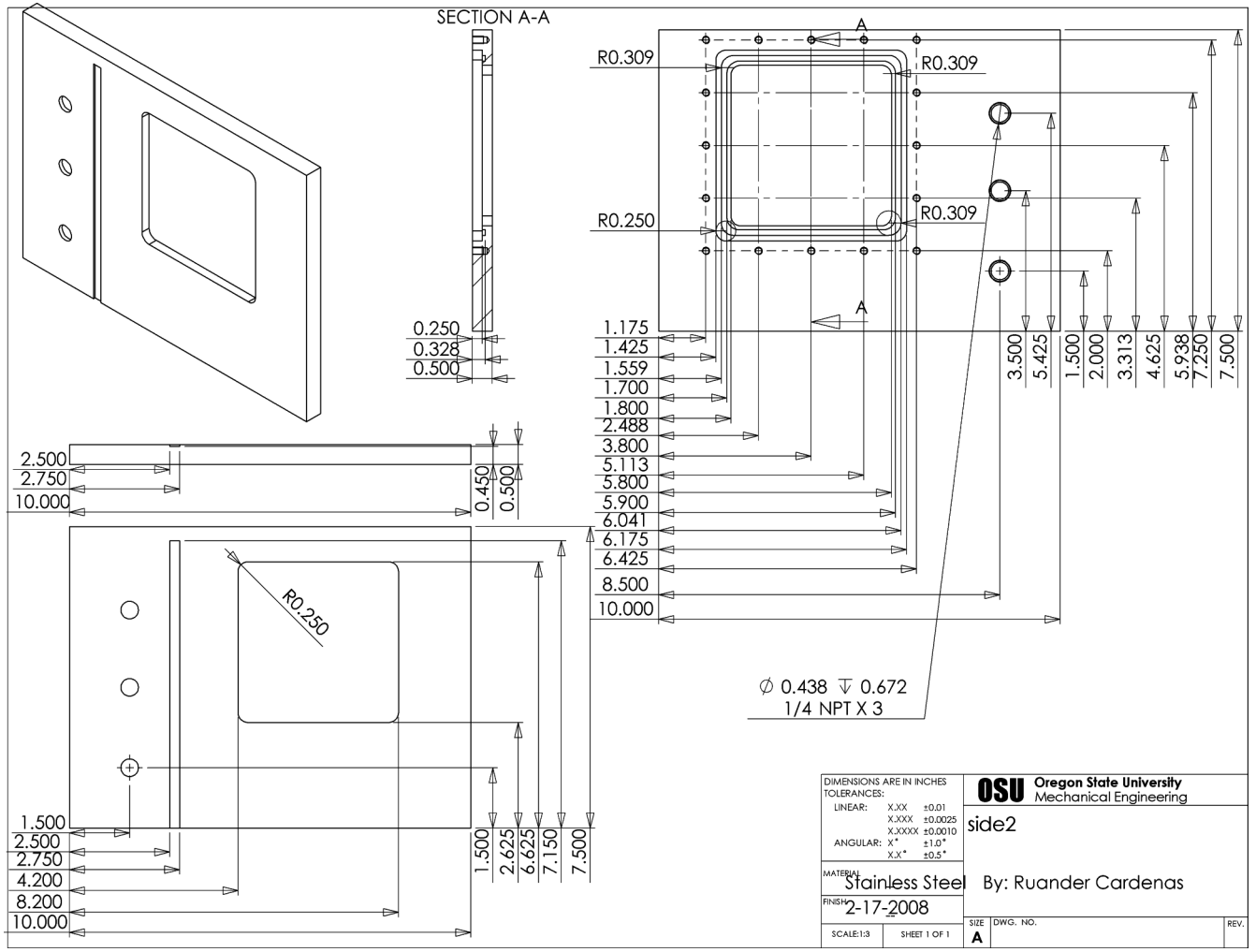

Figure A 11: Test chamber right wall

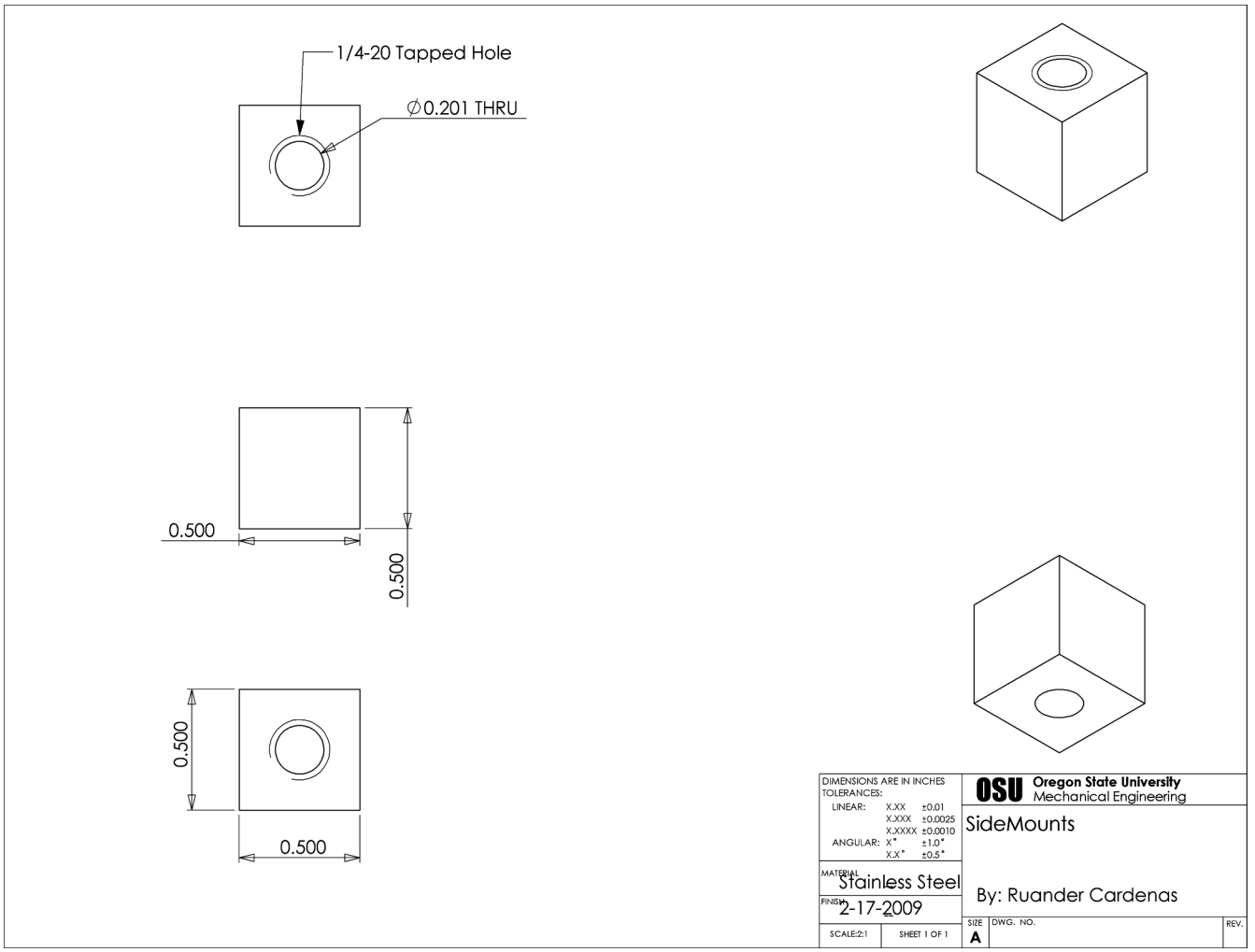

Figure A 12: Test chamber side mounts for top chamber plate

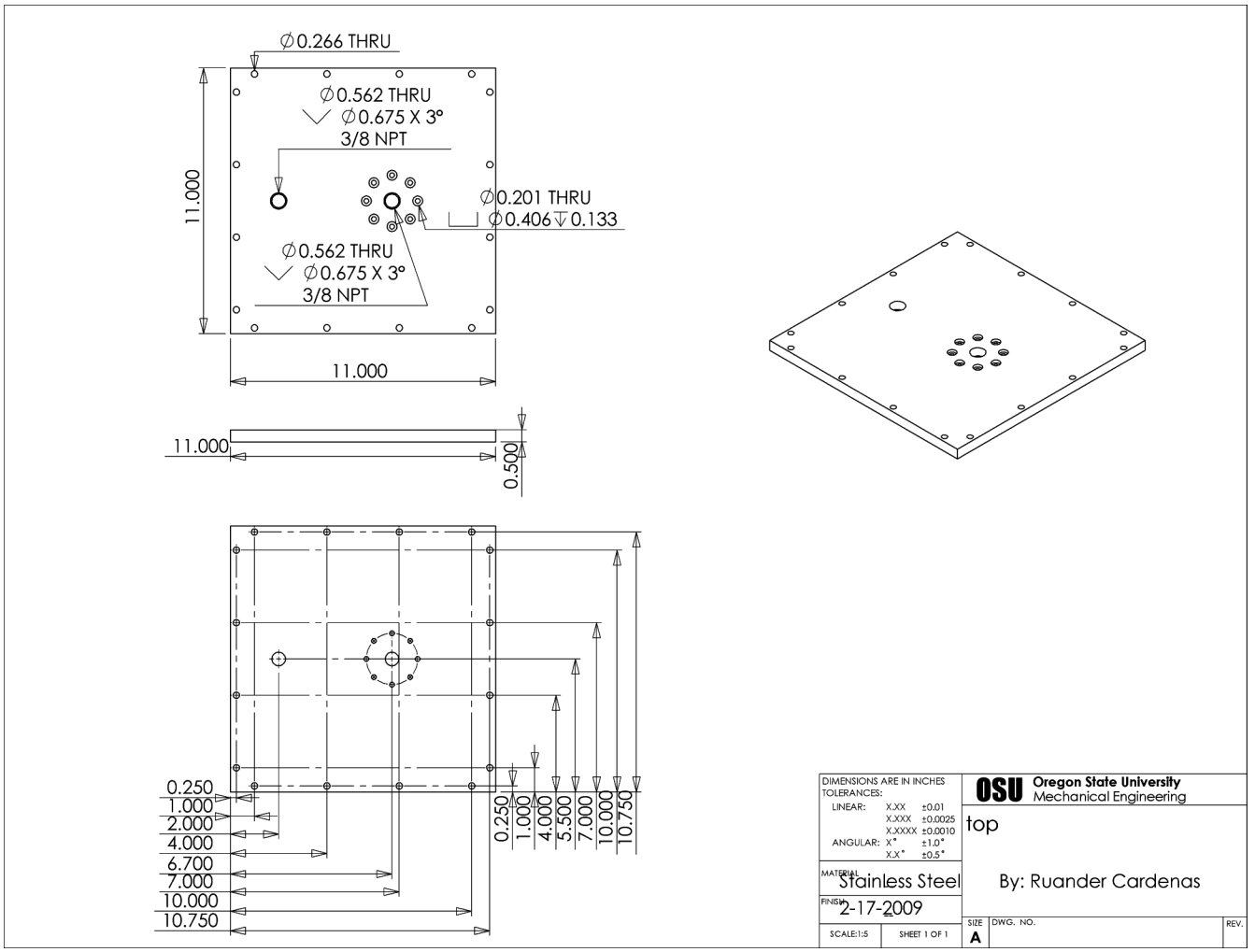

Figure A 13: Test chamber top plate

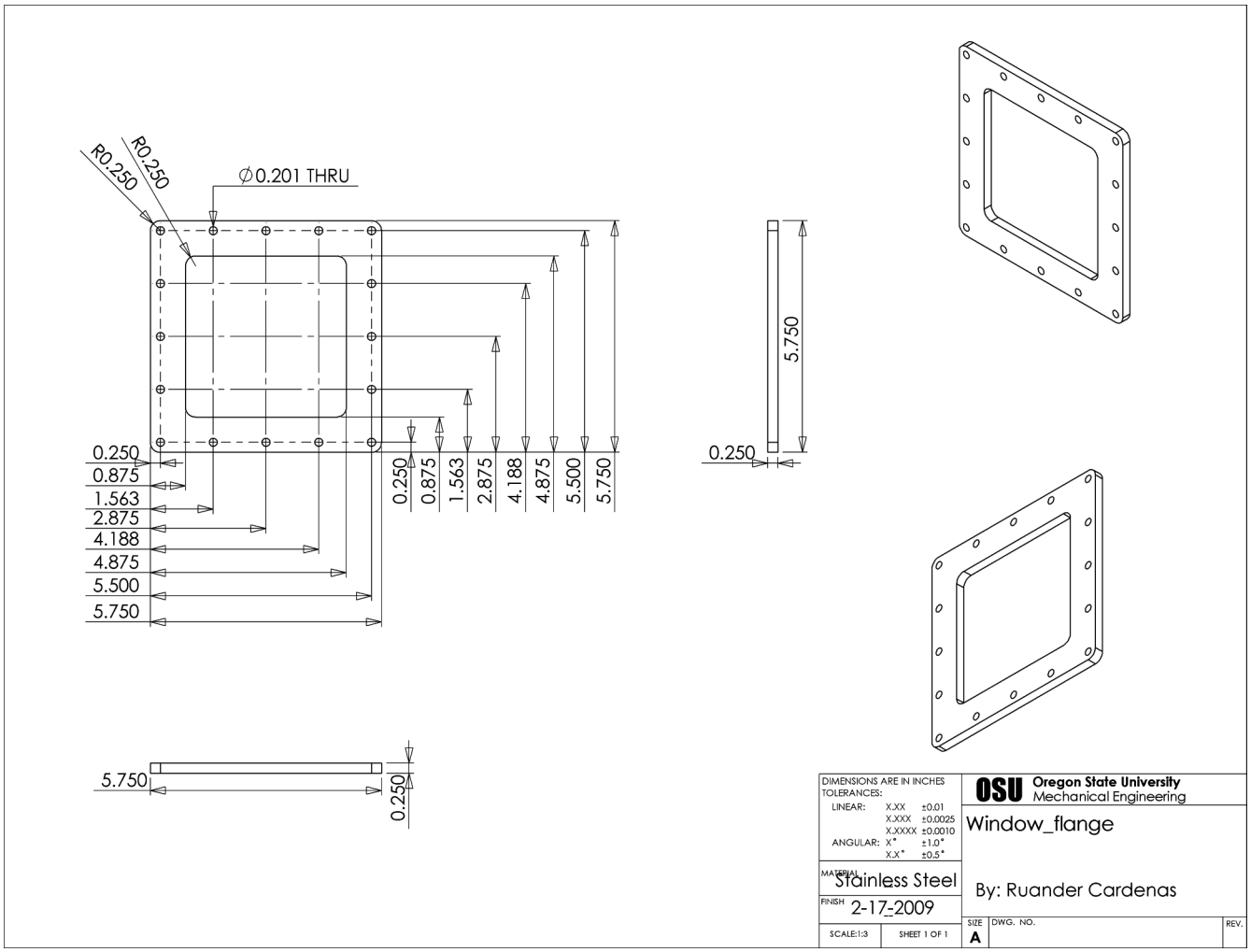

Figure A 14: Window flange

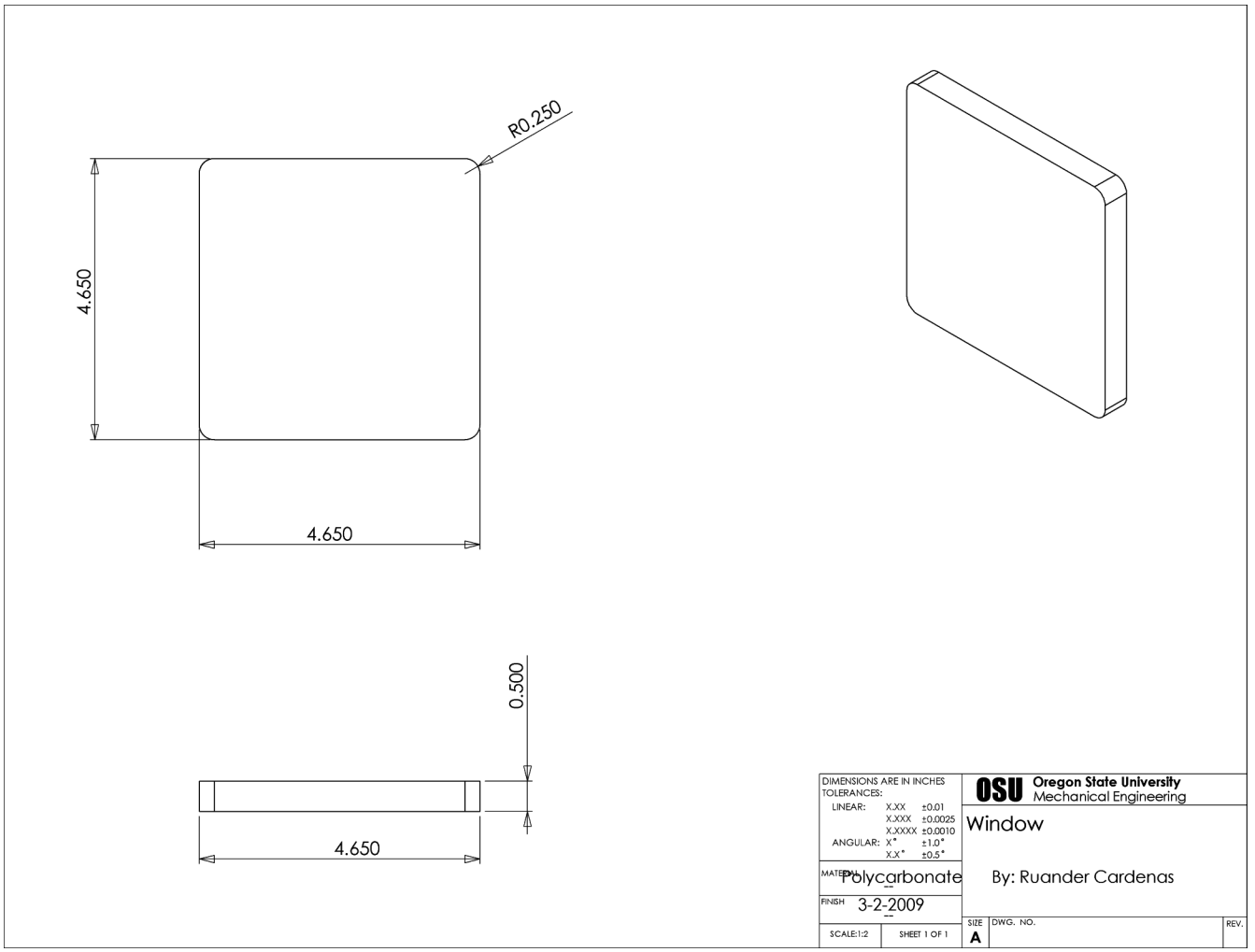

Figure A 15: Test chamber windows

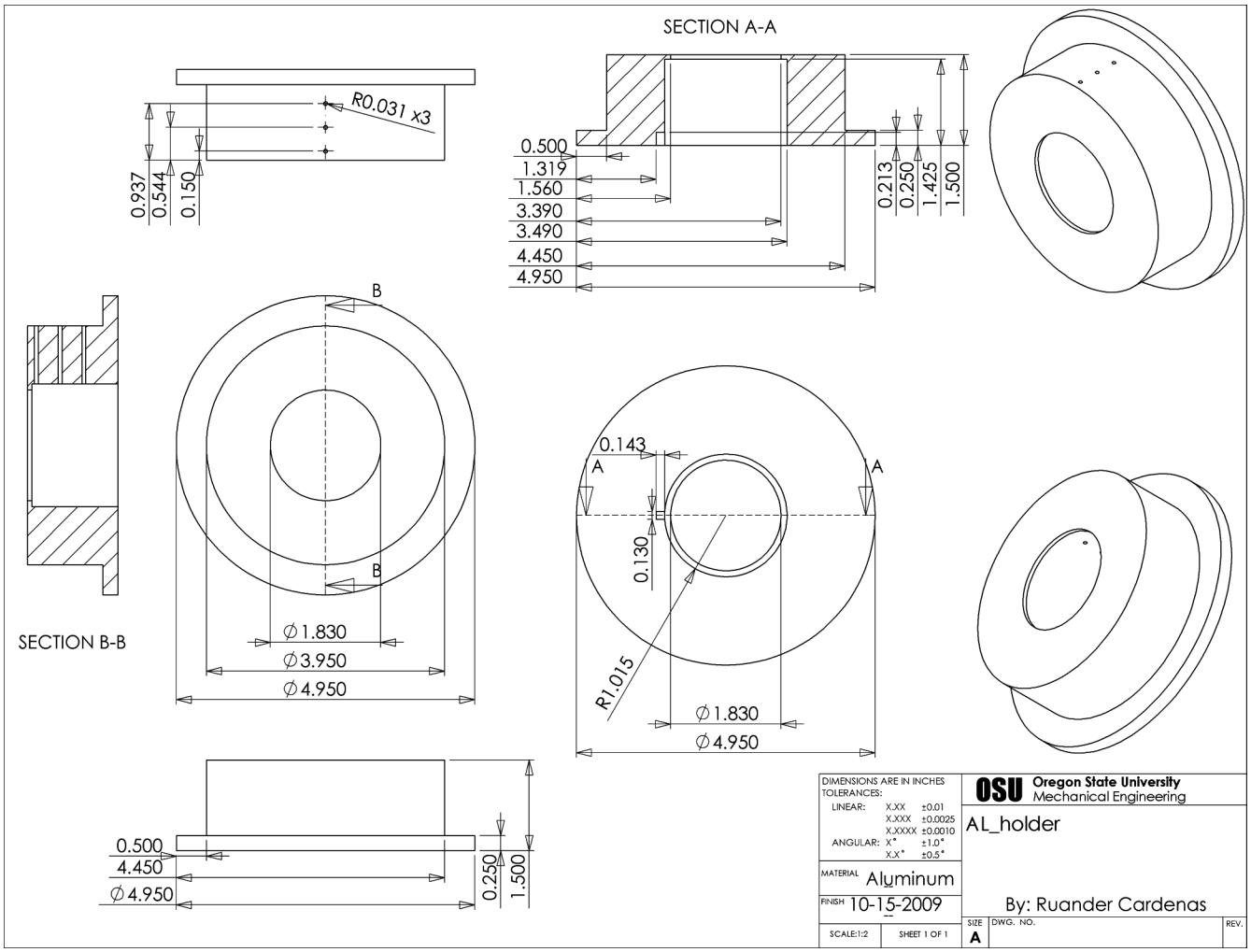

Figure A 16: Test section aluminum housing

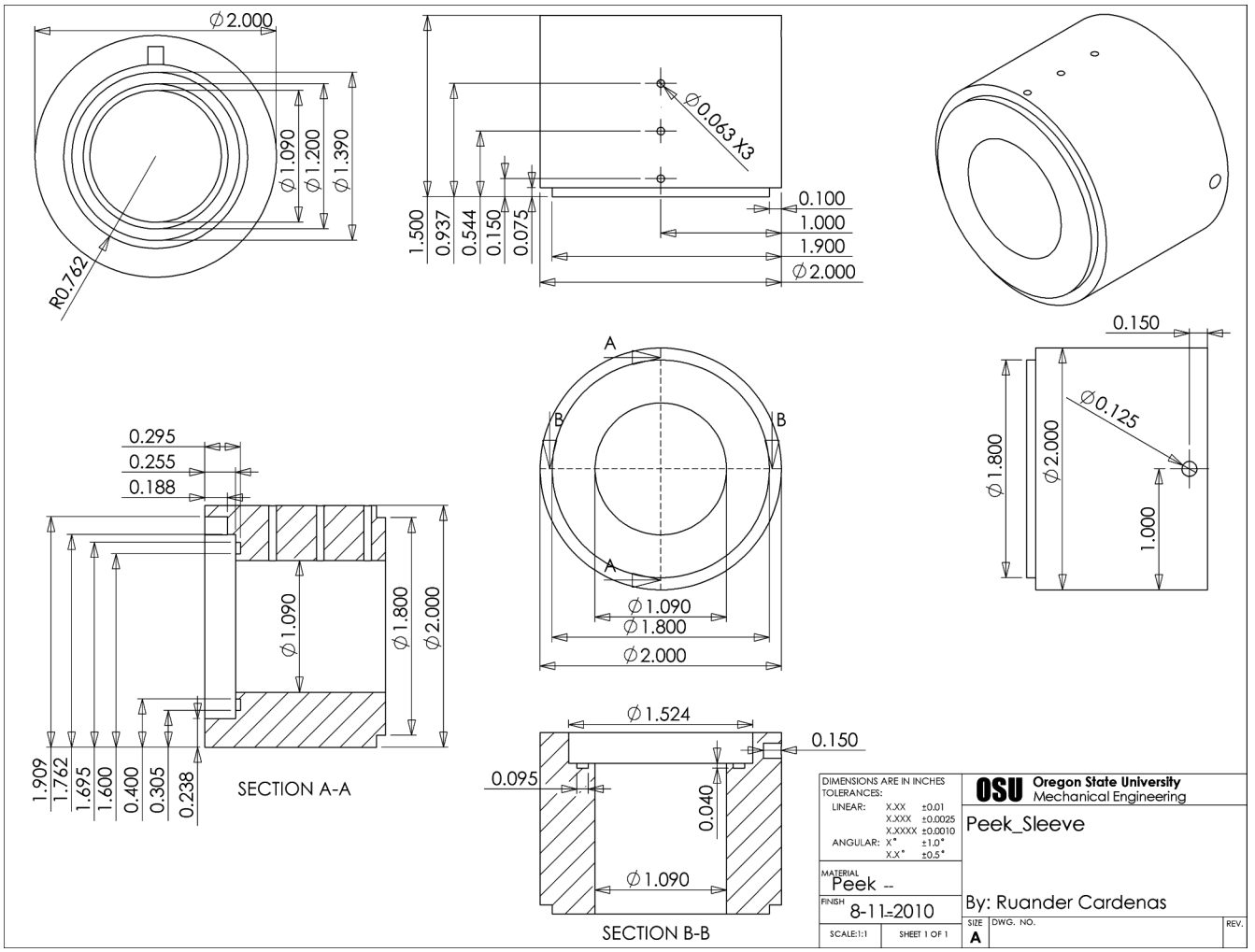

Figure A 17: Test section insulating PEEK sleeve

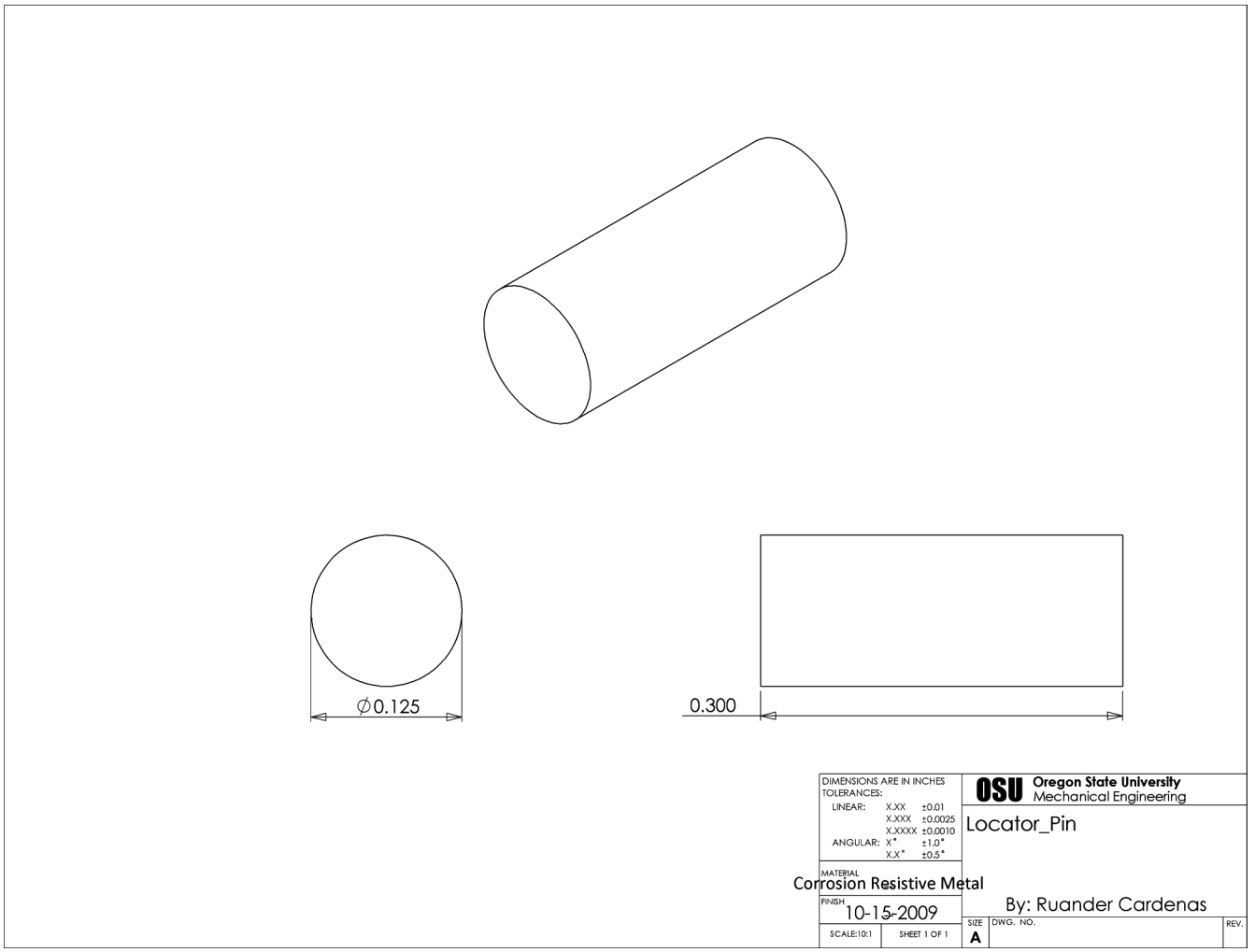

Figure A 18: Test section locator pin

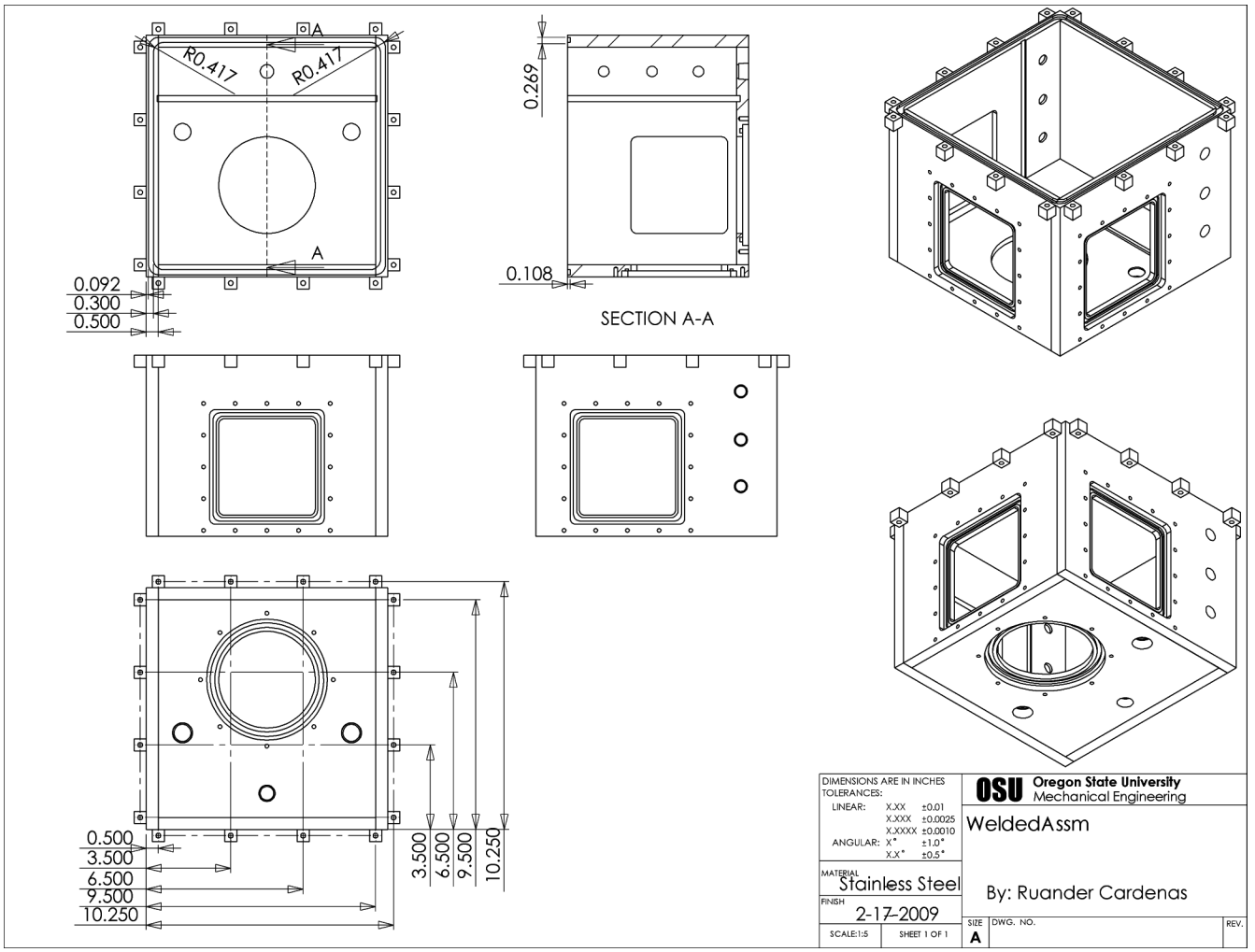

Figure A 19: Welded test chamber assembly

APPENDIX:

4. CALIBRATION CURVES

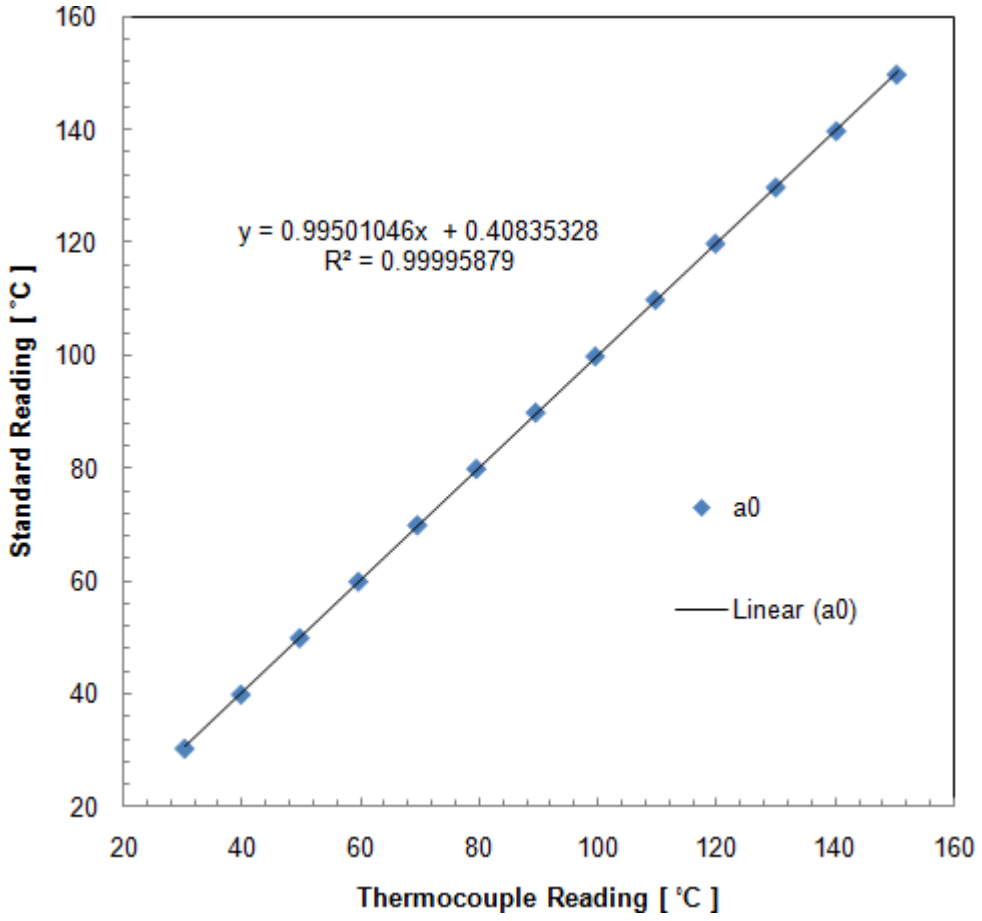

Figure A 20: Test section bottom thermocouple temperature calibration

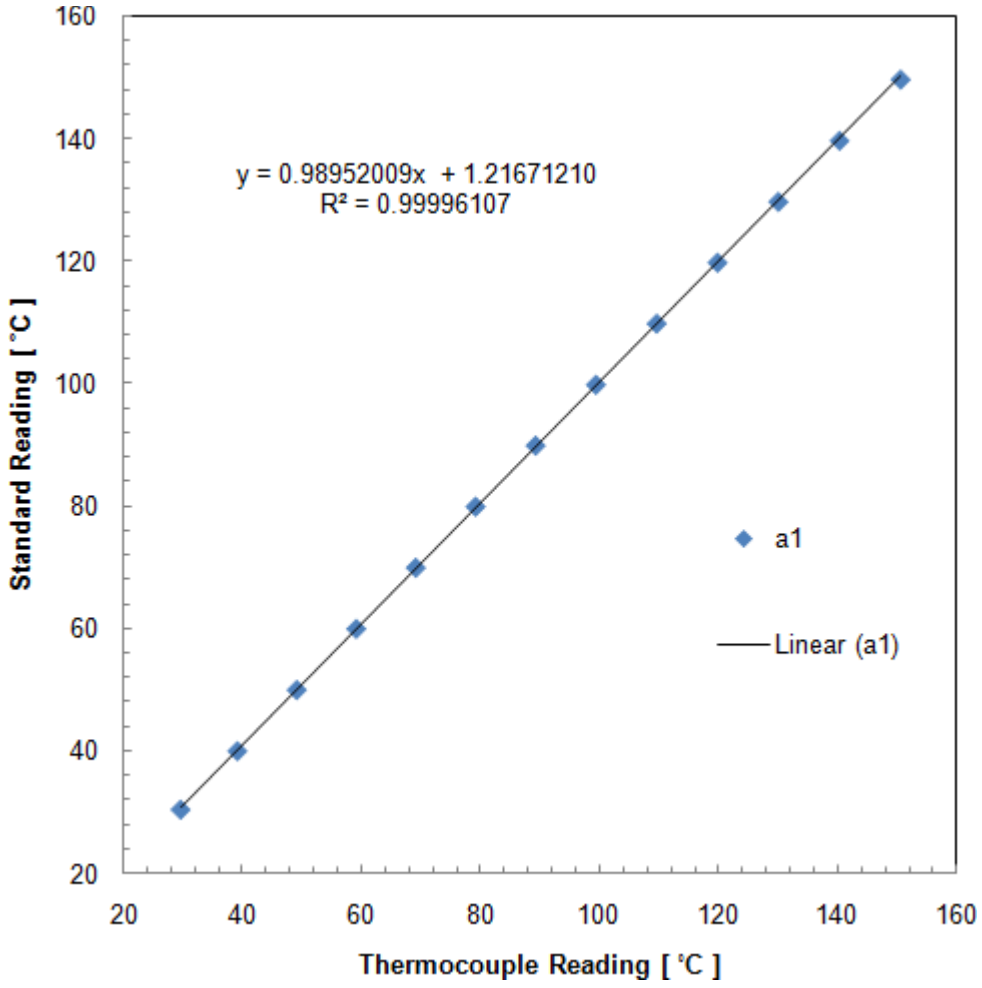

Figure A 21: Test section top thermocouple temperature calibration

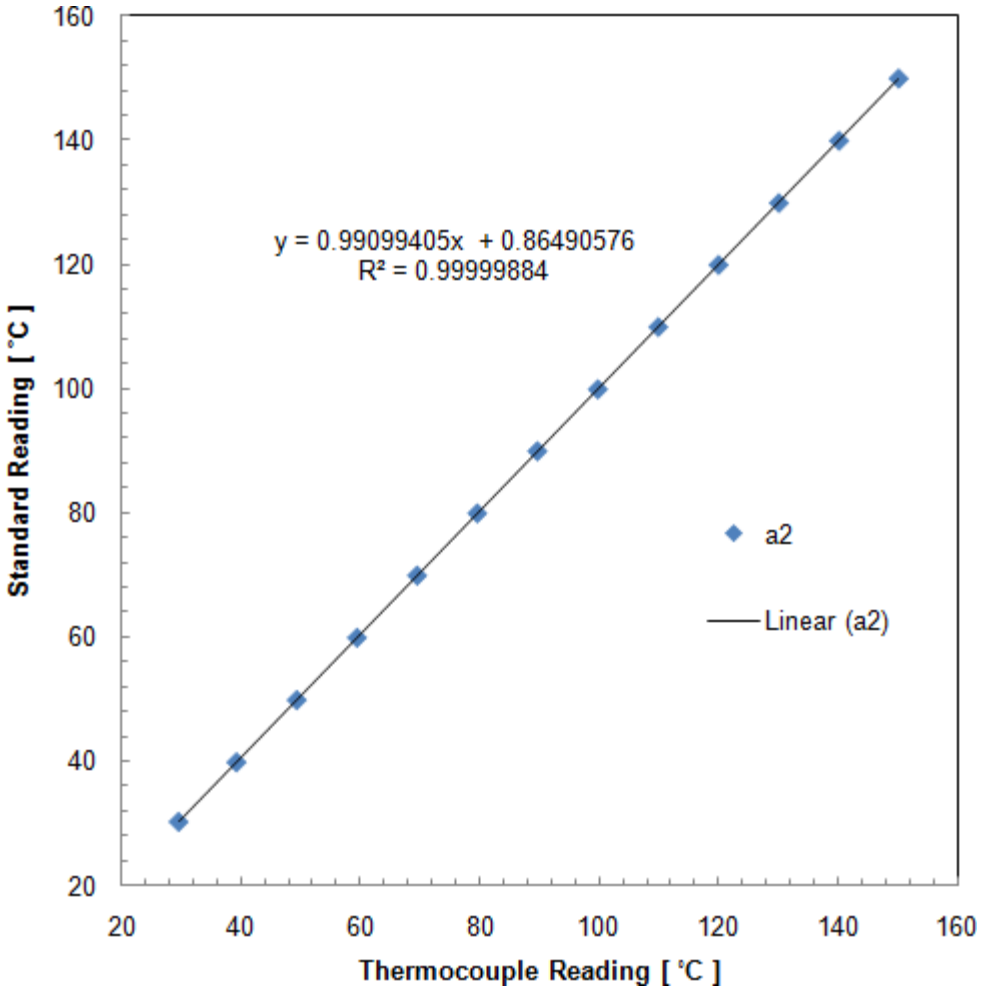

Figure A 22: Jet thermocouple temperature calibration

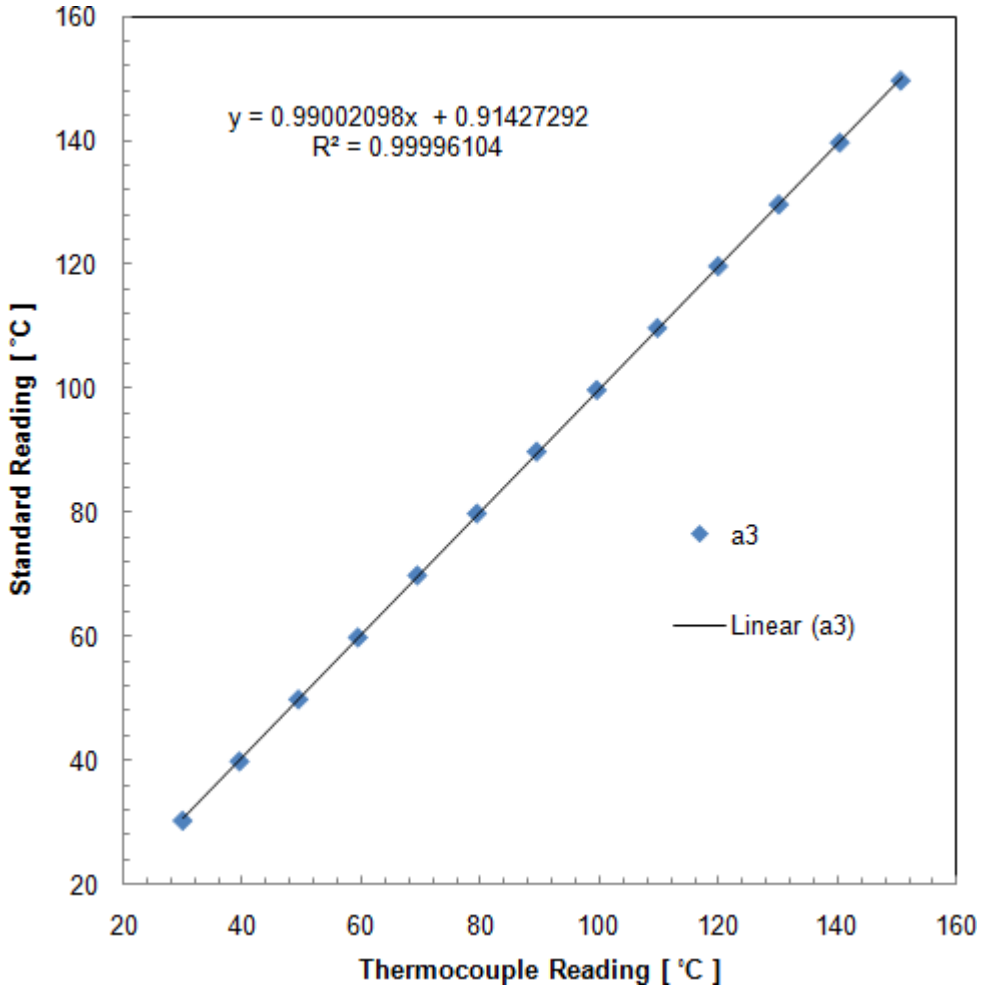

Figure A 23: Test section middle thermocouple temperature calibration

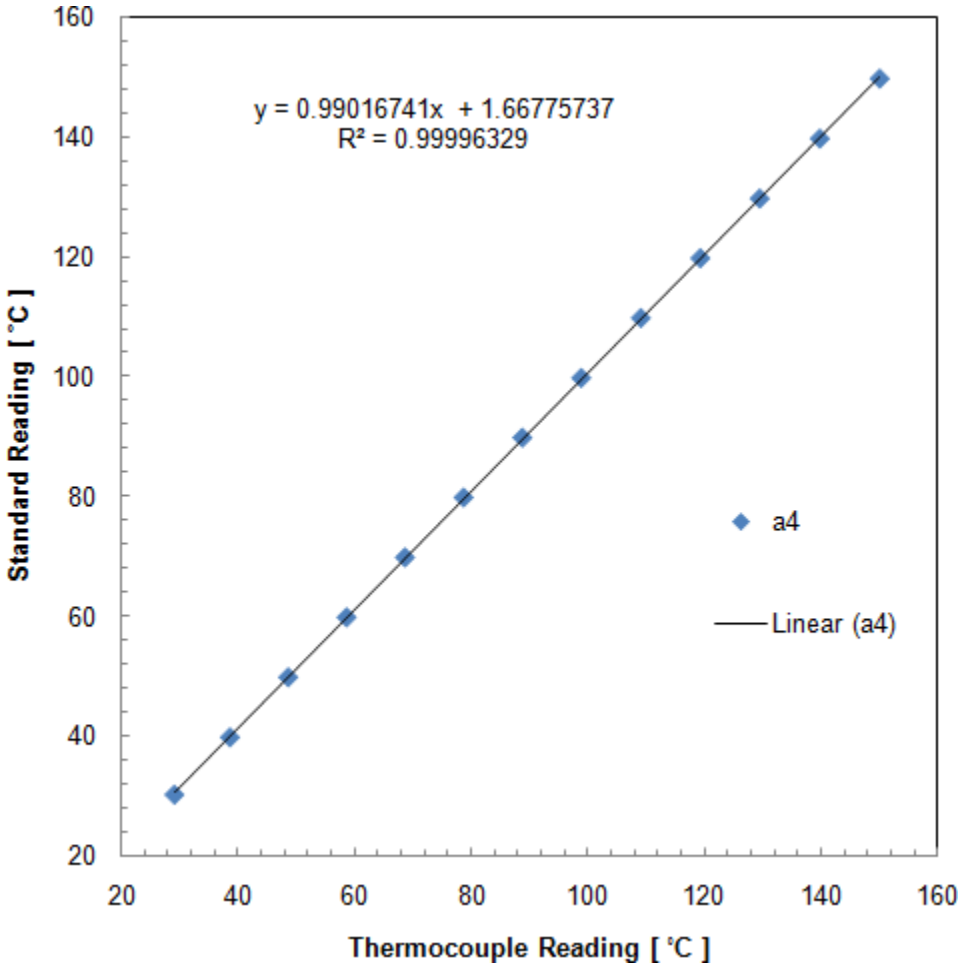

Figure A 24: Test chamber gas thermocouple temperature calibration

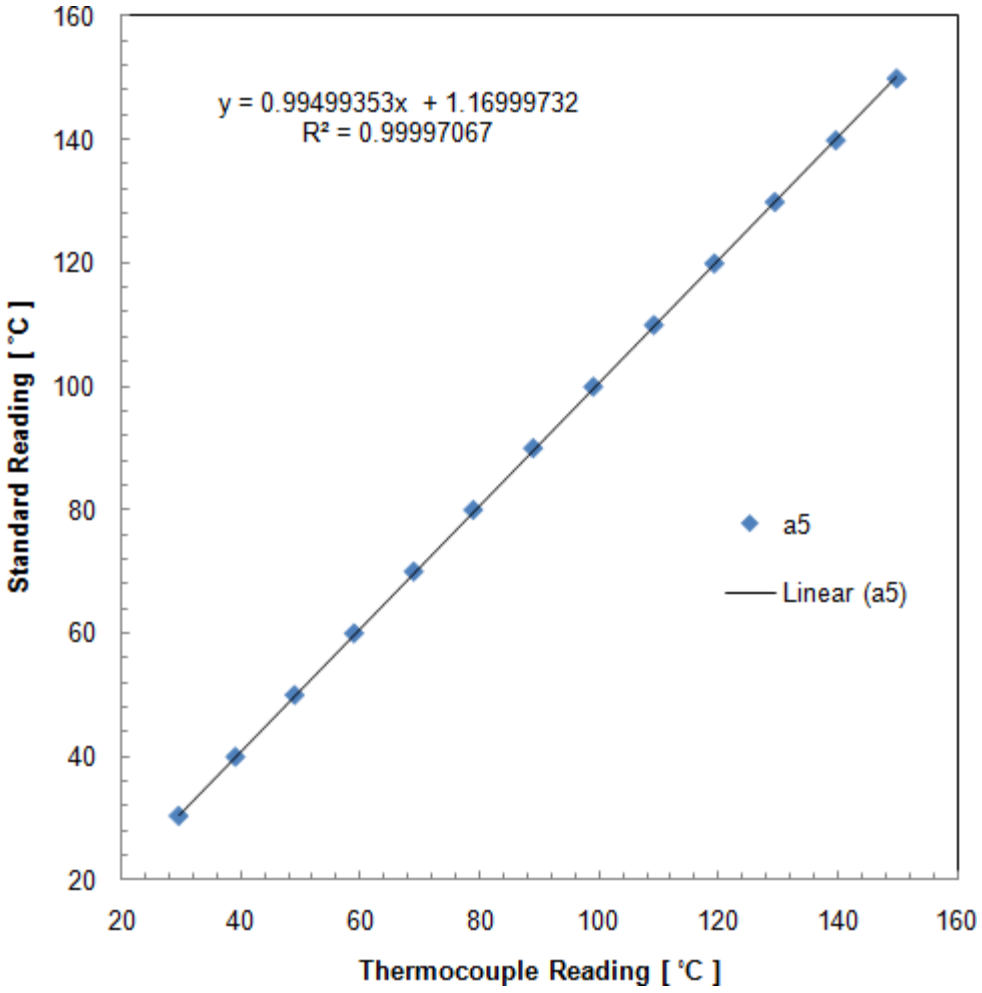

Figure A 25: Test chamber front pool thermocouple temperature calibration

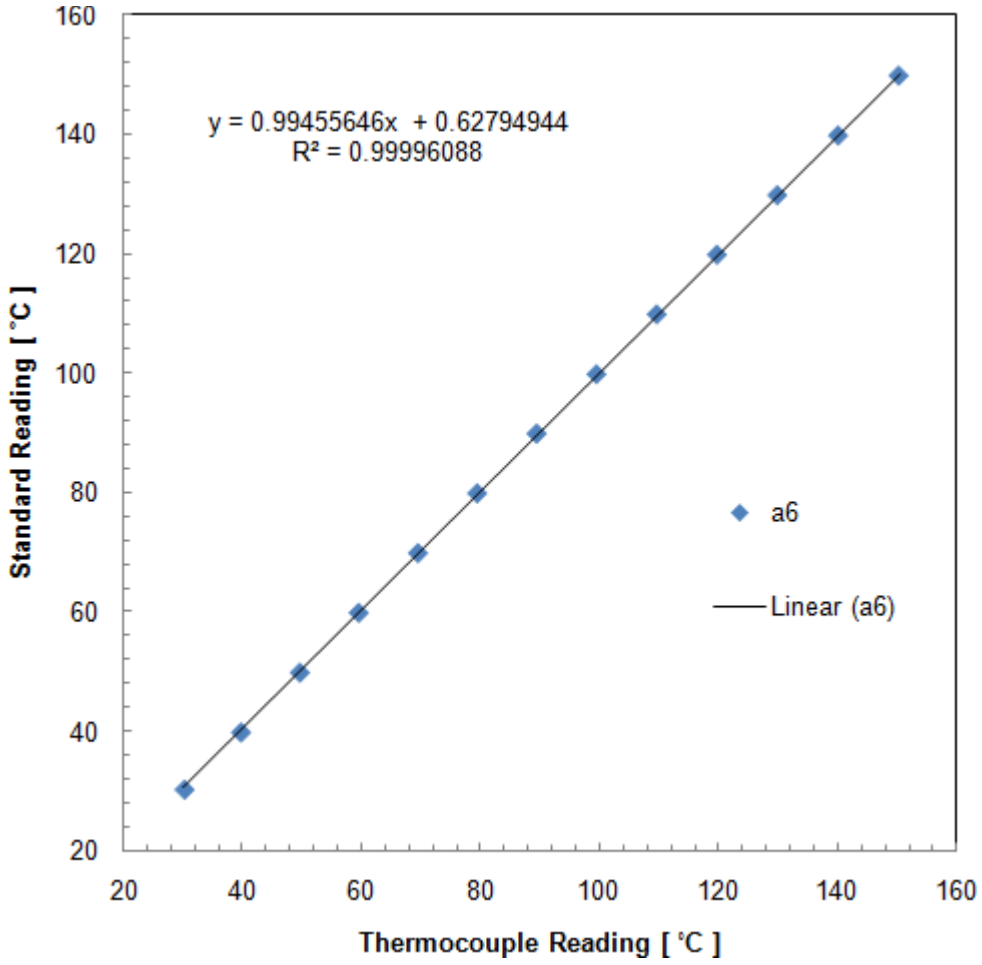

Figure A 26: Test chamber middle pool thermocouple temperature calibration

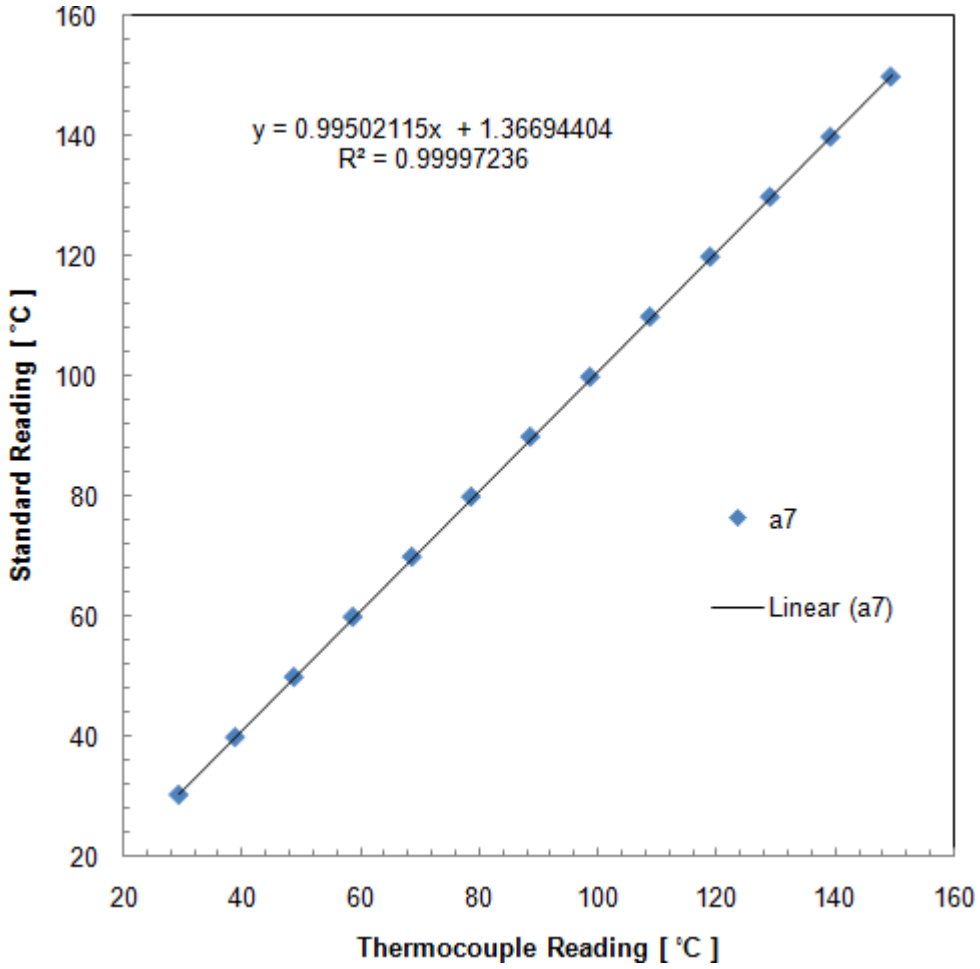

Figure A 27: Test chamber back pool thermocouple temperature calibration

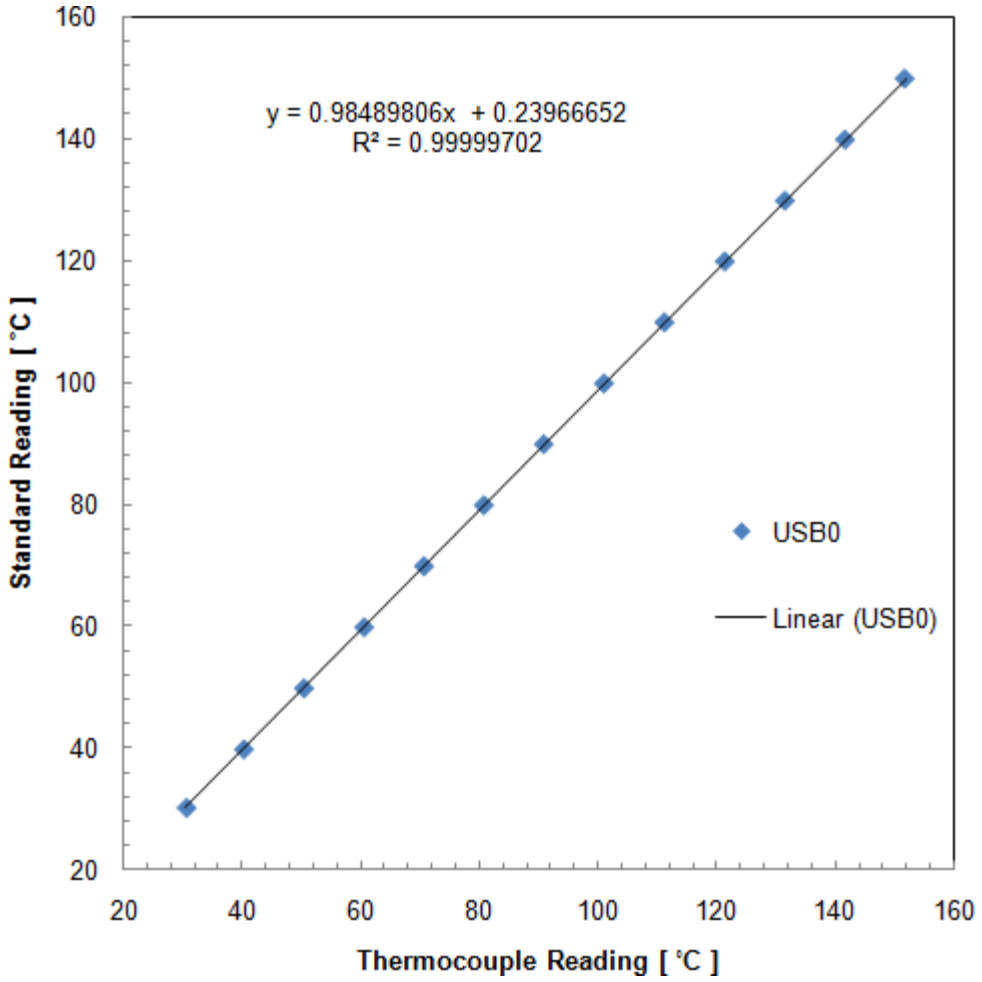

Figure A 28: Test chamber PID thermocouple temperature calibration

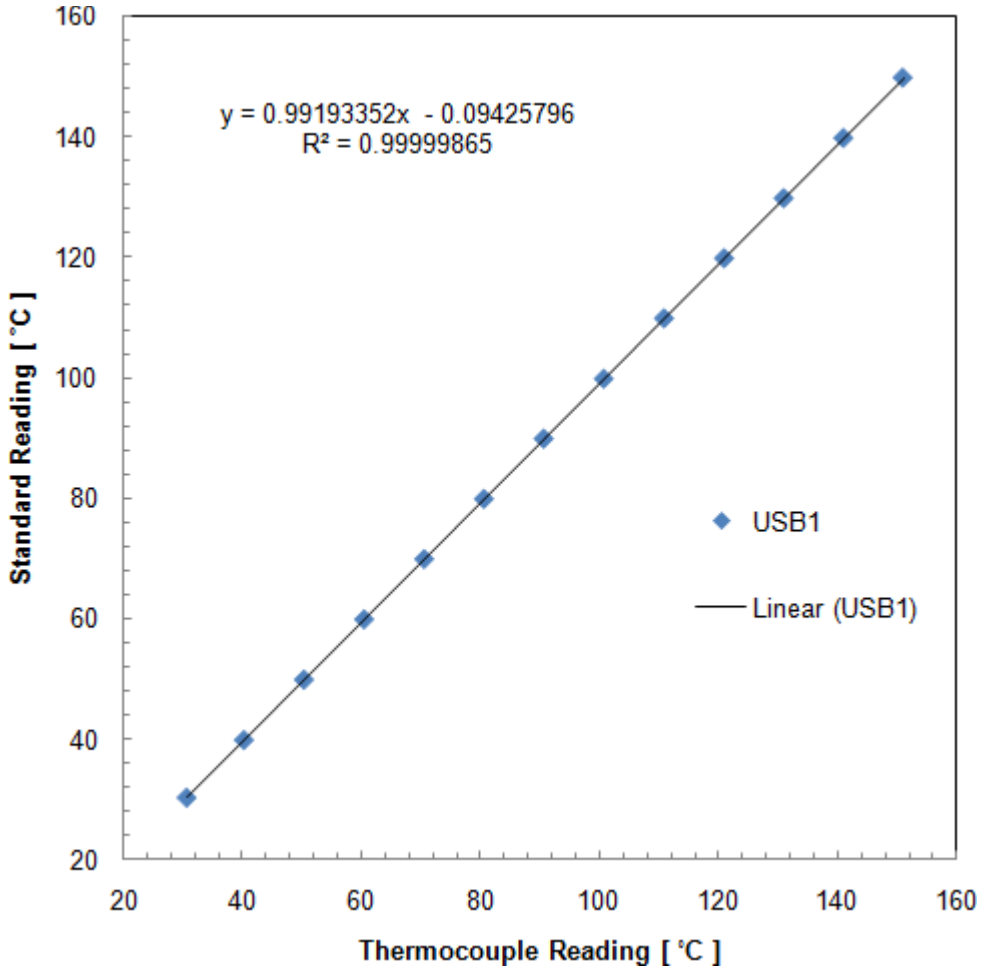

Figure A 29: Room thermocouple temperature calibration

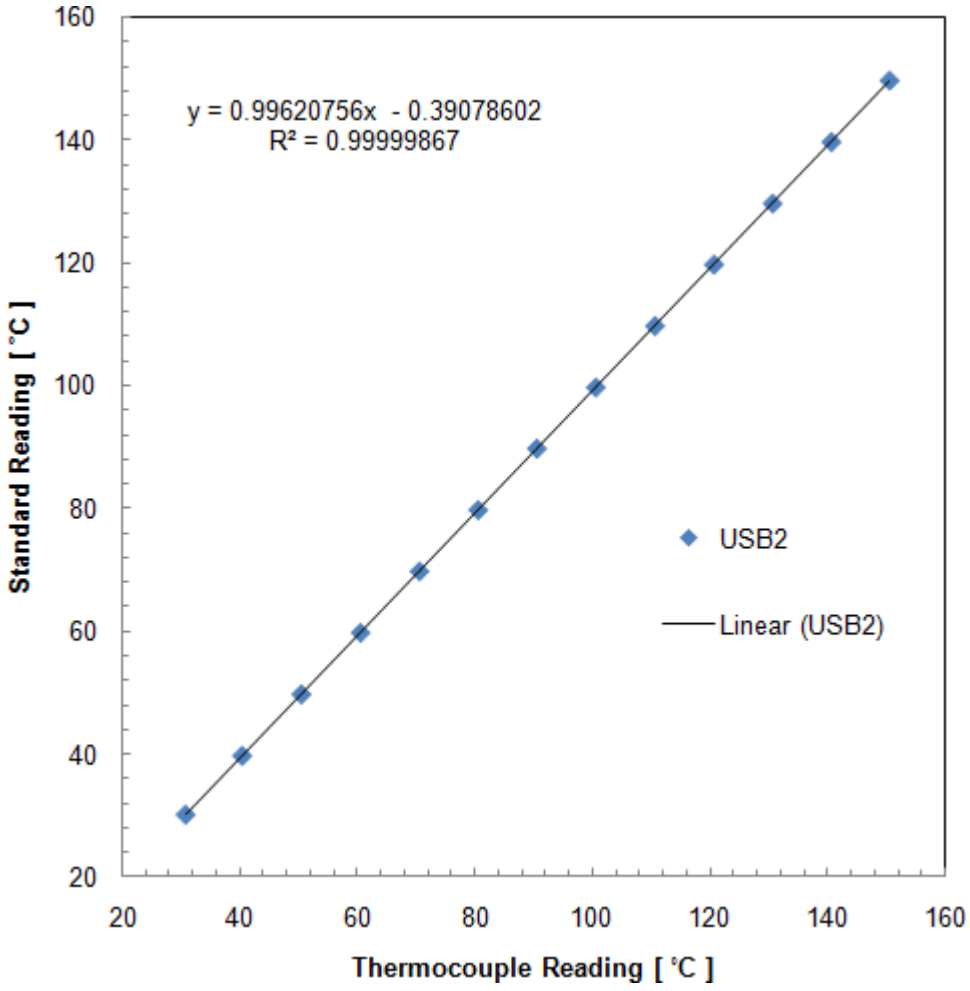

Figure A 30: Room thermocouple temperature calibration

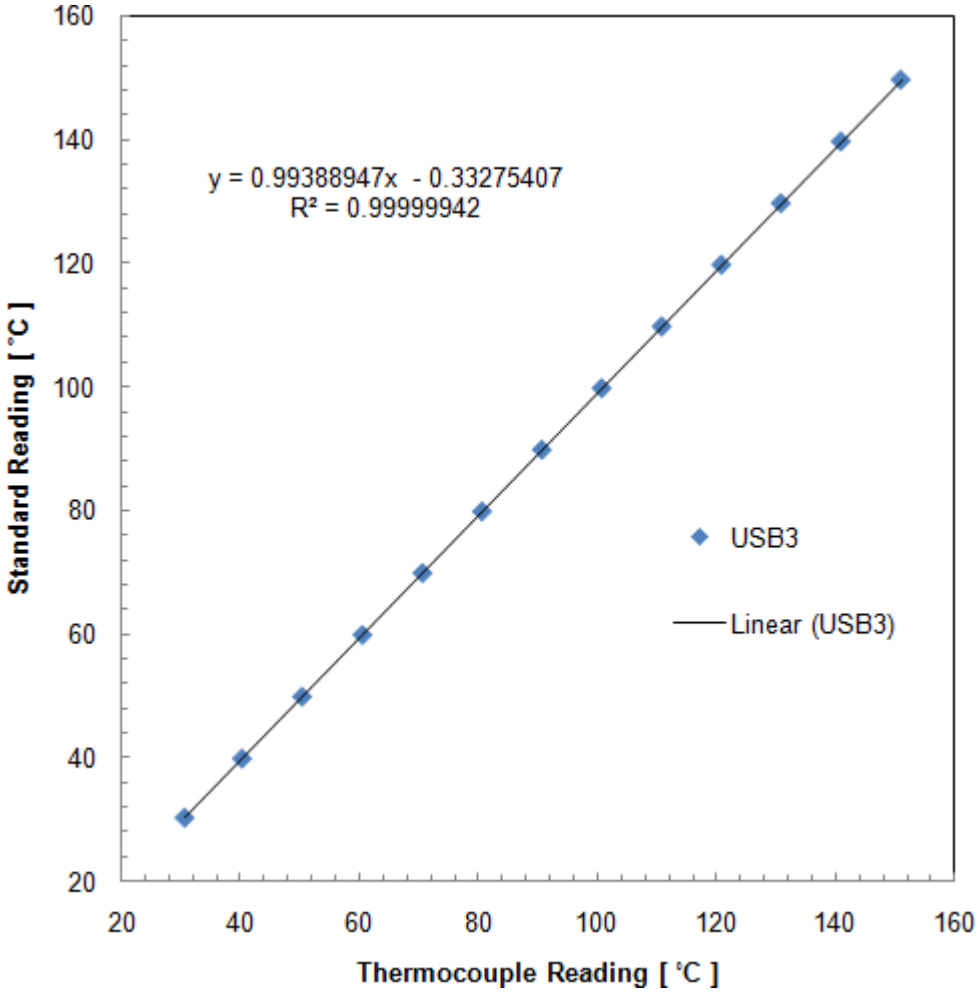

Figure A 31: Room thermocouple temperature calibration

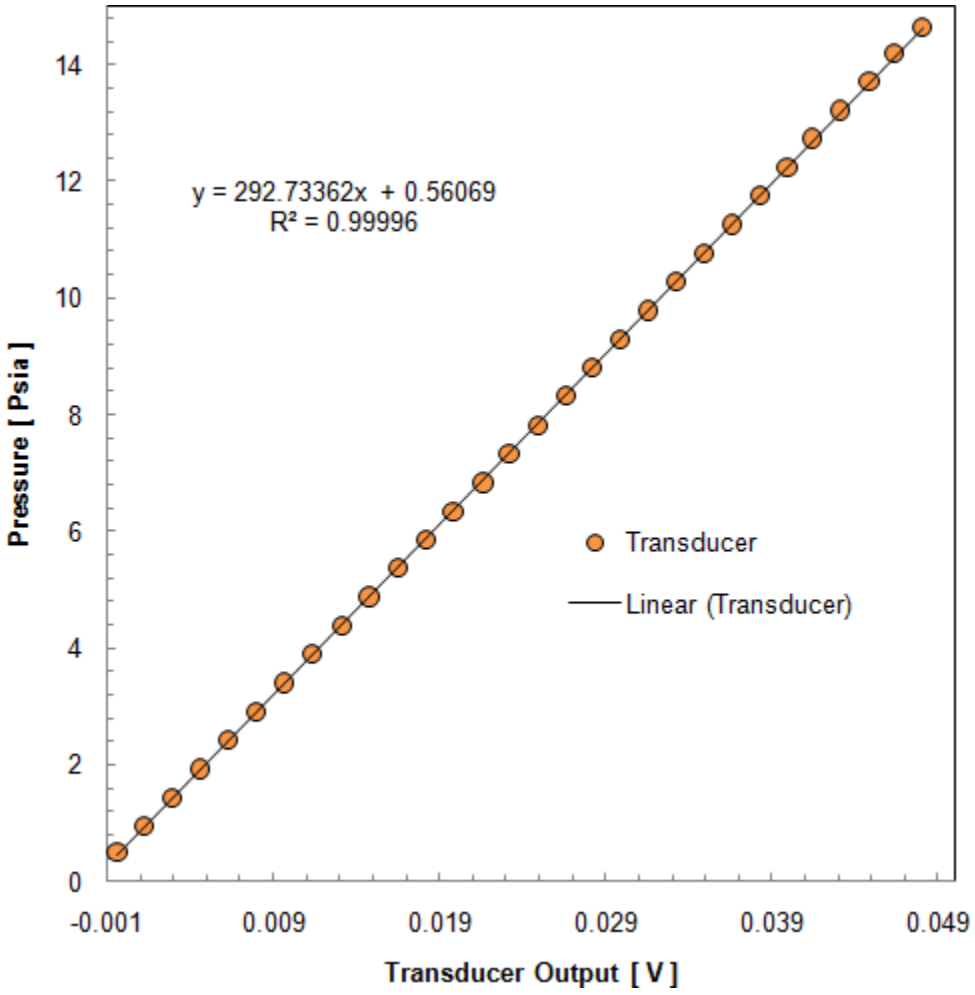

Figure A 32: Pressure transducer calibration

APPENDIX

5. FC-72 FLUID PROPERTIES

Latent heat of vaporization [44]:

$$h_{lv}=88 \text{ [kJ/kg]}$$

Specific Heat [44]:

$$Cp_l = 1014 + 1.554T\left(^oC\right) \text{ [J/kg-}^oC]$$

Thermal Conductivity [44]:

$$k_l = 0.060 - 0.00011T\left(^oC\right) \text{[W/m-}^oC]$$

Liquid Density [44]:

$$\rho_l = 1740 - 2.61T\left(^oC\right) \text{[kg/m}^3]$$

Critical Temperature (Source: email correspondence with 3M):

$$T_c=451.33 \text{ [K]}$$

Surface Tension (Source: email correspondence with 3M):

$$\sigma = 40.4609\left(1 - \frac{T(K)}{T_c}\right)^{1.2382} \text{ [mN/m]}$$

Liquid Viscosity (Source: email correspondence with 3M):

$$LZ = 10^{\left[11.9334 - 5.2769 \times \log_{10}(T(K))\right]}$$
$$Z7 = 10^{LZ} - 0.7$$
$$\nu = Z7 - \exp\left(-0.7487 - 3.295 \times Z7 + 0.6119 \times Z7^2 - 0.3193 \times Z7^3\right) \quad [cSt]$$
$$\mu = \left(\nu \times \rho_l\right) \times 10^{-6} \quad [Pa - s]$$

Saturated vapor density [3]:

$$\rho_v = 13.43 \text{ [kg/m}^3]$$

APPENDIX:

6. COMPARISON OF JOINT CHF MODEL WITH DATA

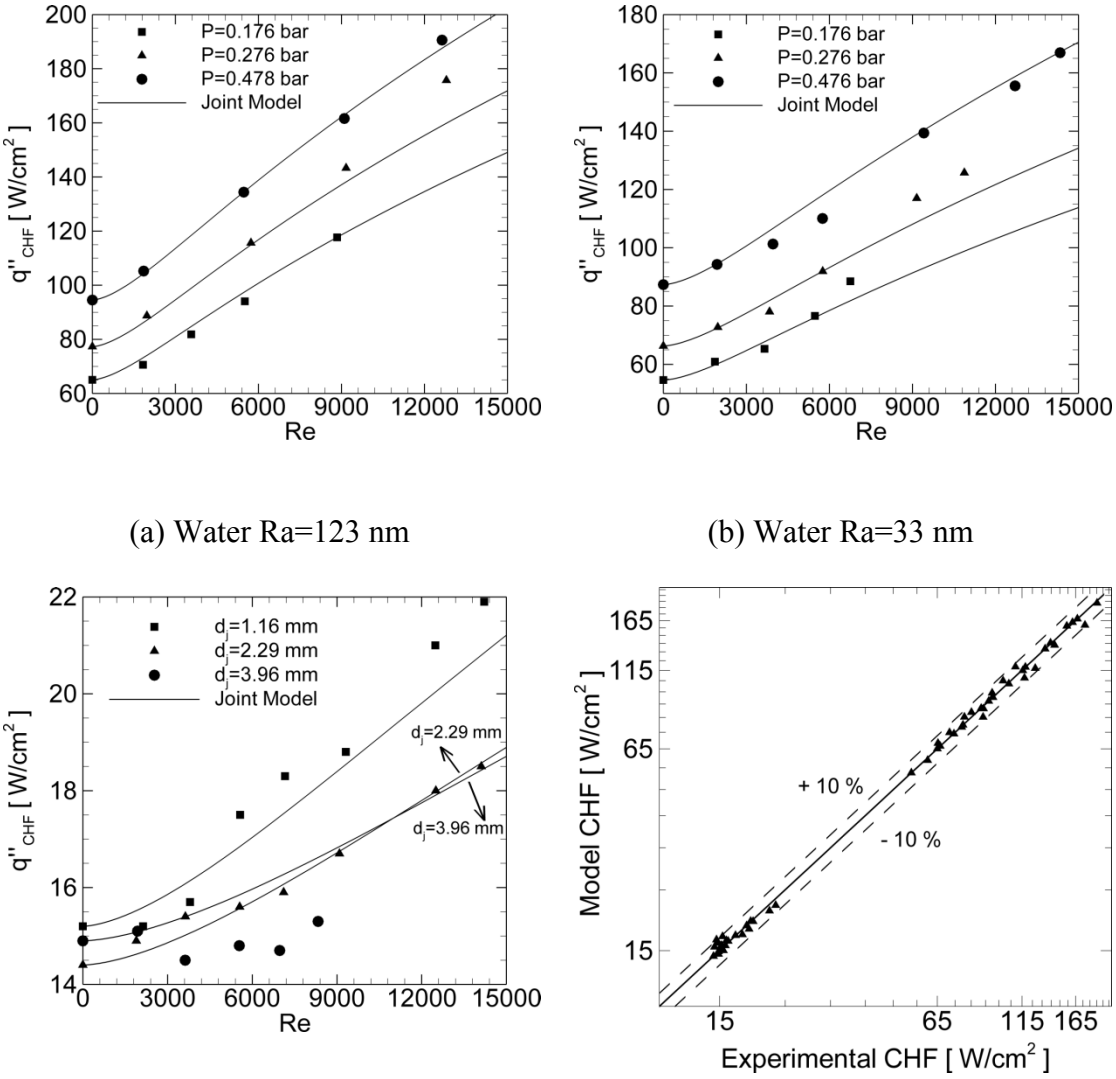

(a) Water Ra=123 nm

(b) Water Ra=33 nm

(c) FC-72 Ra=33 nm

(d) General predictions from joint model

Figure A 33: Comparison of joint CHF model with jet impingement CHF data